CRANFIELD UNIVERSITY

SCHOOL OF ENGINEERING

PhD THESIS

Academic Year 2008-2009

J. Gomez-Parada

Parametric Analysis of the Drag Produced by a VHBR Engine using CFD

Supervisors:
S. Ogaji
R. Singh

October 2009

CRANFIELD UNIVERSITY

SCHOOL OF ENGINEERING

PhD THESIS

Academic Year 2008-2009

J. Gomez-Parada

Parametric Analysis of the Drag Produced by a VHBR Engine using CFD

Supervisors:
S. Ogaji
R. Singh

October 2009

Every great achievement is the victory of a flaming heart.

Ralph Waldo Emerson

i. Abstract

The future of the civil aeronautics industry will be determined by the decreasing oil supplies around the world and by more environmentally friendly aircraft designs. Future Gas Turbine engines are being designed focusing on the fuel economy reducing emissions and noise.

This project is on the application of Computational Fluid Dynamics (CFD) techniques to the computation and parametric analysis of drag produced by the nacelle of Very High By-pass Ratio (VHBR) engines as integrated into the airframe. Engines based on VHBR concept are consistent with the objectives of VITAL which is an EU project for creating environmentally friendly engine without SFC penalties or impairing other benefits. Three main architectures for the fan were considered for the task, a geared turbofan, contra rotating turbofan and direct drive turbofan. The long range geared turbofan is the one considered in this project.

Increasing the BPR for turbofan engines is one of the best options for decreasing the SFC and noise produced by the power plant, unfortunately there are some issues to be considered. One of the major drawbacks when the BPR reaches very high values (VHBR) is the integration to the airframe because of the very large size of the fan. The drag produced by the nacelle has to be countered with propulsive force and therefore decreasing the propulsive efficiency and increasing the SFC.

CFD can be used for parametric analysis of drag produced by turbofan nacelles. The analysis was carried out in 3 basic stages. 2D geometry analyses of the afterbody and forebody are the first stage. Small changes to the basic geometry parameters were made in order to form conclusions about which parameters are more significant for drag generation in each section of the nacelle.

In the second stage of the project a 3D geometric analysis was carried out with the whole nacelle. The important parameters from the 2D simulations and some of the parameters required for 3D geometry were varied in the analysis. Conclusions were made about the influence of each of the parameters in drag generation and their influence on the interaction between forebody and afterbody.

In the third stage of the project, the influence on drag of the positioning of the engine relative to the wing is analyzed. No geometry changes were made and no pylon was used.

Conclusions were made from the changes of pressure distribution and supersonic zones and their impact on the drag.

ii. Acknowledgements

I would like to thank The National Council for Science and Technology of Mexico (CONACYT) for the financial support during my studies.

Thanks also to all of my friends giving support to me during the good and bad times in Cranfield, especially Jacinto, Osvaldo, Edwin, Quike, Birute, Lydiane, Nafsika, Hara, Sharon, Matthieu, Dimitrious and Joanna. Special thanks to those close friends that were not only a moral support but also academic, without them this project would have never been finished. Fernando Colmenares, always a friend helping me to stay on the right track. Birute Bunkute, she always provided me her knowledge and shoulder to keep on standing.

I have learnt a great deal from those lecturers and researchers working with me over these years and gratefully acknowledge my debt to them, especially Stephen Ogaji, Pericles Pilidis, Philip Rubini, Riti Singh and Darrell Williams. Special mention has to be made of Mark Savill, his guidance was a real breakthrough during my work. Thanks to Mark's knowledge and support I was able to continue until the end.

Everyone in Mitchell Hall and Cranberries staff were very important to me. They are like my family. They not only gave food to me, they also helped me to keep on smiling during all of these years.

To those of you who already passed away but are still with me. Manchas, please keep behind me on the uphill and in front of me on the downhill. Abi, keep on praying, you are with me, always. Grandfather, you are the best engineer I have ever met, I will keep on wearing your hat.

My family is always the most important. My mom, when I was happy she was there, when I was crying she was there, she has always been there. Betsa, my little sister, I specially love that girl always in parties and having fun. Cesar, my brother, is always working but also staying there when support for me was needed. Sosa family, forever my other family. My dad, is my database of knowledge when I need him.

For all of you, and anyone else I might have forgotten, receive my eternal gratitude.

iii. List of Contents

i. Abstract i
ii. Acknowledgements iii
iii. List of Contents iv
iv. List of Figures viii
v. List of Tables xv
vi. List of Symbols and abbreviations xvi
vii. Subscripts xviii
1 Introduction 1
1.1 EnVIronmenTALly Friendly Aero Engine (VITAL) 2
1.1.1 Integration of the Engine into the Airframe 3
1.2 Objectives of the project 3
1.3 Contribution to knowledge 4
1.3.1 Achievements 4
2 Contribution to knowledge 6
3 Methodology 8
3.1 Literature review 9
3.2 2D Analysis 9
3.2.1 Choosing parameters to be analyzed 10
3.2.2 Afterbody methodology 10
3.2.3 Forebody methodology 11
3.2.4 Results Analysis 11
3.3 3D Isolated Nacelle Analysis 11
3.3.1 CAD geometry generation 12
3.3.2 Mesh generation 12

3.3.3 Parametric calculations 12
3.3.4 Results analysis 13
3.4 3D Integrated Nacelle Analysis 13
3.4.1 WB Analysis 13
3.4.2 WBN Analysis 14
4 Literature Review 18
4.1 VHBR Engine 18
4.2 Installation of the propulsion system 21
4.2.1 Drag 23
4.2.2 Interference Effects 27
4.2.3 Integration Methodology 29
4.3 CFD 34
4.3.1 Turbulence modelling 37
4.3.2 Use of Computational Fluid Dynamics for integration 40
4.3.3 Grid Generation 44
5 Isolated nacelle (2D simulations) 45
5.1 Geometric Model Design 45
5.1.1 Forebody profile 46
5.1.2 Afterbody profile 47
5.2 Parameters variation 48
5.3 Meshing strategy 49
5.3.1 Afterbody 49
5.3.2 Forebody 51
5.4 CFD 54
5.4.1 Simulation Parameters and Solver 54

5.4.2 Convergence 55
5.5 Initial Conditions 56
5.6 y+ parameter 57
5.7 Afterbody simulations 57
5.7.1 Main parameters 57
5.7.2 Mesh Dependency Analysis 58
5.7.3 y+ analysis 61
5.7.4 Parameters to be analyzed 61
5.7.5 Results and analysis 63
5.8 Forebody simulations 70
5.8.1 Main parameters 70
5.8.2 Mesh Dependency Analysis 71
5.8.3 y+ analysis 73
5.8.4 Parameters to be analyzed 74
5.8.5 Results and analysis 76
6 Isolated Nacelle (3D simulations) 83
6.1 Geometry 83
6.1.1 Parameters analyzed 85
6.2 Grid Generation 86
6.2.1 Meshing strategy 86
6.3 Simulation setup 88
6.3.1 Boundary conditions 88
6.3.2 Solver 90
6.3.3 Convergence Analysis 90
6.4 Result analysis 91

6.4.1 Maximum Diameter (Dmax) change analysis 94
6.4.2 Highlight Diameter (Dhigh) change analysis 101
6.4.3 Total nacelle length variation analysis 108
7 Integrated Nacelle to an airframe 115
7.1 Introduction 115
7.2 Methodology 116
7.3 Geometry 116
7.4 Meshing strategy 118
7.4.1 WB system grid 118
7.4.2 WBN grid 120
7.5 Simulation Setup 121
7.6 Simulation 122
7.6.1 Convergence 122
7.7 Parameters 124
7.8 Results and analysis 126
8 Final Observations 139
9 Conclusions 141
10 Further work 143
11 References 145
12 Appendixes 153
A. Mach Number Contours of 3D Isolated Nacelle simulations 153
B. Profiles of Cp and Ma number of 3D Isolated Nacelle simulations 165
C. Cp profiles at the far section of the wing (w/Dmax=6.3). 171

iv. List of Figures

Figure 4.1 Optimization of fan pressure ratio (Cohen, 1987, p. 99) 19
Figure 4.2 Relation between Efficiency and Bypass Ratio (Lecordix, 1992) 20
Figure 4.3 Fuel consumption improvements (Burgsmueller, 1996) 21
Figure 4.4 Installed Nacelle Components (Mullender, 1996) 22
Figure 4.5 All of the forces acting on a short cowl nacelle 26
Figure 4.6 Forebody forces 27
Figure 4.7 Afterbody forces 27
Figure 4.8 Spanwise lift distribution with and without nacelles (Rossow, 1992) 28
Figure 4.9 Variation of Interference Drag with Engine Bypass Ratio for a given application (Cedar, 1993) 29
Figure 4.10 Relation between the Interference Drag and the position of the engine (Rossow, 1994) 29
Figure 4.11 Factors influencing nacelle installation design (Berry, 1994) 30
Figure 4.12 Decomposition for Thrust/Drag bookkeeping (von Geyr, 2005) 32
Figure 4.13 Pressure based solver, segregated and coupled algorithms (Fluent 6.2 Documentation, 2007) 35
Figure 4.14 Density based solver (Fluent 6.2 documentation, 2007) 36
Figure 4.15 Grids for an isolated Inlet and an installed Nacelle (Joubert, 1993) 42
Figure 4.16 Chimera Grid generation Technique (Cedar, 1993) 43
Figure 4.17 Capabilities of different numerical approaches (Rudnik, 2002) 43
Figure 5.1 Super ellipse parameters 47
Figure 5.2 Nacelle design parameters 48
Figure 5.3 Afterbody grid zones (Coarse mesh shown) 50
Figure 5.4 Grids created in order to evaluate the mesh independence of the nozzle. 51
Figure 5.5 Forebody meshing sections 53
Figure 5.6 Three meshes created to analyze the mesh independency 54
Figure 5.7 Simulation residuals got asymptotic (Afterbody simulation shown) 55
Figure 5.8 Drag Coefficient Convergence criterion (Afterbody simulation shown) 56
Figure 5.9 Boundary Conditions for The afterbody (not to scale) 58

Figure 5.10 Comparison of the Cf for the afterbody 59
Figure 5.11 Comparison of the Cp for the afterbody 60
Figure 5.12 The y+ parameter for one of the Afterbody simulations 61
Figure 5.13 Afterbody contours of Pressure Coefficient 63
Figure 5.14 Afterbody contours of Mach number for a small maximum diameter nacelle . 64
Figure 5.15 After body contours of Mach number for a large maximum diameter nacelle . 64
Figure 5.16 Comparing the Viscous drag coefficient changing the maximum diameter 66
Figure 5.17 Comparing the Viscous drag coefficient changing the exhaust angle 67
Figure 5.18 Pressure profiles over the Afterbody for changing of maximum diameter 68
Figure 5.19 Influence of Dmax on viscous, pressure and drag coefficients on the AB 68
Figure 5.20 Pressure profiles over the Afterbody for changing of exhaust angle 69
Figure 5.21 Drag change for the change of the maximum diameter and the bypass exhaust angle 70
Figure 5.22 Forebody boundary conditions (not to scale) 71
Figure 5.23 Forebody Cf comparison for the mesh independence analysis 72
Figure 5.24 Forebody Cp comparison for the mesh independence analysis 72
Figure 5.25 Comparing the Cf and Cp of the coarse and medium meshes with the fine one 73
Figure 5.26 Y+ analysis for the Forebody 74
Figure 5.27 Drag Change with respect to the lip length 74
Figure 5.28 Mach number profiles for a forebody model 76
Figure 5.29 Pressure coefficient profiles for a forebody model 77
Figure 5.30 Velocity vectors at the highlight point of an intake 77
Figure 5.31 Supersonic areas for a small Dmax with a small (left) and large (right) Dhigh 78
Figure 5.32 Supersonic areas for a large Dmax with a small (left) and large (right) Dhigh 78
Figure 5.33 Change of total drag changed by the variation of Dmax and Dhigh 80
Figure 5.34 Variation of pre entry force (drag) with respect of the change of Dhigh and Dmax 81
Figure 5.35 Change of Drag and its components related to the variation of the throath diameter. 82
Figure 5.36 Drag and its components variation due to a change of intake cowl length 82

Figure 6.1 Isolated nacelle domain dimensions..... 86
Figure 6.2 Annular shape of every block of the domain. 87
Figure 6.3 Mesh at the symmetry plane. The areas filled with red colour are where an unstructured mesh was used. 88
Figure 6.4 Boundary conditions (image not to scale)..... 89
Figure 6.5 Side view of a short bypass nacelle, the top part of it is called the crown section and the lower part the keel section. 91
Figure 6.6 Total nacelle force change with respect of the change of each of the analysis parameter 93
Figure 6.7 Pre-entry drag change with respect of the change of each of the analysis parameter 93
Figure 6.8 Mach number profiles of the side section of the nacelle of a Maximum diameter of - 6.0 % change with respect to the reference nacelle. (Mach number profiles are in the range of 0.6 and lower for blue to 1.2 and higher for red). 94
Figure 6.9 Mach number profiles of the side section of the nacelle of a Maximum diameter of + 6.0 % change with respect to the reference nacelle. (Mach number profiles are in the range of 0.6 and lower for blue to 1.2 and higher for red). 95
Figure 6.10 Axial component of viscous force changes at the Afterbody (AB), Midbody (MB) and Forebody (FB) for Dmax change percentage..... 97
Figure 6.11 Pressure coefficient profiles along the crown (a), side (b) and keel (c) sections of the four nacelles shown with the percentage change of maximum diameters. 99
Figure 6.12 Change of pressure force on the Afterbody and Forebody related to the change of the daximum diameter..... 100
Figure 6.13 Total force applied to each of the nacelle sections. 101
Figure 6.14 Mach number profiles of the side section of the nacelle of a Highlight diameter of - 6.0 % change with respect to the reference nacelle. (Mach number profiles are in the range of 0.6 and lower for blue to 1.2 and higher for red). 102
Figure 6.15 Mach number profiles of the side section of the nacelle of a Highlight diameter of + 6.0 % change with respect to the reference nacelle. (Mach number profiles are in the range of 0.6 and lower for blue to 1.2 and higher for red). 103

Figure 6.16 Applied viscous force changes at the three sections of the nacelle versus the percentage of highlight diameter change. 104
Figure 6.17 Pressure coefficient profiles along the crown (a), side (b) and keel (c) sections of the four nacelles shown with the percentage change of highlight diameters. 105
Figure 6.18 Pressure force changes over the forebody and afterbody related to the highlight diameter changes. 106
Figure 6.19 Pressure coefficient (Cp) distribution over the projected area of the FB to the axial component of the geometries with a Dhigh increase of 2.0% (left) and 6.0% (right). 107
Figure 6.20 Total force variations at the three sections of the nacelle with respect to the changes of the highlight diameter. 108
Figure 6.21 The effect of the change of total nacelle length in the viscous force. 109
Figure 6.22 Mach number profiles of the side section of the nacelle of a length of - 6.0 % change with respect to the reference nacelle. (Mach number profiles are in the range of 0.6 and lower for blue to 1.2 and higher for red). 110
Figure 6.23 Mach number profiles of the side section of the nacelle of a Length of + 6.0 % change with respect to the reference nacelle. (Mach number profiles are in the range of 0.6 and lower for blue to 1.2 and higher for red). 110
Figure 6.24 Pressure coefficient profiles along the crown (a), side (b) and keel (c) sections of the four nacelles shown with the percentage change of total nacelle length. 112
Figure 6.25 Effect of total nacelle length changes in the pressure force. 113
Figure 6.26 Effect of the total nacelle length changes in the total force. 113
Figure 6.27 Impact of the nacelle length on the viscous and pressure force percentage on total force (a) and the force of the FB, MB, and AB percentage on the total force (b). 114
Figure 7.1 MRT-7 project of Aircraft and Vehicle Design of Cranfield University 117
Figure 7.2 Simplified geometry of the MRT-7 project 118
Figure 7.3 Airframe domain 119
Figure 7.4 WB mesh 120
Figure 7.5 Integrated nacelle grid 121
Figure 7.6 Convergence criteria. (a) residuals, (b) Cd and Cl history and (c) mass flow history 123

Figure 7.7 Main parameters for engine positioning 125
Figure 7.8 Impact of penetration and vertical positioning on total drag 127
Figure 7.9 Pressure (a) and viscous force (b) on the nacelle 128
Figure 7.10 Sections of the nacelle chosen for analyzing the influence of the nacelle position on the Cp distribution 129
Figure 7.11 Selected nacelle Cp distribution lines along the nacelle of four different simulations (a) h/D=0.6, x/l=0.75 (b) h/D=0.55, x/l=0.75 (c) h/D=0.6, x/l=0.7 (d) h/D=0.6, x/l=0.8 130
Figure 7.12 Mach number profiles for nacelles positioned at (a) h/D=0.6, x/l=0.7, (b) h/D=0.6, x/l=0.8 and (c) h/D=0.5, x/l=0.8 132
Figure 7.13 Impact of penetration and vertical positioning on wing drag 134
Figure 7.14 Wing Sections analyzed (not drawn to scale) 135
Figure 7.15 Three selected wing airfoil profiles. (a) and (b) h/D=0.55, x/l=0.75, (c) and (d) h/D=0.6, x/l=0.75 and (e) and (f) h/D=0.6, x/l=0.8 136
Figure 7.16 Airfoil Cp profiles. for the nacelle of (a) h/D=0.65, x/l=0.65, at w/Dmax=2.26 (b) h/D=0.65, x/l=0.65, at w/Dmax=3.27, (c) h/D=0.65, x/l=0.7, at w/Dmax=2.26 and (d) h/D=0.65, x/l=0.7, at w/Dmax=2.26 137
Figure 7.17 Detailed profiles of Mach number for the simulations of (a) h/D=0.65, x/l=0.65 and (b) h/D=0.65, x/l=0.7 137
Figure 7.18 Impact of penetration and vertical positioning on interference drag. 138
Figure A. 1 Mach number profiles of the Crown (top), Side (middle) and keel (bottom) sections of the nacelle of a Maximum diameter of - 6.0 % change with respect to the reference nacelle. 153
Figure A. 2 Mach number profiles of the Crown (top), Side (middle) and keel (bottom) sections of the nacelle of a Maximum diameter of - 2.0 % change with respect to the reference nacelle. 154
Figure A. 3 Mach number profiles of the Crown (top), Side (middle) and keel (bottom) sections of the nacelle of a Maximum diameter of + 2.0 % change with respect to the reference nacelle. 155

Figure A. 4 Mach number profiles of the Crown (top), Side (middle) and keel (bottom) sections of the nacelle of a Maximum diameter of + 6.0 % change with respect to the reference nacelle 156
Figure A. 5 Mach number profiles of the Crown (top), Side (middle) and keel (bottom) sections of the nacelle of a Highlight diameter of -6.0 % change with respect to the reference nacelle. 157
Figure A. 6 Mach number profiles of the Crown (top), Side (middle) and keel (bottom) sections of the nacelle of a Highlight diameter of - 2.0 % change with respect to the reference nacelle. 158
Figure A. 7 Mach number profiles of the Crown (top), Side (middle) and keel (bottom) sections of the nacelle of a Highlight diameter of + 2.0 % change with respect to the reference nacelle. 159
Figure A. 8 Mach number profiles of the Crown (top), Side (middle) and keel (bottom) sections of the nacelle of a Highlight diameter of + 6.0 % change with respect to the reference nacelle. 160
Figure A. 9 Mach number profiles of the Crown (top), Side (middle) and keel (bottom) sections of the nacelle of a length of - 6.0 % change with respect to the reference nacelle. 161
Figure A. 10 Mach number profiles of the Crown (top), Side (middle) and keel (bottom) sections of the nacelle of a length of - 2.0 % change with respect to the reference nacelle. 162
Figure A. 11 Mach number profiles of the Crown (top), Side (middle) and keel (bottom) sections of the nacelle of a length of + 2.0 % change with respect to the reference nacelle. 163
Figure A. 12 Mach number profiles of the Crown (top), Side (middle) and keel (bottom) sections of the nacelle of a length of + 6.0 % change with respect to the reference nacelle. 164
Figure B. 1 Cp profiles of 3D Isolated nacelle simulations with Dmax variations 165
Figure B. 2 Ma profiles of 3D Isolated nacelle simulations with Dmax variations 166
Figure B. 3 Cp profiles of 3D Isolated nacelle simulations with Dhigh variations 167
Figure B. 4 Ma profiles of 3D Isolated nacelle simulations with Dhigh variations 168

Figure B. 5 Cp profiles of 3D Isolated nacelle simulations with length variations..... 169
Figure B. 6 Ma profiles of 3D Isolated nacelle simulations with length variations..... 170
Figure C. 1 (a) h/Dmax= 0.547, x/l=0.7223 (Base value); (b) h/Dmax= 0.5, x/l=0.8; (d) h/Dmax=0.55 , x/l=0.75; (e) h/Dmax=0.6, x/l=0.7 171
Figure C. 2 (a) h/Dmax=0.6 , x/l=0.75; (b) h/Dmax=0.6 , x/l=0.8; (d) h/Dmax= 0.65, x/l=0.65; (e) h/Dmax=0.65 , x/l=0.7..... 172

v. List of Tables

Table 1 Afterbody mesh dependency Cf and Cp comparison 60
Table 2 Values to be analyzed for the 2D Afterbody simulations (relative to a reference value) 62
Table 3 Afterbody pressure, viscous and drag coefficients for different maximum diameters 65
Table 4 Afterbody pressure, viscous and drag forces for different exhaust angles 65
Table 5 Relation of the NPR and ideal post-exit force taken from Aircraft Engine Integration Notes of Mr. D. Williams (2006). 66
Table 6 Change of Maximum Diameter and Highlight Diameters for the different geometries 75
Table 7 Change of Throat Diameter and Total Nacelle Length 76
Table 8 Forebody force changes (the bold figures are the data from the base geometry) 79
Table 9 Parameter values for the analysis and their variation with respect to the base values(Shaded cells are the base values) 125
Table 10 Combination of the parameters. 126

vi. List of Symbols and abbreviations

2D	Two dimension
3D	Three dimension
AB	After-Body
AIAA	American Institute of Aeronautics and Astronautics
BPR	Bypass Ratio
CAD	Computer Aided Design
C_f	Force Coefficient
CFD	Computational Fluid Dynamics
Cp	Pressure Coefficient
CRTF	Contra Rotational Fan
$C\mu$	Viscous Force Coefficient
D	Diameter
DDTF	Direct Drive Turbo Fan
DLR	German Aerospace Centre
DPW	Drag Prediction Workshop
EU	European Union
FB	Fore-Body
FEM	Finite Element Method
F_G	Gross Thrust
F_{int}	Intrinsic Thrust
F_N	Net Thrust
FPR	Fan Pressure Ratio
GTE	Gas Turbine Engine
GTF	Geared Turbofan
h	Up/Down position for an integrated nacelle
HBR	High Bypass Ratio
k	turbulent kinetic energy
$k - \varepsilon$	$k - \varepsilon$ turbulence model
$k - \omega$	$k - \omega$ turbulence model
L	length
LES	Large Eddy Simulation
LPC	Low Pressure Compressor
LPT	Low Pressure Turbine
m	Mass
MB	Mid-Body
NASA	National Aeronautics and Space Administration
NOx	Nitrogen Oxides
NPF	Net Propulsive Force
ONERA	National Office of Aerospatiale Studies and Research
OPR	Overall Pressure Ratio
RANS	Reynolds Averaged Navier-Stokes

RSM	Reynolds Stress Model
S-A	Spalart Allmaras turbulence model
SFC	Specific Fuel Consuption
SS	Steady State
TD	Time Dependent
TET	Turbine Entry Temperature
UHBR	Ultra-High Bypass Ratio
u_τ	Friction coefficient
v	velocity
VHBR	Very-High Bypass Ratio
VITAL	Environment Friendly Aero-Engine
w	Mass flow
WB	Wing Body
WBN	Wing Body Nacelle
WBPN	Wing Body Pylon Nacelle
x	abscise

Greek Symbols

α	angle
ν	Viscosity
ε	Dissipation per unit mass
ρ	density
τ	Shear stress
φ	Force
ω	Specific dissipation rate

vii. Subscripts

AB	After-Body
FB	Fore-Body
high	highlight
insc	inscidence
int	intrinsic
k	turbulent kinetic energy
max	Maximum
Plug	Plug (Exhaust cone)
pot	potential
Pre	Pre-entry
ref	reference
rel	relative
th	Throat

1 Introduction

The design of a new engine for a subsonic civil transportation aircraft has to be done taking into consideration several points of view. Every aspect considered will have an impact on the final user. For airline companies, fuel economy is one of the most important issues to consider for the selection of a new aircraft. For this reason, aircraft manufacturers present different options of engine suitable for the final aircraft system. Each engine manufacturer offers different options of performance, not only for structural and flight requirements, but also economical issues. Environmental issues are other important aspects to consider in the aeronautic industry because the regulations of noise and emission levels are becoming very demanding.

Gas turbine engines are commonly used to power aircraft. There are four variants of gas turbine engines used for this task; turbo-jet used mostly for military combat aircraft, turbo-shaft used mainly in helicopters, turbo-props for low velocity transport aircraft, and turbo-fan, being the one most used in the civil transportation industry. In a turbofan engine the low pressure compressor, usually called fan, delivers part of the air to the next compressor of the engine and the other part by-passes the core of the engine going to a nozzle to produce thrust.

The amount of air by-passing the core is one of the most important design parameters of a turbofan engine. The Bypass Ratio (BPR) is a variable used to measure the ratio of flow going around the core to that through the core. The bypass flow was conceived as a method of improving the propulsive efficiency of the engine by reducing the jet velocity. Also, noise is reduced due to the jet velocity diminution.

The BPR is a very important parameter due to its effect in the Specific Fuel Consumption (SFC) and the Specific thrust. The effect of an increase of BPR would be the decrease of the optimum SFC. The optimum SFC with a higher BPR is at a lower Fan Pressure Ratio (FPR). These two diminutions have a direct influence in the weight of the aircraft (including the loads) due to the amount of fuel required to complete the mission. The pressure ratio reduction also influences the technology required (and the cost) of the design and fabrication of the fan. Therefore the increase of a turbofan BPR decreases the cost and complexity of the fan.

Unfortunately, there are some disadvantages of increasing the BPR of an engine. The size of the fan grows. There is a minimum SFC attainable by increasing the BPR due to the increase of the installed drag produced by the increase of the fan size (Rudnik, 2002). There are many other problems regarding the increased size of a VHBR engine like the ground clearance limitations and the weight increase, amongst many others. These make it more difficult to continue to improve the engine performance by increasing the BPR.

Many difficulties need to be worked out to continue the development of aircraft technologies. This is where projects like VITAL take the stage, to make a breakthrough in the available knowledge that will allow the technology to continue improving.

1.1 EnVIronmenTALly Friendly Aero Engine (VITAL)

VITAL will provide a breakthrough in noise and emissions engine architecture. This breakthrough will be achieved by the development of new commercial engines taking advantage of the novel lightweight and low noise technologies. With this improvement the SFC is going to be reduced without having an impact on noise and emissions.

VITAL will design, manufacture and rig test three novel fan architectures of turbofan engines for commercial aircraft. These new technologies (Direct Drive Turbofan, Geared Fan Turbofan and Contra-Rotating Turbofan) will provide a breakthrough in noise and emission reduction.

VITAL will provide a major advance in developing the next generation of commercial aircraft engines. The aim of VITAL is the development and validation of engine technologies that alone will provide the following:

1. 6 dB noise reduction
2. 7% reduction in CO_2 emissions

These objectives will be achieved by the design, manufacture and rig scale testing of the following new technologies:

1. Three novel fan architectures
    a. Low speed Direct Drive Turbofan (DDTF)
    b. Geared Turbofan (GTF)

   c. Contra Rotating Turbofan (CRTF)
2. Low-pressure compressor concepts and technologies
3. Lightweight structures
4. Shaft technologies
5. Low pressure turbine technologies
6. Optimal installation of VHBR engines

Combining these technologies, noise reduction will be attained without any combustion penalties. In VITAL two different paths will be taken to achieve the main objectives; the first is the increase of BPR to between 9 and 12, considered VHBR values. The second is decreasing the fan tip speed by using new fan technologies, e.g. the Contra Rotating Turbofan (CRTF).

1.1.1 Integration of the Engine into the Airframe

The engines will be installed under the wing. The noise levels will be diminished by the use of innovative technologies in the integration of the engine to the airframe, e.g. chevron nozzles and new concepts of thrust reverser.

For VITAL the most important aspects of the engine/airframe integration is the reduction of emissions and noise with the least number of penalties possible for the performance of the engine. Also the thrust loss due to the installed drag has to be as low as possible in order to avoid extra fuel burning.

1.2 Objectives of the project

The main objectives of the project are the following:

1. Create a methodology for modelling the behaviour of the drag produced by an installed VHBR engine.
2. Create a model of the drag produced by a VHBR engine using the results obtained from CFD calculations. The model could be used in the optimization of a VHBR engine. This model should save time resources because it could be used instead of CFD calculations.
3. To simulate the behaviour of the flow around a nacelle for a VHBR engine at different flight stages and using different geometries for each of the nacelle components.

4. To link drag force with the different parameters considered in the project. These parameters are divided in two categories: nacelle geometry parameters (including Dmax, Dhigh, length, Forebody length and scarf angle) and distance to the wing (including nacelle penetration and vertical distance to the wing). This relationship will allow modelling a correlation of the drag with some parameters related to the installation.

1.3 Contribution to knowledge

The concept of VHBR is currently under development and different issues arise from the research being carried out. One of the main difficulties of this concept is the size of the fan. Some of the most important variables involved in the overall design are the weight and the frontal area of the fan. The integration of the engine to the airframe is essential to take advantage of the benefits obtained from the VHBR concept.

The integration of a VHBR engine requires a highly coupled Wing-Body-Nacelle-Pylon system to avoid the production of undesirable effects. Also, when on the ground, the space available to install the engine is very limited making integration of big engines, like a VHBR engine, a very complex task. For a detailed analysis of a VHBR integration methodology see the work carried out by Berry (1994).

This novel project consists of a study about the influence of the installation of a VHBR engine on the installed thrust by evaluating the drag produced by the engine.

1.3.1 Achievements

Achievement is defined in the Oxford Dictionary (2000) as “a thing that somebody had done successfully, especially using their own effort and skill”. For this project several achievements were reached, not only related to the VITAL project but personal improvement and knowledge. The achievements for the project can be divided in three different groups: 1) project, 2) knowledge and 3) personal achievements.

The project VITAL was not directly linked to the integration of the engine. The large size of the fan required extra activities to be performed in order to include the effect on the performance as was required from the initial objectives of VITAL.

1. The CFD calculations carried out in this project helped to generate the basis for the parametric study required for the optimization analysis of the installed performance of a VHBR engine in the design process.
2. Achievements were made in the improvement of knowledge and ability of the use of Computational Fluid Dynamics, aerodynamics and their application to aircraft propulsion. Before starting the project CFD was seen by the author just as software to obtain data about the fluid dynamics involved in a flow. Now, CFD is understood in detail. Although the codes involved in Fluent (the CFD software used) unknown, the user now knows the calculations involved in it, the models used, the way some approximations are taken, and how to diagnose faults.
3. In the physics area knowledge of aerodynamics has improved, as well as understanding of nacelle design.
4. Analysis of some of the parameters involved in the project highlighted the importance of the small variations in these.
5. The intake as a section of the nacelle and the engine itself were proven to be two of the most important parts of the integration process, a computational error could generate problems with several aspects of the engine like pressure recovery, spillage drag, and structural issues among others.
6. Generated performance data related to drag caused by fore and after body of VHBR turbofan engines by relating various geometric parameters to drag using CFD analysis.

2 Contribution to knowledge

The demand for oil fuels is increasing in the world. One of the biggest goals of engineering and science for the 21st century is to supply energy and reduce the rate of increase of consumption of oil fuels. The optimal use of fuels has become a critical part of engineering in the world. Aeronautics is not the exception, novel concepts of airplanes and engines are appearing in order to reduce the demand of fuels and also make the aeronautical industry more environmentally friendly.

This project was created to complement the VITAL project. VITAL was about creating a VHBR engine with the capabilities of decreasing noise and emissions without compromising fuel consumption (see section 1.1.) The dimensions of the fan proposed by VITAL engineers required a very large fan. A fan of those proportions requires extra research into airframe/engine integration. The research done in this project has never been done before and is a step forward in the research of optimization of VHBR engine integration.

In this project there are two contributions to knowledge. The first and most important is the research into the creation of a methodology for CFD parametric analysis of the nacelle and integration of a VHBR engine. The second contribution to knowledge is taking the first steps to performing parametric drag analysis of VHBR engines.

The VHBR engines are still being developed therefore several aspects of the research are still going in progress. The nacelle is a crucial aspect to allow the engine to be useful in the aeronautic industry. A proper methodology for the analysis of the nacelle and its interactions with the airframe is required in order to get suitable results and the uniform values that allow engineers to compare them. With the methodology planned and used in this project, an analysis was carried out gradually to identify the parameters that have more impact on the drag. The methodology is explained in more detail in section 3.

By using CFD a detailed analysis was made on the drag produced by the nacelle of a VHBR engine. The first stages were based on making variations to some of the variables of the geometry of the nacelle (see sections 5 and 6 for more details.) After considering the geometry of the nacelle, the research focused on changing the position with respect to the wing (see section 7 for more details.) This kind of analysis is not available in the public domain. The results are the first steps to comparing the drag which is produced by

VHBR engines. 2D and 3D analysis are required for identifying the main parameters to be analysed in order to get the optimum geometry of the nacelle and its position with respect to the wing.

The two main contributions to knowledge are regarding the VHBR turbofans and aircraft/engine integration. This project also adds more knowledge about CFD applied to aeronautics by evaluating the use of different methods, models and procedures in the simulation and meshing. Drag, as a very crucial part of aeronautics, is analyzed in a detailed way by using CFD.

3 Methodology

The way of evaluating the drag produced by a VHBR nacelle was divided into three stages, each one of them further subdivided in order to get an integrated analysis. The basic structure of the project is as follows:

1. Literature review
    A. VHBR engines
    B. Aircraft/Engine integration
    C. Aerodynamics
    D. CFD
        I. Meshing
        II. Modelling
    E. Software information
        I. Fluent
        II. CATIA
2. 2D analysis
    A. AB analysis
        I. Geometry design
        II. Meshing
            a. Mesh independence
        III. Simulation setup
        IV. Running Simulation
        V. Results analysis
    B. FB analysis
        I. Geometry design
        II. Meshing
            a. Mesh independence
        III. Simulation setup
        IV. Running Simulation
        V. Results analysis
3. 3D isolated nacelle
    A. Geometry design
    B. Meshing

I. Mesh independence

C. Simulation setup

D. Running Simulation

E. Results analysis

F. Integration of 2D and 3D results

4. 3D integrated nacelle

A. WB analysis

I. Geometry design

II. Meshing

a. Mesh independence

III. Simulation setup

IV. Running Simulation

V. Results analysis

B. WBN analysis

I. Geometry design

II. Meshing

a. Mesh independence

III. Simulation setup

IV. Running Simulation

V. Results analysis

5. Evaluation and analysis of all of the results of the project

3.1 Literature review

The first stage of every research project is to know "where we stand." Researching what is the current position of science and engineering is crucial to avoid repeating work done by other people. Getting the most information about all of the subjects that could be involved about the project is very important.

The main subjects involved are VHBR engines Aircraft/Engine integration, Aerodynamics, CFD, and Software information.

3.2 2D Analysis

The first simulations carried out are 2D simulations of the nacelle divided into two sections, the afterbody (AB) and forebody (FB.) For each one of them an independent

parametric analysis was carried out. The methodology of the analysis for each section, although similar, is described below.

3.2.1 Choosing parameters to be analyzed

Before any computational work could be done the parameters for each section were decided. First some research was carried out looking for the most influential parameters that could influence the drag produced by an isolated engine. Then, based on the information found and the geometry of the engine, which would remain invariable, the parameters were set (for more details see section 5.1.)

3.2.2 Afterbody methodology

The first stage of the afterbody analysis was to generate a geometry based on the dimensions provided by VITAL. As there was no geometry provided by VITAL (just the basic dimensions) several decisions were taken about the profiles to be used.

After having the CAD model of the geometry of the AB, the domain of the simulation was set for the base geometry. To set the domain several options were tried in order to use the most appropriate for the CFD simulations for all of the analysis. Different combinations of mesh structures and domain geometries were tried. For the final structure the mesh independency analysis was done.

After choosing the mesh and domain structure for the base geometry, the geometry of the AB was changed according to the parameter variations previously established. The mesh for all of the geometries was generated using the same meshing structure and dimensions used for the base geometry.

The simulation setup was done with the most basic simulation methods in Fluent. Most of the decisions were based on the models used. The decisions taken were based on trial and error methods looking for the best results and those which consume the least resources.

The simulations were run in a parallel solving method. The method was carried out automatically by the software Fluent. For more information see Chapter 31, “Parallel Processing” of Fluent manual (Fluent 6.2 documentation, 2007.)

3.2.3 Forebody methodology

Methodology for the FB was similar to that for the AB. The main difference is the geometry used and the parameters required for its design. Comparing the AB and FB, there are more ways to change the geometry of the intake; therefore there are more available parameters to be analyzed and more possible combinations in the FB than in the AB.

The geometry was generated with CATIA software. The main geometry was created by using the dimensions given by VITAL. The intake profiles are described in section 5.1.1. The profiles were parameterized to allow quick geometry generation. Different geometries were created. A matrix of the geometries to be generated was decided according to the parameters.

The domain for the simulation was generated in a similar way as for the AB. For the FB the mesh generation was more focused on a C-type mesh. Based on this, the shape and size of the mesh blocks for the intake were changed to get the best and fastest results.

With the domain and mesh structure already created for the base geometry, the other geometries' domains and grids were created using the same structure as the base geometry.

CFD setup was done in a very similar way to the AB so that the results are based on the very similar parameters, models and variables used for running the simulation. Running was also done in a parallel solving method.

3.2.4 Results Analysis

The results were analyzed separately for AB and FB. For each one of them parametric analysis was carried out in order to set the more important parameters influencing the drag. By doing this the parametric analysis for the 3D models would be restricted to the parameters that were found to be more significant for the drag generation.

3.3 3D Isolated Nacelle Analysis

3D parametric analysis was started on the results of the 2D analysis then more parameters were used for designing the entire nacelle. The geometries were created in CATIA. The

mesh for most of the geometries was created in Gambit. CFD simulations were run in Fluent.

3.3.1 CAD geometry generation

One of the major difficulties of the 3D analysis was the geometry generation. There were no CAD models available to work with, therefore, time had to be invested in generating the 3D models.

The main difficulty of creating the 3D geometric models is to link the borders of the curved shapes. Several surfaces are to be joined together and at the borders most of them are to be tangent. The parameterization of the dimensions of the model is an extra issue.

By using parameters to create the geometric model the geometries required for the project were able to be created without the necessity of investing time in creating the geometry from scratch. The different geometries were created just by changing one (or two) of the parameter values. Then the software (CATIA) would re-generate all of the geometry. Individual attention had to be paid to the borders of each of the surfaces for all of the geometries. Special care on the border's fit and tangency should be taken.

3.3.2 Mesh generation

The mesh was decided to be a symmetric grid to allow a larger mesh and reducing the running time.

Several domain shapes were tried. Also several mesh structures were used to run the simulations. At the end the grid that converged and gave the best results was used. The base geometry was used to design the mesh. The mesh for all of the other geometries was created in the same way as that for the base geometry.

3.3.3 Parametric calculations

The parameters used for the 3D analysis were chosen from the analysis of the results obtained from the 2D simulations. Each of the values of the parameters was based on the base geometry and varied in a percentage set previously. If the resulting drag changed by a large amount then more simulations were to be carried out with different values for the parameter analyzed.

3.3.4 Results analysis

The analysis of every parameter was done individually. Each analysis is performed in several ways. The influence of the each of the parameters in the variations of pressure and viscous forces was analyzed separately. The impact in the different sections of the nacelle and the difference of the crown and keel sections were also considered in the analysis.

Drag considerations are very important in engines of the size considered in this project. Individual analysis of the AB, FB and MB as well as separate analysis of the viscous and pressure drag were carried out. To evaluate the drag over the different sections of the nacelle when the nacelle design stage is focusing on one of the design parameters.

3.4 3D Integrated Nacelle Analysis

The Integrated nacelle analysis requires an examination of the airframe to be integrated with the nacelle. Therefore, the first steps in the study of the WBN system is the study of the airframe (WB) it will be working with.

3.4.1 WB Analysis

The analysis of the WB system in this project is a basic CFD study to get the necessary values for comparison with the results of the WBN system. By comparing the CFD results of the WB and WBN conclusions can be taken about the influence of the nacelle on the total drag of the airplane and to calculate the interaction drag.

The airframe geometry required was not available therefore an alternative option was required. The geometry was generously provided by the School of Aeronautics of Cranfield University. The airframe geometry and capabilities of the aircraft were analyzed to evaluate the suitability for this project. The analysis was based on the range, payload and dimensions that the aircraft was designed for.

After evaluating the suitability of the aircraft the geometry was to be simplified in order to be used in a CFD analysis. All of the details of the aircraft as well as many aerodynamic and structural components were removed. The geometry left for the analysis was just the fuselage and the wing. For more details refer to section 7.3.

3.4.1.1 Mesh generation

The simulation is symmetric with respect to the airframe symmetry plane. The domain for the simulation was based on the length of the fuselage. The inlet and outlet of the domain were set far from the wing. The WBN system was also considered for generating the domain because both the WB and WBN meshes were created using similar methodologies.

The meshing of the airframe is based on the wing mesh. The meshing of the leading and trailing edges of the wing generated the mesh for the rest of the wing. Special care was taken in avoiding coarsening of the mesh at the mid sections of the wings to avoid reducing the accuracy in the results. Also, the cell size was set to be fine close to the airframe surfaces to evaluate the small changes close to the airframe and avoid losing accuracy by coarse cells near the airframe surfaces.

3.4.1.2 Simulation running

As there was no information available the flow conditions for the airframe, the conditions for the inflow were the same as the free flow conditions for the VITAL engine. The direction of the flow was set to be coaxial with the fuselage.

3.4.1.3 Results

The results were not analyzed at this stage. At this stage the results of the airframe simulation were just taken in order to be compared with the results of the simulations with the integrated nacelle.

The data obtained from the results are the pressure, viscous and total forces of the top of the wing and under the wing. The wing is divided into top-wing and under-wing by the leading and trailing edges.

3.4.2 WBN Analysis

The methodology for the WBN analysis is based on the isolated nacelle and the WB methodologies combined.

3.4.2.1 Geometry Generation

The geometry required for this stage was already available. The fuselage and wing system was the one used for the WB analysis and the nacelle would be the base geometry used for the isolated nacelle analysis.

The only variations here were not the dimensions of the geometries involved but the relative position of the nacelle from the wing.

3.4.2.2 Mesh Generation

The domain used was the same as the one used for the WB. The mesh was generated in the same way it was for the WB system. The only difference was a finer meshing under the wing near the nacelle.

The meshing on the nacelle surface was considered to be similar to the mesh of the isolated nacelle. The entire geometry of the nacelle would be simulated and not like the isolated nacelle analysis where only one half of the nacelle was required. Working with all of the nacelle would generate a much bigger mesh if the same meshing conditions as for the isolated analysis were used. Unfortunately the resources were not able to handle a mesh with the resulting size. The size of the nacelle surface meshing would be approximately 75% coarser than the mesh of the isolated nacelle.

The meshing of the under-wing and the leading edge near the nacelle would also change from geometry to geometry depending on the closeness of the nacelle. If the nacelle were close to the wing then it would generate a much finer mesh than a nacelle positioned further from the wing.

3.4.2.3 Parameter analysis

The parameters as mentioned previously were not changing the geometry but the positioning of the nacelle. There are five parameters defining the position of an under-wing nacelle. Few of them could be taken into account for the analysis required in this project. Some of these parameters were not able to be used in the parametric analysis and were set as constants.

Due to limitations in computational resources and time, the analysis was not as extensive as in the previous stages of the project. Only two of the five possible parameters were

analyzed because of these limitations. For this reason the parametric analysis was done using a different approach.

After choosing the parameters, the set of possible parameter combinations was made. It was not possible to generate a simulation for every combination. The approach was a follows:

1. Set the values for the parameters to be constant.
2. Set the base geometry. The base geometry was considered to be the VITAL nacelle positioned at the same place as that of the original engine of the aircraft given by the School of Aeronautics.
3. Eliminate the combinations that would be of no use or impossible to run. The geometries with the nacelle too far away from the wing were not run because those positions would be unsuitable due to inadequate ground clearance, structural problems and other issues.

   Some of the geometries did not fit under the wing therefore were not considered to be included in the research. Alternative installation architecture would be required in order to analyze the unsuitable positions, such as an embedded engine, unfortunately this analysis is out of the scope of this project.
4. Run the simulations for the base geometry until satisfactory results are obtained.
5. With the same CFD set-up of the base geometry, the geometries with extreme positioning, the closest and farthest away from the wing, were run. Depending on the result variations other parameter combinations were run. If the variation of the drag result was not significantly changed no more simulations would be done for geometries in that direction.[1] After some simulations there would be a good overview of the drag change produced by the positioning of the engine.

3.4.2.4 Simulation set-up

The set-up of the simulation parameters was done using the same models and solvers as for the WB simulation.

[1] The significance variation was considered after being compared with the drag variation of the other simulations.

For the engine the cruise conditions were used for setting up the boundary conditions of the engine.

3.4.2.5 Results analysis

The results are analyzed in three different aspects.

1. Total drag at the nacelle
    a. Pressure
    b. Viscous drag
2. Wing drag
    a. Pressure distribution
3. Interference drag

The analysis of these aspects enables an overall view of the impact of the engine positioning to be gained.

All of the analyses were done by comparing the results of each simulation with the one obtained from the base geometry. The final results are comparisons of the rate of change of drag with respect to the parameter changed.

The drag of the nacelle just takes into consideration the drag produced on the nacelle surfaces. The forces on the nacelle can be divided into pressure and viscous drag. It is assumed the pre-entry drag would be equal for all of the simulations (the geometry of the nacelle and the operating conditions are the same) therefore the difference of drag would cancel the pre-entry drag value.

The wing drag is calculated including the lift drag (pressure) and viscous drag. Only the forces on the wing surfaces are taken into account. The fuselage is not considered in the analysis.

For the interference drag three different simulations have to be taken into account: the isolated nacelle (base geometry), WB system, and WBN. From the results of each of the simulations some calculations were made. The final results will give an overview of the impact of the positioning of the engine on the interference drag at cruise conditions.

For more details about the WB and WBN simulations and results refer to section 7.

4 Literature Review

4.1 VHBR Engine

One of the most important advantages of the Gas Turbine Engine over other power sources is the high power/weight ratio. This is one of the main reasons why in 1929 Sir Frank Whittle submitted to his superiors his idea of using a gas turbine engine instead of piston engines to power aircraft (The Jet engine, 1986). He built his first experimental engine in 1937. From that point on the technologies used in Gas Turbine Engines have been improving to get a better performance.

The performance requirements of the engines vary depending on the type of mission the aircraft will be designed for. For a civil aircraft engine design thrust and fuel consumption are two of the most important parameters to be considered from the performance point of view. The range of an aircraft is defined by the fuel consumption and fuel capacity. Specific Fuel Consumption in turbofan engines is lower than in turbojet engines. (Cohen, 1987)

The optimization of a turbojet is based on two variables mainly; overall pressure ratio (OPR) and turbine inlet temperature (TET). In a turbofan two more variables are included for the optimization, the bypass ratio (BPR) and fan pressure ratio (FPR). Assuming the optimization is done based on getting the lowest SFC possible, there is an optimum FPR value for every BPR. Therefore there are only three performance optimization parameters, Overall Pressure Ratio, Turbine Entry Temperature and Bypass Ratio as can be seen in Figure 4.1 (Cohen, 1987).

The SFC, being one of the most important values due to its direct impact on the cost of using an engine, is constantly being reduced. An important factor for the SFC reduction of the engines used in commercial transports is the BPR. The trend has been toward increasing the BPR to reduce the SFC. As the BPR increases the name given to the engine changes from high bypass ratio (HBR) to very high bypass ratio (VHBR) to ultra high bypass ratio (UHBR) engines. It is not very well established as to what are the boundaries in considering a turbofan as a VHBR engine. Some authors like Hoheisel (1997) do not use the term UHBR turbofans, in his work a geared fan engine is called an Advanced Ducted Propfan. Zimbrick (1990) works with two engines, one with a BPR of 9.6 and the other 17.5 and calls both of them VHBR. On the other hand, Burgsmüller (2000) uses a

HBR, a VHBR and UHBR engines each with a BPR of 5, 9.2 and 16 respectively. Generally Very High Bypass Ratio engines are considered to have a BPR above 9.0 because of the novel technologies required (Lecordix, 1992).

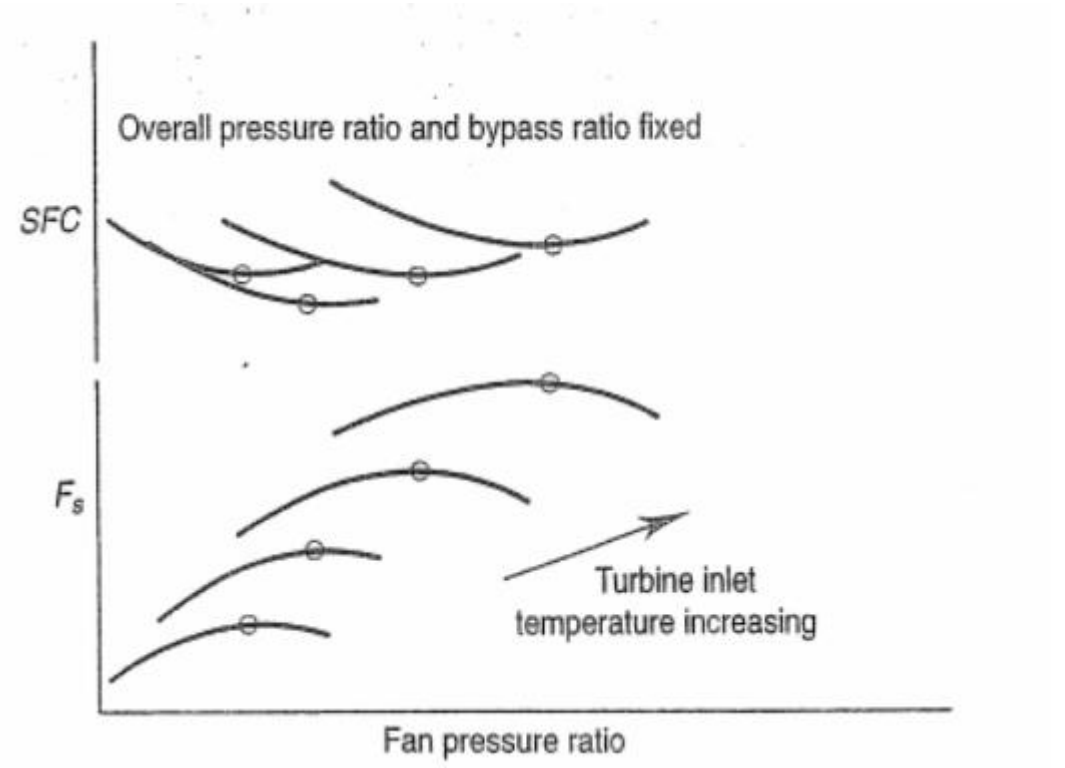

Figure 4.1 Optimization of fan pressure ratio (Cohen, 1987, p. 99)

The VHBR engines certainly lower the fuel consumed by the engine. Colmenares (2007) worked in a model that calculated the feasibility of a geared VHBR engine. His results show an improvement of the levels of SFC, CO_2 and noise with a penalty on the NOx emissions and direct operating cost.

One of the big issues of increasing the BPR above 9.0 is the reduction of the thrust. A VHBR needs a larger amount of airflow going through the fan in order to produce the thrust required to overcome the drag generated by the airframe, therefore the fan diameter is increased. This size increase creates more problems, e.g. larger weight load, drag generated, integration issues[2]. The major drawback for using Very High Bypass Ratio (VHBR) engines is their size. A VHBR fan produces much more drag than a HBR engine

[2] The installed performance parameters take into account the effects of the installation of the power plant on the airframe, usually drag and flow distortions.

therefore the drag produced has a strong impact on the installed SFC and turning an increase in BPR to be counterproductive in terms of the installed engine performance.

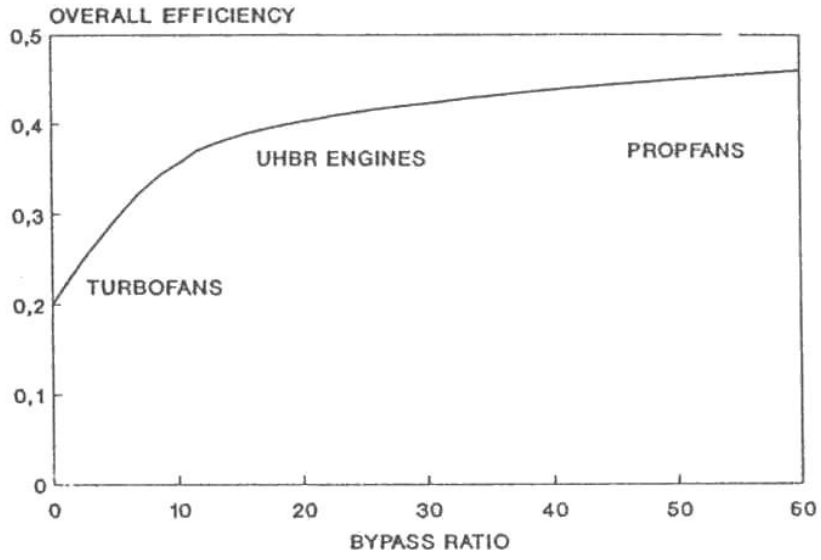

Figure 4.2 Relation between Efficiency and Bypass Ratio (Lecordix, 1992)

The trend to improve the SFC by increasing the BPR will no longer be suitable using the technology available because the installation effects will be unacceptable. There is a value of BPR that will produce a minimum to the SFC; any other value would make the engine consume more fuel. With the current turbofan technology available, an engine with a BPR value close to 9.0 would consume the minimum possible fuel amount (Zimbrick, 1988). Novel technologies for improving the engine performance by increasing the BPR will also increase the size of the entire engine therefore, very high engine/nacelle/airframe integration will be required.

One of the big issues of the VHBR engines is the coupling of the fan and the low pressure turbine (LPT). The size of the fan requires a very large amount of energy extracted from the LPT. This requires more turbine stages or a larger rotational speed of the shaft. A geared fan is a new technology used for large BPR turbofans. Although the gear drive can reduce the efficiency by a small amount it allows the low pressure turbomachinery to operate at higher rotational speeds reducing the stages of the turbine (Koff, 2004).

Another method of increasing the power extracted from the core engine without increasing the airflow is to increase the turbine entry temperature. Unfortunately a higher

TET increases the NOx emissions. High levels of NOx do not comply with environmental regulations (Koff, 2004).

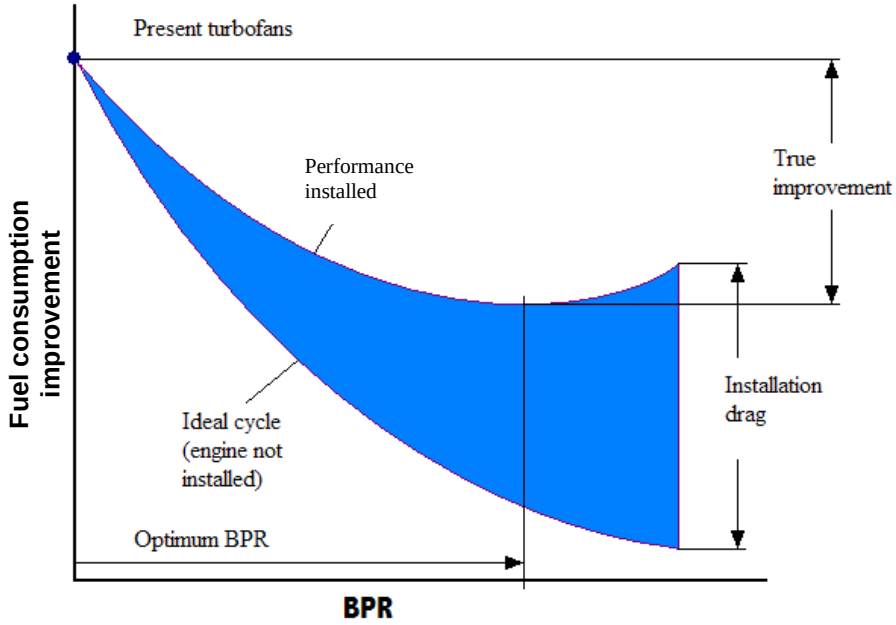

Figure 4.3 Fuel consumption improvements (Burgsmueller, 1996)

4.2 Installation of the propulsion system

There is a distinction between two types of performance of an engine. One is called uninstalled performance which is the ideal performance without taking into account the effects of the nacelle, pylon or wing. The uninstalled performance is the main concern of engine manufacturers and is the data given to aircraft manufacturers. Unfortunately the installation of engines will produce external forces making the total drag increase and consequently decreasing the Net Propulsive Force and increasing the SFC without producing any benefit to the overall performance of the aircraft (Williams, 2006.)

The analysis for the integration of the engine can be done in three separate parts, the forebody, afterbody and midbody (See Figure 4.4). The use of midbody in the design of a nacelle has the advantage of separating the forebody and afterbody, allowing analysing each one of them separately with very little influence. Most modern nacelles are designed without a midbody because the high BPR of the engine requires very large fan diameters; consequently the area of the midbody would be very large and produce high drag.

Without large midbody cowl the interaction between the forebody and afterbody increases, this requires the integration analysis to be for the entire nacelle.

The nacelle forebody is composed mainly of the intake. The primary purpose of the inlet is to change the free stream air to the conditions required for the Low Pressure Compressor (LPC) to work. The cruise speed for a commercial carrier is approximately a Mach number of 0.8. At this speed the fan would not work at its best, because usually the compressors require air flowing at a Mach number of about 0.5. According to Mattingly (2002), the performance of an inlet can be evaluated according to the following characteristics:

- Total pressure ratio
- Flow matching
- Uniformity of flow
- Installation drag
- Starting and stability
- Signatures (acoustic, radar and infrared)
- Weight and cost
- Life and reliability

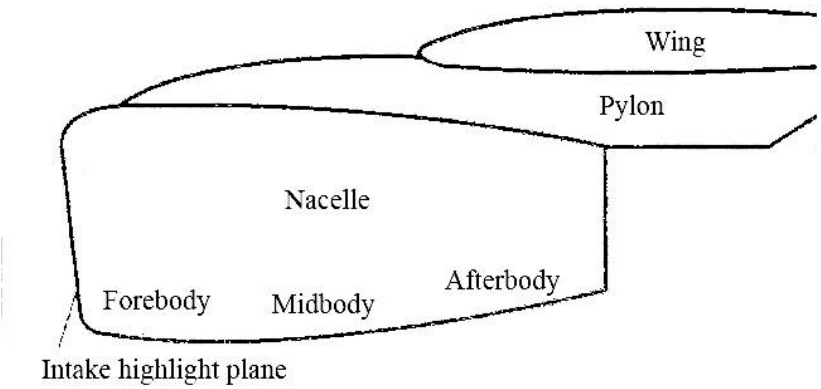

Figure 4.4 Installed Nacelle Components (Mullender, 1996)

Some of the improvements of these characteristics would be at the expense of others therefore the design process requires a balance of the variables depending on the requirements of the whole system.

The design of the afterbody is focused on the nozzle. For subsonic aircraft the nozzle used is a convergent nozzle due to the low pressure ratio across it. Convergent-divergent nozzle is a very expensive technology due to the extra weight added to the nacelle and the low benefit obtained from it for a subsonic commercial aircraft (Cohen, 1987). The main concern of nozzle designers is thrust, but the boundary layer separation and noise production are also very important. A bad design would produce an early separation of the boundary layer decreasing the pressure behind the nacelle and deliver more drag.

4.2.1 Drag

In the work of the Aeronautical Research Council (1958) to set the definitions used in the description and analysis on drag, they have defined the following:

"The Total Drag associated with the external flow is given by the rate of decrease of momentum of the external flow in a direction parallel to the undisturbed stream, this decrease being calculated between stations at infinite distances upstream and downstream of the body" (Aeronautical Research Council, 1958)

In this work other very useful concepts are defined. The forces acting normally and tangential to a surface can be called Normal-Pressure Drag and Surface Friction Drag respectively and the adding of these two results into Total Drag previously defined. Also other definitions are set, Boundary-Layer Drag, Wave Drag, Intrinsic Drag, Pre-entry and Post-exit drag, Spillage drag and Lift Dependent Drag.

In a short cowl nacelle with an exhaust cone, the Drag must be calculated in a different way from a simple exhaust nacelle. The pre-entry forces are calculated by using the stream force theorem. The post-exit forces must be calculated taking into account the forces on the core cowl for the bypass stream tube and the exhaust cone forces in the core stream tube (Williams, 2006).

The spillage drag is the force difference between pre-entry force and the cowl pressure force. At subsonic speeds, when the flow is smooth around the nacelle the pre-entry force and the cowl pressure force are considered to be the same, this makes the spillage drag to

be equal to zero (Seddon, Goldsmith, 1999). What produces spillage drag is the effect of boundary layer separation and shock waves at the intake making the cowl suction force lose its effect.

The drag over a well designed nacelle with the absence of boundary layer separations and shockwaves will be produced almost entirely by viscous forces (Covert, 1985).

4.2.1.1 Drag calculations

Mr. Darrell Williams was a great support to the understanding of the meaning of Drag and the calculation procedure. Drag is not a force for a ducted body. The drag of an engine must be calculated in a different way from the way it is calculated for an airframe.

Also depends on the way the force book keeping system is chosen. In Figure 4.5 all of the forces acting on a short cowl nacelle are shown and all of these must be taken into account, either for the thrust or drag. The Net Propulsive Force (NPF) is the most important parameter for an aircraft manufacturer because it is the sum of all of the forces acting on the engine, and depending on the throttle state it will speed up or slow down the airplane. The NPF must be the same for every book keeping system.

The NPF will be chosen based on the Standard Net Thrust (F_N) or the Intrinsic Thrust (F_{int}) depending what suits the best and makes the calculations easier.

The formulas for thrust and drag calculations are the following:

Standard Net Thrust	$F_N = F_{G,9} + F_{G,19} - F_{G,0}$	(1)
Intrinsic Thrust	$F_{int} = F_{G,9} + F_{G,19} - F_{G,1}$	(2)
Modified Standard Gross Thrusts	$F^*_{G,9} = F_{G,9} - \varphi_{plug}$	(3)
	$F^*_{G,19} = F_{G,19} - \varphi_{AB}$	(4)
Modified Standard Net Thrust	$F^*_N = F^*_{G,9} + F^*_{G,19} - F_{G,0}$	(5)
Modified Intrinsic Thrust	$F^*_{int} = F^*_{G,9} + F^*_{G,19} - F_{G,1}$	(6)
Drag Definition	$D = \varphi - \varphi_{pot}$	(7)

Net Propulsive Force $NPF = F^*_N - \varphi_{pre} - \varphi_{cowl}$ (8)

$NPF = F^*int - \varphi_{cowl}$ (9)

$NPF = F^*_N - \varphi_{post} - D_{cowl}$ (10)

The modified intrinsic and standard net thrust will used instead of the original assuming the gross thrust will include the core cowl (φ_{AB})and plug forces (φ_{plug}).

By splitting the Nacelle into three, Afterbody, Midbody and Forebody, the calculations will be easier. For the Forebody a suction force will be applied on the intake, but it cannot be considered a "negative" drag. To calculate the drag the pre entry force (usually called pre entry drag) must be taken into account (see Figure 4.6). To calculate φ_{pre} and $\varphi_{cowl,FB}$ from the CFD calculations, ascertain the sum of the forces acting axially on each cell over the intake cowl to get the suction force and over the highlight area for the force F_{G1} to calculate the pre entry force with the Stream Force Theorem (Bore, 1993).

$$\phi_{pre} = F_{G,1} - F_{G,0} \quad (11)$$

$$D_{intake} = \phi_{cowl} + \phi_{pre} \quad (12)$$

The same can be done for the Afterbody but in this case the calculation of Drag would be complicated due to the mixing of the free stream and the engine streams. This is one of the reasons why the standard net thrust is used. Therefore the only parameter to be calculated is the Afterbody cowl force ($\varphi_{cowl,AB}$). It is calculated from the sum of all of the axial forces on the nozzle cowl.

The analysis of the drag was made separately between pressure and friction. The Pressure coefficient (C_p) and friction coefficient (C_f) were used to avoid using absolute values. At each cell the C_p and C_f are calculated with the following formulas:

$$C_p = \frac{(p - p_{ref})}{\frac{1}{2}\rho_{ref} v_{ref}^2} \quad (13)$$

$$C_f = \frac{\tau_w}{\frac{1}{2}\rho_{ref} v_{ref}^2} \quad (14)$$

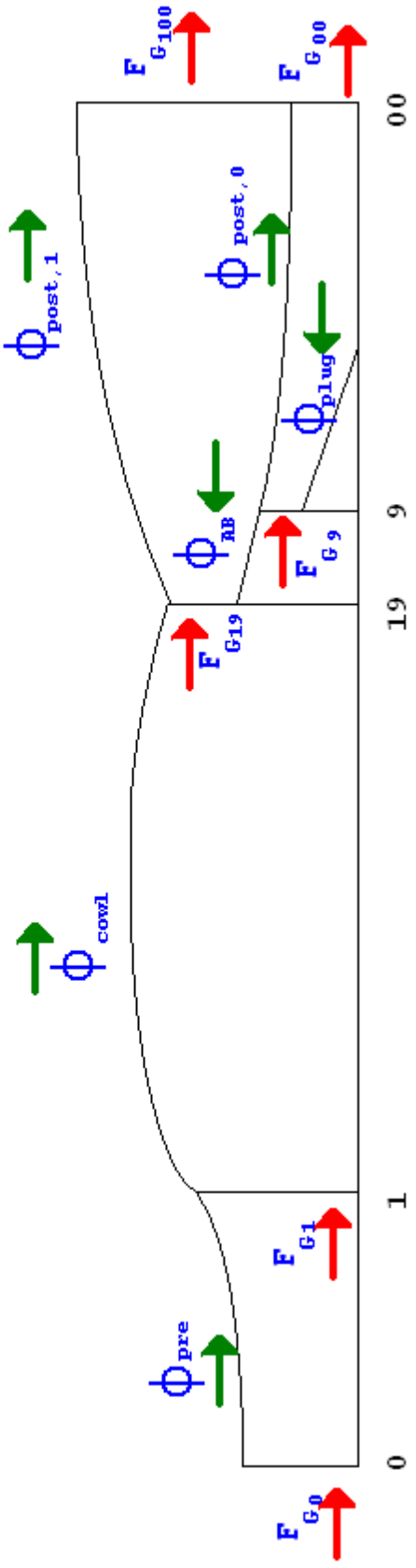

Figure 4.5 All of the forces acting on a short cowl nacelle

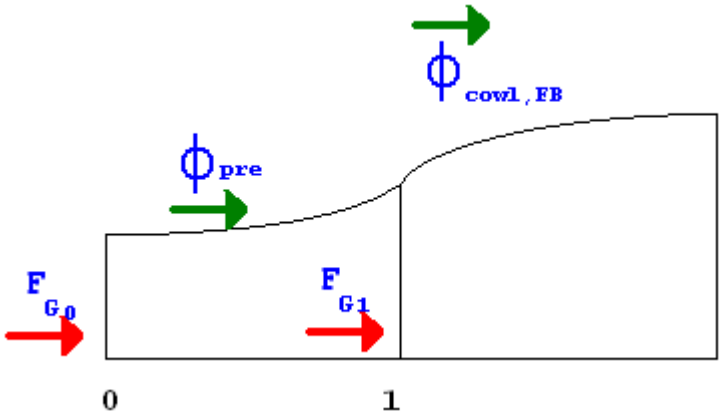

Figure 4.6 Forebody forces

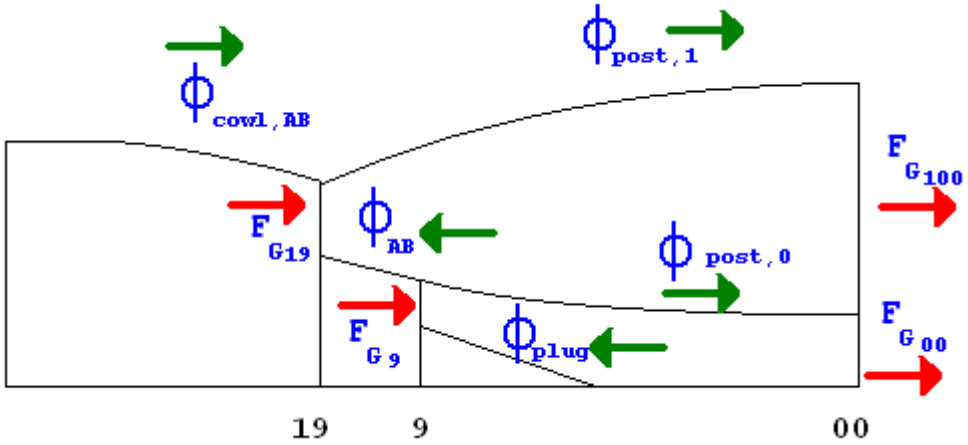

Figure 4.7 Afterbody forces

4.2.2 Interference Effects

The engine installation produces a flow velocity increase on the lower surface of the wing with a pressure decrease. The effects on the performance of the aircraft are lift losses, vortex drag penalty and flow, separation as can be seen in Figure 4.8. The amount of lift lost is related to the nacelle size, this is one of the reasons why the integration of a VHBR is very important to the overall aircraft performance.

By altering the geometry of the nacelle and the position of the engine the lift losses could be minimized. Unfortunately this would be at the expense of increasing drag or other inconvenient effects in the performance of the engine or the aircraft.

The position of the engine on the wing is a very important variable for an aircraft design because the lift losses decrease as the distance from the engine to the aircraft centreline

increases. Unfortunately, if the engine is installed far from the fuselage, an engine failure would require a very long tail stabilizer to balance the thrust differences.

The lift differences produced by the installation of an engine are due to the alteration of the conditions of the airflow around the wing, especially close to the engine. For early engine designs, when engines were not very big, the wing clearance was kept to large values in order to minimize the interference effects. For modern HBR engines this is not possible due to the limited space available to install the engine with proper values of wing and ground clearance. Another way to deal with wing interference is to bring the engine forward. Although by bringing the engine forward there would be more space available to locate the engine in an optimum position, high engine/nacelle/wing/pylon integration is required. The air coming from the engine would flow very close to the wing altering the wing performance. Also a high integration of the engine and the airframe requires very detailed analysis for all of the flying conditions.

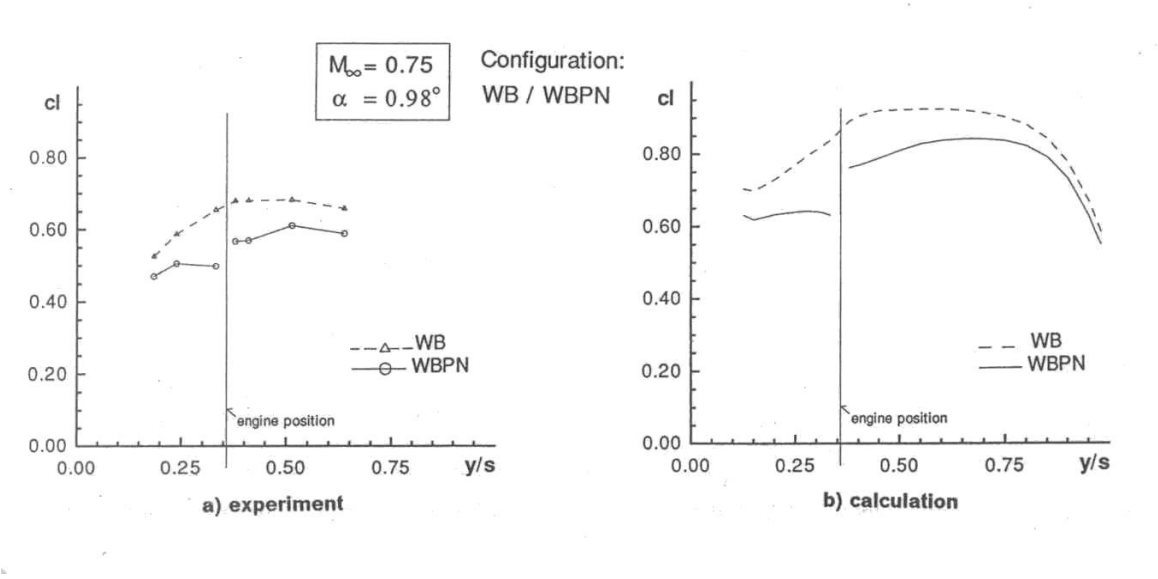

Figure 4.8 Spanwise lift distribution with and without nacelles (Rossow, 1992)

The interference drag is another effect produced by the installation of the engine (Cedar, 1993). Figure 4.9 shows how the most important value the interference drag is the BPR. The position of the nacelle is also very important in the interference drag generated. In Figure 4.10 the relation between the vertical and horizontal position of the engine are related to the interference drag, showing that an engine located close to the wing would produce unacceptable drag (Rossow, 1994).

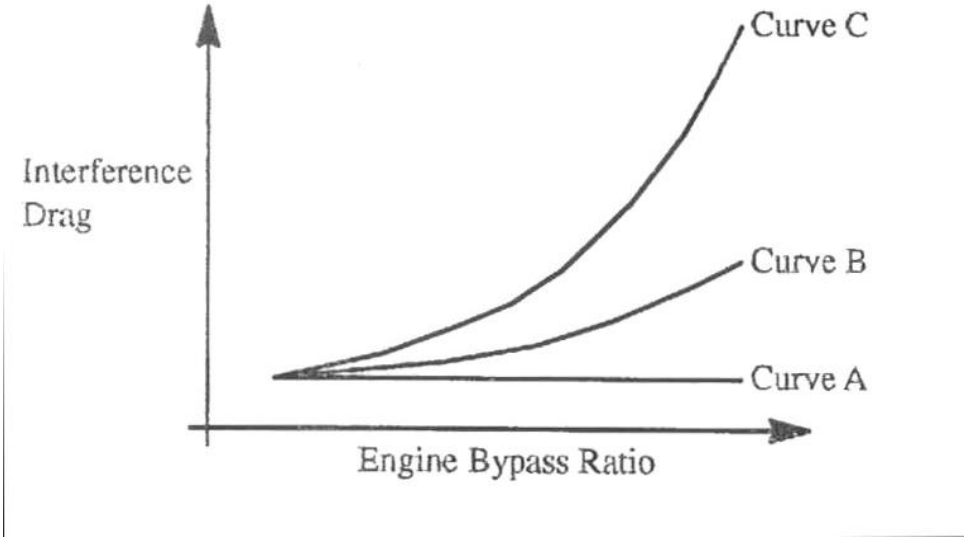

Figure 4.9 Variation of Interference Drag with Engine Bypass Ratio for a given application (Cedar, 1993)

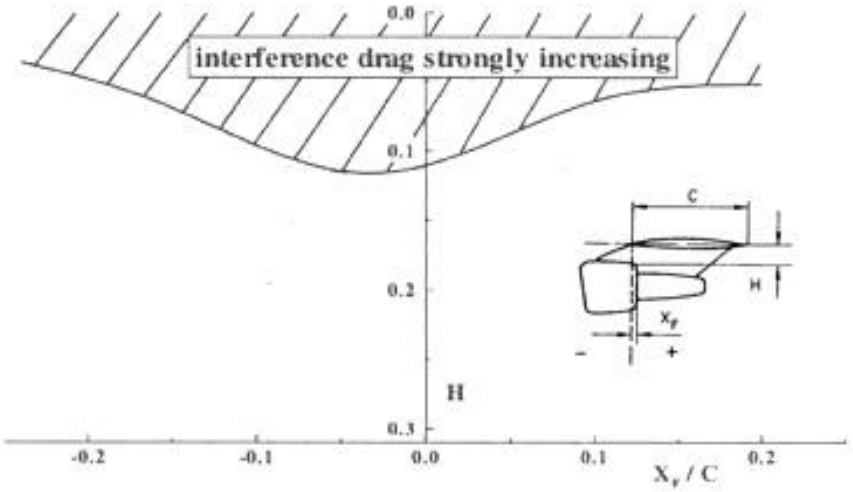

Figure 4.10 Relation between the Interference Drag and the position of the engine (Rossow, 1994)

4.2.3 Integration Methodology

For the integration of an engine different problems have to be solved and for each one of them many aspects have to be taken into account. Some of them depend on the engine, aircraft or the relationship between them.

The aspects to be taken into account can be divided into two different categories, aerodynamic and non-aerodynamic. These aspects are related to the different problems arising from the integration of an engine. The issues to be solved are divided into performance of the engine, aircraft performance and safety (see the factors proposed by Berry (1994) in Figure 4.11).

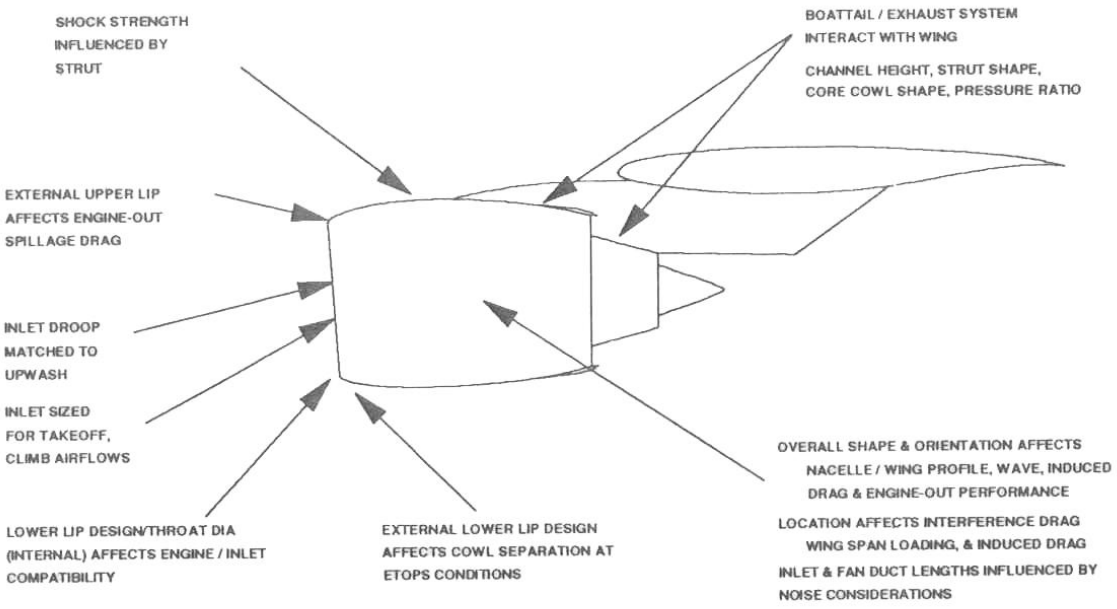

Figure 4.11 Factors influencing nacelle installation design (Berry, 1994)

The main factors considered are:

- Aerodynamic Factors
  - Overall shape and orientation of the nacelle
    - Penetration
    - Gully depth
    - Span position
  - Location of the engine
  - External contours
  - Inlet internal geometry
  - Strut contours clearance
  - Exhaust systems and jet designs
  - Wing sweep

- Lift distribution
- Pylon design

- Non-aerodynamic factors
  - Engine size and BPR
  - Ground, runway and taxi clearances
  - Roll clearance
  - Escape slide clearance
  - Collapsed gear clearance
  - Disk burst zones
  - Foreign object ingestion prevention
  - Noise minimization
  - Flutter requirements
  - Thrust reverser
    - Avoid controllability problems
    - Reingestion prevention
    - Avoid Flap/slat interference

Another consideration that has to be taken into account is how the thrust and drag are bookkept. According to Berry (1994), the bookkeeping system is used to properly take into account all the forces between companies and avoid double bookkeeping. The system used for engine integration in the Boeing 777 was consistent with traditional methods. The method used is to account as thrust the losses inside the inlet captured streamtube and inside the fan jet boundary, while forces outside this boundary as drag (See Figure 4.12). This book keeping method was proposed by the Aeronautical Research Council in 1955 .

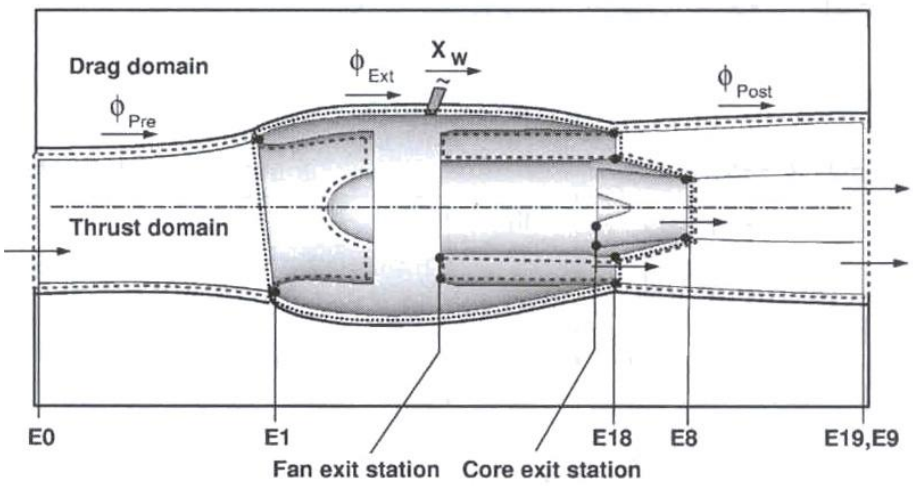

Figure 4.12 Decomposition for Thrust/Drag bookkeeping (von Geyr, 2005)

By using this bookkeeping method a theorem was proposed to calculate the forces generated inside a duct, like a GTE. In the traditional approach the total force is calculated by calculating the difference of the momentum and pressure force between the "in" and "out" of the duct. In the stream force approach the stream forces are added at the ends and the result is the force created. This approach simplifies the problem of the flow going in and out in oblique angles like a Harrier.

Taking into account a stream tube with only one inlet and one outlet and assigning stations 0 and 1 respectively, the stream force generated can be calculated in the following way:

$$G = \frac{1+1.4M^2}{(1+0.2M^2)^{3.5}} \tag{15}$$

$$F_1 = A \cdot p_0 \left(\frac{p_{T1}}{p_0} G(M_1) - 1 \right) \tag{16}$$

Equations (15) and (16) are be used to calculate the stream force, which is the force on the borders of the stream tube going through the engine and around the nacelle. Adding the stream forces between the inlet and outlet will give the thrust or drag, accordingly. The stream theorem is stated below, as quoted from Bore (1993).

"When fluid flows in a duct (or section of ducting) the resultant force on the interior surface of the duct is equal to the resultant of the stream forces at the ends of the duct"

The first step for the integration of an engine and airframe is to identify the thrust requirements of the functioning aircraft system according to the objective for which it is designed.

The nacelle has to be designed isolated with no influence from the wing or other external factors. The main stages of nacelle design are the nozzle, mid-body cowl and intake. The considerations that have to be taken into account for each of these stages are different. For the inlet the main consideration is to lower the airflow velocity to a proper velocity with minimal pressure losses and to make the pressure distribution at the fan frontal area as uniform as possible. Another very important factor for the inlet design is the minimization of spillage drag.

For mid-body design the main concern is drag minimization. There are two options for the mid-body design that depend on the exhaust system. The design of a mixed exhaust system would need a long fan cowl (with a long mid-body) while the separate exhaust system requires only a proper integration of the inlet with the nozzle. The main core cowl requirement is the minimization of losses produced by the interaction of the cold and hot jets.

For the nozzles, although the main function is the pressure transformation into thrust, noise is also a very important issue. As nozzles are basically convergent ducts, the prevention of flow separation is also important in their design.

In air transport industry CFD and rig testing are used for the design of isolated nacelles. CFD is used for the initial design of the nacelle taking into account large ranges of values for the different design variables involved. After CFD has been used, rig testing is required to test the real-life behaviour of the nacelle and validate the calculations made with CFD.

The following stage is the design of wing/body/nacelle integration. For this stage the nacelle has to be located at the best position available for the engine taking into account some of the aspects previously mentioned. The most important aspects to be taken into

account are the minimization of the wing interference and safety issues. The position of the engine is a crucial step for a proper optimization of the performance of the aircraft and the engine, and it is done at this stage.

The pylon is to be designed to produce the least drag possible, have the structural resistance required to hold the engine and vibrations produced during a mission, and have space for the ducts necessary for the engine operation (e.g. fuel and cables). The pylon modifies the properties of airflow around the wing; therefore the profile of the pylon can be modified to minimize the losses and avoid undesirable effects[3].

The final stage of the integration is the positioning of the engine. The position from the aerodynamic point of view involves the effect of the flow around the airframe affecting the overall performance of the aircraft. In a civil aircraft, with underwing installation, the effect of the engine on the lift creates a need for a wing redesign in order to keep the lift values required (Greff, 1993.)

Oliveira (2003) considers that there are some extra steps to be taken into account. He mentions that when closed coupling is achieved by an iterative design process the wing design should be changed as well. These extra steps mentioned by Oliveira are the wing local modifications and Nacelle vortex generators.

4.3 CFD

CFD is a way of solving fluid flow problems by using numerical methods. There are many models and equations to be solved. The most basic equations to be solved are the Navier-Stokes equations that are the equations describing the motion of fluid substances.

In CFD, FEM are used which means the domain of the flow must be divided in a grid. The accuracy and consistency of the results of the CFD simulation depends greatly on cell size.

To solve the flow concerning variables, the Navier-Stokes equations are to be solved for each cell, also if there are more effects to be considered in the flow (i.e. heat transfer,

[3] The Integration method and nacelle design are based on the notes of Williams (2006)

compressibility, turbulence, chemical reactions, etc.) more equations representing these effects are needed and the calculations would be more complicated.

In Fluent (one of the CFD software available at Cranfield University) there are two numerical methods to be used as solver of the flow, these are Pressure and density based solver. To solve the Navier-Stokes equations by the numerical methods used by Fluent the basic approaches are the following. In both methods the velocity is obtained by solving the momentum equation. The Pressure based solver uses a pressure correction equation to obtain the pressure value, on the other hand the density solver is determined from the equation of state. The density is determined in the density based solver by the continuity equation.

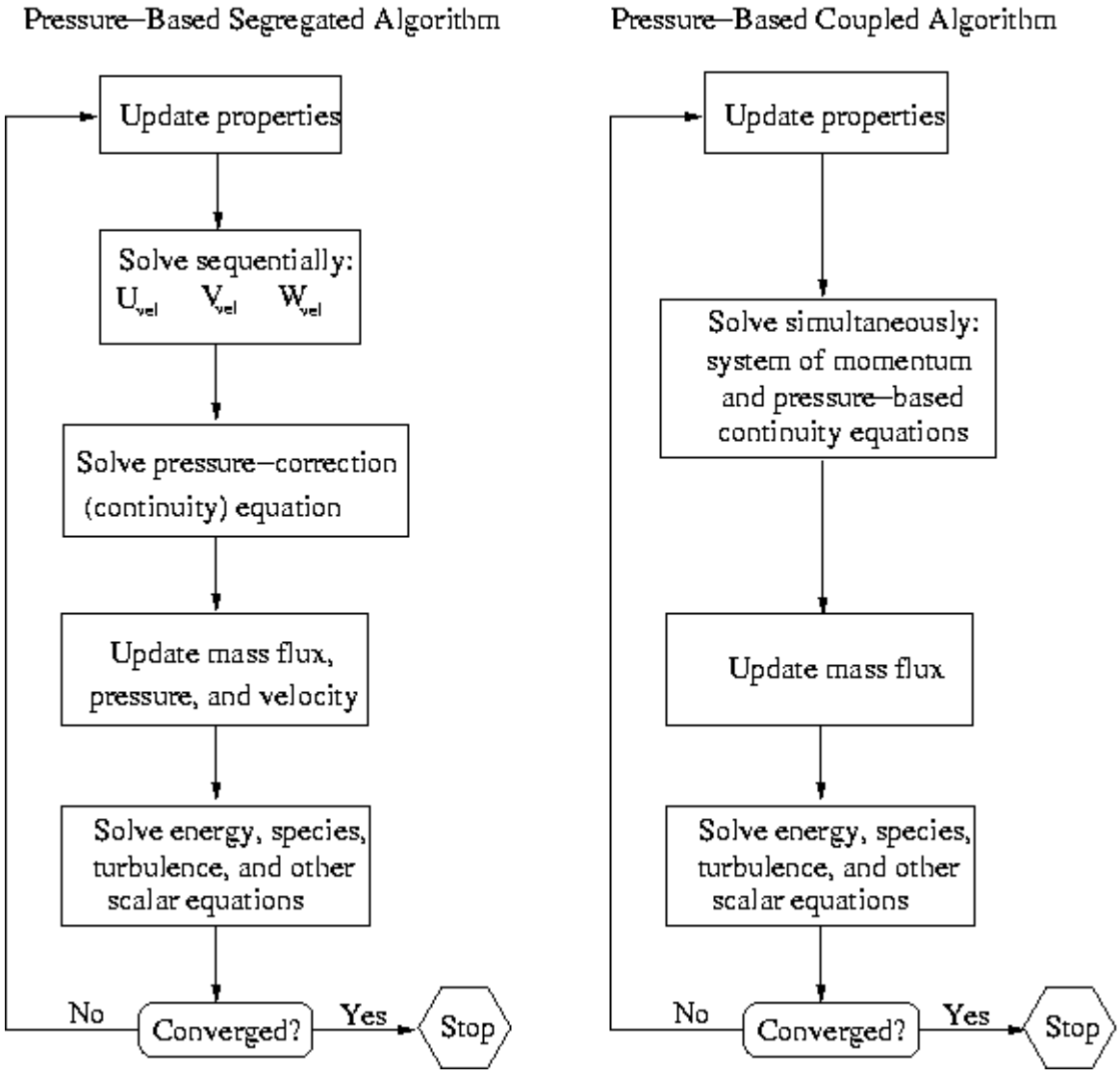

Figure 4.13 Pressure based solver, segregated and coupled algorithms (Fluent 6.2 Documentation, 2007)

The main difference between two solver methods is the way all of the variables are solved. In the pressure based solver a projection method is used to determine all of the variables. In this method there are two algorithms available, the segregated and coupled algorithm. In the segregated algorithm the governing equations are solved sequentially. The equations governing the flow are solved simultaneously in the coupled algorithm. A basic diagram is shown at

Figure 4.13.

The density solves the continuity, momentum and, where appropriate, energy and species equations simultaneously, as a coupled algorithm. Other scalars would be solved afterwards sequentially. The main steps are illustrated bellow.

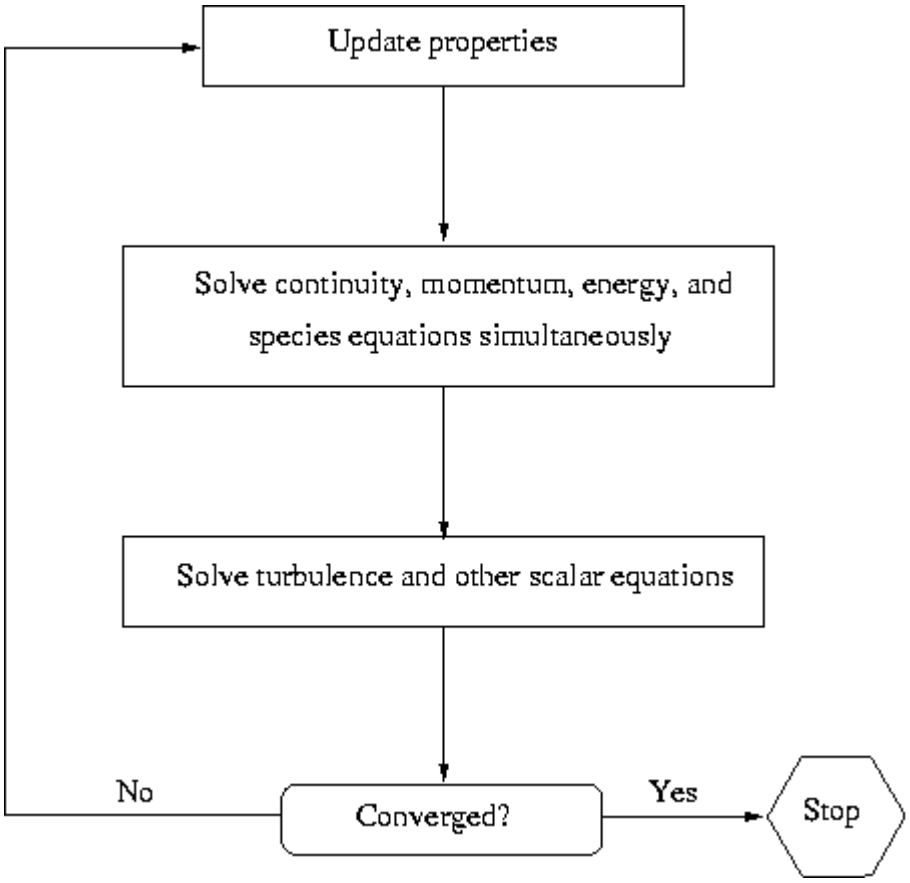

Figure 4.14 Density based solver (Fluent 6.2 documentation, 2007)

In the density based solver, the governing equations are solved simultaneously using two different linearization methods, the implicit and explicit method. The implicit method uses both existing and unknown values from neighbouring cells. The explicit method uses only existing values (Fluent 6.2 documentation, 2007).

4.3.1 Turbulence modelling

Turbulence is very important in the calculation of drag. Pressure and velocity will have small variations that would change to fit the turbulent flow going around any object in a flow stream. The changes have to be as accurate as possible to get the proper results. Different models would give different results, and each model is suitable for different types of flow according to the conditions established.

The most basic equation for turbulent kinetic energy used in almost all of the turbulence models is the following:

$$\frac{\partial k}{\partial t} + U_j \frac{\partial k}{\partial x_j} = \tau_{ij} \frac{\partial U_i}{\partial x_j} - \epsilon + \frac{\partial}{\partial x_j}\left[(\nu + \nu_T/\sigma_k)\frac{\partial k}{\partial x_j}\right] \quad (17)$$

For modelling turbulence the following choices are available in Fluent:

- Spalart-Allmaras model (S-A)
- k - ε models
- k - ω models
- v^2 - f model (addon)
- Reynolds stress model (RSM)
- Detached eddy simulation (DES) model
- Large eddy simulation (LES) model

The S-A, k – ε and k – ω models and their variations are Reynolds Average Navier Stokes (RANS). S-A is a one equation model while k – ε and k – ω are two equation models. In LES model the large eddies are explicitly calculated being more accurate but more computer resource demanding.

S-A model is written in terms of the eddy viscosity, instead of the turbulent kinetic energy (k). Its main advantages are the following (Fluent 6.2 documentation, 2007):

1. It is simple. It is not necessary to calculate a length scale related to the local shear layer thickness.

2. It was designed specifically for aerospace applications.
3. As it is a one equation model, the calculations are faster than two equations models.

It is defined as follows.

Kinematic Eddy Viscosity:

$$\nu_T = \tilde{\nu} f_{v1} \tag{18}$$

Eddy Viscosity Equation:

$$\frac{\partial \tilde{\nu}}{\partial t} + U_j \frac{\partial \tilde{\nu}}{\partial x_j} = c_{b1}\tilde{S}\tilde{\nu} - c_{w1} f_w \left(\frac{\tilde{\nu}}{d}\right)^2 + \frac{1}{\sigma}\frac{\partial}{\partial x_k}\left[(\nu + \tilde{\nu})\frac{\partial \tilde{\nu}}{\partial x_k}\right] + \frac{c_{b2}}{\sigma}\frac{\partial \tilde{\nu}}{\partial x_k}\frac{\partial \tilde{\nu}}{\partial x_k} \tag{19}$$

Closure Coefficients and Auxiliary Relations:

$$c_{b1} = 0.1355, \qquad c_{b2} = 0.622, \qquad c_{v1} = 7.1, \qquad \sigma = 2/3 \tag{20}$$

$$c_{w1} = \frac{c_{b1}}{\kappa^2} + \frac{(1+c_{b2})}{\sigma}, \quad c_{w2} = 0.3\,, \quad c_{w3} = 2, \qquad \kappa = 0.41 \tag{21}$$

$$f_{v1} = \frac{\chi^3}{\chi^3 + {c_{v1}}^3}, \qquad f_{v2} = 1 - \frac{\chi}{1+\chi f_{v1}}, \qquad f_w = g\left[\frac{1+{c_{w3}}^6}{g^6+{c_{w3}}^6}\right]^{1/6} \tag{22}$$

$$\chi = \frac{\tilde{\nu}}{\nu}, \qquad g = r + c_{w2}(r^6 - r), \qquad r = \frac{\tilde{\nu}}{\tilde{S}\kappa^2 d^2} \tag{23}$$

$$\tilde{S} = S + \frac{\tilde{\nu}}{\kappa^2 d^2} f_{v2}, \qquad S = \sqrt{2\Omega_{ij}\Omega_{ij}} \tag{24}$$

The S-A model was created and optimized for aerodynamic applications, mostly for the flow past a wing.

Two equation models use the turbulent kinetic energy and the turbulence length or any equivalent. The Boussinesq approximation equation (25) and turbulence kinetic equation (17) is where most of the two dimension models start.

$$\tau_{ij} = 2\nu_T S_{ij} - \frac{2}{3}k\delta_{ij} \tag{25}$$

The k-ω model is based on the turbulence kinetic energy (k) and specific dissipation (ω), first proposed by Kolmorog in 1942. Since then research on this model has improved and the ω equation has evolved since it was first proposed.

The equations and coefficients used for this model are shown below.

Kinematic Eddy Viscosity:

$$\nu_T = {}^{k}/_{\omega} \tag{26}$$

Turbulence Kinetic Energy:

$$\frac{\partial \omega}{\partial t} + U_j \frac{\partial \omega}{\partial x_j} = \tau_{ij} \frac{\partial U_i}{\partial x_j} - \beta^* k\omega + \frac{\partial}{\partial x_j}\left[(\nu + \sigma^* \nu_T)\frac{\partial k}{\partial x_j}\right] \tag{27}$$

Specific Dissipation Rate:

$$\frac{\partial \omega}{\partial t} + U_j \frac{\partial \omega}{\partial x_j} = \alpha \frac{\omega}{k} \tau_{ij} \frac{\partial U_i}{\partial x_j} - \beta \omega^2 + \frac{\partial}{\partial x_j}\left[(\nu + \sigma \nu_T)\frac{\partial \omega}{\partial x_j}\right] \tag{28}$$

Closure Coefficients and Auxiliary Relations:

$$\alpha = \frac{13}{25}, \qquad \beta = \beta_0 f_\beta, \qquad \beta^* = {\beta_0}^* f_{\beta^*}, \qquad \sigma = 1/2, \qquad \sigma^* = 1/2 \tag{29}$$

$$\beta_0 = \frac{9}{125}, \qquad f_\beta = \frac{1+70\chi_\omega}{1+80\chi_\omega}, \qquad \chi_\omega = \left|\frac{\Omega_{ij}\Omega_{jk}S_{ki}}{(\beta_0^* \omega)^3}\right| \tag{30}$$

$$\beta_0^* = \frac{9}{100}, \qquad f_\beta^* = \begin{cases} 1, & \chi_\omega \le 0 \\ \frac{1+680{\chi_k}^2}{1+400{\chi_k}^2}, & \chi_\omega > 0 \end{cases}, \qquad \chi_\omega = \frac{1}{\omega^3}\frac{\partial k}{\partial x_j}\frac{\partial \omega}{\partial x_j} \tag{31}$$

$$\epsilon = \beta^* \omega k \qquad \text{and} \qquad \ell = k^{1/2}/\omega \tag{32}$$

The other two equation model in Fluent is the k-ε model, the most popular two-equation model according to Wilcox. The model is based on defining the exact equation for ε at a precise moment in the N-S equations. The conditions of the flow should satisfy the following equation:

$$2\nu \overline{\frac{\partial u_i'}{\partial x_J}\frac{\partial}{\partial x_J}[\mathbb{N}(u_\iota)]} = 0 \tag{33}$$

Where $\mathbb{N}(u_i)$ is defined as:

$$\mathbb{N}(u_i) = \rho \frac{\partial u_i}{\partial t} + \rho u_k \frac{\partial u_i}{\partial x_k} + \frac{\partial p}{\partial x_i} - \mu \frac{\partial^2 u_i}{\partial x_k \partial x_k} \quad (34)$$

Unfortunately introducing the previous equations to the N-S equations would include extra difficulties which include several unknown double and triple correlations of velocity pressure and velocity gradients. Close approximations have been made to the resulting differential model and is called the Standard k-ε model. The model is defined as follows.

Kinematic Eddy Viscosity

$$\nu_T = C_\mu k^2/\epsilon \quad (35)$$

Turbulence Kinetic Energy

$$\frac{\partial k}{\partial t} + U_j \frac{\partial k}{\partial x_j} = \tau_{ij} \frac{\partial U_i}{\partial x_j} - \epsilon + \frac{\partial}{\partial x_j}\left[(\nu + \nu_T/\sigma_k)\frac{\partial k}{\partial x_j}\right] \quad (36)$$

Dissipation Rate

$$\frac{\partial \epsilon}{\partial t} + U_j \frac{\partial \epsilon}{\partial x_j} = C_{\epsilon 1} \frac{\epsilon}{k} \tau_{ij} \frac{\partial U_i}{\partial x_j} - C_{\epsilon 2} \frac{\epsilon^2}{k} + \frac{\partial}{\partial x_j}\left[(\nu + \nu_T/\sigma_\epsilon)\frac{\partial \epsilon}{\partial x_j}\right] \quad (37)$$

Closure coefficients and Auxiliary Relations

$$C_{\epsilon 1} = 1.44, \quad C_{\epsilon 2} = 1.92, \quad C_\mu = 0.09, \quad \sigma_k = 1.0, \quad \sigma_\epsilon = 1.3 \quad (38)$$

$$\omega = \epsilon/(C_\mu k) \quad \text{and} \quad \ell = C_\mu k^{3/2}/\epsilon \quad (39)$$

4.3.2 Use of Computational Fluid Dynamics for integration

The use of CFD in the design of a nacelle and its integration with the airframe has improved the understanding of the physics involved. This allows improving the design of different elements and reducing the wind tunnel testing required for design or research. As the computer technology improves, so does the capacity for a more detailed simulation thereby improving the performance of installed engines with fewer resources used on rig testing. However, CFD will never completely substitute model testing because the results of simulations need validation to be reliable. Kern shows, how in 1988, CFD was seen as a future tool to improve many aspects for engine integration, from Nacelle design to Engine/airframe integration.

The nacelle design process can be divided into three phases, preliminary/conceptual design, detailed design and post-test modification phase. According to Cedar (1993), CFD is used mostly in the detailed design phase, but it would be more useful in the conceptual design because that is the phase when more decisions are to be made, however CFD simulation results are not reliable due their inaccuracy. Cedar (1993) says "*CFD had had limited impact due to the accuracy requirements in the preliminary/conceptual design phase. It is however, in the preliminary/conceptual design phase that installation CFD can have the greatest impact, as it is in this phase that the most important design decisions are made".* The use of CFD for nacelle design at the second stage of design is very useful because the grids used for the analysis of isolated and installed nacelles can be the same.

Chimera is a CFD grid generation technique used in GE for engine integration. Chimera is a grid block structure method where the blocks for each component can be overlapped. In Figure 4.16 there is an example of the different blocks that can be used for the integration of an airframe and an engine. The main difference with a standard multi-block grid and a Chimera overset grid system is the method of transferring the information between blocks. For the standard system the blocks must share faces, if these blocks share points, the information transfer is simple substitution, in case the points do not match the information is transferred with a 2D interpolation in every plane. For Chimera the basis is the same but for overlapping volumes, the interpolation is 3D. The penalty of this method is an extra step required for interpolation and has to be inserted between grid generation and flow solver phases. The big advantage of the method is that the complexity of the analysis can be increased in stages through the design process (Cedar, 1993).

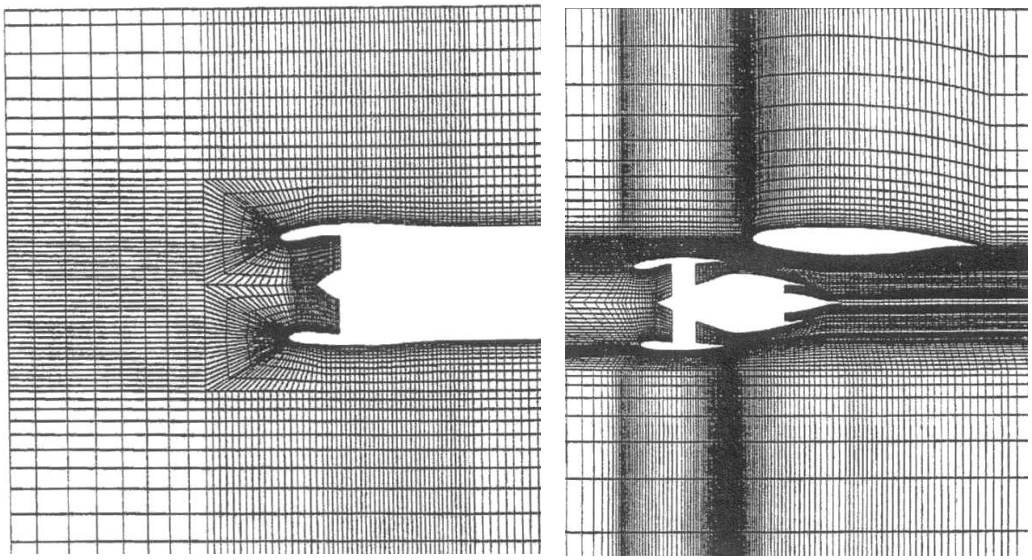

Figure 4.15 Grids for an isolated Inlet and an installed Nacelle (Joubert, 1993)

The design of the isolated nacelle can be divided in two steps, design of the inlet and the design of the exhaust system. Each one of these steps can be divided into four steps (basically the same as described above) these are: 1. Preliminary Design, 2. Geometric Optimization, 3. Performances Optimization and 4. Scale model test.

Computer Aided Design (CAD) is used for the Preliminary stage design. CFD is used for the second and third stages. Joubert (1993) uses different models to make the calculations for each of the stages; Inverse axisymetric potential and 3D Euler methods are used for the inlet design and Axisymetric Euler solver and Navier Stokes simulations for the Exhaust system.

There are three methods used for solving CFD problems (Rudnik, 2001). These are Euler, Euler with boundary layer displacement and Navier Stokes methods (see Figure 4.17). The simplest one is the Euler method and can be used where the flow can be considered inviscid without altering the final results substantially. There is an improvement for the Euler method which is the addition of a boundary layer displacement. The displacement helps for a more precise calculation of some viscous effects. The Navier Stokes methods take into account viscous effects making the results closer to experimental methods. The drawback of Navier Stokes methods is their computational costs as simulations based in Navier Stokes methods use four times more resources than Euler with viscous effects methods.

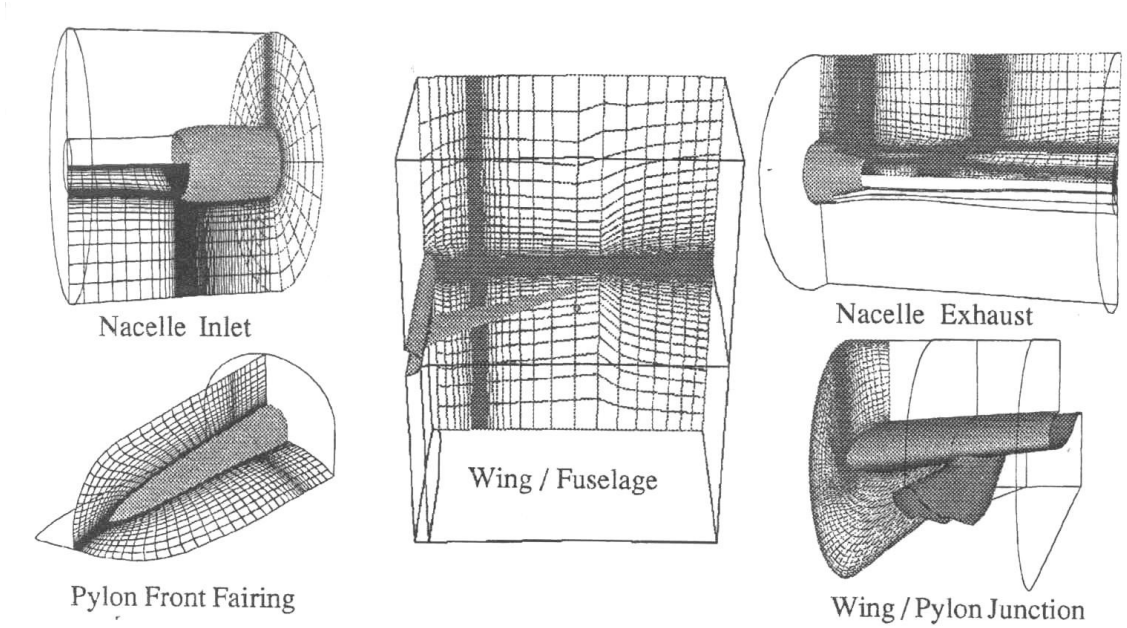

Figure 4.16 Chimera Grid generation Technique (Cedar, 1993)

Both Euler and Navier Stokes methods were used in a work carried out by Paté (1995) to compare the results from both methods. The results obtained from the analysis on an isolated nacelle are very similar for cruise condition showing better results for the top of the nacelle with the Navier Stokes methods. At high speeds the Navier Stokes method is significantly more accurate for shock positions. For spillage drag calculations both methods are very inaccurate, with the Navier-Stokes slightly being better.

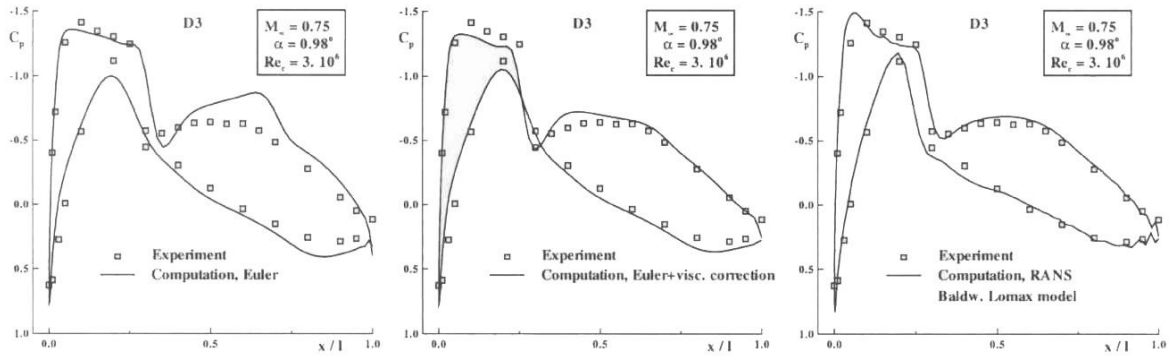

Figure 4.17 Capabilities of different numerical approaches (Rudnik, 2002)

Two Drag prediction workshops have been proposed by AIAA. Several companies including Boeing, Airbus, NASA, Fluent Inc., CFX and others took part in the research.

The results for the second Drag Prediction Workshop (DPW) where shown in Reno, USA. Each simulation has its own approach, including different types of mesh, turbulence models and solver. Two required cases were considered by all of the researching partners and two other optional cases were simulated. The simulations are based on the DLR-F6 geometry designed by DLR. The wind tunnel tests were performed in cooperation between ONERA ("National Office of Aerospatiale Studies and Research" in France) and DLR ("German Aerospace Centre"). For a detailed description of methodologies and results see the paper written by Lafin *et al*. (2004).

4.3.3 Grid Generation

The quality of a CFD simulation depends mostly on the grid used. Grid generation is based upon structured (typically quad cells are used in 2D models and hexagonal for 3D models) and unstructured meshes (triangular cells are the most common type in 2D and tetragonal for 3D models) each one of them with advantages and disadvantages. A structured mesh should be used if the geometry of the model influences specific characteristics (Rubini, 2004). Blocked grids is a method for meshing that allows combining different types of grids according to the requirements of the simulation or the flow characteristics at different sections of the domain.

There are several types of structured grids that can be used, most of them are based on two types of grids, C and H grids. In the literature regarding CFD for engine/airframe integration different types of grids are used. The most common mesh used is a block with C grid near the intake and H type at the far field and nozzle (Joubert, 1993; Keith, 1993; Li, 2000; Pate, 1995). On the other hand, simulations have been carried out using other type of meshes like unstructured (Devine, 2004) or H-type throughout the domain (Uenishi, 1990) and obtained good results.

Unstructured meshes also have been used for integration. Devine (2004) tried to study effects of a nacelle/pylon in a modern aircraft using an unstructured mesh of around 10,000,000 nodes. Koc (2005) was concerned about the drag and shock strength of the pylon surface at climb condition with an unstructured mesh of more than 2,500,000 cells.

5 Isolated nacelle (2D simulations)

5.1 Geometric Model Design

The first stage of the project is based on 2D simulations of the isolated nacelle. The nacelle was split in two different models. The two models are the afterbody (intake) and forebody (nozzle). Both models are axisymmetric. The results of this stage of the project set the basis for the next stage.

The model generated is a nacelle for a turbofan of a VHBR. The overall dimensions of the nacelle were given by VITAL. These dimensions are for a real nacelle, therefore the keel and crown have different values for many of the geometric parameters, mainly for the inlet. To create an axisymmetric model of a nacelle based on real dimensions it is necessary to set standard values. Special attention should be given to boundary layer separation in the generated model. The consideration for the base design values given below:

- Intake tip diameter is the average of both the keel and crown diameters given by VITAL.
- The throat base diameter is set to keep the same throat area. It is circular with the centre between the keel and the crown. The average of the diameter of the throat at both points is the diameter of the axisymmetric model.
- The outside diameter is the average diameter of both maximum diameters.
- The nozzle outlet diameters were set according to the area required by the cycle design.
- For the length of the intake cowl, an average of the lengths of the keel and crown given was taken.
- Also the inner lengths were given and were different. An average was used.
- The other dimensions were taken from those provided by VITAL or assumed.

A NACA-1 profile was chosen for the external shape of the fan, a super ellipse for the lip and a sp-line for the nozzle cowl and the inner part of the intake.

5.1.1 Forebody profile

Three main sections were designed for the intake. A NACA-1 profile was used for the bypass cowl, a super ellipse for the lip and a sp-line for the diffuser of the intake.

The NACA-1 profile was calculated using the method shown by Seddon and Goldsmith (1999). For the calculations of the profile shape only the length and maximum diameter are required.

The lip geometry is designed as a super ellipse. The super ellipse features four main parameters ‘a’, ‘b’, ‘m’ and ‘n’ (see Figure 5.1). The curve equation is:

$$\left(\frac{x}{b}\right)^m + \left(\frac{y}{a}\right)^n = 1 \qquad (40)$$

A super ellipse is a closed curve. For the lip geometry only one section of the curve is required. The section needed is one quarter of the curve. It can be plotted using the following equation derived from equation (40).

$$y = a\left(1 - \left(\frac{x}{b}\right)^m\right)^{\frac{1}{n}} \qquad (41)$$

In the project, the parameters ‘m’, ‘n’ and ‘a’ are assumed. The parameter ‘b’ is obtained from the relationship between the throat and highlight diameters. ‘a’ is a parameter that is going to be obtained from a relationship with ‘b’, instead of using ‘a’ the relationship ‘a/b’ is to be used. ‘a/b’ is a parameter that should be always above 1. Also ‘m’ should be above ‘n’ (Aimer 2005, Balkota 2005).

The inner shape of the diffuser is a sp-line. The parameters required for the curve were assumed to start at the throat with an angle parallel to the engine axis. The shape is a smooth curve to avoid boundary layer separation. At the end of the curve the diameter has to be the same as the fan diameter and be parallel to the engine axis. The length around the inner shape of the intake (lip and diffuser) was set as the average of the crown and keel dimensions of the ‘a’ parameter of the super ellipse and the diffuser length given by VITAL.

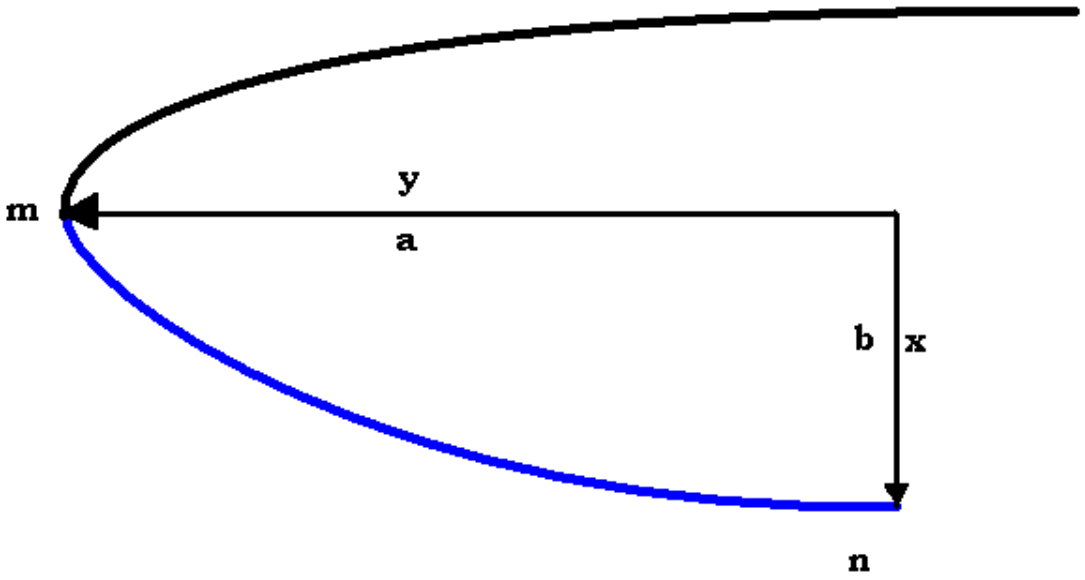

Figure 5.1 Super ellipse parameters

The final curve taken into account is the mid body. The mid body is a straight line, parallel to the axis. The line is assumed to be long enough to prevent any of the aerodynamic effects produced by the intake that would affect the outflow of the domain.

5.1.2 Afterbody profile

The afterbody profile design is based on four different curves. These are the midbody, the bypass cowl, core cowl and the exhaust cone.

The bypass cowl is designed to avoid a boundary layer separation at the top and to produce the least turbulence possible. The curvature has to be the same (or very similar) to the midbody to avoid the boundary layer separation. This is due to the high flow velocities around the cowl combined with the changes of pressure produced by the decrease in velocity. The bypass outlet should have a specific angle and the cowl of the nozzle should end in a very similar angle to avoid turbulence, also the air flow should be as smooth as possible. Because of these reasons the bypass cowl profile starts with a circumference tangential to MB until the profile angle is the same as the flow exhaust angle. The circumference section is followed by a straight line with the same angle with the axis determined by the data given by VITAL.

The core cowl is a surface between two airflows with a high speed and temperature. Therefore the shape has to be very similar for both airflow directions. The shape chosen was a straight line making an angle similar to the nozzle of the core exhaust. The angle has to be chosen to avoid producing turbulence. Therefore the angle must be larger than the bypass nozzle angle and very similar to the core nozzle exhaust angle.

Finally, the exhaust cone is set as a straight line with an angle larger than the core exhaust angle to allow a smooth expansion and long enough to avoid a boundary layer separation produced by the pressure fall.

The overall dimensions for both afterbody and forebody are shown in the image below. Notice that in the 2D the axis spinner was not designed due to the low influence of the spinner over the drag produced by the nacelle in axial flow.

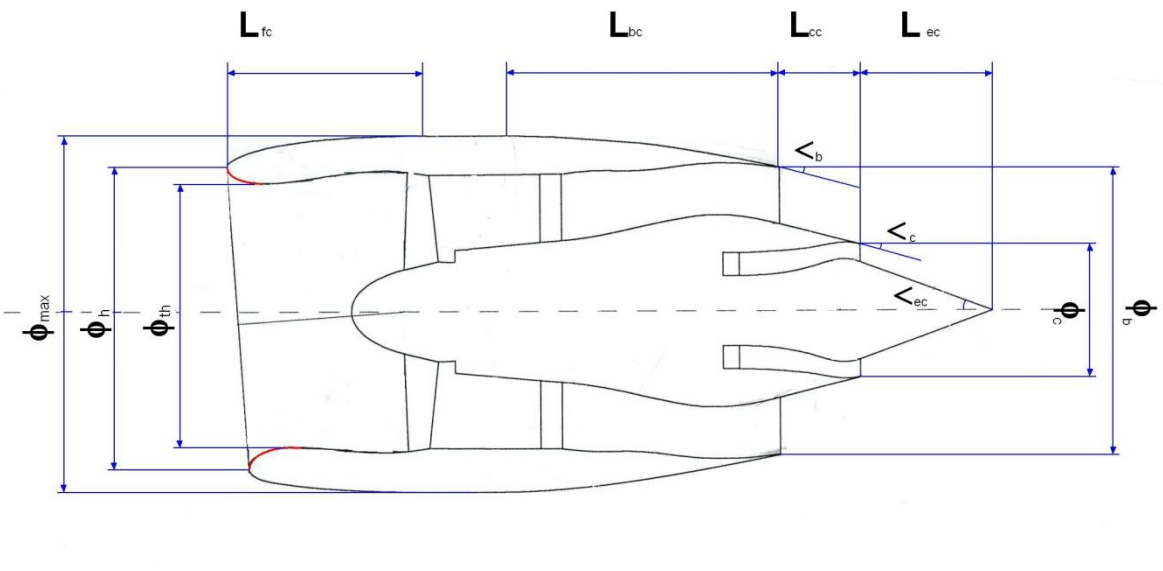

Figure 5.2 Nacelle design parameters[4]

5.2 Parameters variation

To perform the drag analysis a variation of the most important parameters is required. For the afterbody only two parameters were used. The drag bookkeeping system only requires

[4] In Figure 5.2 a real nacelle is shown. The parameters in the figure are sufficient for an axisymmetric design. To design a real nacelle more parameters are required. The values for the crown and keel design parameters are different.

data from the flow around the nacelle, because of this only the shape of the bypass exhaust is changed. The forebody requires more detail in the design. The properties of the flow going into the engine affect the flow going around, therefore the influence of the inner section parameters of the engine are to be analyzed as well.

The afterbody is analysed by changing the bypass external diameter[5] (D_b) and angle (α_b). The D_b is changed by increasing it by 2.5 and 1.25%, and decreasing it by 1.25, 2.5, 3.75, 5, 6.25 and 7.5% with respect to the base geometry. α_b was changed in a range of -10% to 20%. Each parameter was changed independently and with the other kept at base value. There are a total eighteen different models of the afterbody; nine models are varying D_b and ten with different α_b (in both sets the base model is included).

For the analysis of the forebody five parameters analysed: maximum diameter (D_{max}), highlight diameter (Dhigh), throat diameter (D_{th}), intake length (L) and the parameter 'a' of the lip curve. In all of the models created only one parameter value was changed at a time in 1% increments or decrements. Only D_{max} and Dhigh were changed at the same time, giving 4 different values to each parameter, 16 models were designed. Five values were given to the other three parameters. In total 28 models were created (fifteen changing D_{max} and Dhigh, four changing D_{th}, four changing L, four changing the lip length ('a') and the base model).

5.3 Meshing strategy

5.3.1 Afterbody

For the grid of the afterbody different models were used. Different structures were used in order to achieve a convergent CFD model. None of the non-convergent grids is described in this document. Different shapes for the far-field were considered and H and C meshes were created in order to achieve convergence.

In order to get the convergence, the nozzle cell was designed to be as a structured mesh over all of the domain. Fine cells were used near the nozzle and they expanded as it went away from the nacelle.

[5] The internal diameter is set by the area required by the nozzle.

Due to the pressure differences required for the nozzle of the engine a fine mesh was required after the exhaust plane. The mesh was created in several sections. A total of seven sections were required. The zones which were used can be seen in Figure 5.3. These zones were created in order to have a better control of the distribution of the cells and their size. The total number of cells in the meshes was different for each one of the models created but for all of them it is above 450,000.

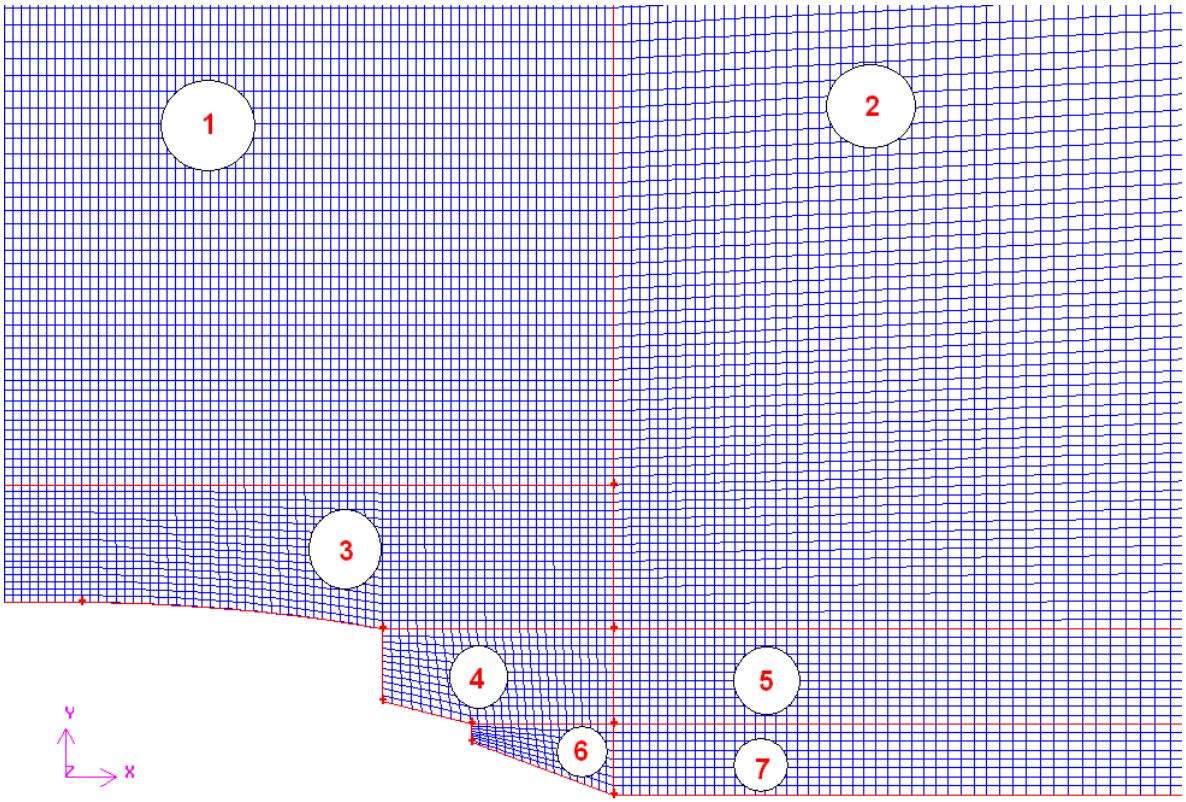

Figure 5.3 Afterbody grid zones (Coarse mesh shown)

5.3.1.1 Mesh independence

To evaluate the mesh independence another two grids were created with different cell sizes and a triangular mesh (Figure 5.4). A coarse mesh with 25% of the total number of cells was created. The number of nodes was cut by half on each segment therefore the number of cells in each section was reduced by one quarter.

A finer mesh with four times bigger than the original was created. The fine mesh was created by doubling the number of nodes on each section.

The last mesh is an unstructured triangular mesh. The zones used for the structured mesh were deleted and the unstructured one is made of one zone only. The parameters used are

very similar to the medium sized one although some sides are different in order for the grid to be created.

Coarse

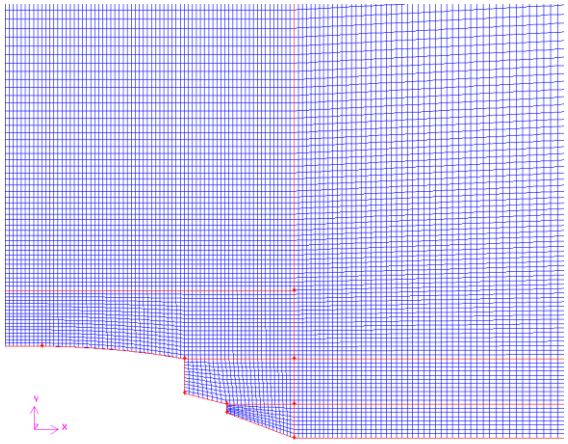

Medium

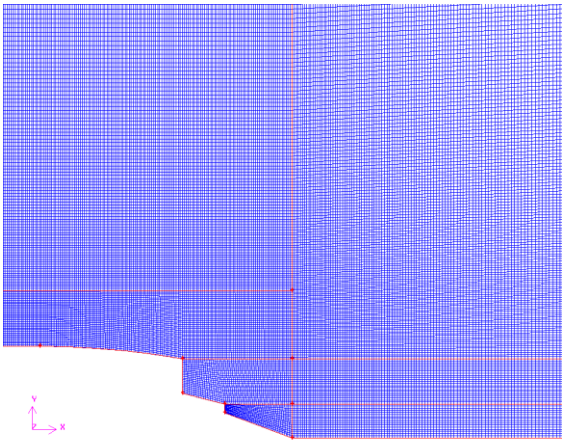

Fine

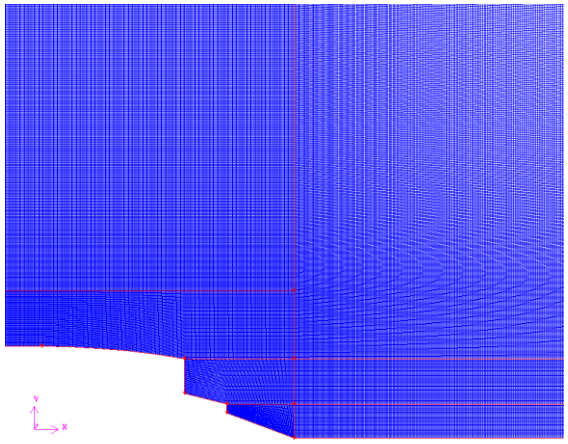

Triangular

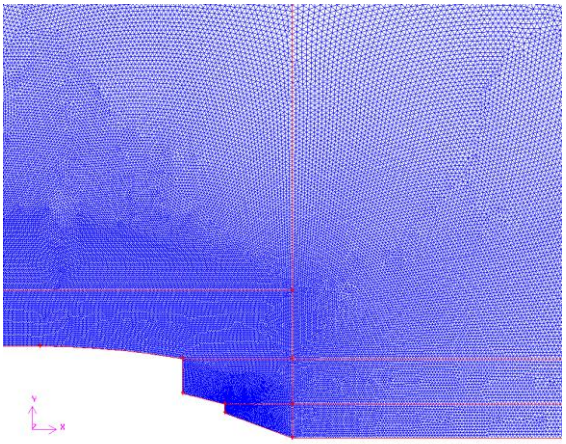

Figure 5.4 Grids created in order to evaluate the mesh independence of the nozzle.

5.3.2 Forebody

Different grids were created for the intake. Only the mesh that converged is presented in this document. Several kinds of meshes were tried for this model. The final mesh was a hybrid mesh of a C mesh around the intake and an unstructured mesh near the axis, around the C mesh and the far field.

The mesh was created by separating the entire domain in seven sections with different characteristics, see Figure 5.5. The separation was made to control the shape and distribution of the cells. Section one and two (midbody and inner body respectively) were

meshed in order to evaluate the flow effects on the boundary layer. The length of all of the cells on the x axis (the nacelle) are the same, for the y axis the length is very small length near the nacelle and increases as it separates from it. Section three (intake cowl) is also meshed with four side elements. The side element representing the intake cowl starts with a cell length similar that of section one and decreases until it gets to the nacelle highlight where section three finishes. The grid for section four was designed by using five sides, the most important are for the lip and the expansion section. The expansion section cell lengths decrease from the length similar to those in section two and to a very short length. This short length is constant for the lip section. Section five is an unstructured triangular mesh which includes the area around the cowl in both the outflow and inside the intake. The boundaries of section five with the exception of the structured mesh, have the same size for each cell. Sections six and seven cover the rest of the domain with an unstructured triangular mesh. Near the intake the size of the cells is similar to section five and it expands as it gets further from the nacelle until it gets to the far field borders.

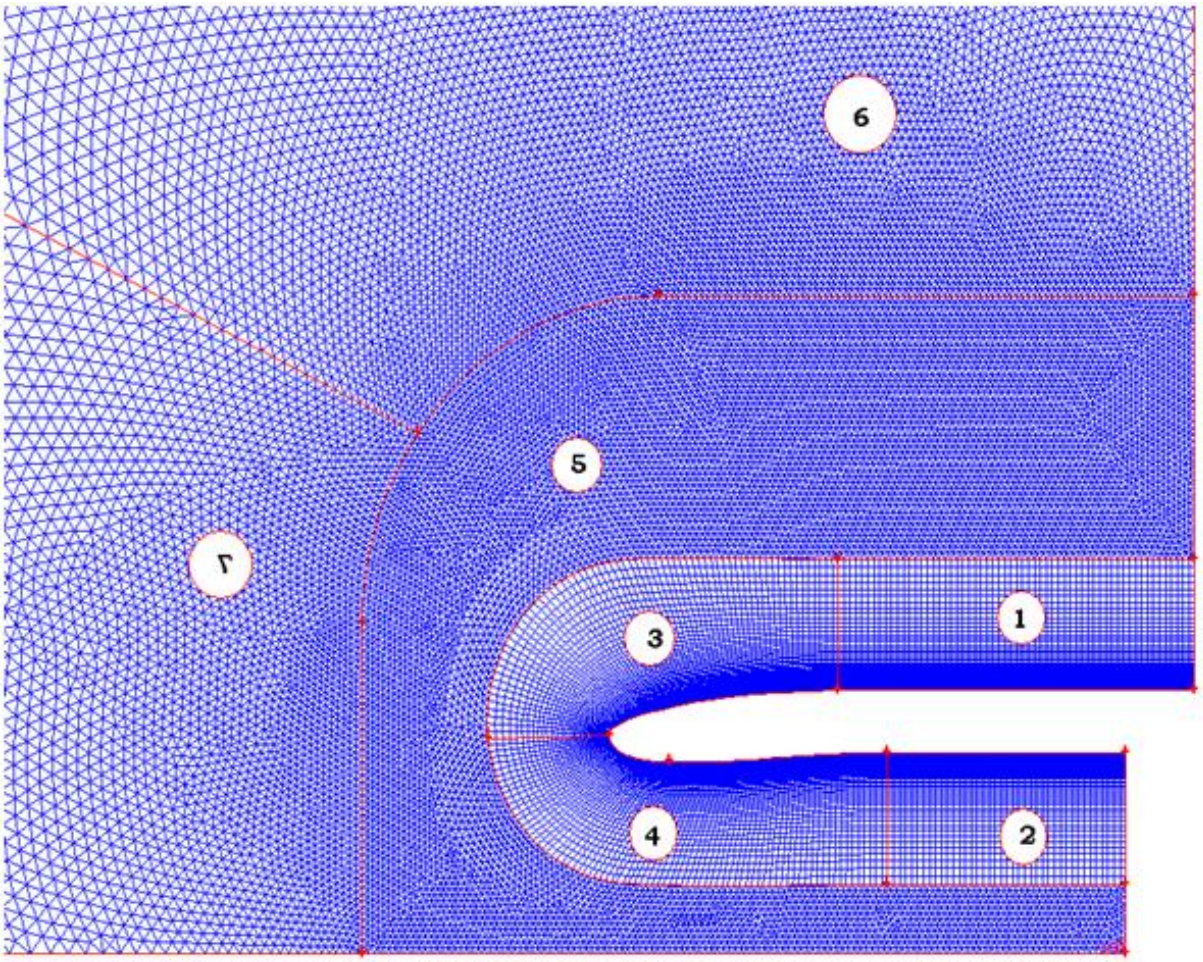

Figure 5.5 Forebody meshing sections

5.3.2.1 Mesh independence

Two meshes were generated for the grid independence analysis. One grid was set as the reference. A finer grid was generated by decreasing the number of cells at each boundary by half and therefore reducing the total number of cells nearly by one quarter. To increase the number of cells the number of sections at each of the boundaries was doubled and therefore the total number of cells was approximately quadrupled (See the figure below).

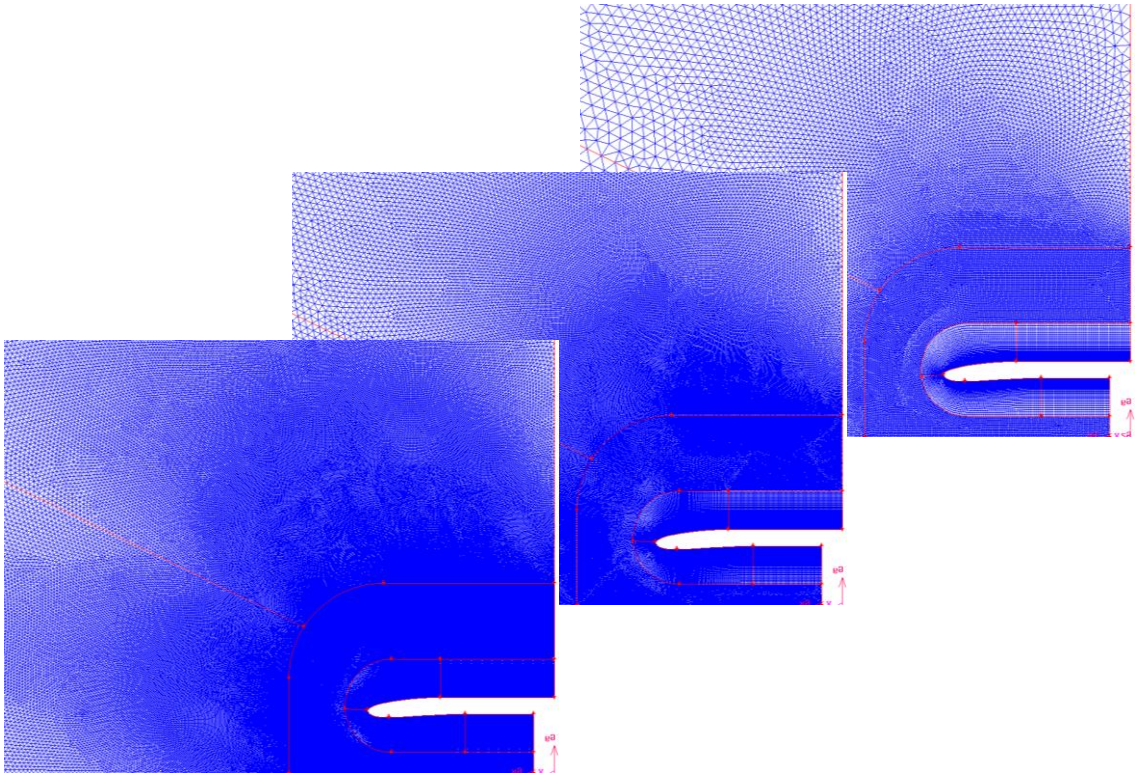

Figure 5.6 Three meshes created to analyze the mesh independency

5.4 CFD

5.4.1 Simulation Parameters and Solver

For the CFD simulation of both of the models there was a problem with their convergence due to their axisymmetric shape. According to Dr. Philip Rubini the convergence of axisymmetric models is more easily achieved by making a transient simulation instead of a steady state one. The time period simulated must be small enough for the model to converge then the model would get into a steady state.

Also, the convergence should be obtained by dividing the simulation into two stages. The first stage was to allow the airflow set with the initial conditions to get out of the domain. Non-viscous flow was used to avoid divergence at the first stage. After the laminar flow simulation stage air viscosity was taken into account to calculate the final result. The time period considered was 10% of the time a particle should take to cross the entire domain in the free stream section.

5.4.2 Convergence

Usually the convergence of a CFD simulation is based on the residuals. For the simulations at this stage the residual could not be set as the convergence parameter due to the size of the grid and the requirements of the result near the wall. The residuals in these simulations got asymptotic above the convergence criteria values (See figure below).

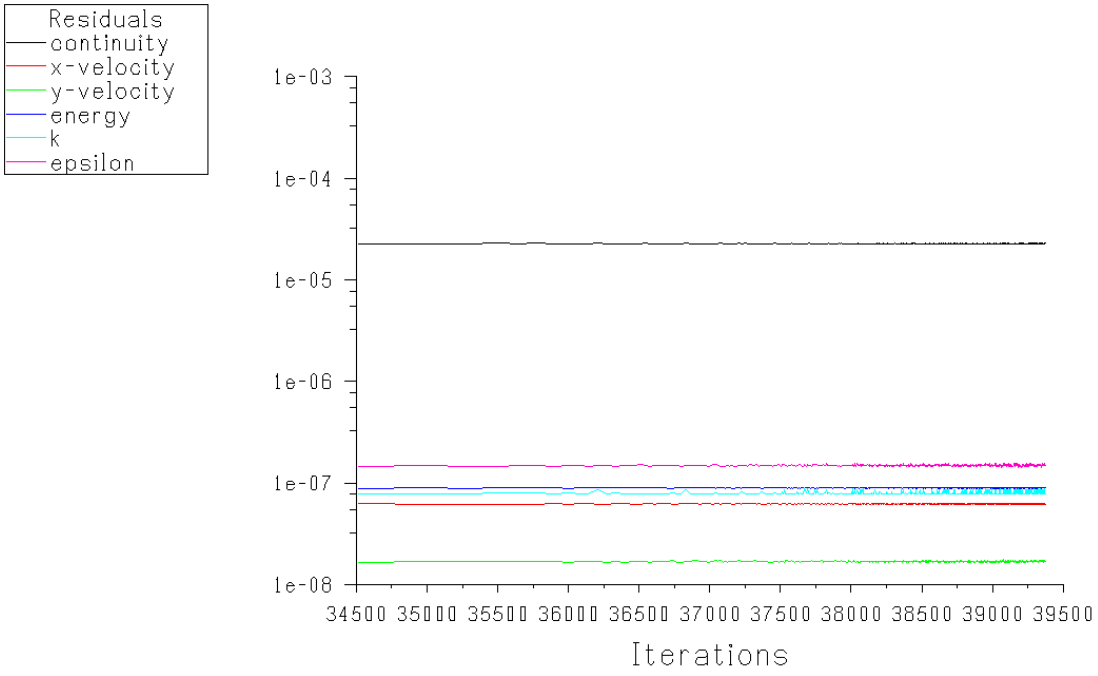

Figure 5.7 Simulation residuals got asymptotic (Afterbody simulation shown)[6]

When the residuals cease to decrease due to meshing size an alternative convergence criterion has to be taken. The convergence was set on a Drag and Lift Coefficients criteria. When they stay constant at a certain value can be considered that the simulation has converged, as is shown in Figure 5.8.

[6] Fluent does not keep registry of all of the residuals history unless required. For this image only the last time steps (the asymptotic section) are shown.

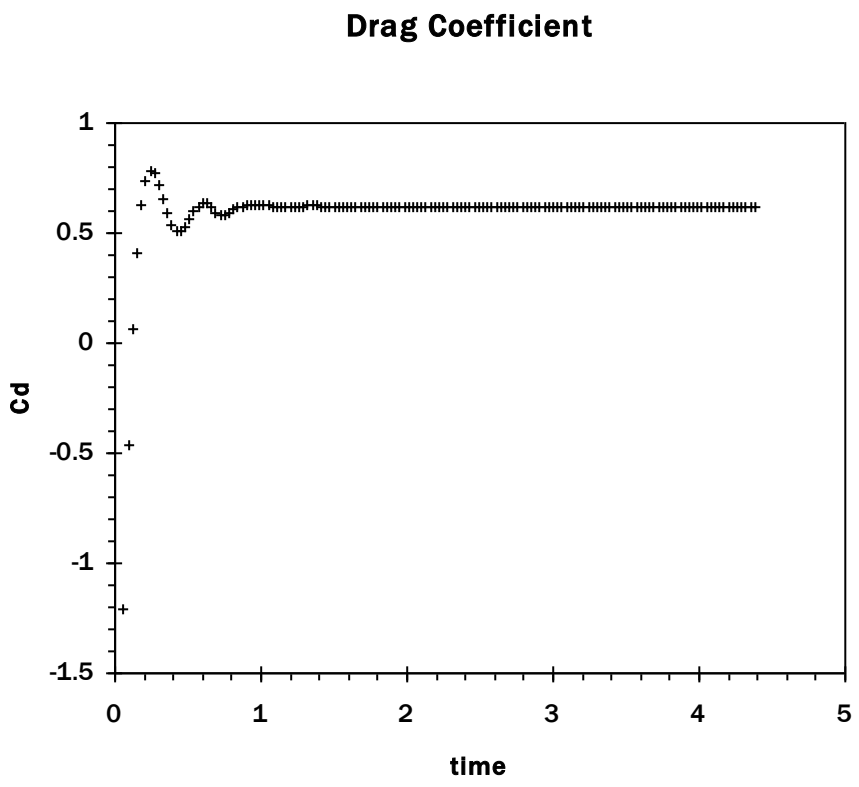

Figure 5.8 Drag Coefficient Convergence criterion (Afterbody simulation shown)

Same criterion was used for both of the simulations, the afterbody and forebody.

5.5 Initial Conditions

For a time dependent simulation it is very important to consider the initial conditions in both convergence and the result accuracy.

The convergence usually depends on the initial conditions. The conditions are based on the free stream but some parameters were changed to avoid divergence. The main parameters to be considered in the initial conditions are the following:

- Density
- Velocity
- Pressure
- Temperature

The most important parameter to be changed in order to avoid divergence is the velocity. The velocity was set to lower values from the Far Field value (Mach number of 0.82).

5.6 y+ parameter

To obtain accurate turbulence results a special consideration on the grid has to be made. As the drag depends on the turbulence of the flow near the nacelle, small cells must be used. The non-dimensional parameter y+ is used to evaluate the size of the meshes to evaluate turbulent dependent parameters.

Y+ is a result-based value calculated using the velocity, shear stress, density and viscosity. It is calculated with the following formula

$$y^+ = \frac{\rho u_\tau y_P}{\mu} \qquad (42)$$

where u_τ is the friction velocity[7], y_P is the distance from point P to the wall, ρ is the fluid density, and μ is the fluid viscosity at point P.

According to Fluent manual, for non-equilibrium wall functions y+ should be in the range of 30<y+<300, a value near 30 is desirable.

5.7 Afterbody simulations

5.7.1 Main parameters

The main parameters for the simulations are given here. The solver used was the Pressure Based, axisymmetric and unsteady solver. The viscous model used was a k-ε standard model.

The Boundary conditions (shown in Figure 5.9) are;

1. Free stream- Pressure inlet
2. Far-field – Pressure far field

[7] Friction velocity is calculated with the formula $u_\tau = \sqrt{\tau_w / \rho_w}$

3. Outflow – Pressure outlet
4. Axis
5. Cold exhaust – mass flow inlet
6. Hot exhaust – mass flow inlet[8]

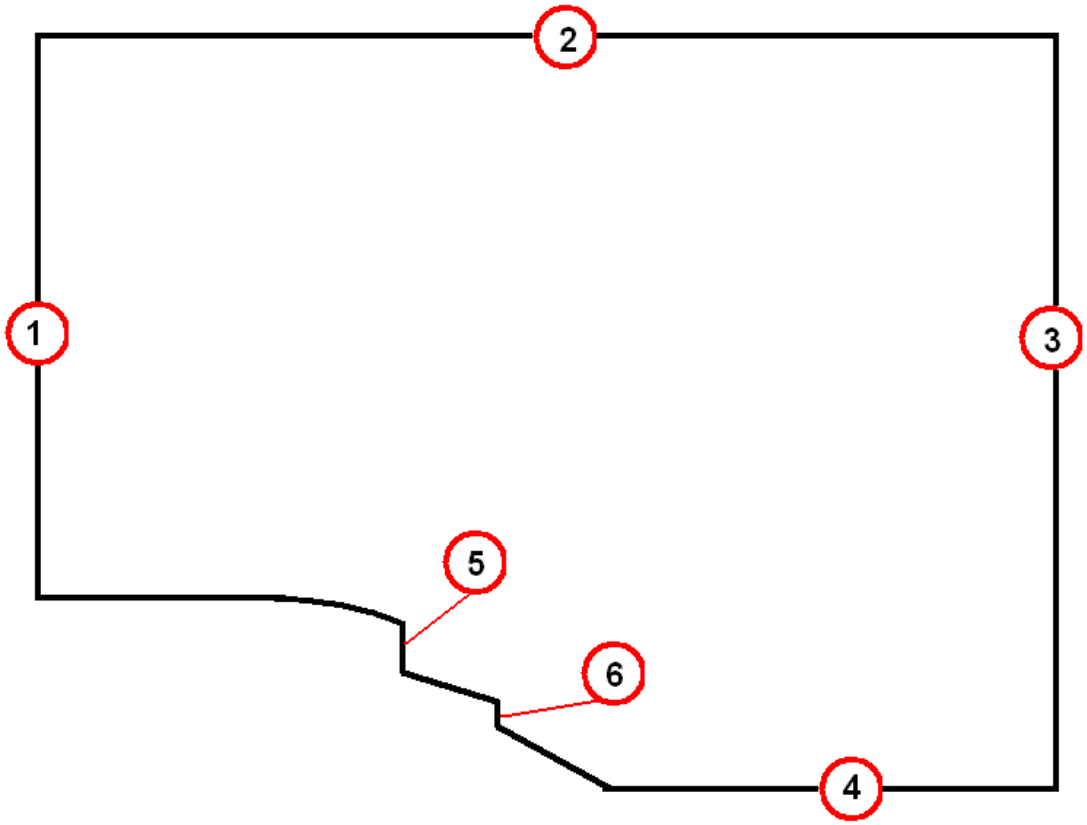

Figure 5.9 Boundary Conditions for The afterbody (not to scale)

5.7.2 Mesh Dependency Analysis

After achieving convergence in one of the simulations an analysis of the mesh independence was carried out. Three more grids were generated each with different cell density and form, see Chapter 5.3.1.1.

[8] The Cold and hot exhausts both are set as inlet. This may seem wrong, because the exhausts are actually outlets of the engine, but both are airflow inlets to the domain of the simulation.

For every simulation the same parameters are used, including the mesh independence analysis. The parameters considered for this analysis are those that have a direct influence on the drag. These are pressure and friction force. These can be analysed in different surfaces, but the surface where the drag is created is on the bypass cowl, therefore is the only one taken into account. The core cowl and exhaust cone also produce axial forces which have to be considered by the engine manufacturer mainly.

The reference values are set in Fluent. These values are used mostly for the parameter of $\frac{1}{2}\rho_{ref}v_{ref}^2$, this is equal to the dynamic head of reference.

For each cell near the cowl there is a different value of C_p and C_f, all of these values are plotted in Figure 5.10 and Figure 5.11.

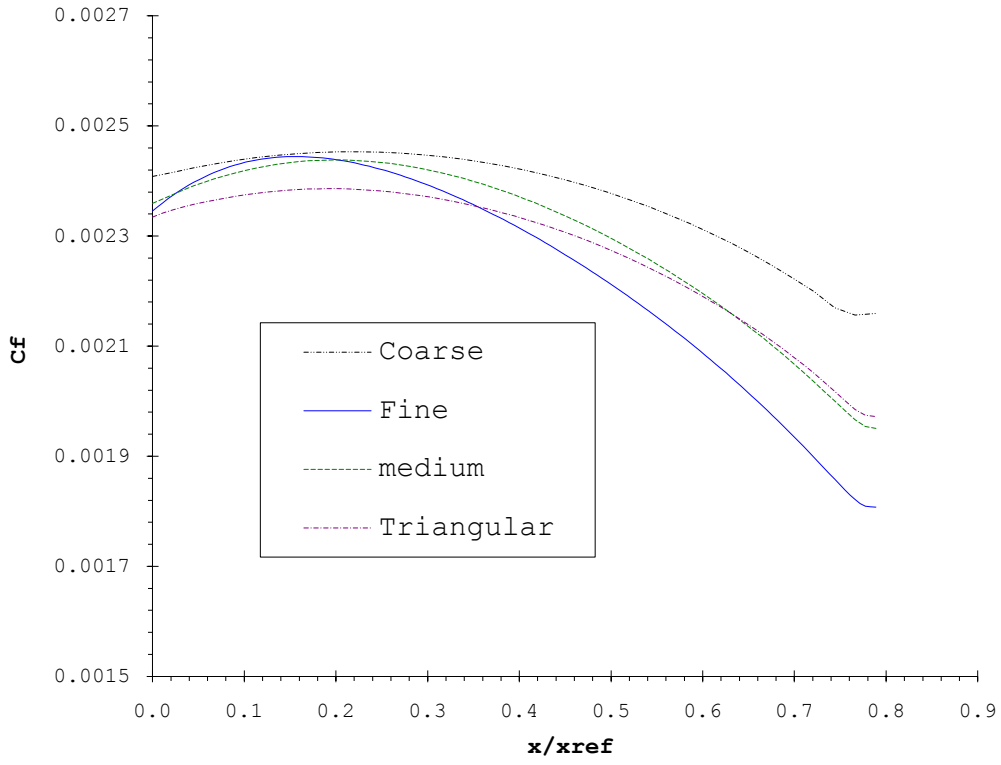

Figure 5.10 Comparison of the Cf for the afterbody

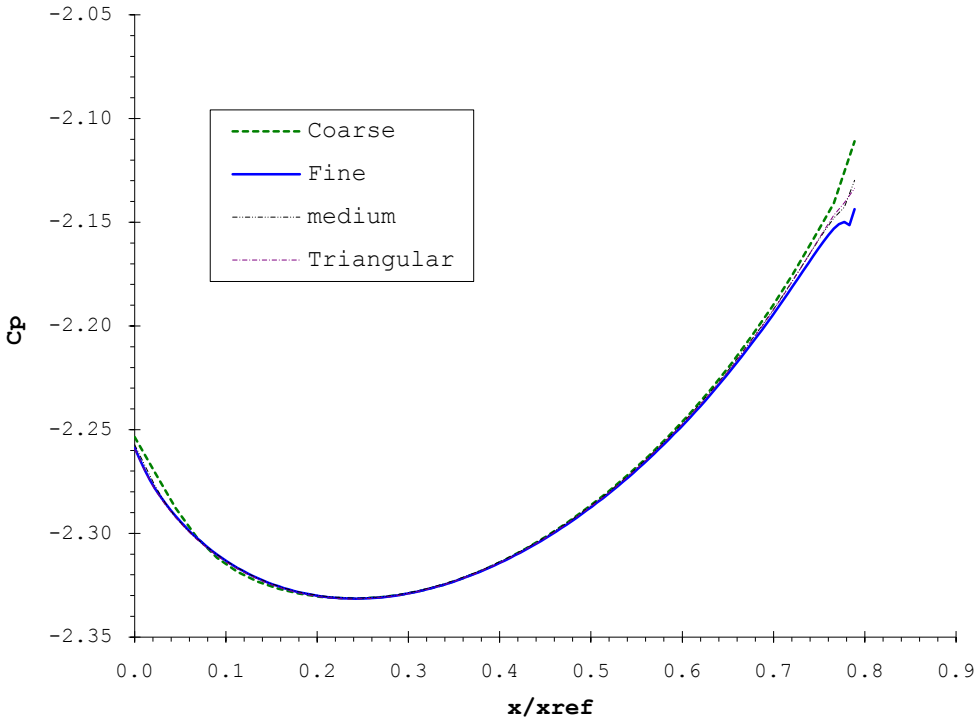

Figure 5.11 Comparison of the Cp for the afterbody

From the figures above it is possible to see that the results obtained from the calculations made with the four grids are very similar. A similarity of the results can be evaluated by calculating the maximum and minimum errors. A reference must be chosen. Assuming that the calculations made with the fine grid are the most accurate then they are chosen as the reference values. The following table shows the comparison data obtained by the statistical analysis.

Table 1 Afterbody mesh dependency Cf and Cp comparison

	Cf	**Cp**
Grid	Maximum error (%)	Maximum error (%)
Coarse	19.48	1.53
Medium	8.01	0.65
Triangular	9.13	0.47

The error values for the pressure coefficient are very small in the three cases, all below 1.5%. For the friction coefficient the error values seem to be large for the coarse mesh but come down to acceptable values for the medium and triangular meshes. The high values of the friction coefficient could be produced by noise generated out of the calculations. Fortunately the value of the AB drag is based mainly on the pressure forces.

5.7.3 y+ analysis

The y+ for the afterbody is calculated only for the bypass cowl without considering the midbody section. In Figure 5.12 is an example of the y+ plots. From all of the afterbody simulations the results are similar to the ones shown below.

The values obtained in this case are between 41 and 46 thereby complying with the requirement mentioned in chapter 5.6.

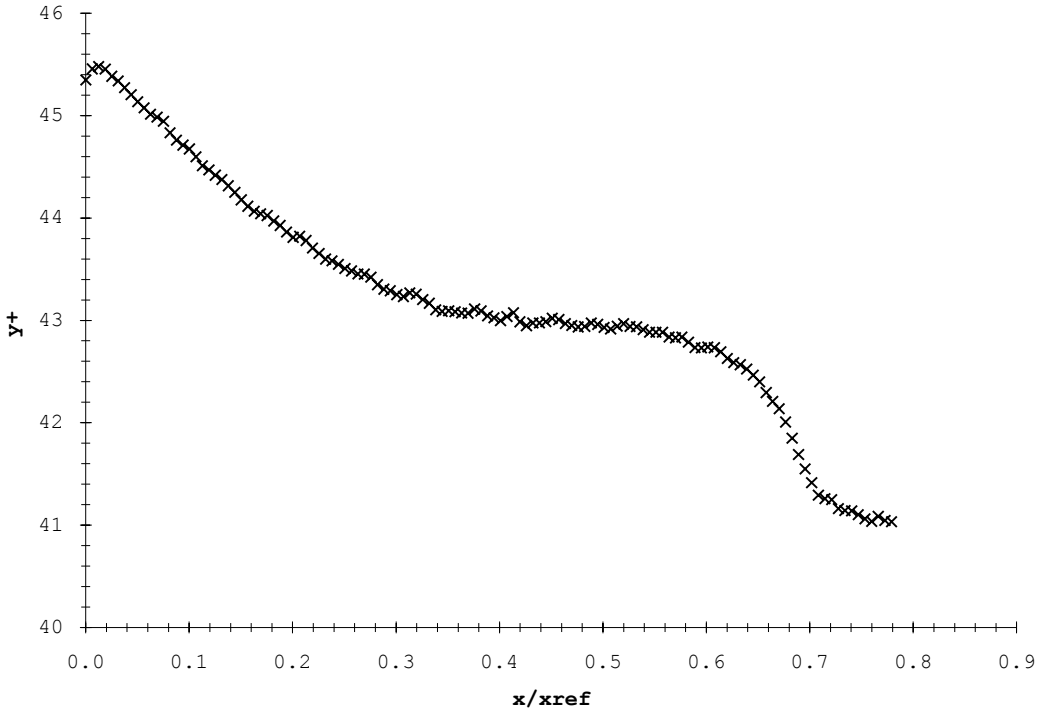

Figure 5.12 The y+ parameter for one of the Afterbody simulations

5.7.4 Parameters to be analyzed

To analyze the drag produced by the AB the main parameters are basically the ones setting the shape of the external nacelle. The shape of the sections of the engine inside the

inner flow remains unchanged because it was assumed that their change would not affect the drag by a significant amount.

The parameters considered for the analysis are the following:

- Maximum Diameter
- Exhaust angle

The exhaust angle is the angle between the axis of symmetry and the tangent of the AB cowl at the maximum down flow point.

The exhaust diameter was not considered in the simulations analysis because it is a parameter set by the engine designers. If the diameter were changed then the core cowl section also would require a modification to keep the same exhaust area and this analysis was not considered in the initial scheme. Changing the bypass exhaust area would change the aerodynamic parameters and would modify the uninstalled performance of the engine.

The numbers shown below are normalized to a reference value. The range of values is given as follows:

Table 2 Values to be analyzed for the 2D Afterbody simulations (relative to a reference value)

D_{max}	α_{bypass}
0.925	0.900
0.938	0.950
0.950	0.970
0.963	0.990
0.975	1.000
0.988	1.010
1.000	1.030
1.013	1.050
1.025	1.200

5.7.5 Results and analysis

The two figures shown below are an example of the profile of pressure and velocity obtained from the simulation. It is worth mentioning that although in Figure 5.14 it appears as if the bypass and core flows are subsonic, in real flow should there be small shockwaves influencing the boundary layer development in both stream flows (Keith, 1993). These shockwaves do not appear in the calculations because the size of the grid is not small enough to show them. Although they not appear in the simulation calculations the influence on the drag calculations is not significant because the error is in the inner flow stream calculations.

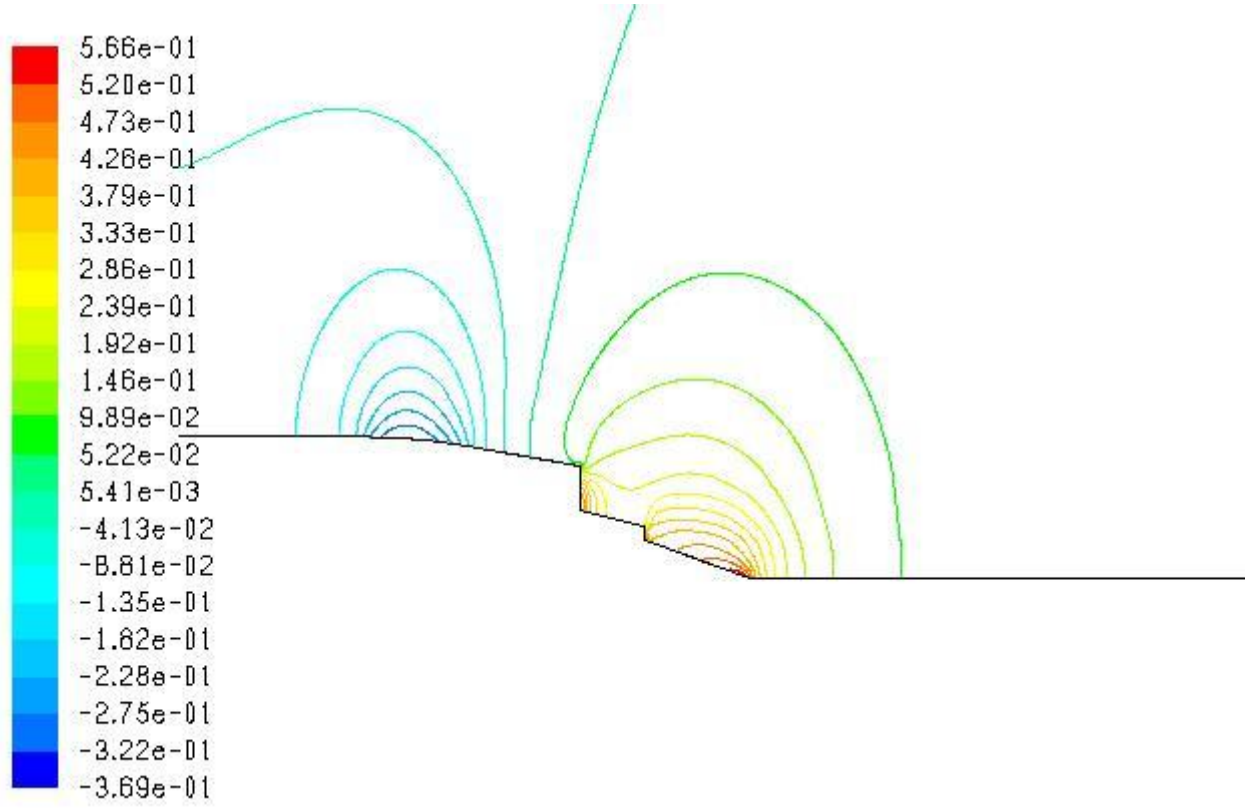

Figure 5.13 Afterbody contours of Pressure Coefficient

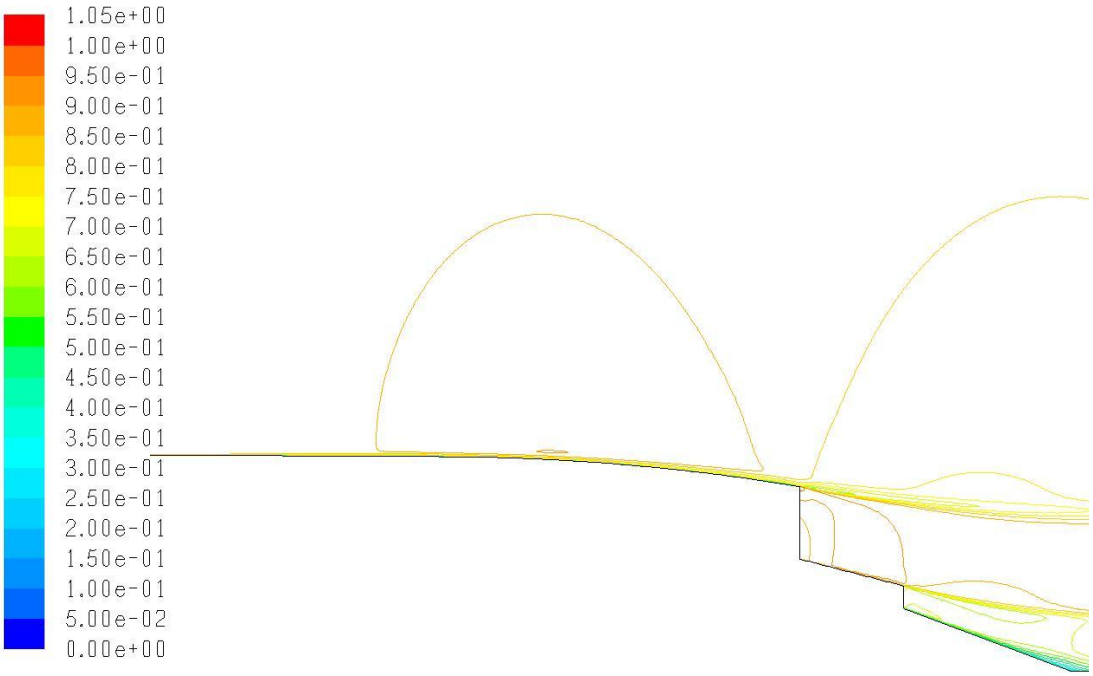

Figure 5.14 Afterbody contours of Mach number for a small maximum diameter nacelle

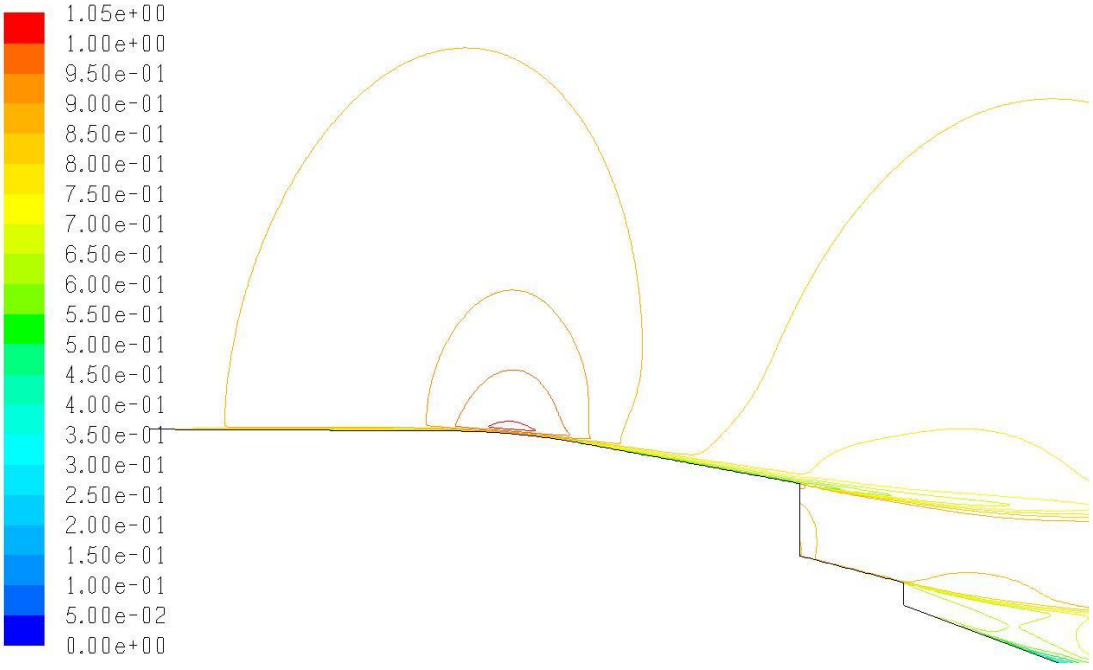

Figure 5.15 After body contours of Mach number for a large maximum diameter nacelle

The results for all of the simulations are shown in the following tables. The plots of the results are shown and analyzed after the tables.

Table 3 Afterbody pressure, viscous and drag coefficients for different maximum diameters

Dmax rel (%)	Cp_rel (%)	Cμ_rel (%)	Cd_rel (%)
-7.50	-33.41	-2.04	-29.70
-6.25	-25.88	-1.27	-23.06
-5.00	-18.96	-0.57	-16.96
-3.75	-13.68	-0.17	-12.31
-2.50	-8.95	0.05	-8.17
-1.25	-4.53	0.12	-4.32
0.00	0.00	0.00	0.00
1.25	4.83	-0.24	3.78
2.50	10.55	-0.63	8.70

Table 4 Afterbody pressure, viscous and drag forces for different exhaust angles

α_rel (%)	Cp_rel (%)	Cμ_rel (%)	Cd_rel (%)
-10.00	-2.96	-0.59	-2.65
-5.00	-3.09	-0.60	-2.76
-3.00	-1.99	-0.36	-1.77
-1.00	-0.80	-0.12	-0.71
0.00	0.00	0.00	0.00
1.00	0.32	0.09	0.29
3.00	1.42	0.28	1.27
5.00	2.50	0.48	2.23
20.00	9.28	1.54	8.25

To calculate the Drag of the afterbody the post-exit force needs to be estimated. In Fluent the drag given by the software is the addition of the pressure and viscous force, but this is not the case for the drag as defined in section 4.2.1; to calculate the AB drag the post-exit

force must be added. The post-exit force is also called post-exit thrust because it is a force in the direction of thrust.

In the notes of Aircraft Engine Integration by Mr D. Williams (2006) it said that a Nozzle Pressure Ratio (NPR) value is enough to calculate a value of the ideal post-exit forces. It may be seen that the ideal post-exit thrust is quite significant. Unfortunately, in real flow the magnitude of this force depends on the type of nozzle employed and the design of the afterbody. The real flow value departs from the ideal flow usually used to calculate this value.

Table 5 Relation of the NPR and ideal post-exit force taken from Aircraft Engine Integration Notes of Mr. D. Williams (2006).

NPR	=	1.853	3	5	10	15	∞
Φ_{post}/F_{G9} (%)	=	0	.83	3.55	8.78	12.1	51.4

The NPR for the bypass nozzle of all of the models is below 1.83. Therefore the post exit force is assumed to be very low and is ignored in the AB drag calculations in this project.

For both of the figures shown below there is a comparison of the change of the viscous drag (Cμ) and the wet surface (A) of the nacelle. The measurement is made from the tip of the AB and the nozzle, the point where the external and bypass flows start to run alongside and mix.

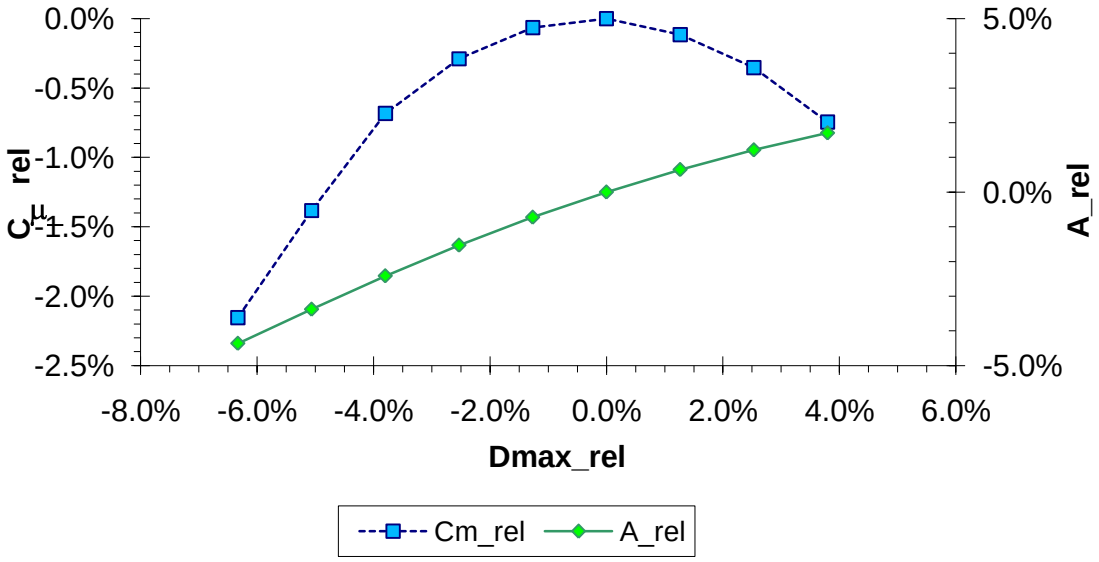

Figure 5.16 Comparing the Viscous drag coefficient changing the maximum diameter

In Figure 5.16 the change of the diameter can be seen to be quite significant to the calculations of viscous drag. A small increase of the maximum diameter would generate a significant change in the wet surface. The area is increasing with the maximum diameter and the drag produced also increases until it gets to a maximum point where the viscous force decreases if the maximum diameter is increased. The viscous drag is decreased because the velocity change is larger with a big maximum diameter than the one with a small diameter therefore the drag is larger at the up-flow point and smaller at the exhaust point (see figures Figure 5.14 and Figure 5.15).

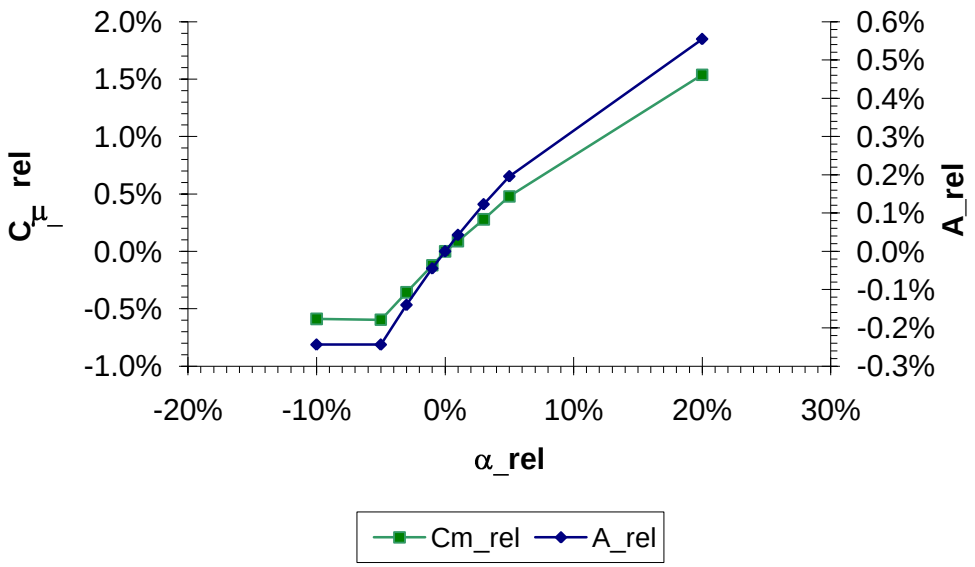

Figure 5.17 Comparing the Viscous drag coefficient changing the exhaust angle

The exhaust angle of the AB is of low significance for the velocity changes. In Figure 5.17 the change of viscous drag can be seen to be closely related to the wet surface area. This is because the velocity profile changes are very small in relation to the angle change.

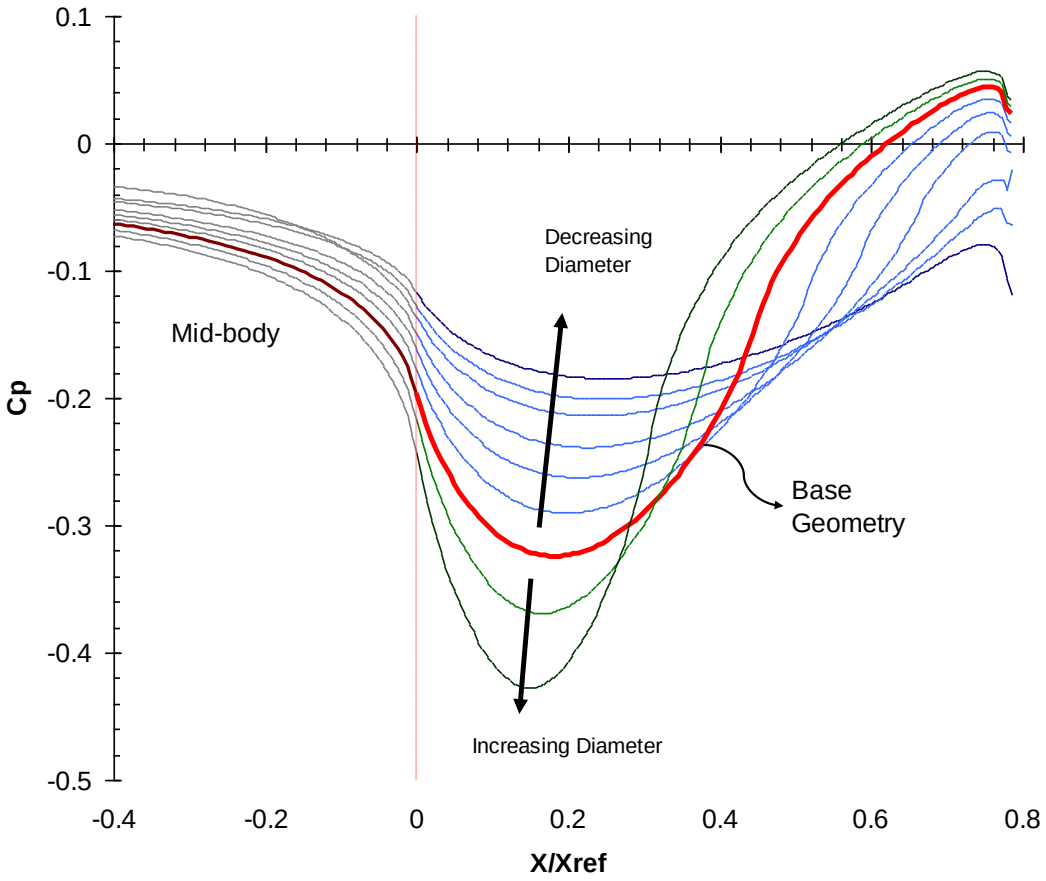

Figure 5.18 Pressure profiles over the Afterbody for changing of maximum diameter

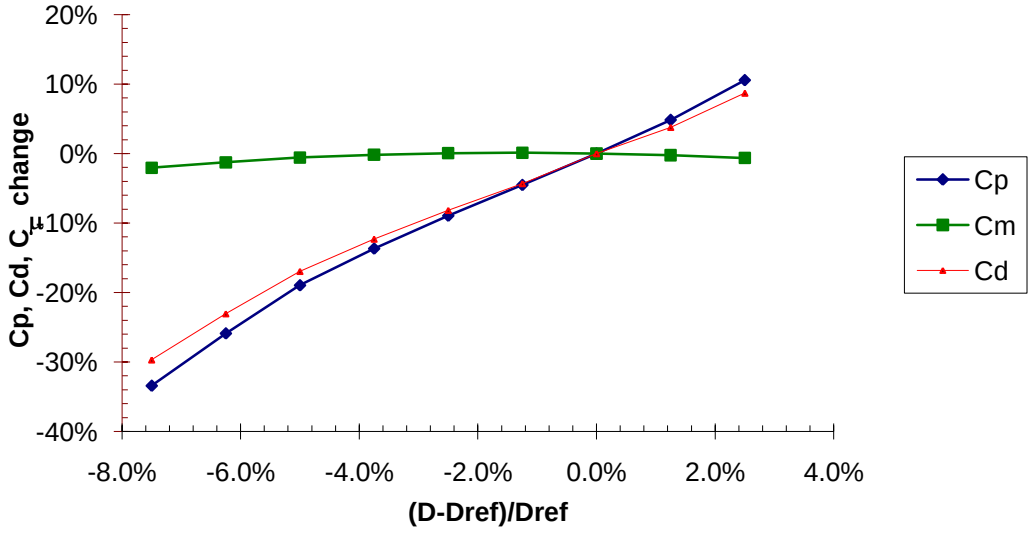

Figure 5.19 Influence of Dmax on viscous, pressure and drag coefficients on the AB

The main influence for AB drag is the pressure, as can be seen in Figure 5.19. The drag changes are linked mostly to the pressure drag and increased or decreased by a small

amount by viscous drag. A nacelle with a large maximum diameter produced a large velocity change, therefore the pressure also changes significantly, as can be seen in Figure 5.18.

At the exhaust point of the AB there is a sudden decrease of pressure in all of the simulations. The pressure on the surface of the AB cowl is very difficult to calculate (Covert, 1985). The main reason for this change is the bypass flow influence on the external flow. The sudden change or pressure could produce a boundary layer separation and turbulence at the end of the boattail.

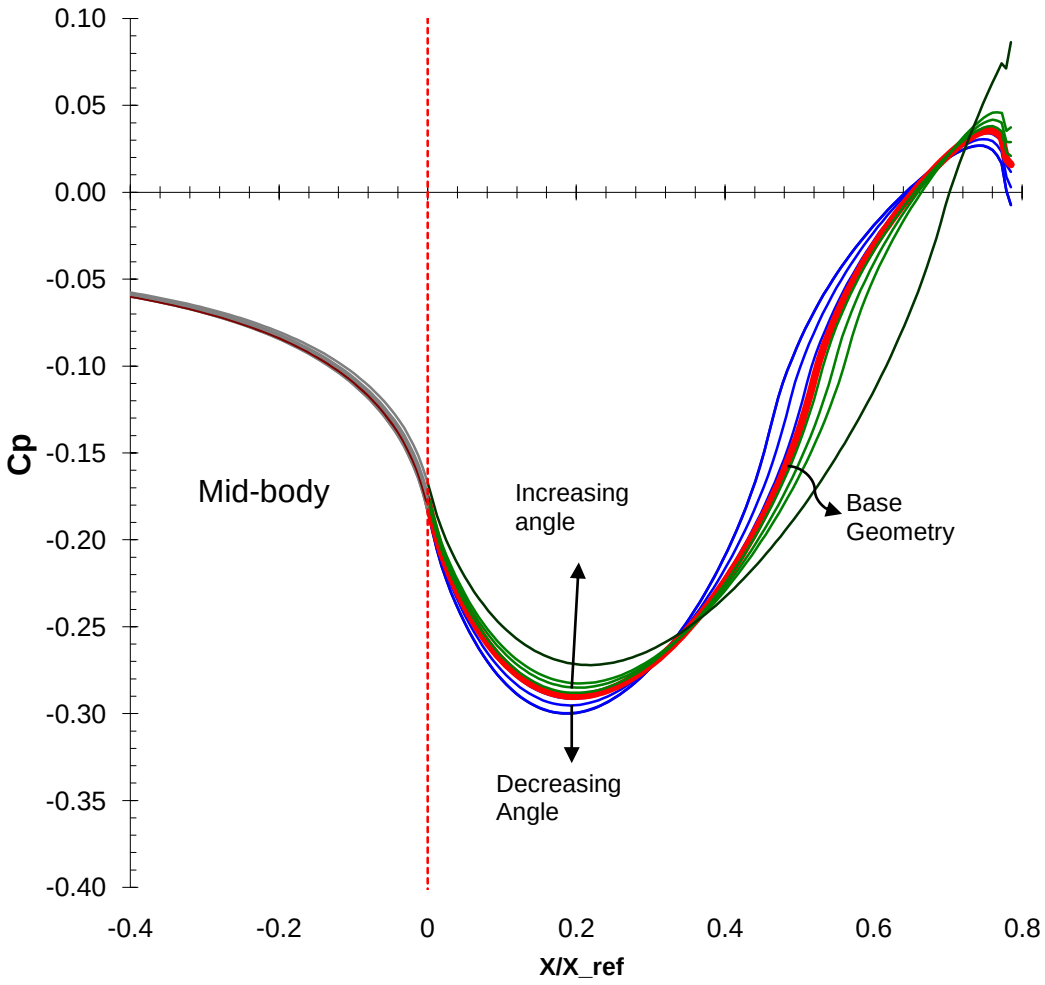

Figure 5.20 Pressure profiles over the Afterbody for changing of exhaust angle

The AB drag is not influenced significantly by the change of the exhaust angle. As can be seen in Figure 5.21 the drag change is below 5% with a change of 10% of the angle. In Figure 5.20 shows how the pressure changes are very small for all of the simulations, even with a large variation (+ 20%) the pressure changes are not very large.

The main issue about the angle is the propensity of causing a boundary layer separation with large angles. The boundary layer separation would decrease the pressure of the boattail generating a pulling pressure force that would make the drag force increase. With the conditions established for the simulations at this stage there is no significant impact in the drag.

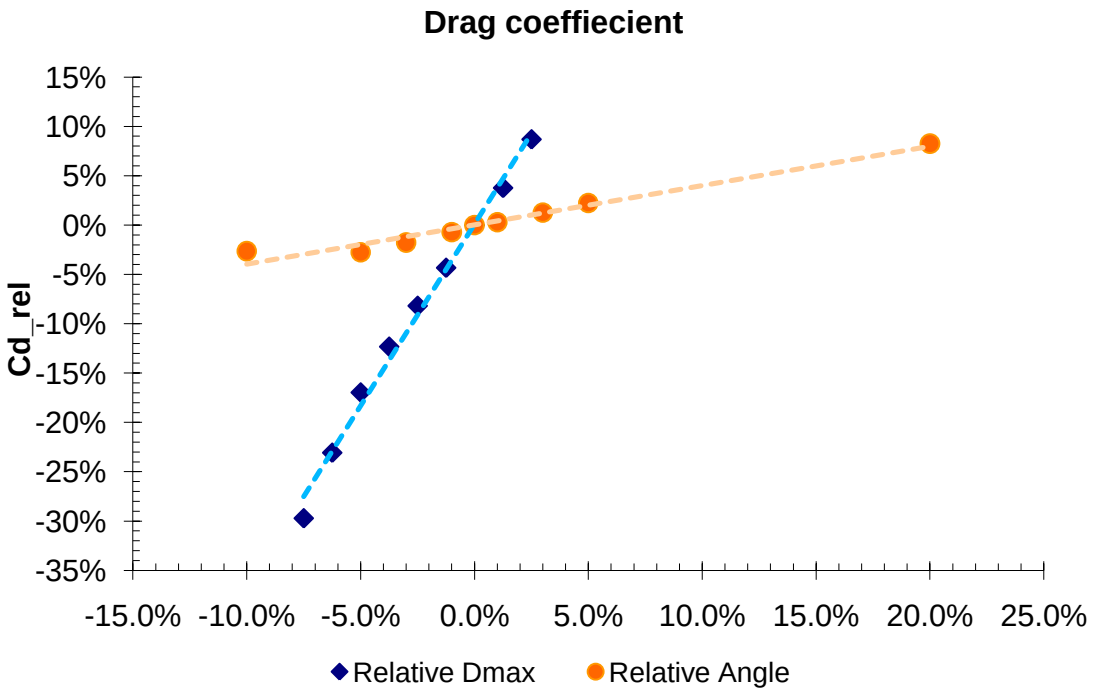

Figure 5.21 Drag change for the change of the maximum diameter and the bypass exhaust angle

5.8 Forebody simulations

5.8.1 Main parameters

For the intake the parameters for the solver are very similar to the Afterbody. The main difference is that it was run in a density based solver. It was also an axisymmetric and unsteady solver. The turbulence model is also a k-ε.

The boundary conditions are the following: (See Figure 5.22)

1. Free stream – Pressure Outlet
2. Far field – Pressure Far Field
3. Inlet – Pressure Far field

4. Axis

5. Fan – Pressure outlet with a Mass Flow set

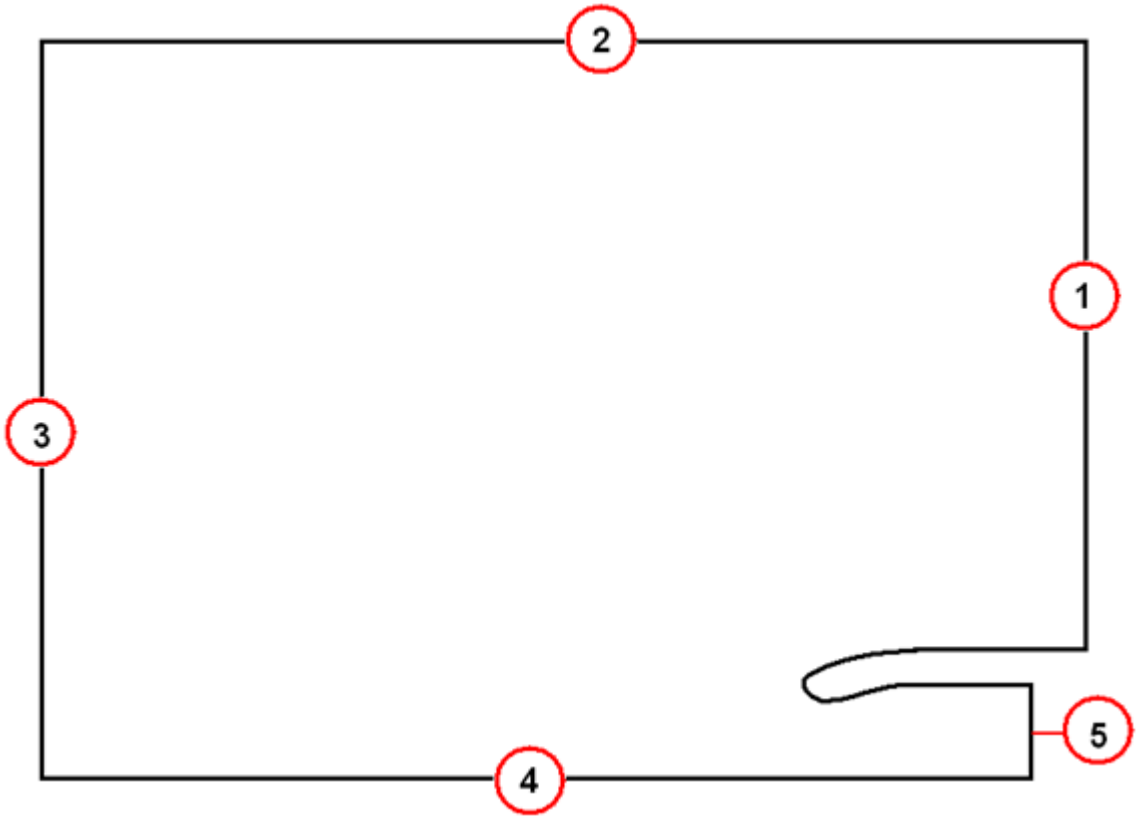

Figure 5.22 Forebody boundary conditions (not to scale)

5.8.2 Mesh Dependency Analysis

For this analysis the meshes generated, as described in section 5.3.2.1, were analysed in cruise conditions. All of the boundary conditions remained the same for all of the simulations and the only parameters changed were those used to get the convergence.

The parameters used previously for the afterbody analysis (Section 5.7.2) were used for the forebody. The results are shown in the figures below. The plots for the three grids are very similar and it is possible to conclude that the results do not depend on the mesh, therefore the medium mesh was used to make the simulations.

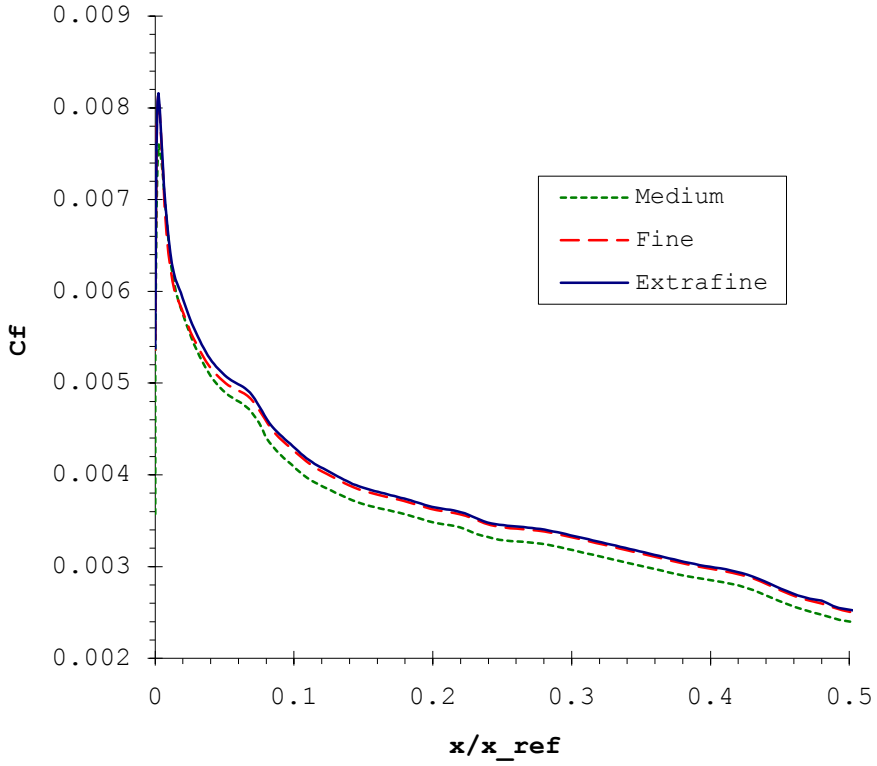

Figure 5.23 Forebody Cf comparison for the mesh independence analysis

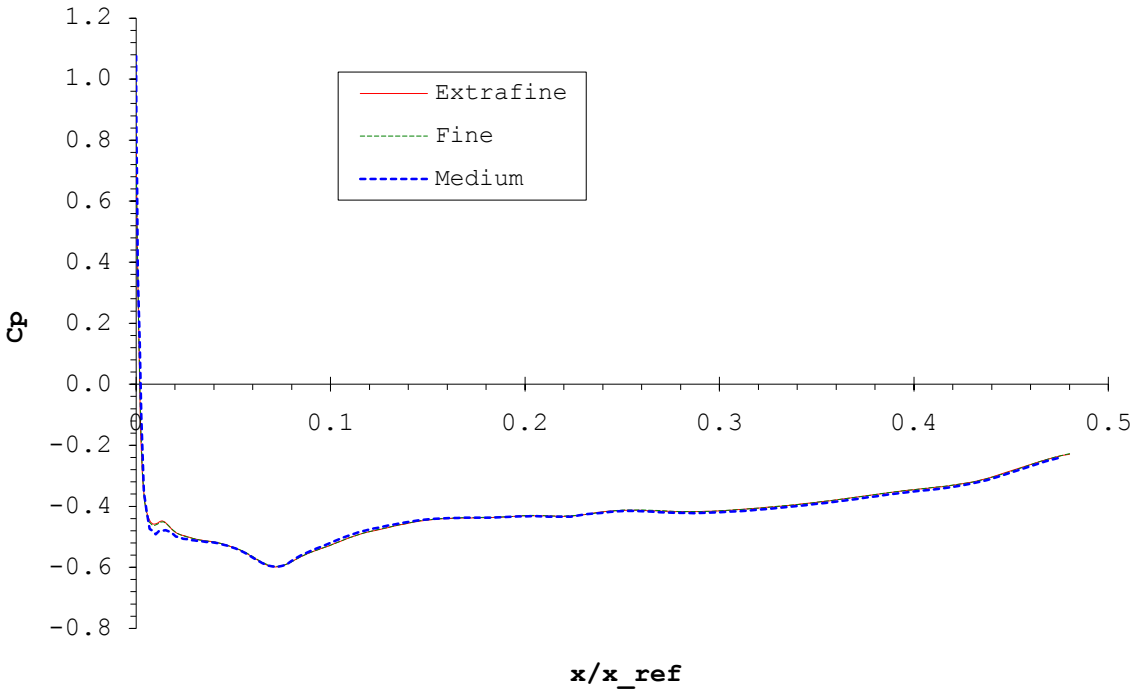

Figure 5.24 Forebody Cp comparison for the mesh independence analysis

The maximum error could not be used for the evaluation of mesh independence because at the stagnation point the velocity values are too low and generate large errors. The errors are much lower away from the stagnation point. In Figure 5.25 it can be seen that away from the stagnation point the error percentage is below 15%, and for the most part below 5%. The high spot of the errors around x/x_ref=1.5 is because there is a point where the velocity and pressure show a slight change of position in the grids which is unnoticeable in Figure 5.23 and Figure 5.24 but is shown in the figure below. because there is a spot where the velocity and pressure have a slightly change that is changed in position in the grids in an unnoticeable way in Figure 5.23 and Figure 5.24, but reflected in the figure below.

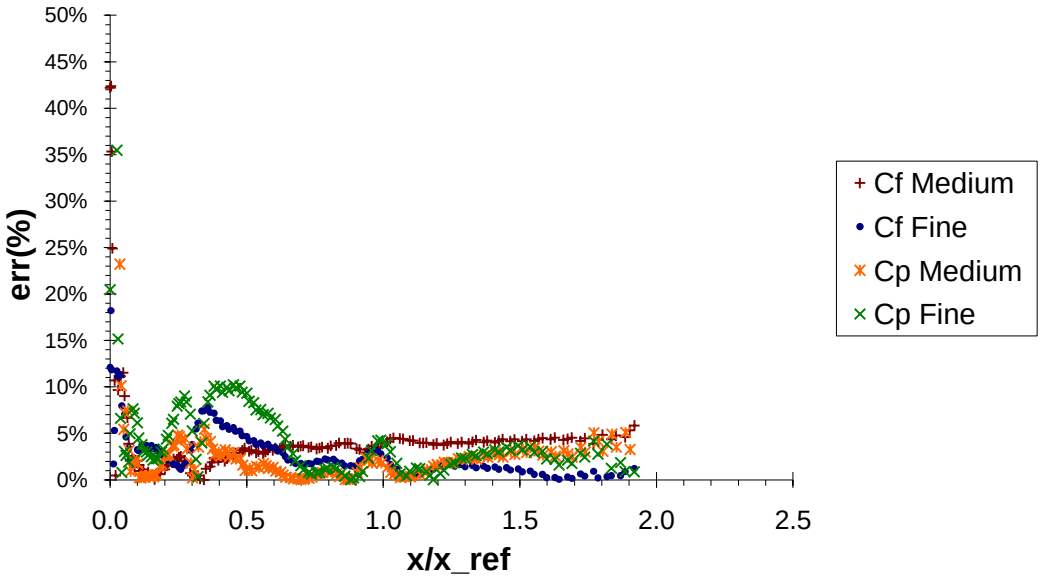

Figure 5.25 Comparing the Cf and Cp of the coarse and medium meshes with the fine one

5.8.3 y+ analysis

For the forebody the flow velocity near the wall increases until it gets near or even above sonic conditions ($M \geq 1$). In the figure below it is possible to see that the size of the mesh is suitable for the analysis of transonic conditions. The y+ parameter for most of the inlet cowl is above 30. Although part of the nacelle is below 30 it is reasonably close to the value and it is not a big section of the mesh. The results unfortunately may be slightly inaccurate near the mid section where these low y+ value spots are found.

Unfortunately the y+ parameters are obtained after the simulations. To get proper values would require going back almost to the beginning of grid design stage. The limitations of

computational resources and time availability did not allow for the remaking all of the simulations. It was assumed that the errors in the results are not highly significant.

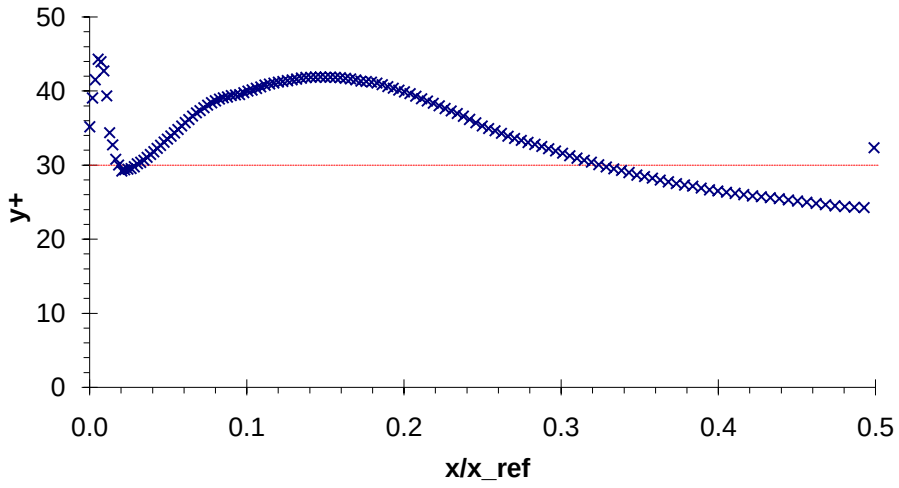

Figure 5.26 Y+ analysis for the Forebody

5.8.4 Parameters to be analyzed

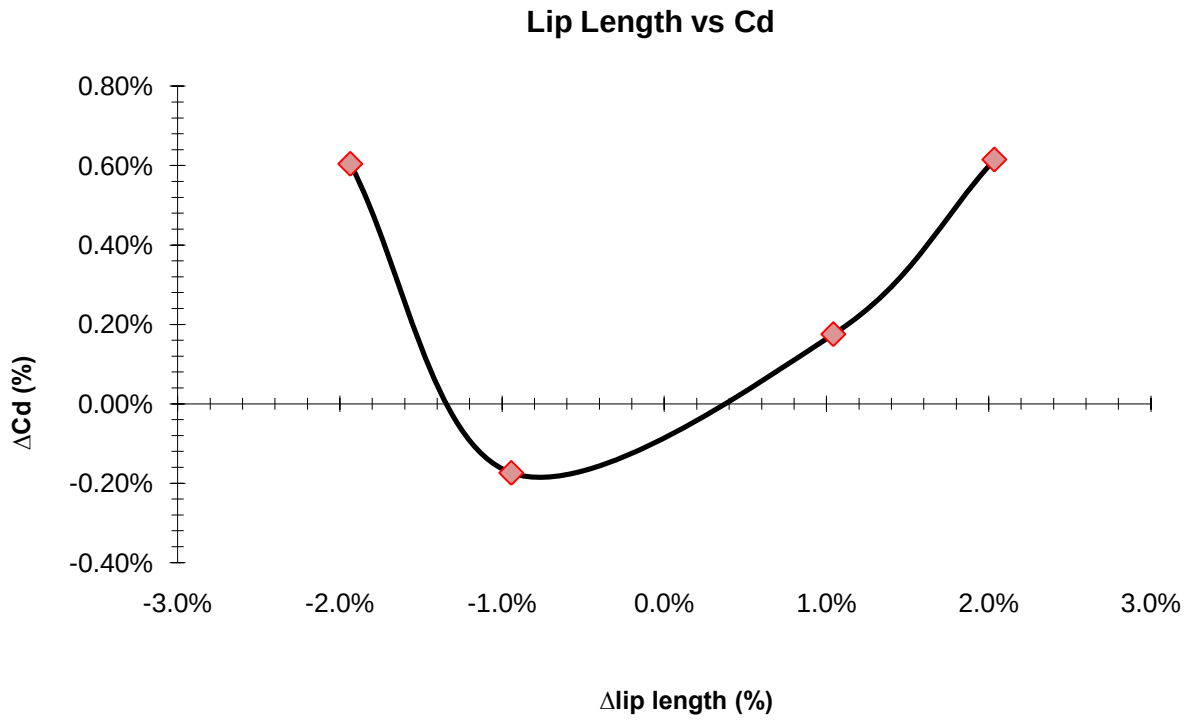

Figure 5.27 Drag Change with respect to the lip length

The parameters analyzed in the forebody are mentioned in section 5.2. The amount changed is shown in the tables below.

There are a total of 29 geometries including the base geometry.

There is also another parameter considered in section 5.2, but it is not included in the tables above. The parameter is the length of the lip. These parameters threw very small changes in the drag (see above). These small variations are considered to be due to the uncertainty of the calculations.

Table 6 Change of Maximum Diameter and Highlight Diameters for the different geometries

Dmax	Dhigh
-2.0%	-2.0%
-1.0%	-2.0%
0.0%	-2.0%
1.0%	-2.0%
-2.0%	-1.0%
-1.0%	-1.0%
0.0%	-1.0%
1.0%	-1.0%
-2.0%	0.0%
-1.0%	0.0%
1.0%	0.0%
-2.0%	1.0%
-1.0%	1.0%
0.0%	1.0%
1.0%	1.0%

The Dmax and Dhigh changes were combined to give a four by four matrix of combinations including the base geometry.

Table 7 Change of Throat Diameter and Total Nacelle Length

Dth	Length
-2.0%	-2.0%
-1.0%	-1.0%
0.0%	0.0%
1.0%	0.5%
2.0%	1.7%

5.8.5 Results and analysis

A few examples of the results obtained from the simulations are shown in the figures below. In Figure 5.28 it is shown how there is a supersonic velocity spot that produces a change in the pressure coefficient profile smoothness (see Figure 5.29.) This high velocity point is created by the spillage flow that has to go faster than the stream flow in order to keep the mass flow constant. There is even a small point where the air flows against the free stream flow (see Figure 5.30) this is why the air can reach supersonic speeds near the intake tip and slows down downstream (see Figure 5.28.)

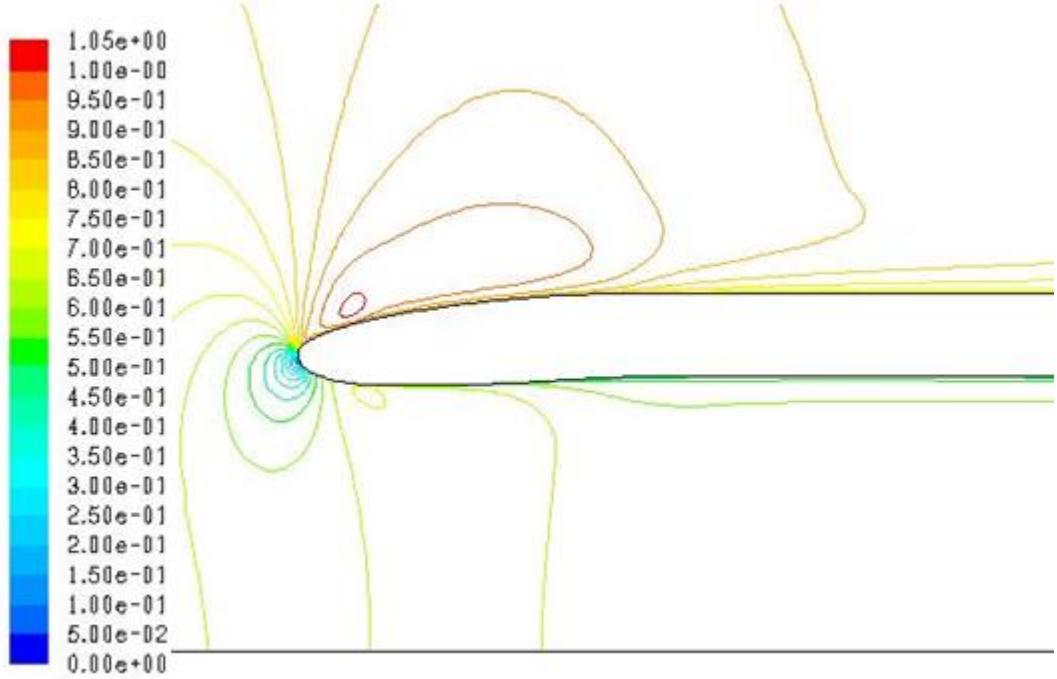

Figure 5.28 Mach number profiles for a forebody model

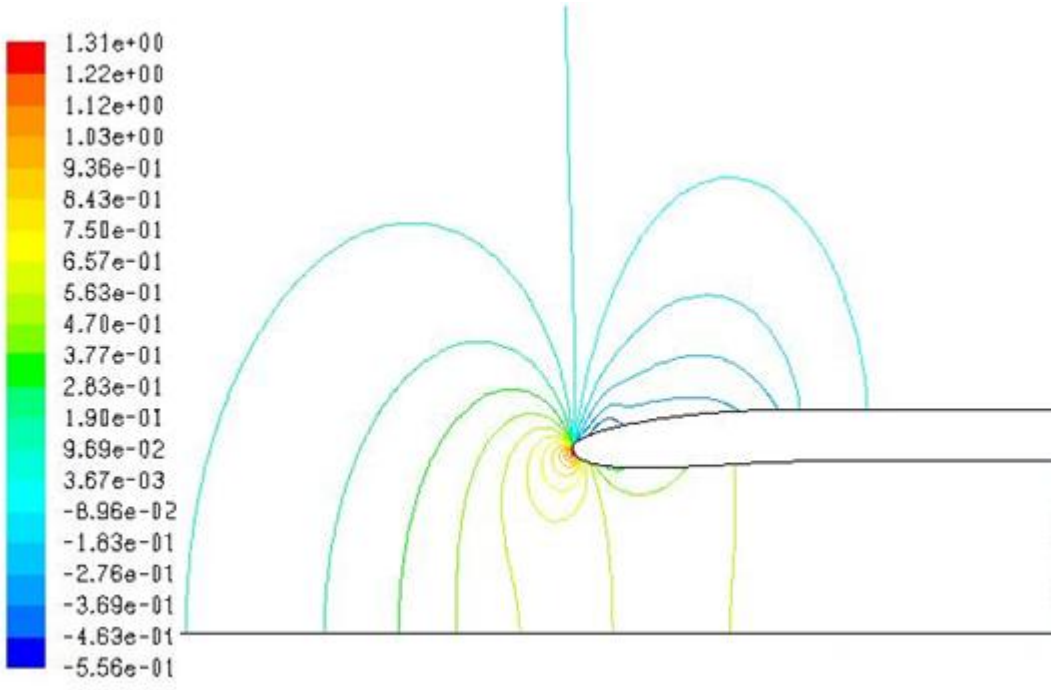

Figure 5.29 Pressure coefficient profiles for a forebody model

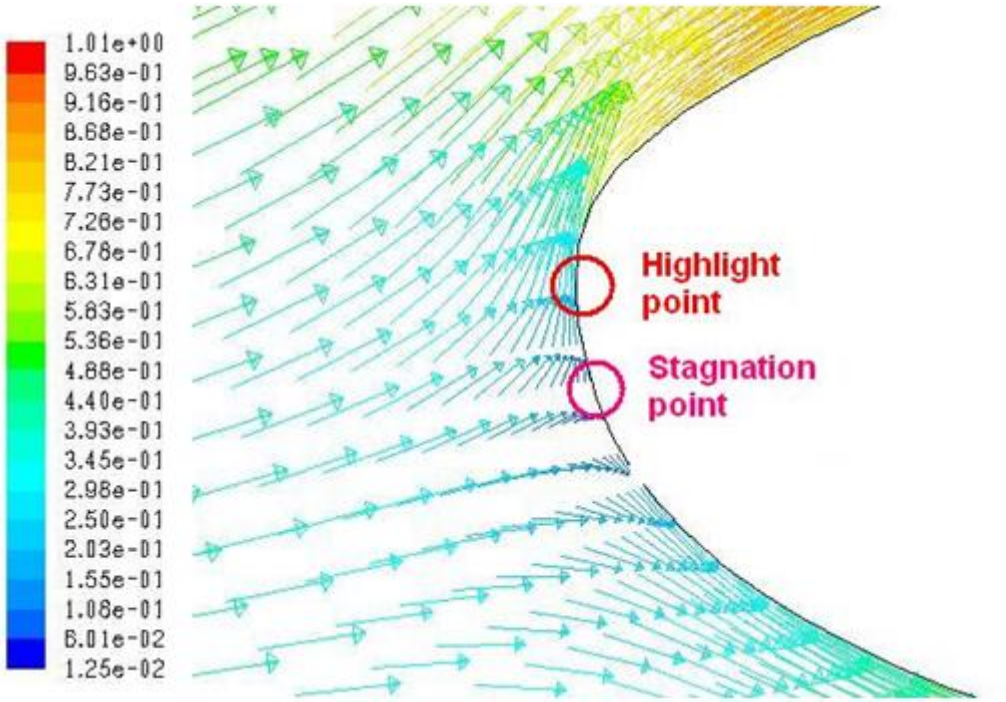

Figure 5.30 Velocity vectors at the highlight point of an intake

The figures below show how the supersonic velocity areas for a cruise condition flow change according to the geometry of the forebody. An increase in the Dhigh would require a more sudden change in the velocity direction of the spillage flow. That is the reason for the high speed flow nearer to the tip.

From the data obtained from the simulations the drag is calculated from the two basic drag parameters, viscous and pressure forces. In Table 8 the impact of each of the parameters used for the drag calculations is shown.

To calculate the pre-entry drag (Cd-pre) some extra measurements are required. The Newton's second law is applied to the internal flow going into the intake. The Momentum Flux and Pressure forces are calculated by integrating the values in the area limited by the stagnation line all around the centre line. In the 2D model this area is defined just by the line perpendicular to a centre line passing and limited by the centre line and the stagnation point.

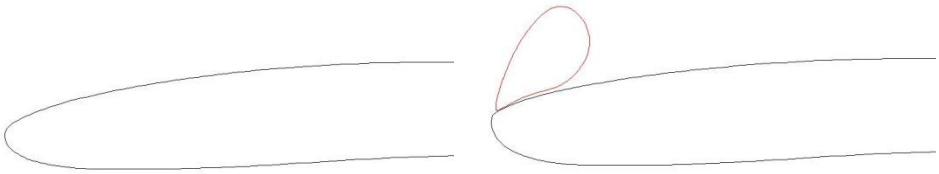

Figure 5.31 Supersonic areas for a small Dmax with a small (left) and large (right) Dhigh

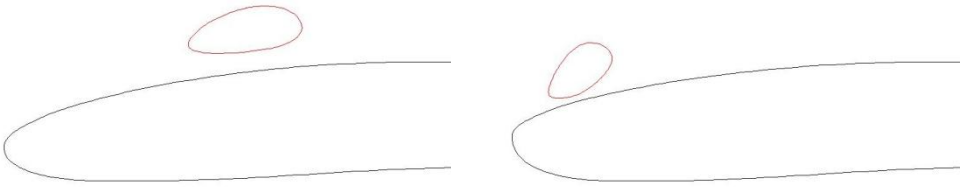

Figure 5.32 Supersonic areas for a large Dmax with a small (left) and large (right) Dhigh

Table 8 Forebody force changes (the bold figures are the data from the base geometry)

Parameters analyzed		Cp	Cμ	Cd	Cd_pre	Cd_tot
Dmax	Dhigh					
-2.00%	-2.00%	-6.55%	-3.09%	-6.91%	-10.92%	-17.03%
-2.00%	-1.00%	-14.42%	-2.78%	-15.63%	-11.17%	-4.38%
-2.00%	0.00%	-10.01%	-3.56%	-10.68%	-0.87%	14.08%
-2.00%	1.00%	1.59%	-1.90%	1.95%	8.00%	17.22%
-0.99%	-2.00%	-6.12%	-1.68%	-6.58%	-10.73%	-17.06%
-0.99%	-1.00%	1.06%	-1.29%	1.31%	-3.13%	-9.90%
-0.99%	0.00%	-8.70%	-1.81%	-9.42%	-4.40%	3.25%
-0.99%	1.00%	3.21%	-1.88%	3.74%	7.29%	12.69%
0.00%	-2.00%	-5.68%	-0.27%	-6.25%	-10.26%	-16.38%
0.00%	-1.00%	0.17%	0.16%	0.17%	-3.77%	-9.77%
0.00%	***0.00%***	***0.00%***	***0.00%***	***0.00%***	***0.00%***	***0.00%***
0.00%	1.00%	4.86%	-0.10%	5.38%	6.81%	8.99%
0.99%	-2.00%	-5.81%	0.86%	-6.51%	-9.98%	-15.28%
0.99%	-1.00%	3.96%	1.26%	4.24%	-1.62%	-10.54%
0.99%	0.00%	1.92%	1.31%	1.99%	1.19%	-0.03%
0.99%	1.00%	7.43%	1.51%	8.05%	7.41%	6.44%
		Cp	Cμ	Cd	Cd_pre	Cd_tot
Dth	-2.01%	-7.12%	0.25%	-7.89%	0.28%	12.72%
	-0.99%	-6.49%	0.15%	-7.18%	-1.95%	6.03%
	0.00%	**0.00%**	**0.00%**	**0.00%**	**0.00%**	**0.00%**
	0.99%	8.77%	0.01%	9.68%	2.93%	-7.35%
	2.01%	1.59%	-0.24%	1.78%	-2.55%	-9.16%
Length	-1.98%	-1.84%	-1.18%	-1.91%	-1.31%	-0.41%
	-0.99%	-0.56%	-0.59%	-0.55%	-0.43%	-0.25%
	0.00%	**0.00%**	**0.00%**	**0.00%**	**0.00%**	**0.00%**
	0.52%	3.57%	0.64%	3.87%	1.89%	-1.13%
	1.67%	4.48%	1.03%	4.84%	2.38%	-1.37%

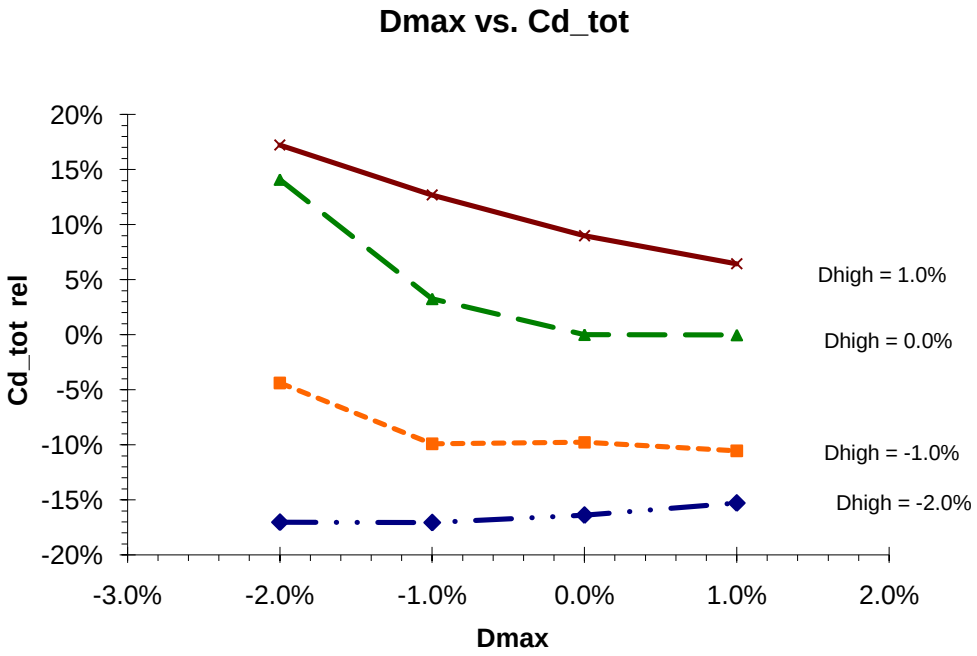

Figure 5.33 Change of total drag changed by the variation of Dmax and Dhigh

The highlight and maximum diameters are closely linked in the drag generation of an intake as shown in Figure 5.33. If the highlight diameter increases drag is expected to increase. The maximum diameter can increase or decrease the drag depending on the highlight diameter value. The Dhigh with one percent larger than the base geometry makes the drag decrease when the Dmax increases, on the other hand, for a Dhigh two percent smaller then the drag and the Dmax will increase.

The increase or decrease of the total drag depends of the shape of the cowl i.e. the relationship between the Dhigh and Dmax. Differences between them will cause the velocity magnitude and pressure to change. The wet surface also changes. Integrating the pressure over the cowl surface makes the final FB pressure cowl force in a direction against the free flow for this geometry. The main component of the drag is the pre-entry drag but it barely changes relate to Dmax and mainly by the change of Dhigh, as shown in Figure 5.34. The third component is the viscous drag (Cμ) over the cowl. This force generates a very small force compared to the other two components and is changed mostly in relation to the Dmax size. The reduction of Dmax of 2.0 % gives a reduction of 3.0 % and the increase of 1.0 % will result into an increase of Cμ of approximately 1.0 %.

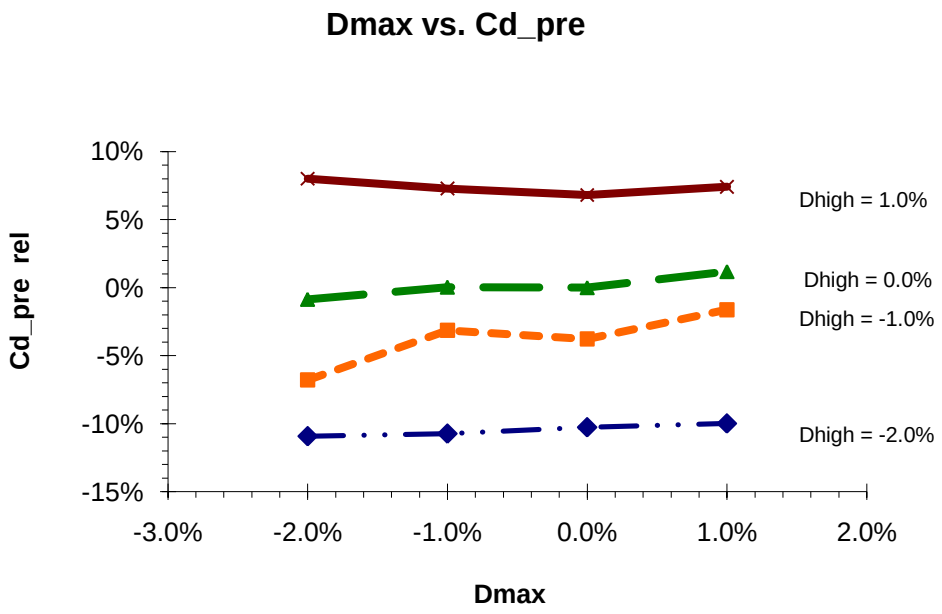

Figure 5.34 Variation of pre entry force (drag) with respect of the change of Dhigh and Dmax

The part each of the components of the total drag is the following: Cμ = 3.7, Cp_cowl = 38.6 % and Cd_pre = 57.8%[9].

Assuming Dmax and Dhigh to be constant and varying the throat diameter (Dth) the drag is changed mostly now by the Cp and Cd_pre.

The Cd_tot decreases as the Dth increases. The reduction of the drag is because the flow speed increases and therefore the pressure decreases. The pressure reduction has an influence on both the Cp and Cd_pre. The changes are small and the Figure 5.35 shows how both changes are less than +/- 5 %.

By changing the length of the intake cowl the pressure around the nacelle remains with very low variations, the only real difference to be taken into account for drag calculations is the small increase of viscous drag.

[9] The percentages may not add up 100 % due to the averaging of each component separately.

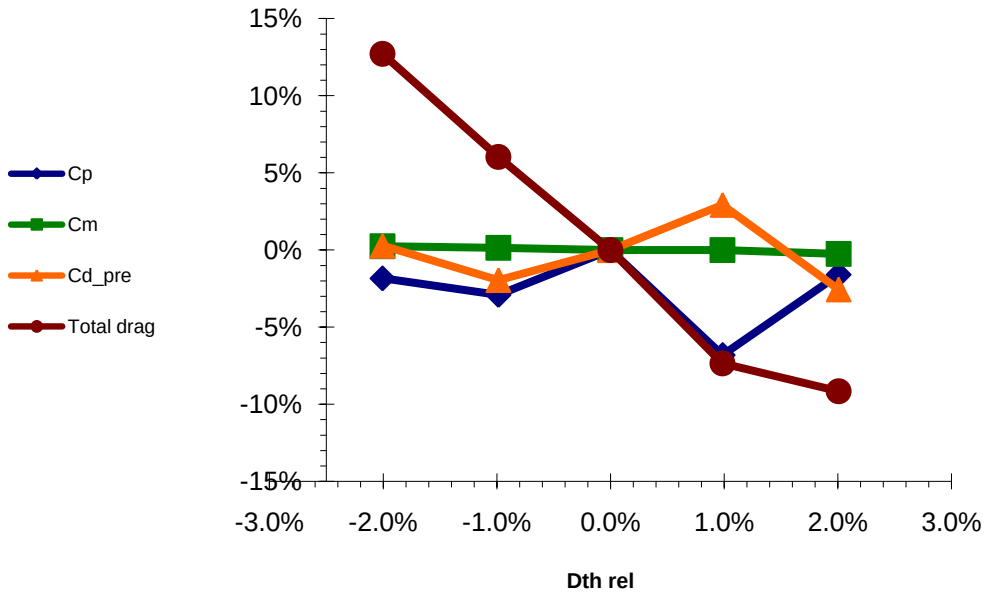

Figure 5.35 Change of Drag and its components related to the variation of the throath diameter.

The pressure forces do not change much because the velocity profiles remain almost the same, also the projected area of the wet surface remains the same. The only real change is on the viscous force, although really small, there is a change because the wet surface changes producing a variation in the viscous drag produced. The forces produced by a +/- 2.0 % of cowl length vary by a very small amount as shown in the figure below.

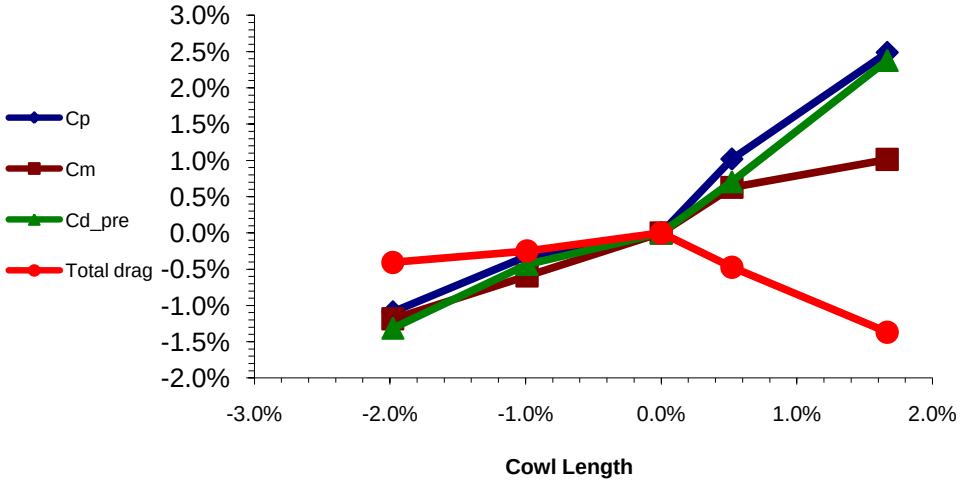

Figure 5.36 Drag and its components variation due to a change of intake cowl length

6 Isolated Nacelle (3D simulations)

A parametric study with parameters similar to the ones studied in the 2D models was carried out. The analysis is based on the drag obtained from the simulations. The interaction between the FB and AB are analyzed and the impact of each of the parameters in the interaction.

6.1 Geometry

The 3D model was created with CATIA software.

The geometry was parameterized based on the parameters analyzed. The entire geometry would change by changing the values of the parameters involved in the analysis. This way only a parameter change is necessary in order to create a completely new geometry and avoiding the creation of several models from scratch.

Symmetric models are used for all of the simulations of this stage.

The geometry of the nacelles is different at the keel and the crown. The surface generation method used for this geometry is variable rotational extrusion. The steps were the following:

1. Choose a centre line. The centre line was collinear with the engine's.

2. Select an initial and final profile. For all cases the crown and keel were the initial and final profiles respectively. To get the proper surfaces the shape of the profiles should be defined in the same way. Both must have the same amount of points along the lines and the initial and final points are the same.

3. Rotate the line profile and vary the shape. The radius of each point varies linearly with respect to the rotated angle.

4. Check the surfaces are smooth and the borders fit the border of the adjacent surface.

The only axisymmetric parts of the nacelle are the exhaust zone and the spinner (part of the intake zone). These parts were created at the end of the whole nacelle geometry generation process. The same procedure was used as for the non-axisymmetric surfaces with the only difference being that the profile is constant along the extrusion.

The geometry of the models is based on five different zones:

- Fore-body (FB)
- Mid-body
- After-body
- Intake
- Exhaust zone

The FB is designed in the same way the 2D model. The NACA-1 profile is used based on the length, highlight diameter and maximum diameter.

The MB profile is a horizontal line parallel to the centre line.

Two sections were used for the AB profile. To get the proper angle at the bypass exhaust a straight line was used. A circumferential arc was used to join the straight line and the MB section. The circumference section is tangent to both of the straight lines of the AB and MB.

The intake profile starts at the highlight point and includes the throat point, diffuser section, the fan and spinner. The lip section extends from the highlight point to the throat point. Its profile is a section of a hyper ellipse (for more details refer to section 5.1.1). For the diffuser section an xpline was used. The fan is a circular ring perpendicular to the nacelle centre line. The dimensions are the tip and root diameters of the fan blades given by VITAL. Finally, the spinner is a circular section cone with the axis collinear to the centre line.

The exhaust region consists of axisymmetric surfaces. The external section of both cold and hot nozzles is an xpline tangent to the cowl tip making the end perpendicular to the exhaust section. The core cowl is a cone section and the exhaust cone is a cone. The values of the angles, lengths and diameters are the ones given by VITAL, also the exhaust areas were confirmed to be the ones given by the project.

The geometry of the diffuser and the nozzles were not set for the project. Therefore xplines where used with default geometries. The geometry was not set in a detailed way

because it was assumed that the geometry of these sections would not change the drag of the nacelle (the main objective of the project) considerably.

6.1.1 Parameters analyzed

The changes were applied to the base geometry according to the dimensions given by VITAL. For the whole nacelle the changing parameters were on the geometry of the FB. The changes of the AB were based mostly on the maximum diameter.

The following parameters were analyzed (the number in parentheses is the number of values assigned):

- Maximum Diameter (4). The Dmax changed the geometry of the FB and AB cowls.
- Highlight Diameter (4). The FB and intake geometries were changed.
- Nacelle cowl length (4). The MB length was changed
- Forebody length (2). The FB cowl and MB length were altered.
- Scarf angle (4). The FB and intake geometries were changed.

For each of the parameter variations a simulation was done. A total of 19 simulations were made, each one of them with different geometries including the base geometry.

As the geometry is non axisymmetric, the two values of the crown and keel must be taken into account. The variations were based on the average values of each the parameters and the ratio between them. The variation was made on the average value. The ratio crown-keel of the base geometry was kept constant to calculate the values at the keel and the crown.

The first two simulations for each of the parameters were made with variations of −6.0% and +6.0 %. For the parameters with a high influence on the drag (Dmax, Dhigh and total length) another two simulations were made with smaller variations (± 2.0%).

6.2 Grid Generation

6.2.1 Meshing strategy

Several procedures for the meshing of the nacelles were tried. Only the final meshing procedure is mentioned. Other grids were not used to make the simulations because no convergence was achieved or the results obtained with them were not accurate.

The geometry of the nacelle is very similar to an axisymmetric model. A symmetric model was used and a half a cylinder domain. Both of the centre lines of the domain and nacelle are coincident. A reference length (Lref) was used to form the dimensions of the domain. From the highlight plane of the nacelle to the inlet plane and to the outlet plane of the domain there is a distance of 13 Lref and 15 Lref respectively. The diameter of the domain cylinder is 20 Lref.

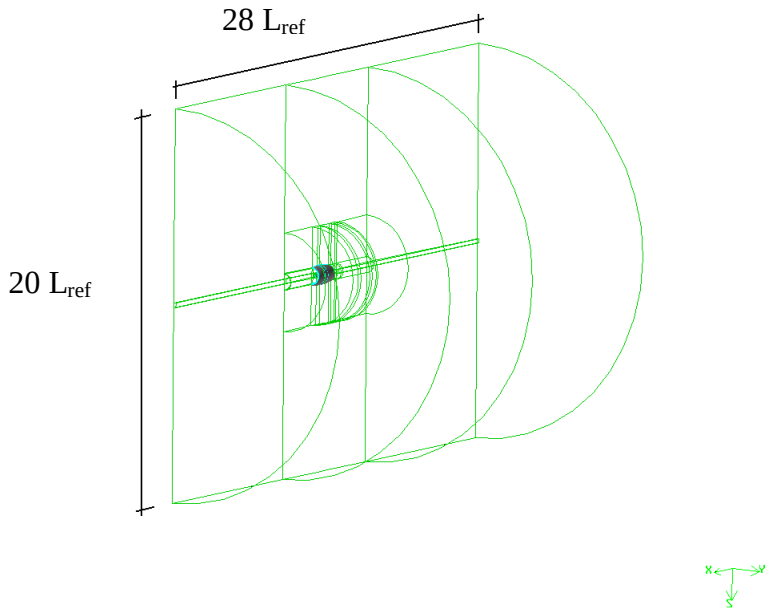

Figure 6.1 Isolated nacelle domain dimensions

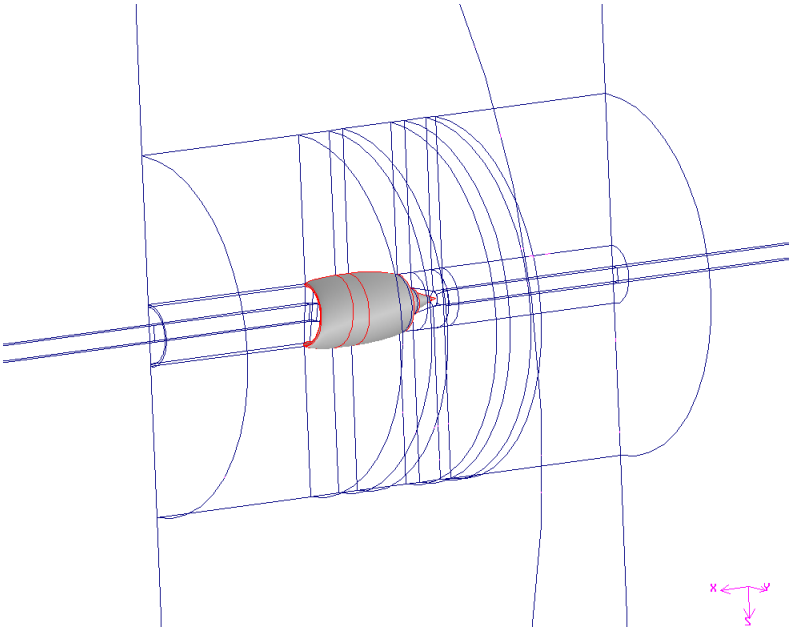

Figure 6.2 Annular shape of every block of the domain.

The domain was divided into several volumes. There are a total of 47 volumes; most of them are annular shaped. The only volumes with an extruded shape are the ones that include the centre line within them. The size and shape of every block was set in order to get the most appropriate cell sizes at every position.

The mesh is an H-shaped structured mesh. The volumes around the tip of the spinner and the exhaust cone are unstructured meshes. The finest cells are at the highlight of the nacelle and the exhaust of the bypass and the core flow.

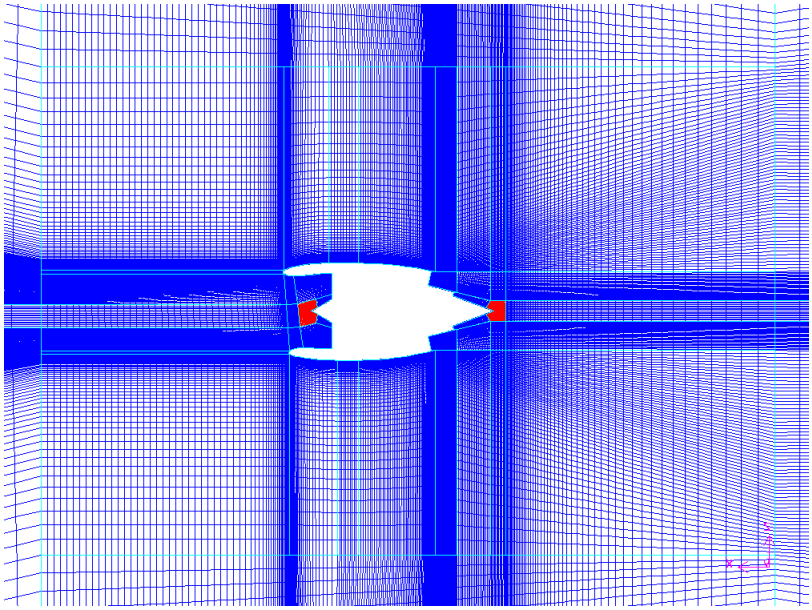

Figure 6.3 Mesh at the symmetry plane. The areas filled with red colour are where an unstructured mesh was used.

The grid of all of the geometries analyzed was created with the same procedure. The difference of the grid size between all of the models is due to the spots where an unstructured mesh was used (see Figure 6.3).

6.3 Simulation setup

The quality of the simulation results depends on several factors. The most important is the grid quality, also the setup of the simulation is an important factor. It includes the viscous model, boundary condition and solver setup, which are all very important issues in CFD simulations.

6.3.1 Boundary conditions

The boundary used for the simulations are the ones shown in Figure 6.4. Each boundary condition is listed below, numbered as in Figure 6.4:

1. Inflow
2. Far-field
3. Outflow
4. Fan
5. Bypass flow exhaust
6. Core flow exhaust

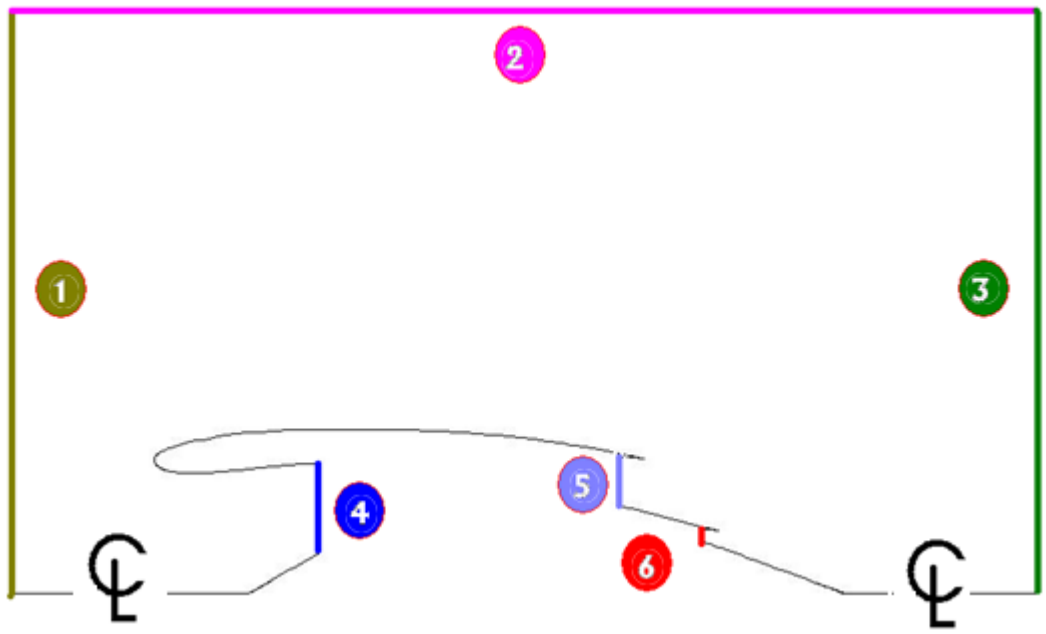

Figure 6.4 Boundary conditions (image not to scale)

The Inflow and Farfield are both defined as pressure-far-field boundary conditions. The parameters set are the gauge pressure, Mach number, flow direction, turbulence parameters and temperature.

The outflow is defined as pressure-outlet. The only parameter required to define the conditions is the gauge pressure. Backflow parameters are required and should be set in order to keep the iterative results directed to convergence.

The Fan is also a pressure-outlet but the conditions of this surface were changed during the simulation. The only parameter set for the fan is the mass-flow and the pressure must be set according to it. For the first iteration of the simulations a pressure value, close to that required for the mass flow, is set. After the simulation passed the divergence stage (usually the early iterations) and the mass flow has converged to the value resulting from the pressure set at the beginning, the pressure-outlet target-mass-flow-rate option is set. By setting the target-mass-flow-rate option the pressure varies until the mass flow converges to the value required.

Both the bypass and core flow exhausts are mass-flow inlets. To define them the mass flow rate and total temperature are required. Also supersonic pressure is required in case the velocity gets to supersonic values. Backflow parameters are also required.

6.3.2 Solver

The solver used was pressure-based. An absolute velocity simulation with a Green-Gauss Cell based gradient option was used. Both the pressure- and density-based solvers were tried during the simulation setup; the pressure-based was the one giving more suitable results and consumed least computational resources of the two. The pressure-based solver was used. The absolute velocity simulation was used because most of the velocity was irrotational.

The most suitable viscous models for the project are the S-A, k-ε or k-ω. Other models are Reynolds Stress, DES, and LES but these are very high resource consuming therefore were not considered. At the first stage of the simulations S-A, k-ε and k-ω models were used to compare the suitability of each one for the project. Apparently one of the k-ω models would have been the most suitable for a nacelle simulation mostly because it is a two equation model based in low Re values near wall. (Fluent 6.2 documentation, 2007) Unfortunately the comparison between the time consumed by using the two equation models (k-ε and k-ω) compared to the one equation model (S-A) was quite significant. Therefore the viscosity model used was the S-A.

The discretization methods of the density, momentum, viscosity, energy and pressure were changed during the simulation in order to avoid divergence. At the beginning of the simulations the standard pressure interpolation method was used. For all of the other variables a first order upwind discretization method was used. After the first iterations when the divergence stage was passed the pressure interpolation method was changed to second order and for the other variables the first order upwind discretization methods were changed for second order methods.

6.3.3 Convergence Analysis

Three methods were used in order to consider the simulations convergence. Plots of the residuals, drag and lift coefficients and fan mass flow were considered for convergence evaluation.

The residual plots after some iterations converged asymptotically to certain values and did not decrease any more. When the residual values do change their values then the simulation is considered to converge; when the drag and lift coefficients converge to a certain value.

The simulations are considered to have converged after the following considerations:

1. The fan mass flow converged to the required value.
2. The residuals values are set to a certain value. They do not decrease or increase.
3. The drag and lift coefficient of the nacelle converged to a certain value.

6.4 Result analysis

The results taken into account are only the forces over the nacelle and not the drag (drag is defined as a momentum loss and not a force). This is because to calculate the drag the pre-entry drag should be calculated and added to the forces from the CFD simulation. The calculation of an aircraft engine drag requires much more and better resources than the ones available. When calculations are done with the data obtained from the simulations the inaccuracy is enlarged.

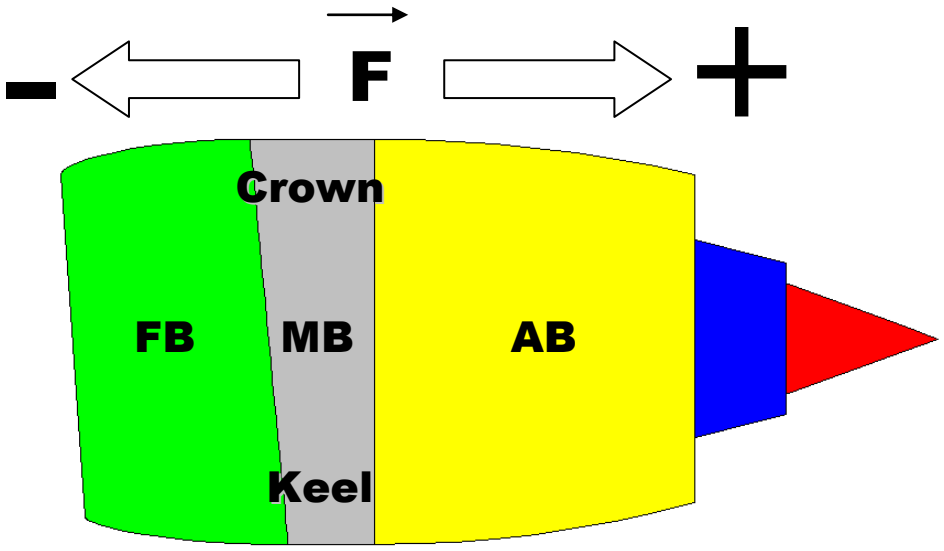

Figure 6.5 Side view of a short bypass nacelle, the top part of it is called the crown section and the lower part the keel section.

The forces considered are the projection in the free stream velocity direction. Other components of these forces would have an impact on other design parameters like lift or structure. For aerodynamic drag calculations only the component mentioned is required.

The positive value is considered in direction of the free stream flow velocity (drag) and negative in the opposite one (thrust) as shown in the figure above.

Figure 6.5 illustrates the different sections and linear segments of a nacelle. The crown segment is at the top of the nacelle and is the longest of the nacelle, it goes from the highlight point to the exhaust point of the bypass nozzle. The keel segment is opposite the crown and is the one with the shortest length. The Forebody (FB) is the section going from the highlight point to the mid-body. In the mid-body (MB) section all angular segments are parallel to the centre line of the nacelle. The afterbody (AB) is the curved section going from the end of the MB to the exhaust point of the bypass nozzle. FB, MB and AB are filled with green, gray and yellow colours respectively in Figure 6.5.

The result analyses are based on the percentage change of the geometry analyzed from the values obtained from the base geometry simulation.

In Figure 6.6 it can be seen how the total force changes with respect to each of the parameters analyzed. At the abscissas axis the change of each parameter is normalized to a reference value. The ordinate axis is the percentage change of the total force, normalized to the force calculated from the base geometry.

From Figure 6.6 and Figure 6.7 some conclusions can be taken. The biggest total force changes are given by the variation of the highlight diameter. The changes of the force with the Scarf angle and the forebody length are quite insignificant compared to the variations of the other three variables.

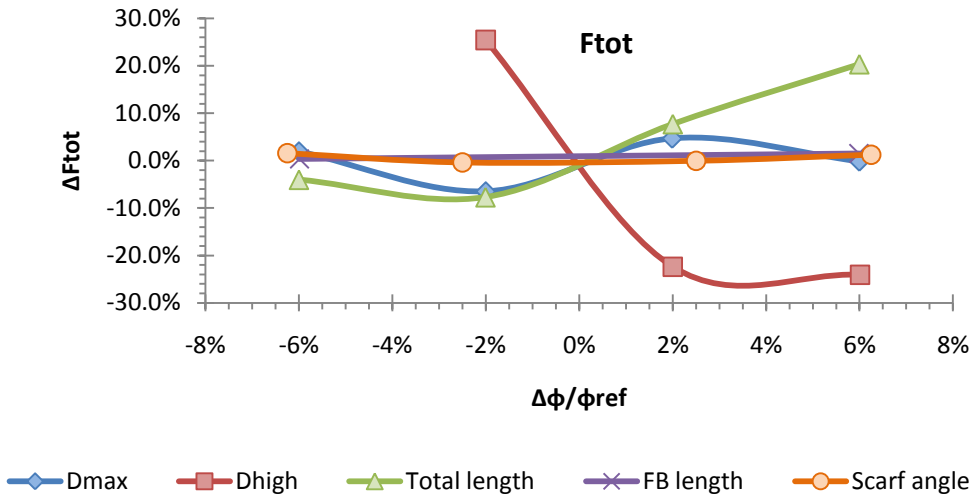

Figure 6.6 Total nacelle force change with respect of the change of each of the analysis parameter

The only parameter having a big impact on the pre-entry drag is the highlight diameter. The maximum diameter and total length also have an impact on it but it is quite small compared with the highlight diameter.

With the analysis of both Figure 6.6 and Figure 6.7 a deeper analysis has to be made of the influence of the three parameters; maximum diameter, highlight diameter and total length.

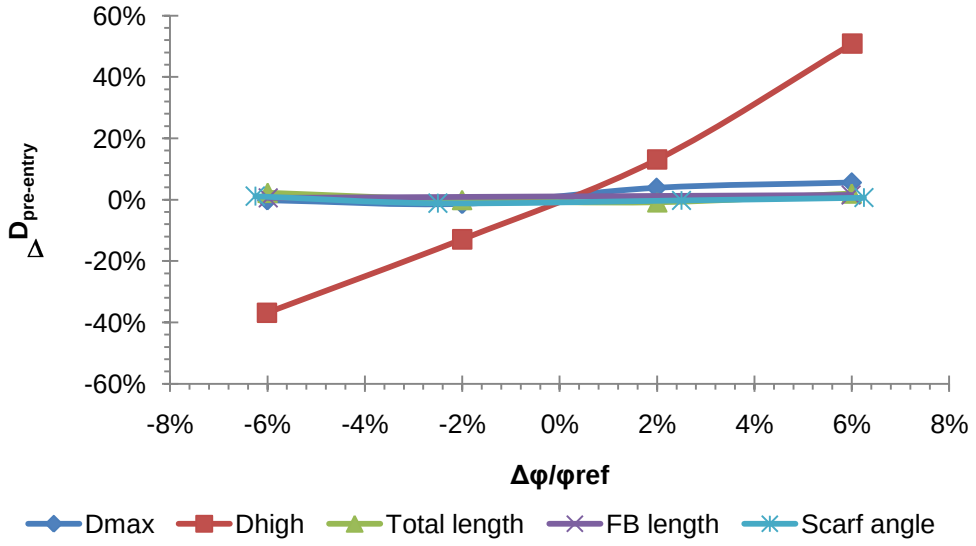

Figure 6.7 Pre-entry drag change with respect of the change of each of the analysis parameter

The analysis of the force changes are based on the split of the viscous and pressure forces, and how the forces change on the three sections of the nacelle, FB, MB and AB.

6.4.1 Maximum Diameter (Dmax) change analysis

A change of the nacelle maximum diameter would alter not only the projected area but also the wet surface. Assuming an equal velocity profile, with the increase of wet surface the viscous force would also increase. The perpendicular projected area would be boosted and therefore the change of the pressure would change with the total force applied to the nacelle. The change of the projected area, wet surface, velocity and pressure profiles combined would give different force behaviours as a result.

Figure 6.8 and Figure 6.9 show the effect of Dmax change on the Mach number around the engine nacelle. From the analysis of Figure 6.8, Figure 6.9 and Figure 6.11 the following observations can be made.

Figure 6.8 Mach number profiles of the side section of the nacelle of a Maximum diameter of - 6.0 % change with respect to the reference nacelle. (Mach number profiles are in the range of 0.6 and lower for blue to 1.2 and higher for red).

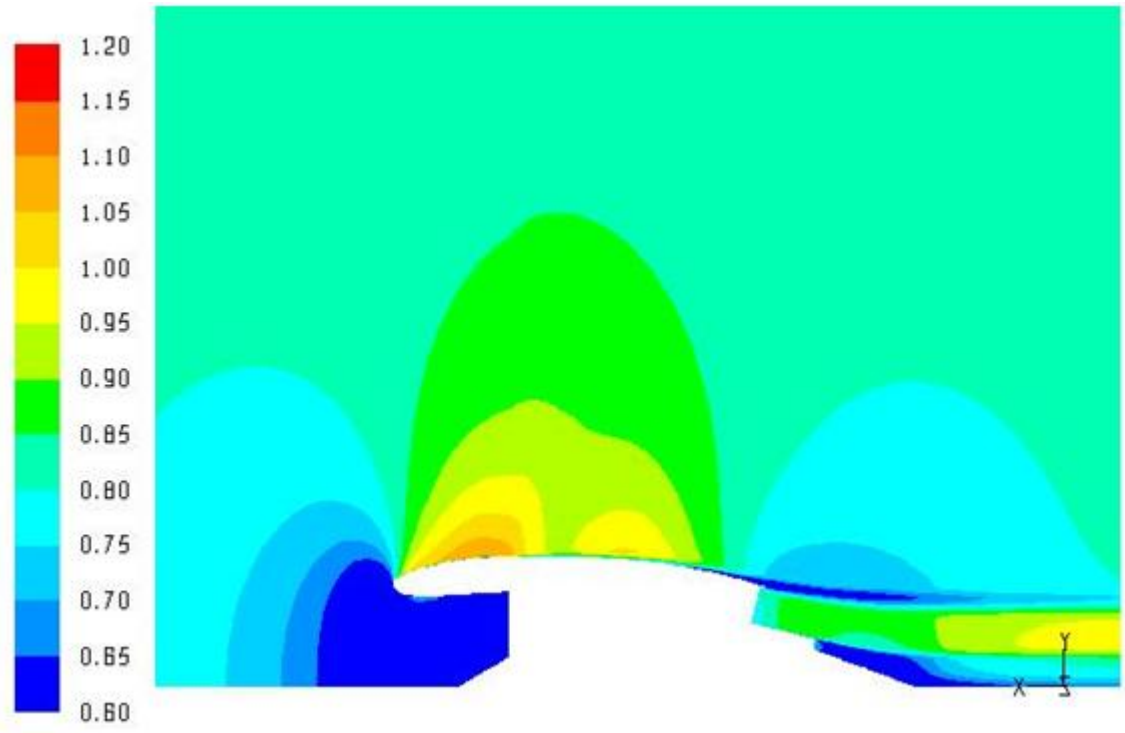

Figure 6.9 Mach number profiles of the side section of the nacelle of a Maximum diameter of + 6.0 % change with respect to the reference nacelle. (Mach number profiles are in the range of 0.6 and lower for blue to 1.2 and higher for red).

The analysis of pressure and profiles on the crown, side and keel linear sections are shown in Figure 6.11. The origin of the plot (x = 0) is at the highlight point and x axis direction is parallel to the free stream air velocity at the far field of the simulation. Forebody is represented from 0.0 to 0.3 and afterbody from 0.5 to 1.0, these values are approximate.

The minimum pressure (and maximum velocity point) for each of the plots is near the intake tip. At the tip of the intake the largest value of the Mach number is for the nacelle with the smallest Dmax and the Mach number decreases as the Dmax increases. The point where the maximum Mach number is located is pushed back (the Cp is the minimum where the Mach number is the maximum.) The biggest value is for the keel section and the smallest for the crown (see Appendix A.)

The velocity at the mid-body is the largest for the biggest Dmax nacelle. As the Dmax decreases the Cp and Ma at the MB get closer to the free flow conditions, i.e. Cp = 0 and Ma = 0.82.

At the keel the flow of the forebody and afterbody are closely linked because of the short length of the MB. At the MB the velocities do not get down to similar values and the Cp plots are more separated than those of the crown and side sections.

In three pressure plots there is a spot at the forebody where the value is very similar for the four nacelles. At this point the pressure of the nacelle with the smallest Dmax turns from the smallest to the largest and the largest Dmax turns from the largest to the smallest.

At the middle of the afterbody there is one spot with the same pressure. The afterbody is the same length and starts at the same spot for all of the nacelles. The reason why equal pressure is at precisely the same spot for all of the geometries is because the AB is the same length, unlike on the forebody where it is not the same.

6.4.1.1 Viscous force

The viscous force of the nacelle depends mainly on the flow velocity (see Figure 6.10). In Figure 6.8 and Figure 6.9 the velocity at MB can be seen to be larger for larger Dmax values. An important effect is the difference between axial components of the viscous forces for each of the nacelles, the axial component is the one taken into account for drag calculations. Although the velocity for a large Dmax is bigger than those for small Dmax nacelles along most of the nacelle, the axial component of the viscous force produced might not be. The term viscous force will be used for the axial component for now on unless otherwise specified.

At the FB and AB there is a similar effect. The viscous force decreases with the Dmax until it gets to a minimum point where the viscous force no longer increases but falls as Dmax enlarges.

The total viscous force depends on the integration along the entire surface of the nacelle component. For the FB, the smaller Dmax nacelle has a very fast flow at the tip slowing down rapidly to a low value. On the other hand, for the biggest Dmax nacelle the velocity is much smaller and the changes are gradual. For this reason there is a minimum point in Figure 6.10 for the viscous force change between the + 2.0% and + 6.0% nacelles. Before this point the small zones with large flow velocities of the small Dmax nacelles produce a larger force than that generated by the big zones with slow velocities of big Dmax nacelles.

For the AB there is a similar effect to the FB. There is a spot where the pressure is the same for all of the nacelles. Before this spot the velocities for the large Dmax nacelles are larger than the velocities for the small Dmax nacelles. The velocities of all of the nacelles fall along the AB, but for the larger nacelles velocity falls more rapidly therefore near the exhaust the velocity is much slower.

The flow of the FB and AB are more closely linked when the distance between them is short, this happens for the geometries with larger Dmax nacelles and at the keel sections. For this reason the air velocity of the nacelle with the maximum diameter decreases more than the one with the second largest diameter. The AB and FB velocities of the nacelles with small diameters are not highly linked (mostly at the side and crown sections) therefore the velocities remain lower than the bigger diameter ones. Because of these combined reasons the velocity of the +2.0% is the largest at most of the FB. The geometry with a variation of +6.0% of the Dmax has the largest velocity at the highlight but it decreases until it has the smallest value of all of the geometries for the FB. The change of the viscous force is approximately 17% between the maximum and minimum values. The nacelle with a 2.0% Dmax increase has the maximum viscous force for the FB (see Figure 6.10).

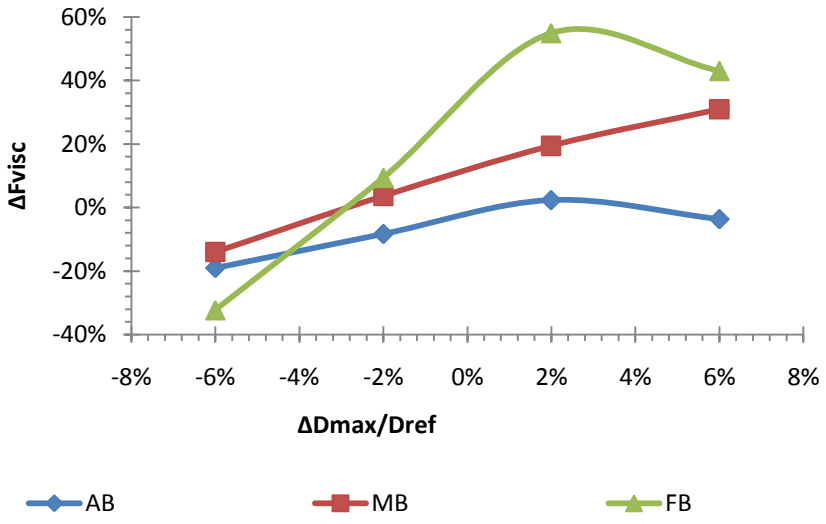

Figure 6.10 Axial component of viscous force changes at the Afterbody (AB), Midbody (MB) and Forebody (FB) for Dmax change percentage

6.4.1.2 Pressure Force

The pressure force is calculated as the integration of the static pressure over the projected perpendicular area to the free stream velocity vector.

The basic observation is that the projected area increases as the Dmax increases. The force produced is increased if the pressure or the area (diameter) is increased and the opposite occurs if they are decreased.

In Figure 6.12 the result of the pressure applied to the correspondent section of the nacelle is shown. These results can be related to Figure 6.11 that shows the pressure distribution over the nacelle at different sections all along the nacelle. The mid section of the nacelle is not shown in Figure 6.12 because its area is perpendicular to the flow, therefore the projected area is null.

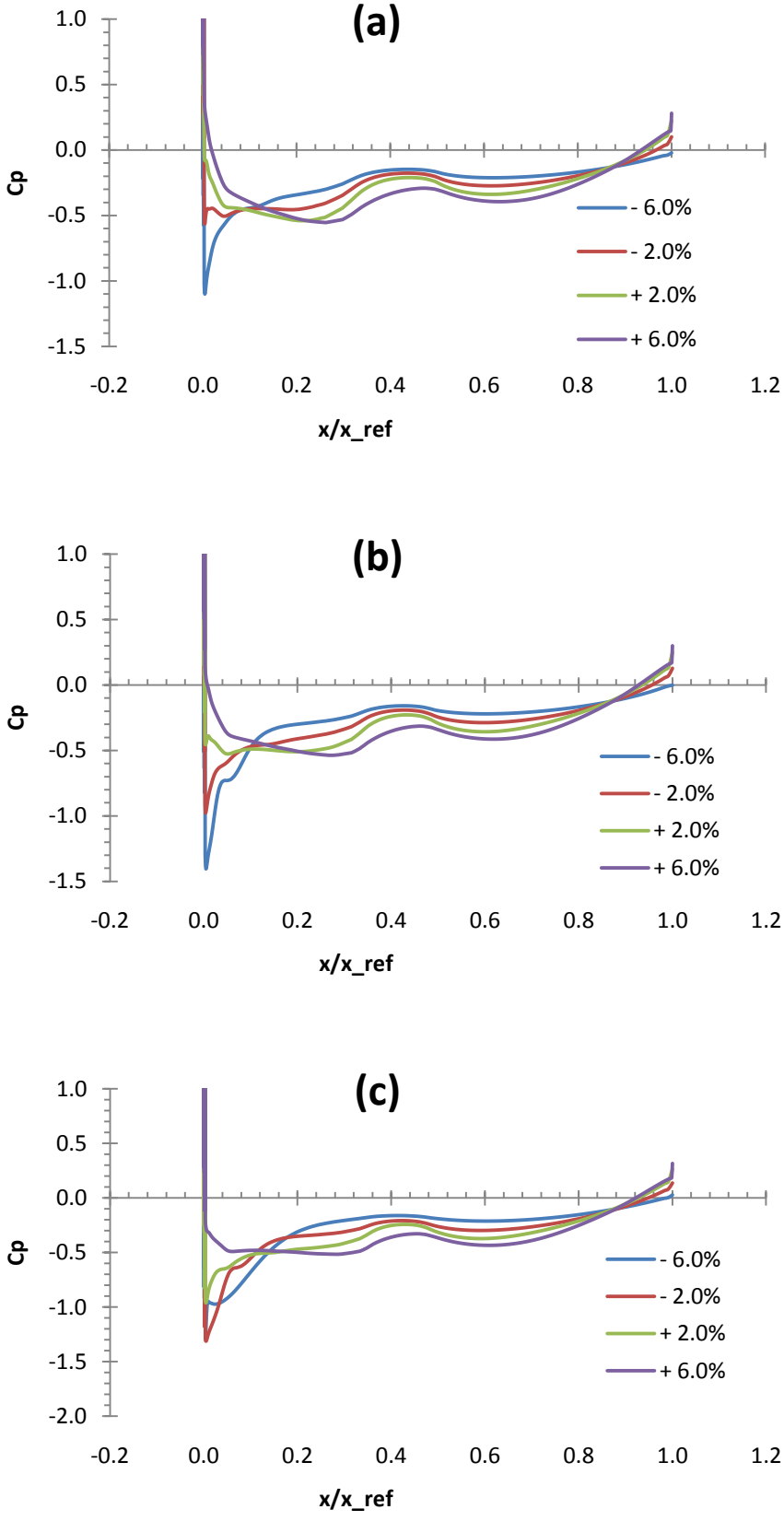

Figure 6.11 Pressure coefficient profiles along the crown (a), side (b) and keel (c) sections of the four nacelles shown with the percentage change of maximum diameters.

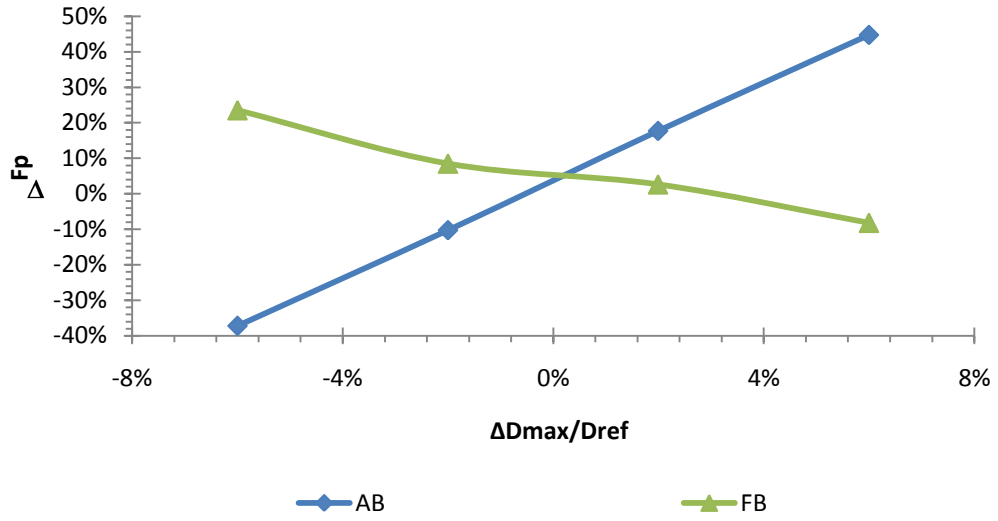

Figure 6.12 Change of pressure force on the Afterbody and Forebody related to the change of the daximum diameter

The pressure force at the forebody decreases approximately 30% from a Dmax change from −6.0% to +6.0% of the base geometry. The pressure for the largest Dmax is much lower than for the smaller Dmax near the intake tip, as can be seen in Figure 6.11. The pressure for the smaller Dmax increases and decreases rapidly until reaching the pressure "crossing point". After this point the pressure of the larger Dmax is higher than the pressure of the small nacelles. Although the pressure is smaller for large nacelles, the projected face is not large enough, therefore the pressure force decreases. The "pulling" force (opposite to the drag direction) increases as the Dmax increases.

The afterbody shows a similar pattern to the forebody. For the afterbody, the pressure at the beginning is higher for large Dmax's and reduces its value for a smaller Dmax. The AB is the largest section of the outside cowl, for all sections it is more than 50% of the total length of the nacelle. For the simulations with large Dmax the pressure difference between the exhaust and the mid-section is much larger than the smaller Dmax (see Figure 6.11). The pressure of the four nacelles analyzed also gets down to the same point, the same pressure is applied at the same abscisa coordinate ($x/x_{ref} \approx 0.84$). After that point the pressure applied over smaller cowls is bigger, and also is the projected area. The force applied is balanced slightly. Integrating all the pressure force applied on the AB, the total increases by increasing the maximum diameter as shown in Figure 6.12.

6.4.1.3 Total force

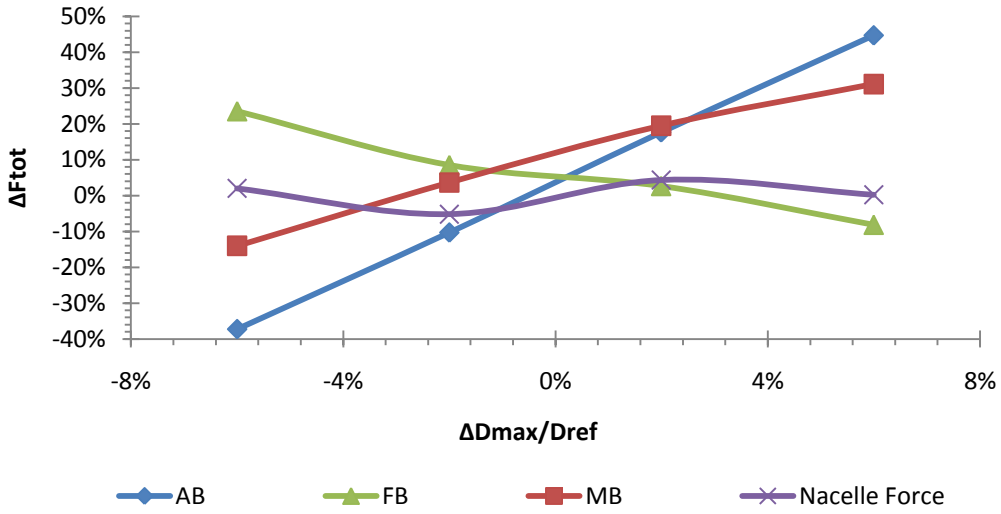

Figure 6.13 Total force applied to each of the nacelle sections.

For the AB and FB the major part of the total force is produced by the pressure, on the other hand for the MB it is only the viscous pressure which is created by the velocity (compare Figure 6.10 and Figure 6.13). The viscous force for the AB and FB sections is slightly bending the plot of the pressure change. Comparing the pressure force with the total pressure on the AB and FB on Figure 6.12 and Figure 6.13 a slight change can be observed. For the FB the differences between pressure and total force plots are approximately 1% for the four points in the plot. In the AB plot, the differences although also very small, are larger than the FB. In Figure 6.12 (pressure force changes) the nacelle with a Dmax change of +6.0% has a pressure force change of approximately –45%, with the effects of the viscous force it increases up to −38% in the total force change plot (Figure 6.13).

6.4.2 Highlight Diameter (Dhigh) change analysis

The variation of Dhigh has more impact on the velocity speeds than pressure. The stagnation point varies because of the geometry of the intake changes. The geometry change generates variations of stream pressure and velocity. This change of stagnation position produces a higher variation in both the velocity and pressure around the highlight of the intake.

In Figure 6.7 the pre-entry force changes much more than all of the other plots. The variation of the inlet area is mostly responsible for producing these big changes. The change of

pre-entry drag is so high because the MFR changes by a significant amount and it changes not only for aerodynamic reasons (with very small changes) but due to the geometry of the intake. The area variations produce stream velocity changes to keep the mass flow unchanged. Both the velocity and pressure are greatly altered by this effect and the stream force at station 1 changes.

The pre-entry drag should be neutralized by a large amount by the total nacelle force (see Figure 6.6) therefore both changes should be similar.

Figure 6.14 and Figure 6.15 show that it is difficult to see a pattern of the velocity around the intake. After mid-body the velocity changes seem to be very small compared to those of FB, it illustrates how the Dhigh has a major impact on the FB.

In the Cp plot it can be seen how the higher impact of the Dhigh value is on the forebody. The Cp plots are quite different for the FB section but for the AB are almost the same. Assuming the differences are due to numerical errors it can be concluded that small changes of the highlight diameter have a major impact only on the FB.

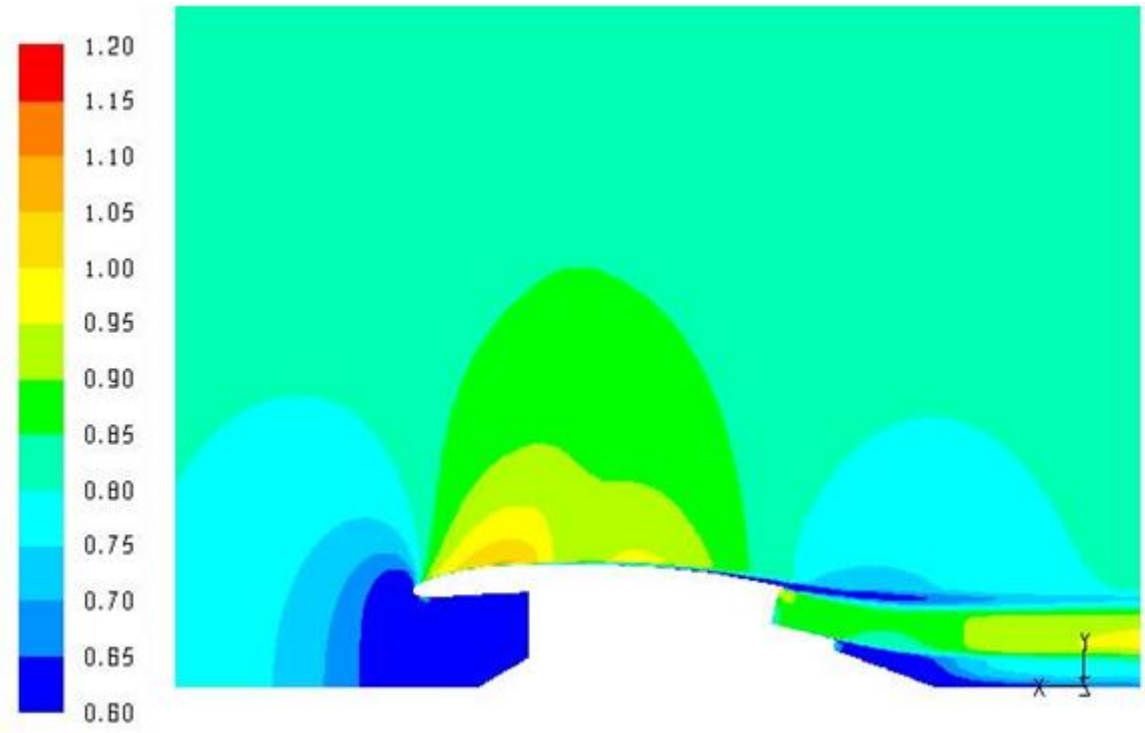

Figure 6.14 Mach number profiles of the side section of the nacelle of a Highlight diameter of - 6.0 % change with respect to the reference nacelle. (Mach number profiles are in the range of 0.6 and lower for blue to 1.2 and higher for red).

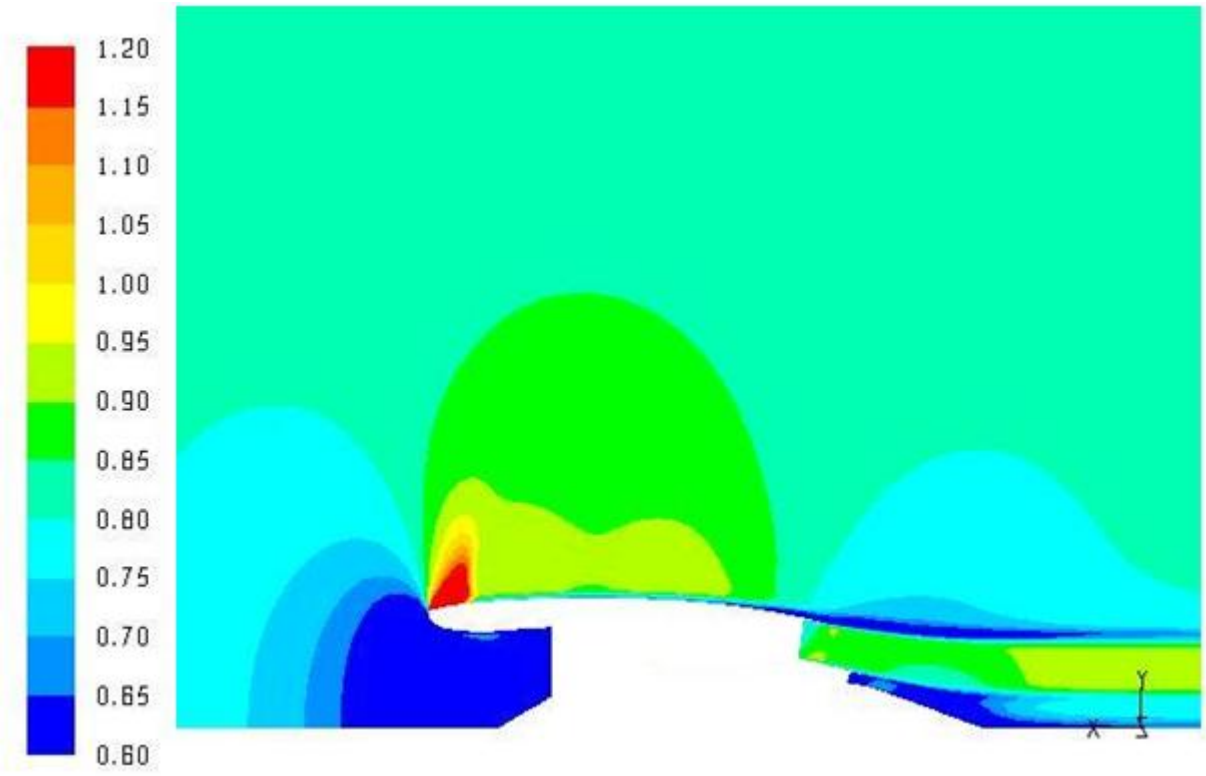

Figure 6.15 Mach number profiles of the side section of the nacelle of a Highlight diameter of ± 6.0 % change with respect to the reference nacelle. (Mach number profiles are in the range of 0.6 and lower for blue to 1.2 and higher for red).

6.4.2.1 Viscous force

The small changes of the Dhigh (± 2.0 %) produce very small changes on the velocities for the AB and MB. These small velocity changes also produce small viscous force changes. The greater changes produce larger viscous forces changes in the three sections of the nacelle.

The section with higher number of changes is the forebody. The force on the FB is the lowest with the smallest Dhigh. The force increases to the maximum values on a nacelle with a Dhigh value close to the reference value[10]. The biggest Dhigh (+ 6.0 %) would decrease the viscous force value.

[10] Dref in this case is equal to the highlight diameter of the geometry provided by VITAL.

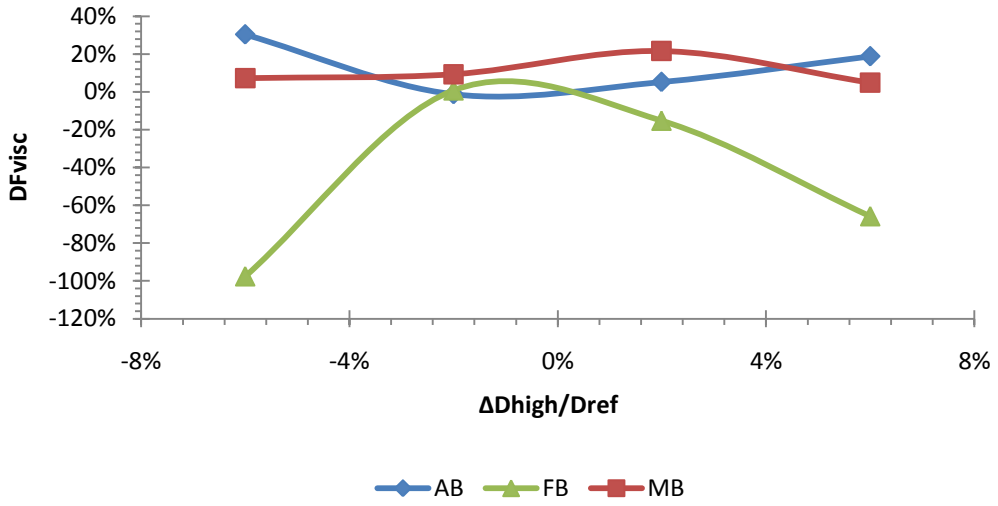

Figure 6.16 Applied viscous force changes at the three sections of the nacelle versus the percentage of highlight diameter change.

6.4.2.2 Pressure Force

The pressure force changes on the FB are produced by both changes of pressure and wet surface. For the AB it is only by the pressure. The projected area of the AB remains constant for all of the simulations.

Lower Dhigh generates higher pressures over the FB surface close to the highlight. On the rest of the surface, the pressure is lower compared to the highlight. The total integration of the pressure force is smaller for small Dhigh than the reference Dhigh as can be seen in Figure 6.18.

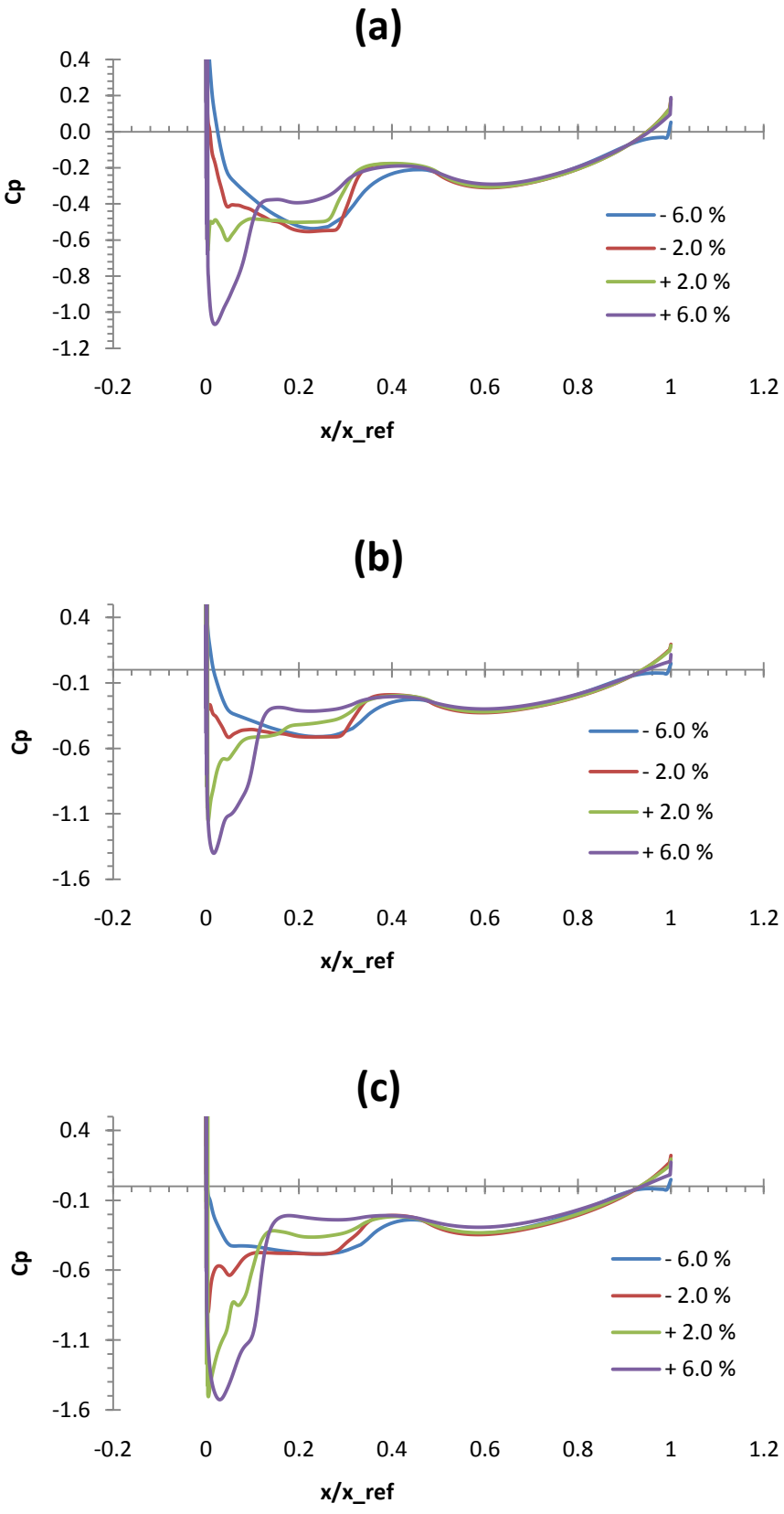

Figure 6.17 Pressure coefficient profiles along the crown (a), side (b) and keel (c) sections of the four nacelles shown with the percentage change of highlight diameters.

For higher Dhigh the pressure near the highlight is very low. Around the MB pressure increases as Dhigh increases (Figure 6.17).

The force plot of the FB (Figure 6.18) does not keep rising as the Dhigh keeps increasing. The pressure force of the FB for Dhigh changes of +2.0% and +6.0% are very close to one another. This is because greater pressure is applied on the surface with very small forward projected area and the suction force on larger nacelles is bigger, therefore the component of the force over the free flow direction is very small as shown in Figure 6.19.

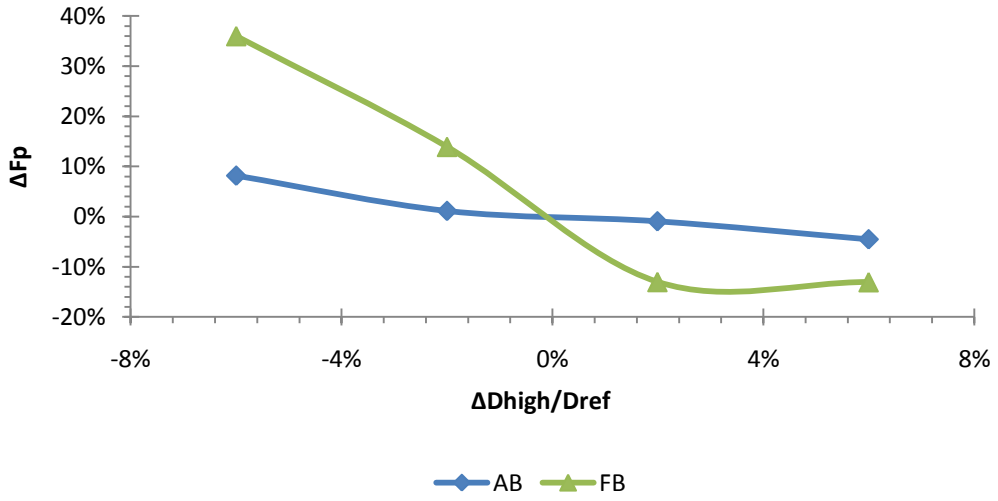

Figure 6.18 Pressure force changes over the forebody and afterbody related to the highlight diameter changes.

The changes of pressure force over the AB are very small. As can be seen in the figure above, the changes of force in a nacelle with a variation of ±2.0% of Dhigh are not more than 2.0%. These small changes are because the pressure variations are very small. With larger Dhigh variations, only slightly increased force changes are produced.

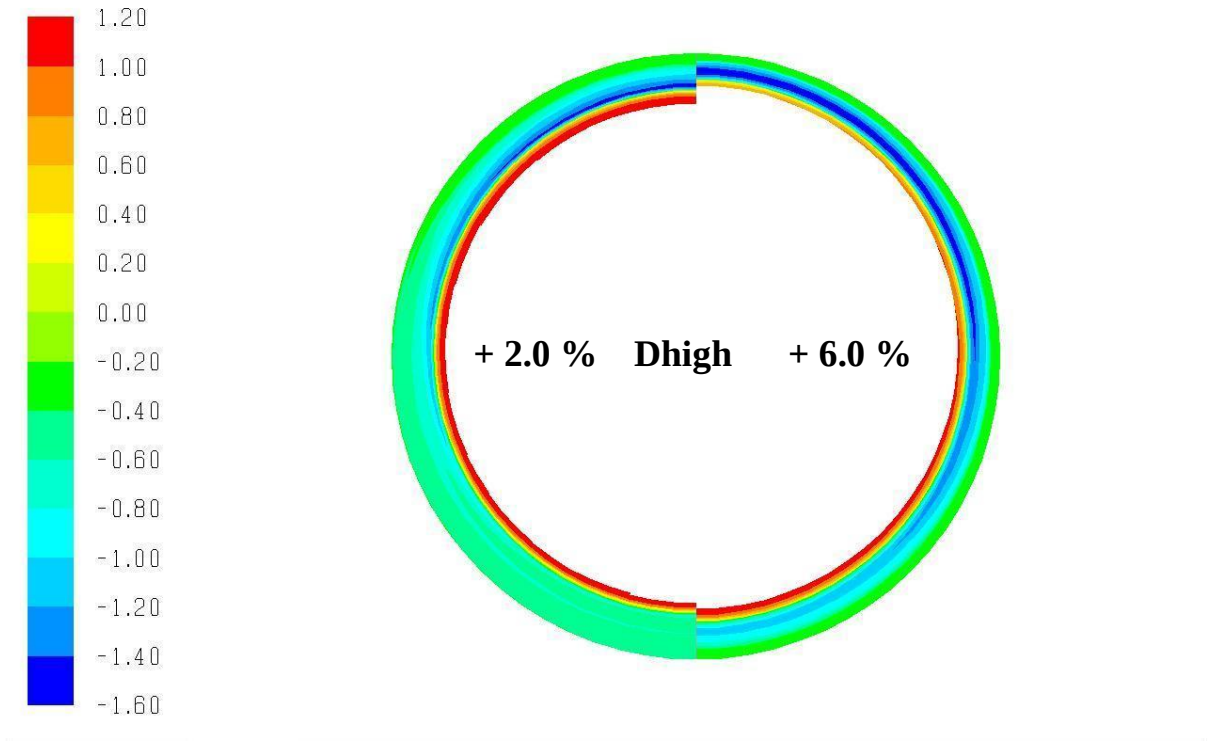

Figure 6.19 Pressure coefficient (Cp) distribution over the projected area of the FB to the axial component of the geometries with a Dhigh increase of 2.0% (left) and 6.0% (right).

6.4.2.3 Total force

The viscous and pressure force added are shown as a total force in Figure 6.20. The most important conclusion that can be taken out of this analysis is the variations of Dhigh have an impact mostly on the FB and MB. In the AB the total force changes by a very small percentage compared to the changes of the other two sections of the nacelle. The changes of the AB are small and smooth however in FB and MB, the changes are more significant with critical points (maximum in FB and minimum in MB).

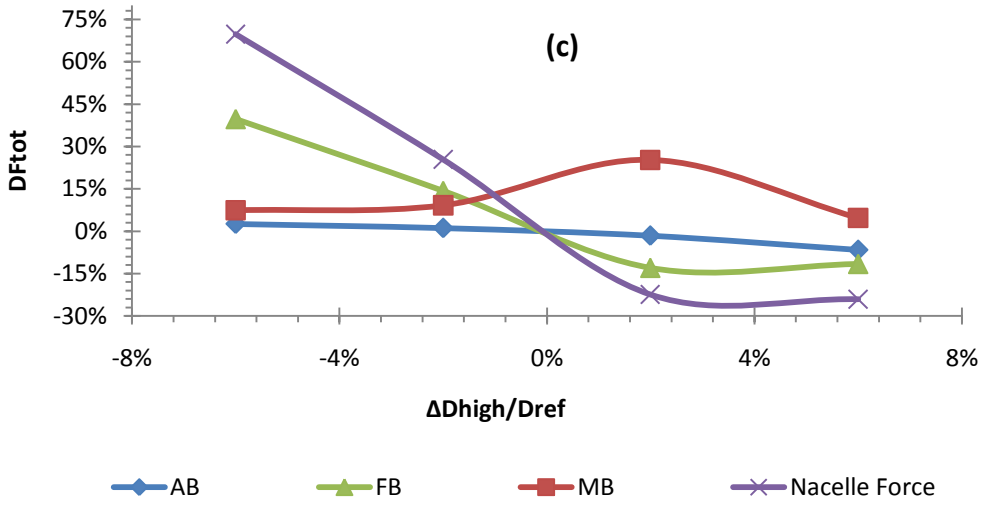

Figure 6.20 Total force variations at the three sections of the nacelle with respect to the changes of the highlight diameter.

6.4.3 Total nacelle length variation analysis

Nacelle length is changed by increasing or diminishing the length of the MB. This way of changing the length would generate small differences in the pressure profiles due to the increase in the distance between the FB and AB and the interaction between them.

The velocity changes, producing the interaction change of FB and AB, would produce small changes of the viscous forces compared to the pressure forces. Changing the length increases the wet area of the MB producing the largest friction force changes compared to any other on that section.

In the Figure 6.24 it can be seen how the pressure, mostly at the FB, varies very slightly with small changes of the length (±2.0%). The interaction is changed by a very small amount.

Large length changes (±6.0%) generate some variations, although not very significant, and are worth analyzing. The shortest length means that the AB and FB are very close to each other, therefore the pressure interaction generates a larger pressure at the FB and lower at the MB as can be seen in Figure 6.24. The pressure distribution is very similar to the mid-section of an ellipsoid of revolution with cylindrical mid-body (Ferri, 1972) and the pressure coefficient stays at lower values.

In the simulation with a significant length increase (+6.0%) there is a larger MB and the Cp over it is closer to zero. A larger cylindrical section will allow pressure to increase

until Cp nears zero. In the plots in Figure 6.24, the maximum Cp value at MB is for the longest nacelle although is only slightly above the other plots. The Cp increase appears to be asymptotic, for this reason the Cp value of the longest nacelle at the MB is just slightly bigger than the other nacelles.

6.4.3.1 Viscous Force

For the analysis based on the nacelle length only the MB section was changed. For this reason the friction force changes on the FB and AB are produced by the velocity. The velocity variations (with the viscous forces created on the nacelle) are produced only by the change of the interaction between FB and AB.

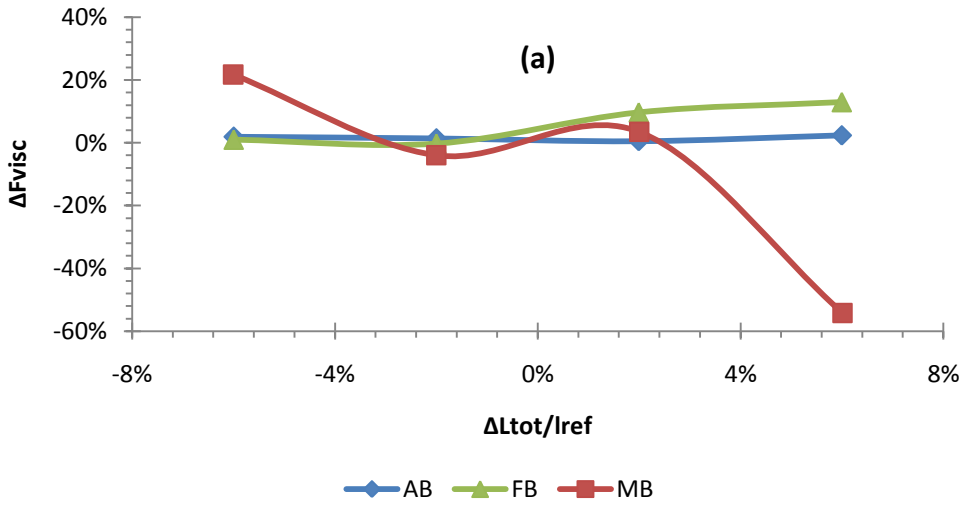

Figure 6.21 The effect of the change of total nacelle length in the viscous force.

Figure 6.21 show how the MB viscous force is decreasing as the length increases. The wet surface increases its area. The interaction between AB and FB decreases therefore the flow velocity over the MB section also decreases. A comparison between Figure 6.22 and Figure 6.23 illustrates the Mach number differences between a short and long nacelle produced by the interaction between the AB and FB.

The AB plot shows how the viscous force variation is not very significant. All of the changes are below ±10.0%. In Figure 6.22 and Figure 6.23 the Mach number profiles are quite similar for both of them, and analyzing figures in Appendix A, the differences are quite small in every one of them.

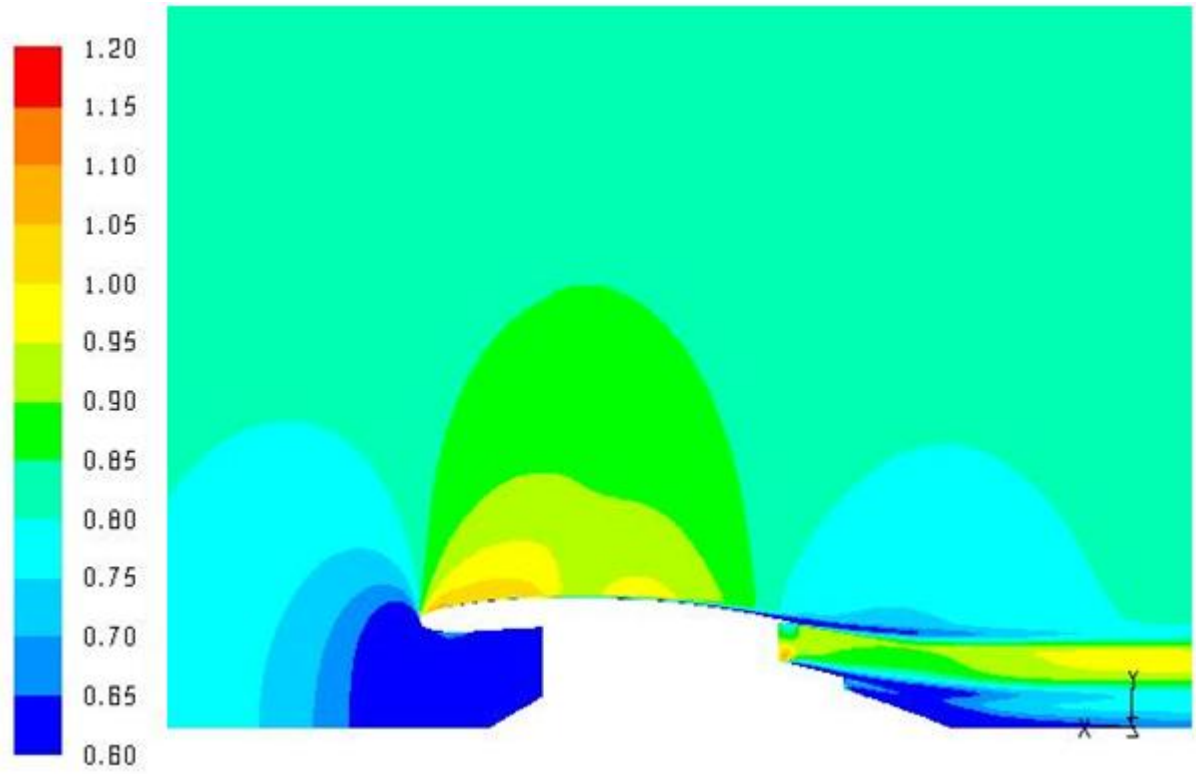

Figure 6.22 Mach number profiles of the side section of the nacelle of a length of - 6.0 % change with respect to the reference nacelle. (Mach number profiles are in the range of 0.6 and lower for blue to 1.2 and higher for red).

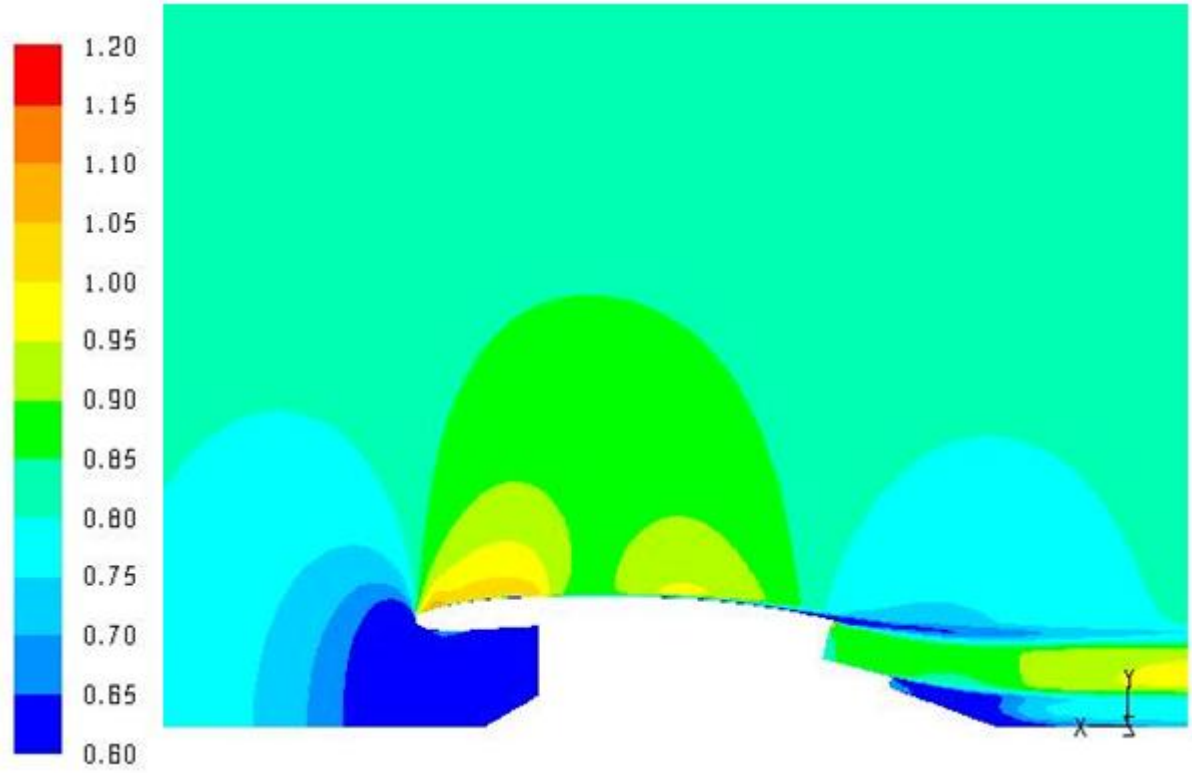

Figure 6.23 Mach number profiles of the side section of the nacelle of a Length of + 6.0 % change with respect to the reference nacelle. (Mach number profiles are in the range of 0.6 and lower for blue to 1.2 and higher for red).

Mach number profiles for the FB are quite different in every picture. The velocity differences along the nacelle are created by the different static pressure that the spillage flow encounters at the MB.

6.4.3.2 Pressure Force

The pressure force plots (Figure 6.24) are where the differences between each nacelle can be seen. As stated before, the FB geometry of every one of the simulations is the same. The only changes start at the MB, the length of which varies according to the length required by the total length analysis. The geometry of the AB does not vary, what does vary is its relative position away from the FB (the length of the MB).

The variation of the pressure is very small at the FB. The variations would require a more detailed analysis to evaluate if they are due to a numeric error, mesh variation or an aerodynamic variation. In the case of aerodynamic variation a more detailed analysis would be required.

The pressure distribution at three different sections of each one of the simulations can be observed on page 112. In those pressure distribution plots similar behaviours can be observed.

- FB pressure distribution plots are very similar in each of the three sections shown.
- At MB the pressure is greater as the length increases. Pressure coefficient increases asymptotically to Cp = 0.
- AB profiles are quite similar. The only difference is the Cp value where it starts decreasing.
- The minimum value at the transition between MB and AB has a very similar value for the four simulation profiles. The position of the critical point changes due to the point where the pressure starts falling. After the minimum point the pressure shows a very similar behaviour along the AB.

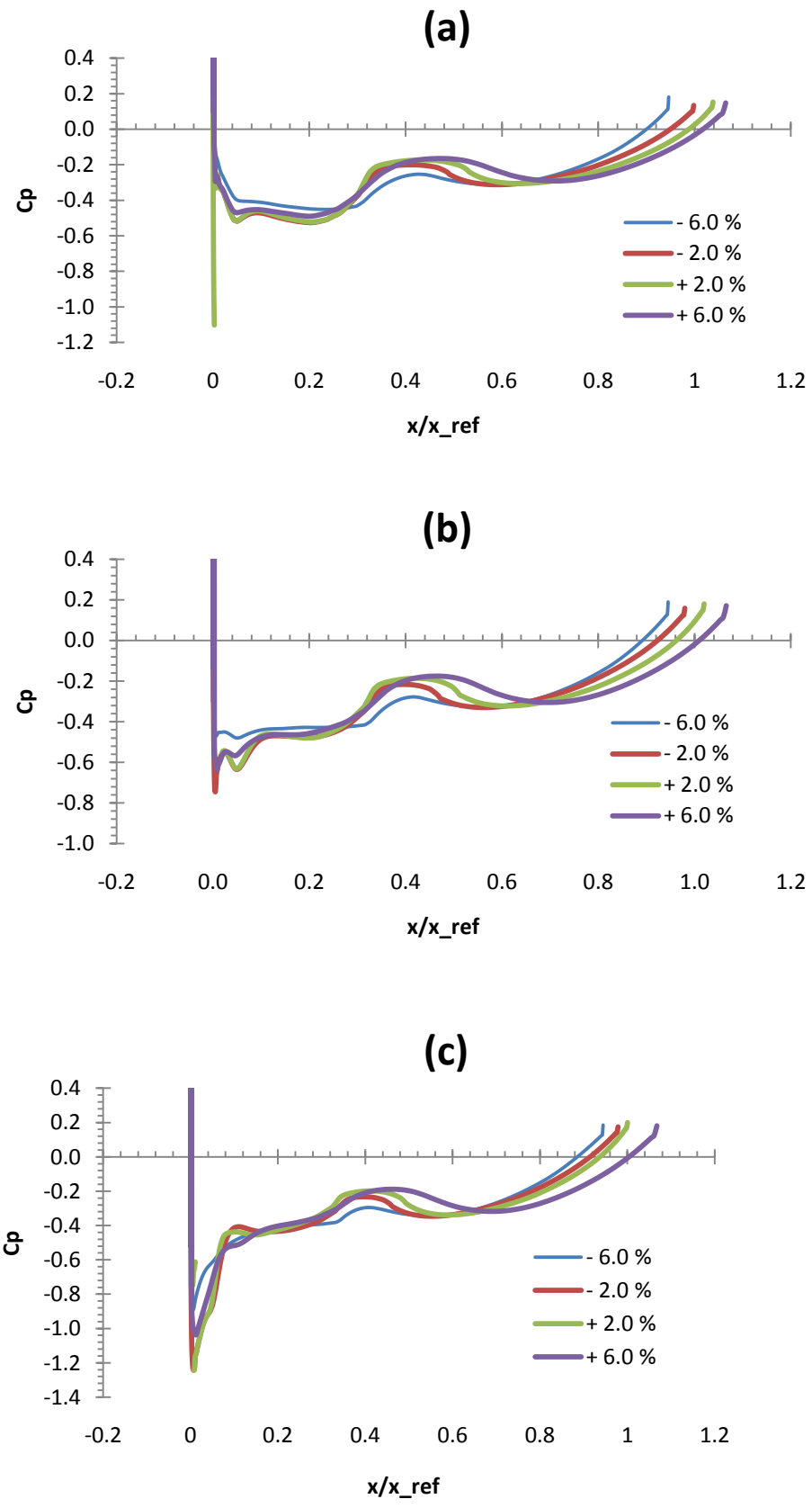

Figure 6.24 Pressure coefficient profiles along the crown (a), side (b) and keel (c) sections of the four nacelles shown with the percentage change of total nacelle length.

After the integration of the pressure over the projected area at the FB and AB of each simulation the resulting force is shown in the plot of Figure 6.25. Changes apparently are very small, most of them below ± 3.0 % (for both AB and FB). The only two simulations out of that range are for the change of + 2.0 % and + 6.0 % with approximate changes of -10% and -13% respectively.

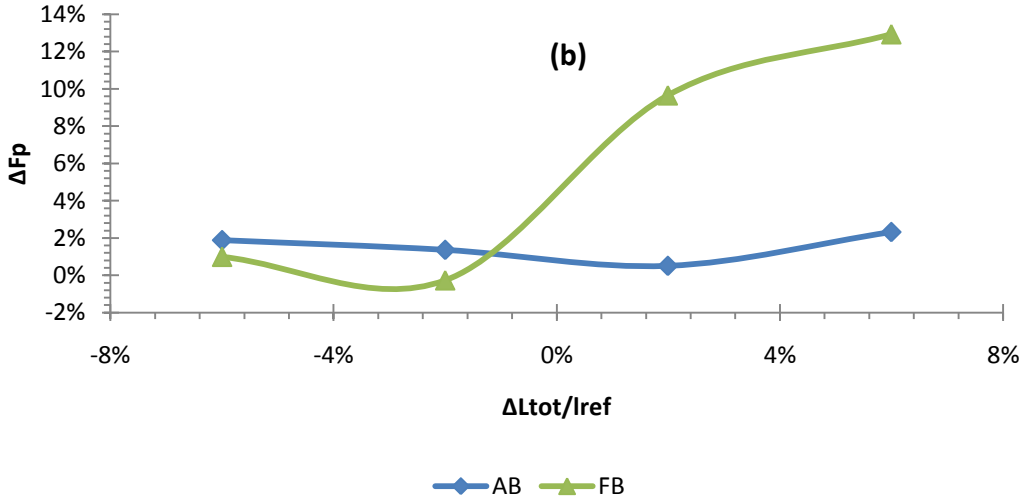

Figure 6.25 Effect of total nacelle length changes in the pressure force.

6.4.3.3 Total force

The total force for the FB and AB of the nacelle is quite similar to the pressure value. The only difference is for the MB where the influence of pressure on the axial forces is almost insignificant.

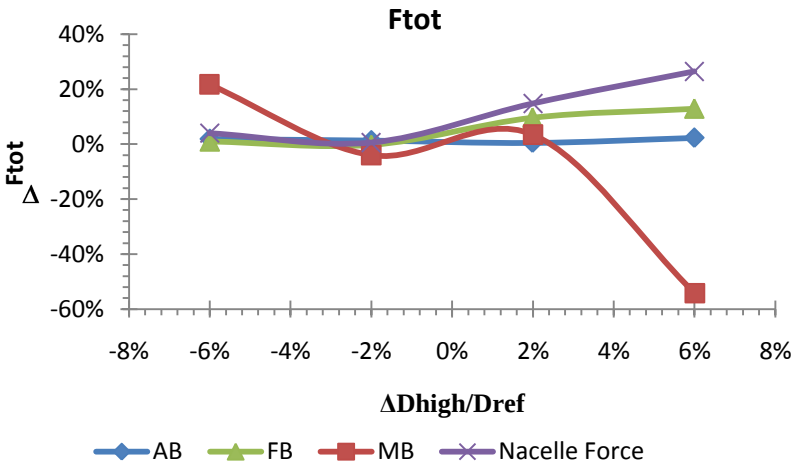

Figure 6.26 Effect of the total nacelle length changes in the total force.

As can be seen in Figure 6.27(a) the viscous force change is very small for the whole nacelle. The influence that viscous force has is quite small on the total force. On the other hand the total force magnitude decreases 26% (Figure 6.6). The fall of the magnitude is mostly because of the pressure force fall on the FB and to a lesser degree due to the slight viscous force decrease of the MB section. The forces on the FB have the largest percentage of the total force of the entire nacelle. Comparing Figure 6.25 and Figure 6.27(b) the AB force remains almost unaffected. On the other hand the pulling force of the FB decreases by a large amount. By adding these two force changes the drag increases.

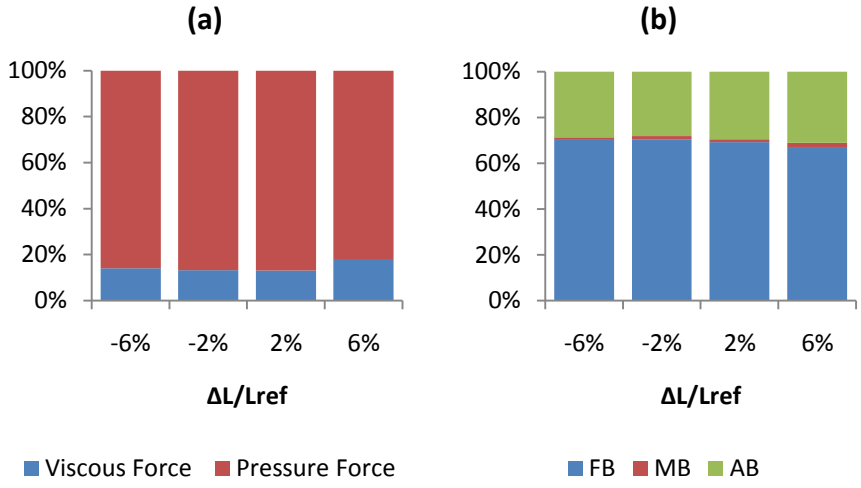

Figure 6.27 Impact of the nacelle length on the viscous and pressure force percentage on total force (a) and the force of the FB, MB, and AB percentage on the total force (b).

7 Integrated Nacelle to an airframe

7.1 Introduction

The available power of an aircraft engine depends on the performance of the engine (thrust) and the drag it produced. Thrust and drag together will determine the Net Propulsive Force which is the available force for the airplane. The drag of an installed engine is determined by the nacelle geometry (already discussed in sections 5 and 6), and the position of the engine with respect to the wing and the fuselage.

The position of the engine has to deal with several issues like safety, aerodynamics and structure. The installation of big engines like a VHBR engine is an even more challenging task than the average HBR engine. The integration of the propulsion systems of the Boeing 777 was a challenging task due to the complexity and size of the engines (Berry 1994). In his work Berry presents many factors involving the integration tasks, including the following aerodynamic factors:

- Overall shape and orientation of the nacelle
- Fore/aft, up/down and spanwise positioning of the powerplant
- Inlet internal and external geometry
- Pylon contours
- Exhaust system

The effects produced by the afore mentioned factors are reflected in several aspects of the performance of the airplane. Some of these are pressure recovery and lose of lift, amongst others. The ones that will be studied in this project are the geometry of the nacelle and some aspects of the positioning of the engine. The pylon, exhaust system and some parameters of positioning will not be studied but could be an interesting topic for future work.

In this chapter the interference drag produced will be analyzed. The Wing Body Nacelle (WBN) system will be studied. The pylon effects will not be studied.

7.2 Methodology

To make the parametric analysis of an integrated nacelle several parameters can be analyzed. Also their relation with many different variables. Due to the limitations of this project it was possible to analyse only a few parameters.

The following is the list of the main steps taken for this stage.

1. Airframe geometry selection
    a. Simplification of the model
    b. Parameters selection
2. Meshing
3. Simulation setup
4. Running the simulation
5. Results analysis
    a. Running extra simulations based on the analysis

Based on this methodology a reliable parametric analysis of the drag produced by the installation can be made.

7.3 Geometry

The geometry of the nacelle used for the simulations is the base geometry provided by the VITAL project. The nacelle geometry remains the same for the installed power plant simulations. For further references of the nacelle geometry go to section 6.1.

The nacelle was created in the frame of the project VITAL and adapted to the geared Turbofan in this case. The GTF is designed to be installed in a twin engine airplane for medium to long range journeys. No specific type of aircraft was imposed in order to study the evolution of the thrust losses due to installation drag.

The aircraft that would fit the requirements for the project are the following:

- Airbus A350 Actually under development
- Airbus A330 Will be soon replaced by the A350
- Boeing 787 Actually under development
- Boeing 777 The largest twin engine in use

None of the commercial airplane geometries is available for academic use due to the high confidentiality in the aerospace industry. The base geometry was provided by the College of Aeronautics of Cranfield University. It is a model developed in the Aircraft & Vehicle Design department in the MRT-7 project, see Figure 7.1. The MRT-7 is a L/R twin engine aircraft.

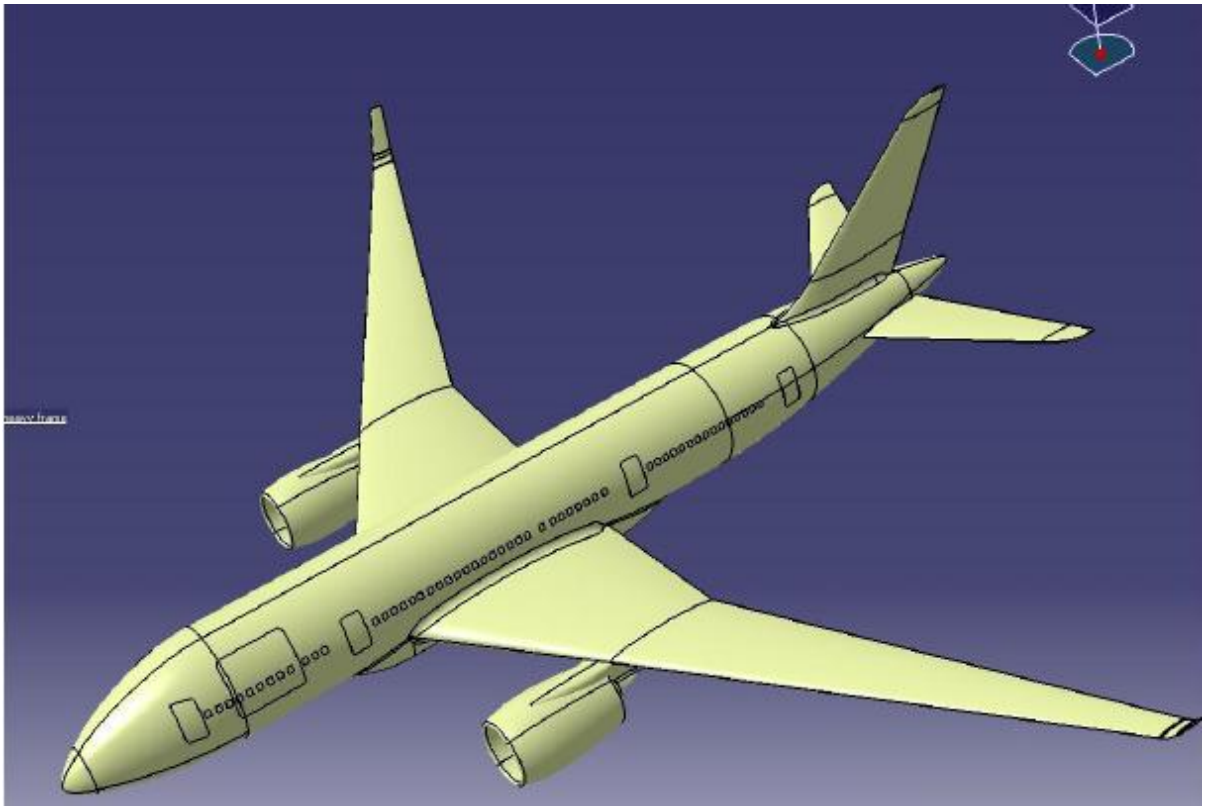

Figure 7.1 MRT-7 project of Aircraft and Vehicle Design of Cranfield University

The model was very complex to be used as the geometry for a CFD simulation therefore it was edited using Dassault Systems, CATIA V5 software.

The modifications made to the CAD model were made by removing the surfaces which were not of real importance for the study. The following sections of the aircraft were deleted:

- details (doors, windows and others)
- engines and pylons
- winglets
- blister
- tailplanes

- tail fin
- fillets between surfaces

As the study is about drag produced by an installed engine the only sections of the airplane having real importance are the fuselage and wing. Also the details of the airplane were removed in order to simplify the model as much as possible in order to create a good mesh. With a good mesh the simulation should run faster and the results might be more accurate. An image of the modified geometric model used for the simulations is shown below. Only the wing and fuselage are shown and they are devoid of detailed design.

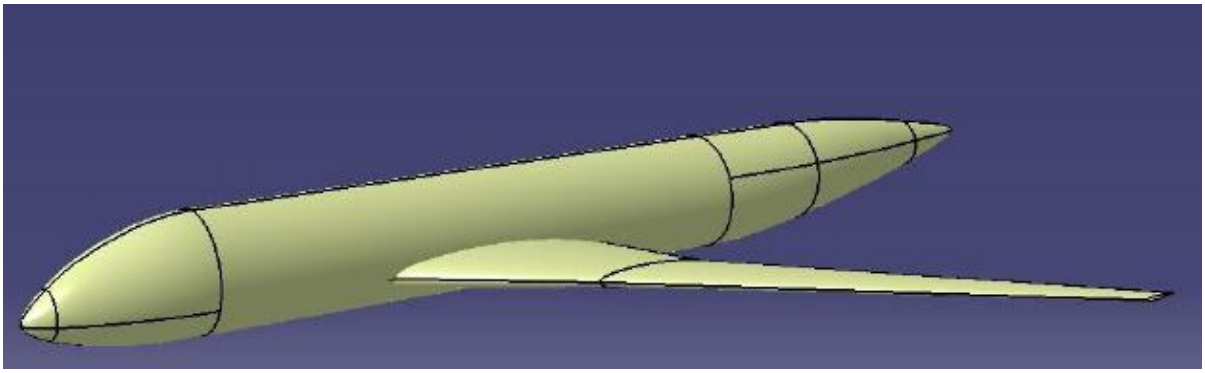

Figure 7.2 Simplified geometry of the MRT-7 project

7.4 Meshing strategy

For both the WB and WBN models several domain shapes and sizes were tested. Also different methods of meshing were tried. The grids shapes and sizes were made to be as similar as possible between the different geometries in order to avoid result variations produced by the grid differences.

7.4.1 WB system grid

The shape of the domain is a symmetric cylinder with half of the geometry of the airframe in it. Based in a reference length, the domain dimensions are the following (see Figure 7.3):

- Length is 6 times reference length (2 fore wind, and 4 back wind)
- Diameter is 4 times reference length

Due to the complexity of the geometry the mesh chosen was unstructured. The finest sections of the mesh are at the tip and tail of the fuselage and the leading and trailing edges of the wing.

Special attention was given to the junctions between the wing and fuselage in order to properly join the two surfaces with different density of cells. Also, at this section the geometry has very step angles and therefore the skewness of the cells at these points is very high.

As integration drag is the primary concern of the project, the mesh of the wing is much finer than of the fuselage (see Figure 7.4).

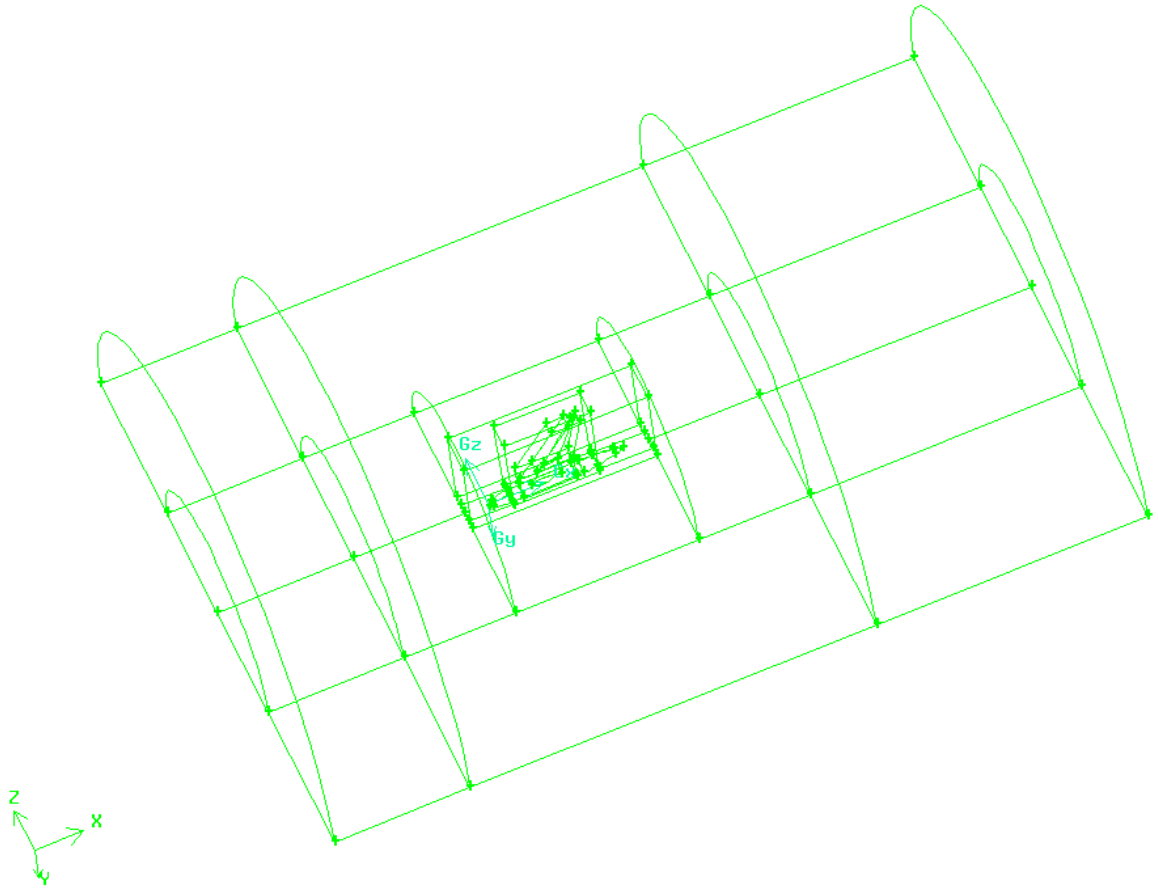

Figure 7.3 Airframe domain

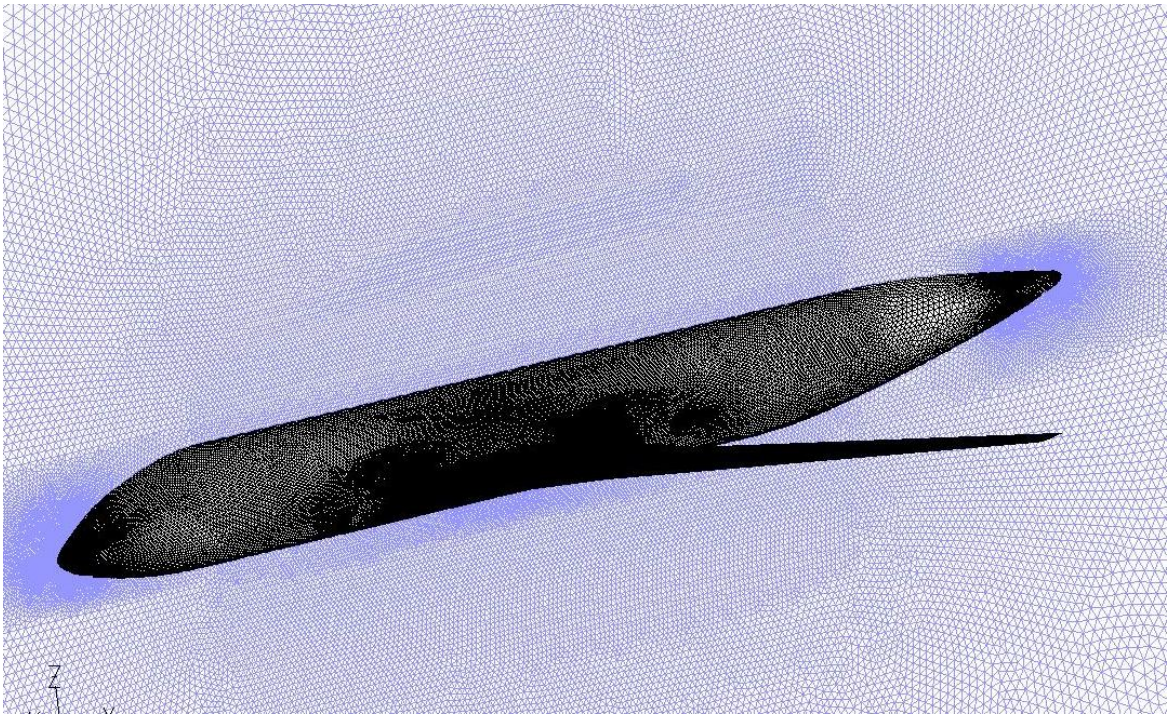

Figure 7.4 WB mesh

7.4.2 WBN grid

The grid for the WBN system is similar to the WB system. The symmetry plane, inflow, outflow, farfield and fuselage grids are built using the same methodology. The integration of the engine into the system requires some changes for the wing meshing. At the spanwise position of the engine the mesh must be finer in order to fit the very fine cell size of the nacelle. This effect is more noticeable in the geometries where the nacelle is very close to the wing.

The nacelle is meshed in a smoother way than the previous stages of the project. The cell density at the intake highlight and midbody are very similar. The reason for this is because the objective of this stage of the project is to measure the interactive drag of the nacelle with the wings. For this reason the grid of the nacelle is not as detailed as in the isolated nacelle analysis. With a nacelle grid similar to the isolated engine analysis the computational resources would be wasted in measuring the nacelle drag, which has already been done. Although the nacelle grid is coarser than previous stages is still much finer than the grid of the wing (see Figure 7.5).

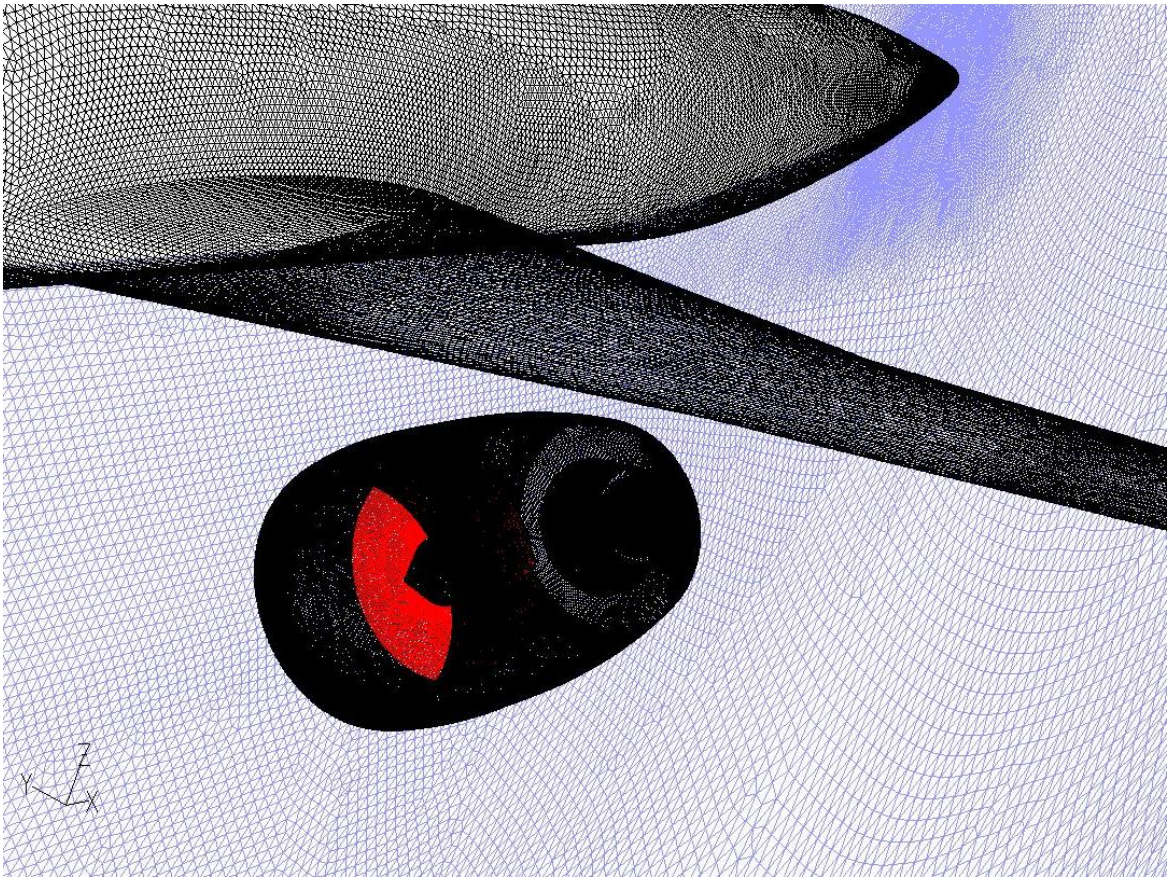

Figure 7.5 Integrated nacelle grid

7.5 Simulation Setup

In order to get results that would match the results of the isolated nacelle the setup was very similar. The main setup characteristics are listed below:

7. Boundary conditions
    a. Inflow - Pressure inlet
    b. Far-field – Pressure far-field
    c. Outflow – Pressure outlet
    d. Fan – Pressure outlet with target mass flow
    e. Bypass flow exhaust – Mass flow inlet
    f. Core flow exhaust – Mass flow inlet
8. Pressure-based solver
    a. Absolute velocity simulation
    b. Green-Gauss Cell-based gradient option
9. S-A turbulence model
10. Discretization methods

a. Second order pressure interpolation method
b. Second order upwind discretization methods

The main difference with the isolated nacelle analysis is that the simulation was not running in steady state (SS) conditions. Although several initial conditions with many changes of solving methods were tried, the SS always generated divergence. To correct this, simulations with time dependent conditions (TD) were used in order to get the convergence. This method is more time consuming but it is certainly more beneficial to achieve a convergence of the simulation. Time steps are set as 1/20 of the time that a free stream particle would take to travel across the domain without any perturbation.

7.6 Simulation

7.6.1 Convergence

To achieve convergence the following criteria were adopted for every one of the simulations:

- The fan mass flow converged to the required value.
- The residuals values are staged at a certain value
- The drag and lift coefficient converged to a certain value.

In Figure 7.6 there is an example of one of the convergence criteria fulfilled for one of the simulations. It is noticeable how all of the residual plots have a peak at every time step change, but they keep falling down to the same value. Cd and Cl are set at one value (a different one for each one of them), and the difference between the fan mass flow and its target value is less than 0.01%. All of these criteria enable the conclusion to be made that the simulation has converged and no more iterations are required.

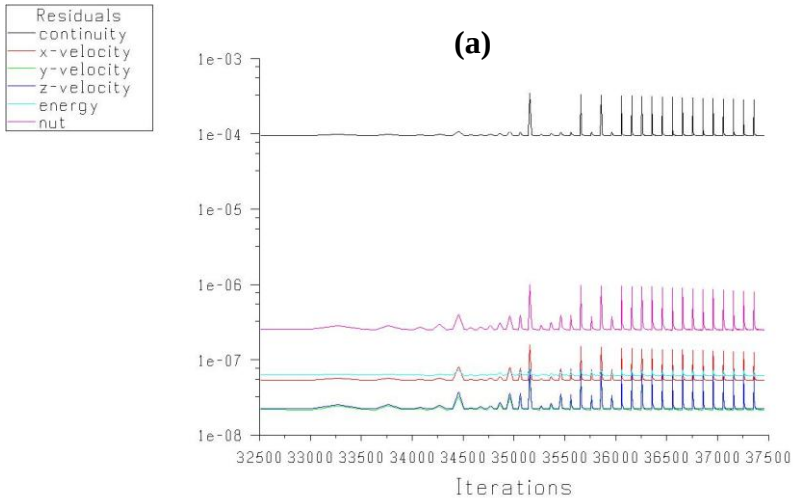

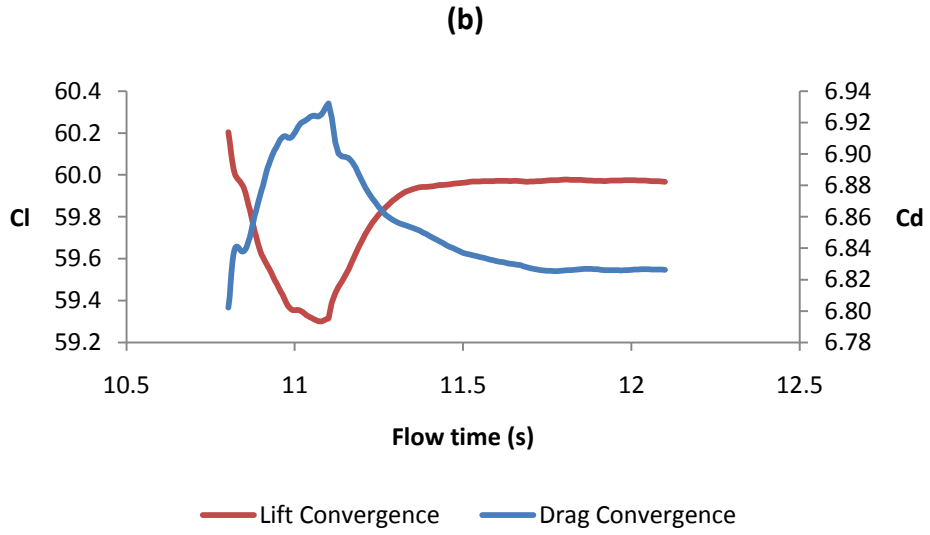

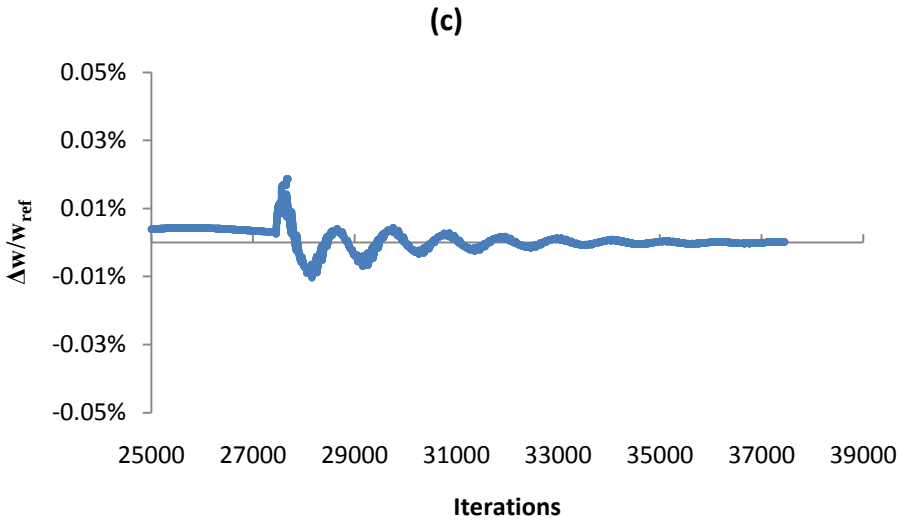

Figure 7.6 Convergence criteria. (a) residuals, (b) Cd and Cl history and (c) mass flow history

7.7 Parameters

There are 5 main design parameters involved in the positioning of the engine (see Figure 7.7).

- Fore/aft position also called penetration (x)
- Up/down position (h)
- Spanwise position (w)
- Tilt angle (α_{tilt})
- Incidence angle (α_{insc})

(a)

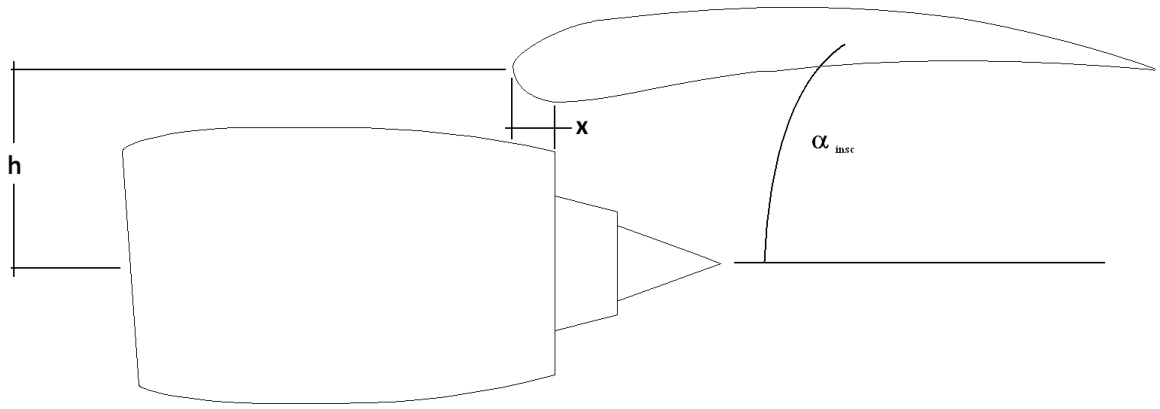

(b)

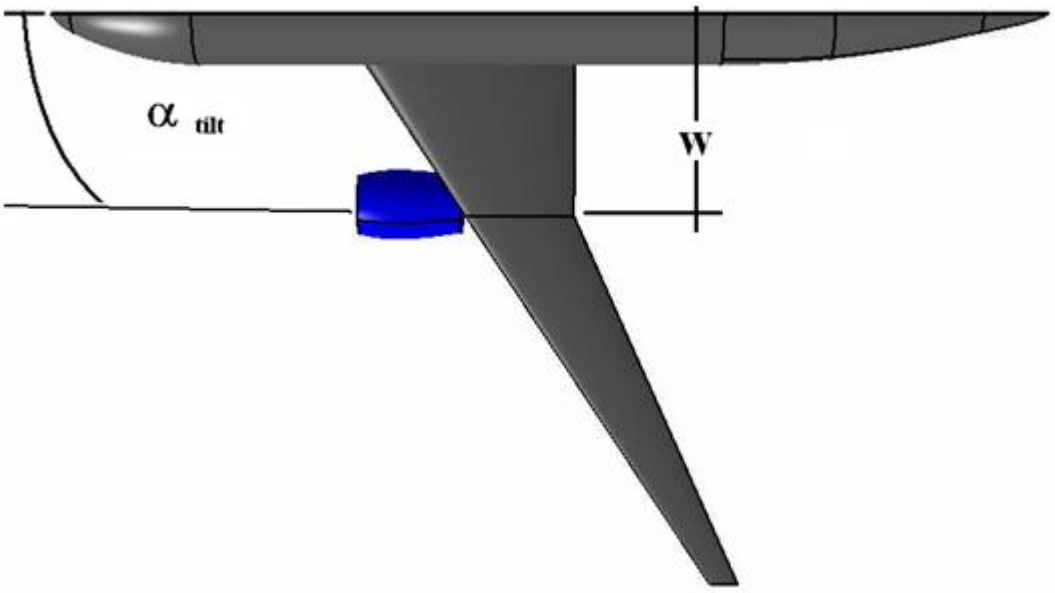

Figure 7.7 Main parameters for engine positioning

The aft/fore (x) and up/down (h) positions have a significant influence on drag. These two parameters are the only parameters analyzed in this project. 'x' is defined as the distance from the centre of the intake plane to the leading edge of the wing. Note x distance is not defined in the same way as is shown in Figure 7.7(a). Parameter 'h' is the vertical distance from the engine centre line to the leading edge of the wing.

The other parameters are defined in the following way:

- Both tilt and incidence angles are set to 0°. The engine centre line is parallel to the free flow direction.
- Wingspan value is set to w/Dmax = 2.772. This is the same value as in the original geometry of the MRT-7 model.

Both x and h parameters are normalized with respect to a reference value. The reference value is different for each of the parameters. The x value is normalised in respect to the total length of the engine and h to maximum engine diameter.

The values considered for each parameter are shown in Table 9. The base values are the values used in the original design of the MRT-7 and are the values used for comparing the drag changes.

Table 9 Parameter values for the analysis and their variation with respect to the base values(Shaded cells are the base values)

h/Dmax	x/length	Δh%	Δx%
0.547	0.722	0	0
0.50	0.65	-8.59	-9.97
0.55	0.70	0.548	-3.05
0.60	0.75	9.69	3.88
0.65	0.80	18.83	10.80

The combinations of values used are those making the engine closer to the wing in either of the two directions or even both of them (see Table 10). After simulating and analyzing some of the combinations it was decided to make more simulations by changing of the parameters that would make the engine either closer to or further from the wing,

depending on the amount of change or the parameter changed. This way the impact of each of the parameters on the drag would be evaluated.

Table 10 Combination of the parameters.

	h/Dmax	x/length
1	0.5	0.8
2	0.55	0.75
3	0.6	0.7
4	0.6	0.75
5	0.6	0.8
6	0.65	0.65
7	0.65	0.7

7.8 Results and analysis

The results used for analysis are the drag and lift values given by the CFD software (Fluent 6.2). The way in which these results are calculated by the software is reported at Fluent 6.3 Reference manual, section 29.3.1. As previously stated Fluent definition of drag is not suitable for engines because they are ducted bodies. The WBN system is actually made of two different bodies: the engine (ducted body) and the airframe. For the engine a proper force bookkeeping is required. Bookkeeping is not necessary for the airframe, as the drag is simply a sum of all of the forces on the surface without any flow (and the energy with it) going through any duct.

To measure the impact of the engine positioning the simulations of the WB system, the Isolated nacelle, and the WBN system are used. The interference drag is calculated by subtracting the isolated engine and WB system forces from the WBN. Unfortunately with this method the uncertainty of the three simulations would be added together and it might be difficult to get proper conclusions from it, especially if there is a high level of inaccuracy of any of the simulations. With more powerful computational resources the simulations might become more accurate therefore this method would increase in reliability.

Although the interactive drag would be difficult to calculate, the change of drag on each section can be measured individually. The trends of the drag variations according to each of the parameter variations would be quite useful in order to come to some conclusions.

The pressure and viscous drag are calculated in order to evaluate the impact of the parameters on each of these and if any parameter has a major influence on the viscous or pressure force.

The parameters shown are the change of drag with respect to the value given by the calculation with the base geometry. The values shown are percentage variation from the base geometry.

When analyzing the total drag variations on the nacelle, the conclusion is that the penetration has resulted in being the most influencing parameter. Figure 7.8 shows how the change of penetration produces a change of drag and the variations of vertical positioning are almost imperceptible. The drag values for the simulations with the same penetration values are virtually the same with the vertical position having an insignificant influence compared to that of penetration. The plots together could be approximated to a straight line in a plot of x versus Cd.

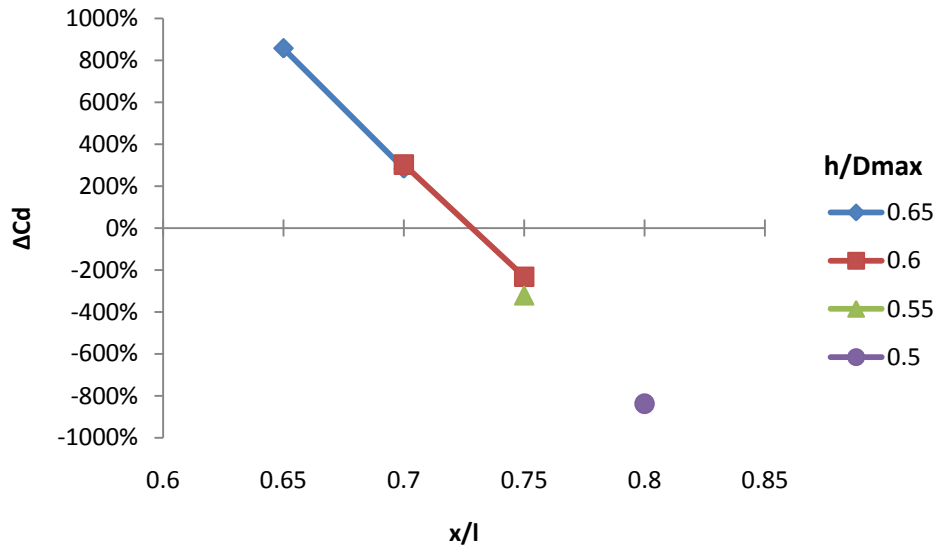

Figure 7.8 Impact of penetration and vertical positioning on total drag

The plots of Figure 7.9 show the viscous drag and pressure drag on the nacelle. The pressure force on the nacelle is also very close to being a straight line making pressure the most important component of the total drag, just as concluded in section 6.4.

The viscous force variations with respect the engine positioning are very small. In fact as the viscous forces are quite small compared to the pressure forces they might seem irrelevant. Still some conclusions can be made from the trends shown in Figure 7.9(b).

- Viscous drag will increase if the vertical distance increases.
- If penetration increases (x decrease) the viscous drag will decrease.

The previous two effects happen because of the wing influence on the stream velocity. When the engine is positioned close to the wing (large penetration or small vertical distance to the wing) the air is slowed down.

With a change of the penetration of ±7% there will be a change of approximately ±3%. For a variation of ±9% the change of the viscous force will change by approximately ±3-4%.

The viscous drag is very small compared to pressure drag, this makes Cp behaviour almost identical to the total drag.

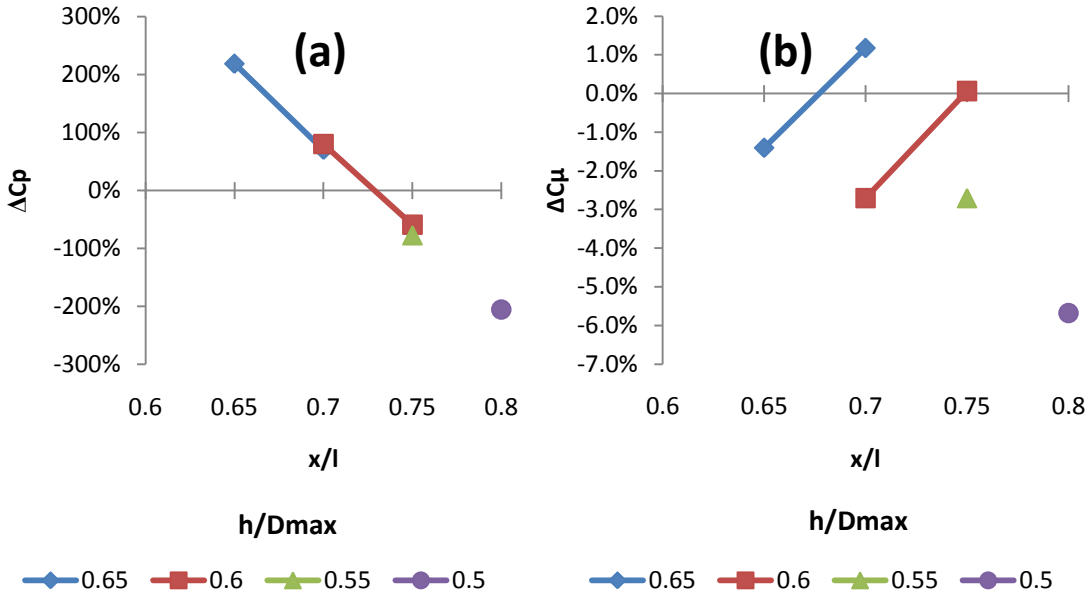

Figure 7.9 Pressure (a) and viscous force (b) on the nacelle

To analyze the behaviour of the Cp on the nacelle, a more detailed analysis of the influence of the parameters is to be made. For the analysis, the Cp profiles are studied at the positions shown in the figure below.

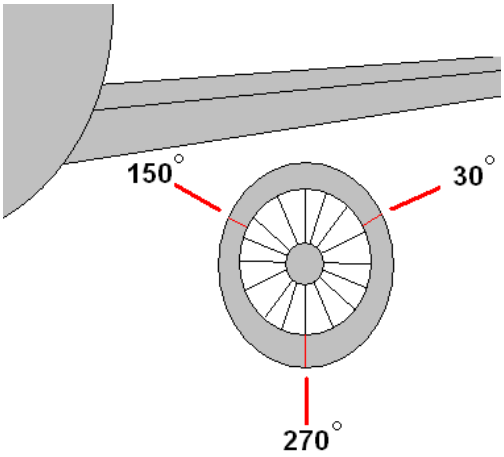

Figure 7.10 Sections of the nacelle chosen for analyzing the influence of the nacelle position on the Cp distribution

In Figure 7.11 the distributions of the Cp are shown. The distribution plots are along the nacelle. The abscise axis represents the axial position normalized with respect the total axial length for the distribution plotted.

When comparing the four plots the first observation to be made is that the position of the nacelle only has a significant influence on the AB. In all of the plots the Cp distributions on the FB and MB are very similar for the three sections of all of the simulations.

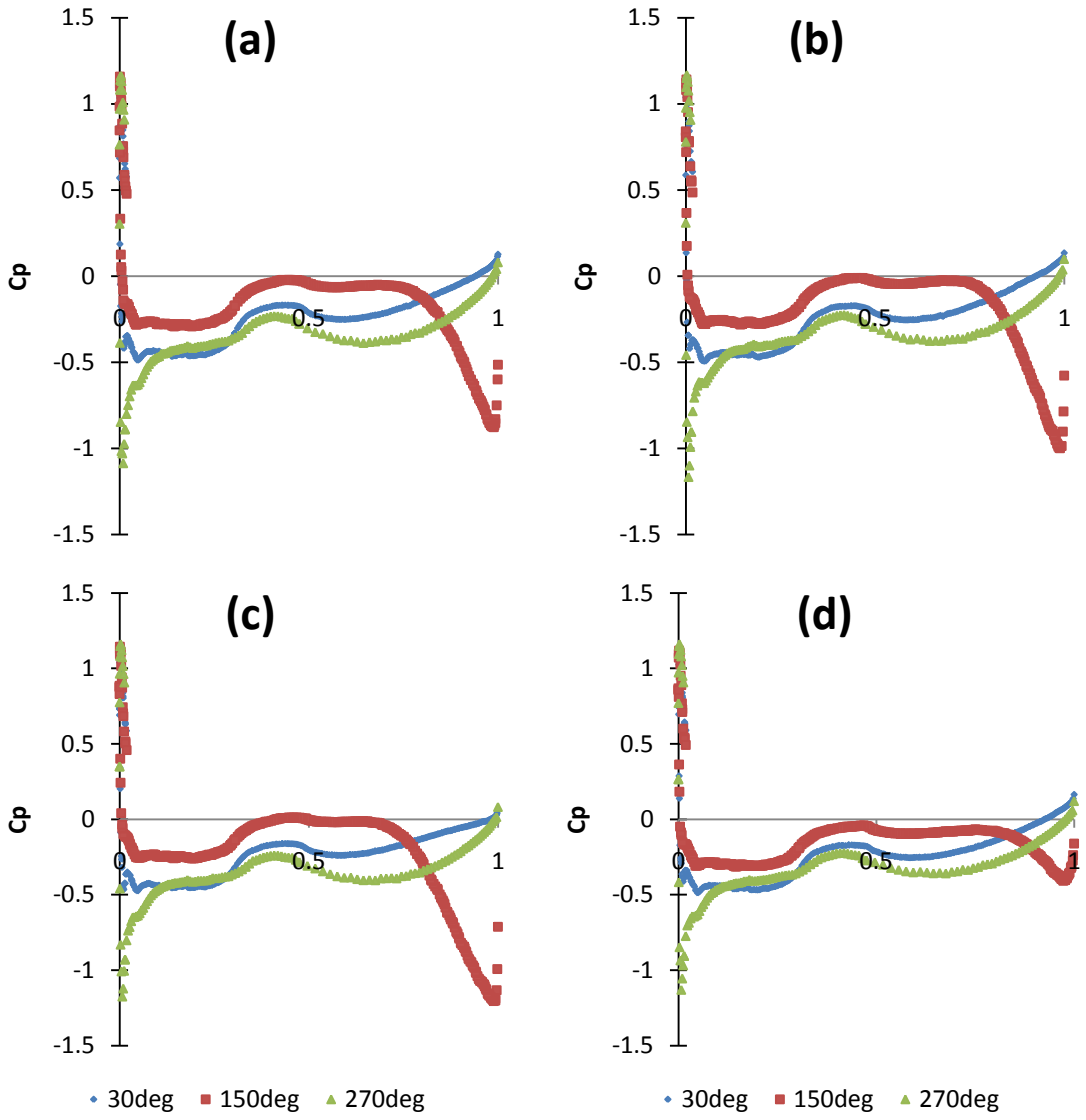

Figure 7.11 Selected nacelle Cp distribution lines along the nacelle of four different simulations (a) h/D=0.6, x/l=0.75 (b) h/D=0.55, x/l=0.75 (c) h/D=0.6, x/l=0.7 (d) h/D=0.6, x/l=0.8

The next observation is that the distributions for the sections far from the wing (30º and 270º sections) remain almost unchanged and actually have a very similar distribution to the isolated nacelle (see Figure 6.24.) For the section of 150º which is the closest to the wing of the three analyzed, there is a fall of pressure close to the nozzle in all of the simulations. The pressure fall is different in each of the nacelle simulations.

Cp distributions of Figure 7.11 (a) and (b) are from the simulations with a constant axial position (x/l=0.75) and varying the vertical position (h/D=0.6 and 0.55). The change is very small, only 10% for the minimum Cp value (with respect of the values of Figure 7.11 (a)). On the other hand, by keeping the vertical position constant and varying the axial position, the changes are much larger. With a h/D=0.6, and changing x/l from 0.75

to 0.70 (moving the nacelle closer), the minimum value decreases 37.4% (see Figure 7.11(a) and (c)). Increasing x/l from 0.75 to 0.8 (moving the nacelle further away from the wing,) the minimum Cp value increases 53% (see Figure 7.11(a) and (d)).

By comparing the previous observations with the plots on Figure 7.8 and Figure 7.9 it can be concluded that the changes of the AB fall of the Cp due to the vertical positioning of the nacelle are very small and the axial position generates a much larger change. The magnitude depends on the distance of the nacelle to the wing therefore with the nacelle positioned far from the wing (large values of x) the pressure fall will be smaller; this effect generates a smaller suction force (smaller drag). The opposite is shown for the nacelle close to the wing where the pressure falls and the suction force is bigger and generates a bigger drag.

The flow speed around the nacelle is related to both parameters (x and h.) Each of the parameters has a different influence on the flow. In Figure 7.12 the profiles around the nacelle and the wing at the mid-section of the nacelle plane are shown. Figure 7.12 (a) and (b) show the simulations with the nacelle at the same vertical position (h/D=0.6) but different penetration. In Figure 7.12 (a) part of the nacelle is actually under the wing (x/l=0.7) and Figure 7.12 (b) is further from the wing (x/l=0.8).

Again the influence of the nacelle positioning over the wing is quite imperceptible for the FB and MB.

The nacelle with a positive penetration (Figure 7.12 (a)) creates a nozzle effect between the nacelle and the wing accelerating the free stream and the bypass stream to supersonic velocities. The zones with supersonic velocities are right under the wing between the nacelle and a big part of the bypass flow right after the nozzle.

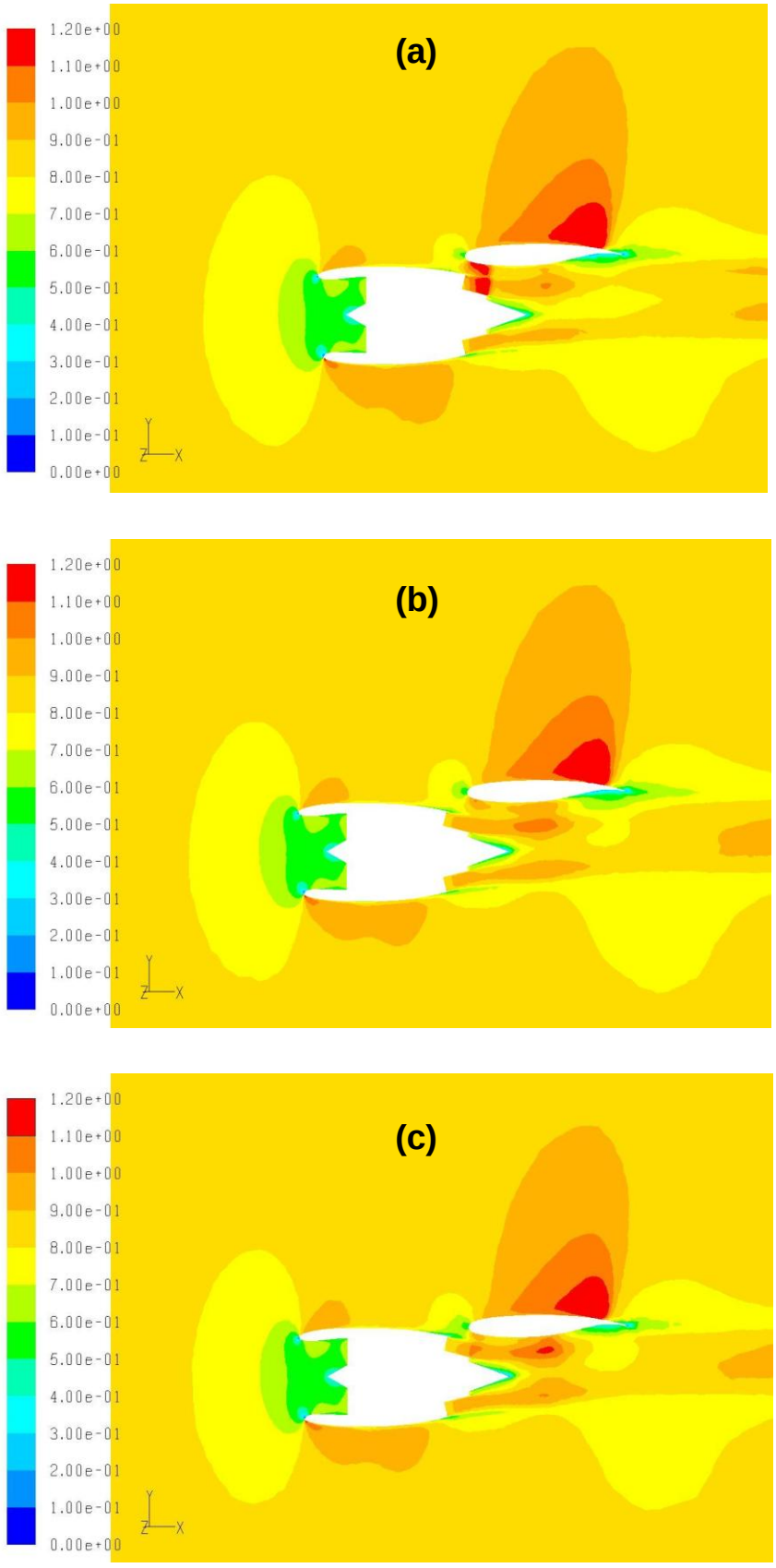

Figure 7.12 Mach number profiles for nacelles positioned at (a) h/D=0.6, x/l=0.7, (b) h/D=0.6, x/l=0.8 and (c) h/D=0.5, x/l=0.8

On the other hand, a nacelle positioned in front of the wing but far from it (see Figure 7.12 (c)) slows down the velocity of the free stream going between the nacelle and the wing, Mach number between 0.6 and 0.7 in the simulation. The flow accelerates by a small amount after the nacelle to keep the boundary layer attached to the wing. There is an increase of velocity in the bypass flow approaching supersonic velocities, but it is not as fast as the velocities for the nacelle positioned under the wing. Also, under the mid-section of the wing there is a small supersonic zone. This section is quite small and is because the free stream going under the wing enters with a large downwards velocity (to go around the nacelle positioned in front of the wing) and the flow must accelerate to follow the wing curvature.

The wing drag changes are quite unpredictable in the conditions analyzed. In Figure 7.13 the Cd changes in respect of the variations of each parameter is shown. In the figure the following can be observed:

- With the vertical distance of 0.65 the drag changes vary from +3.5% to -3.5% (approximate values) when the axial position is varied from 0.65 to 0.7.
- The wing drag for x/l of 0.7 and vertical distance of 0.65 and 0.6 remains almost unchanged. As the vertical distance decreases there is a very slight increase of drag.
- With the data available, a trend is observed of a drag increase when the x/l is increased.
- Decreasing the vertical distance between the engine and the wing produces a drag raise on the wing.

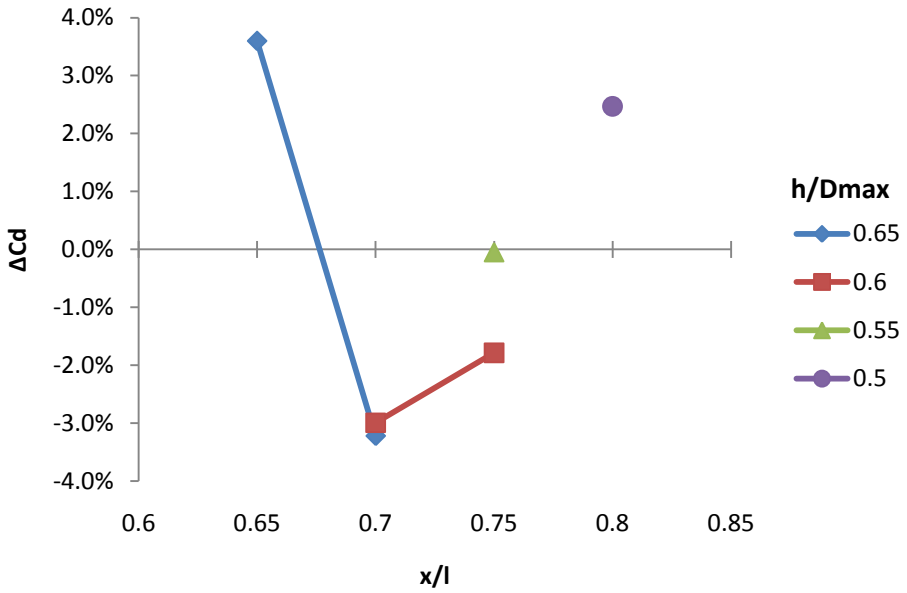

Figure 7.13 Impact of penetration and vertical positioning on wing drag

To analyze the behaviour of the drag on the wing the Cp distribution along three sections of the wing were measured (see Figure 7.14.) The plots of Figure 7.16 are labelled as "in" and "out" referring to the two sections closest to the engine. "In" is the section between the engine and the fuselage and "out" is the section on the other side of the engine. The section at w/Dmax = 6.3 is labelled "far". The far plots are not shown because there is no relevant influence of the parameters studied at that point of the wing (the figures for the far section can be found in Appendix C).

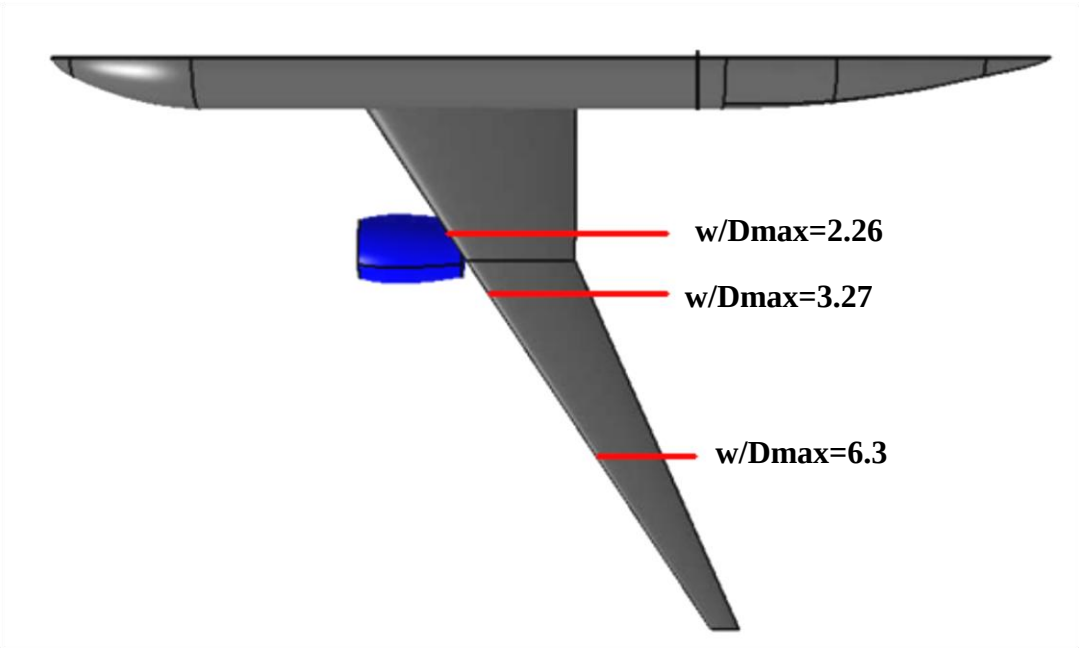

Figure 7.14 Wing Sections analyzed (not drawn to scale)

In Figure 7.15 the sections close to the wing are analyzed for three selected simulations. Keeping the axial position constant at 0.75, Figure 7.15 (a-d), shows with a change in vertical position from 0.55 (a and b) to 0.6 (c and d) the inner section distributions remain in a very similar shape one to the other. There is a small change in the distribution near the leading edge for the outer section on the upper part of the wing (compare Figure 7.15 (b) and (d)). The change of pressure becomes smoother when the nacelle is positioned further from the wing.

With the vertical position kept constant the axial position, (Figure 7.15 (c-f)) the lower part of the wing of the inner section, the one closer to the engine, is varied. The Cp makes more exaggerated changes of the distribution when the nacelle is closer to the wing. Also the minimum value decreases.

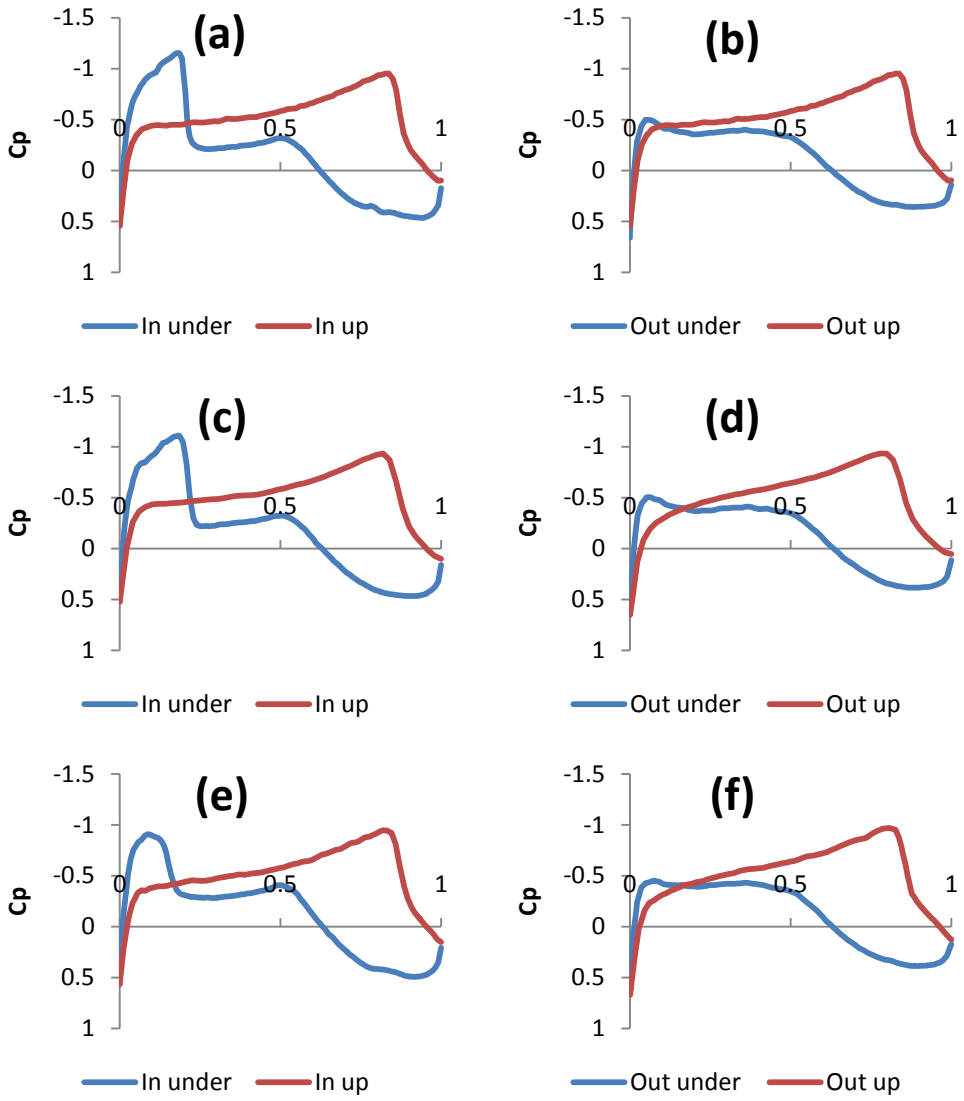

Figure 7.15 Three selected wing airfoil profiles. (a) and (b) h/D=0.55, x/l=0.75, (c) and (d) h/D=0.6, x/l=0.75 and (e) and (f) h/D=0.6, x/l=0.8

The most noticeable part of the wing analysis is the way the drag falls for the two simulations of h/D=0.65 when the axial positions changes from 0.65 to 0.70 (see Figure 7.13). The two simulations are the ones with the nacelle positioned at the furthest vertical distance (h/D=0.65) and with the biggest penetration under the wing (x/l=0.65 and 0.7). Comparing the pressure distributions (Figure 7.16), there is a difference in the curvature of the Cp distribution under the wing in Figure 7.16 (a). The distribution appears to be flatter than all of the other distributions for the downwind section of the wing. The reason for this could be the large supersonic zone between the nacelle and wing for the nacelle with the largest penetration. In Figure 7.17 (a) it can be seen that a larger zone actually reaches the supersonic zone of the bypass flow. This has an obvious impact on the pressure and generates the drag behaviour previously shown in Figure 7.13.

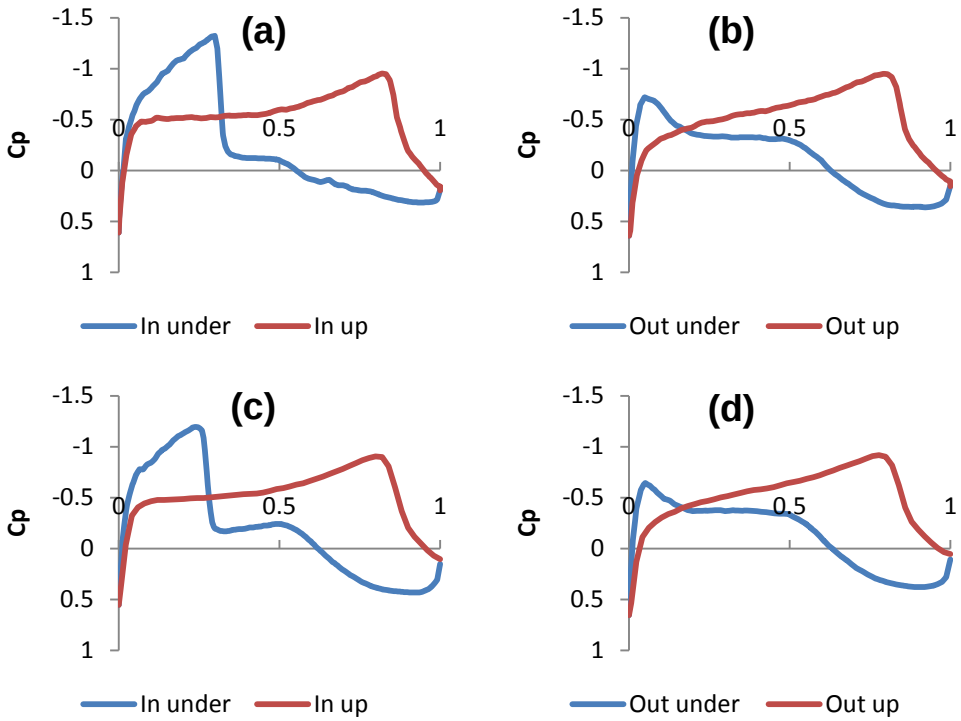

Figure 7.16 Airfoil Cp profiles. for the nacelle of (a) h/D=0.65, x/l=0.65, at w/Dmax=2.26 (b) h/D=0.65, x/l=0.65, at w/Dmax=3.27, (c) h/D=0.65, x/l=0.7, at w/Dmax=2.26 and (d) h/D=0.65, x/l=0.7, at w/Dmax=2.26.

Figure 7.17 Detailed profiles of Mach number for the simulations of (a) h/D=0.65, x/l=0.65 and (b) h/D=0.65, x/l=0.7

The interference drag is the extra drag produced by just the integration of the engine to the airframe. Although more data may be necessary to form solid conclusions about the influence of the positioning of the engine on the interference drag, some observations are possible out of Figure 7.18 made with the data available.

- Interference drag decreases as the engine is positioned further from the wing in a vertical direction (h increasing).
- Decreasing the penetration (x increasing) will produce a reduction on the interaction drag.
- There seems to be a point where the interaction drag changes are very small. Keeping the vertical distance at the maximum value (h/Dmax = 0.65) in the

simulations with the biggest penetration values (x/l = 0.65 and 0.7) the drag values are apparently unchanged; actually both seem to be very similar to the base value (Drag change of nearly 0%).

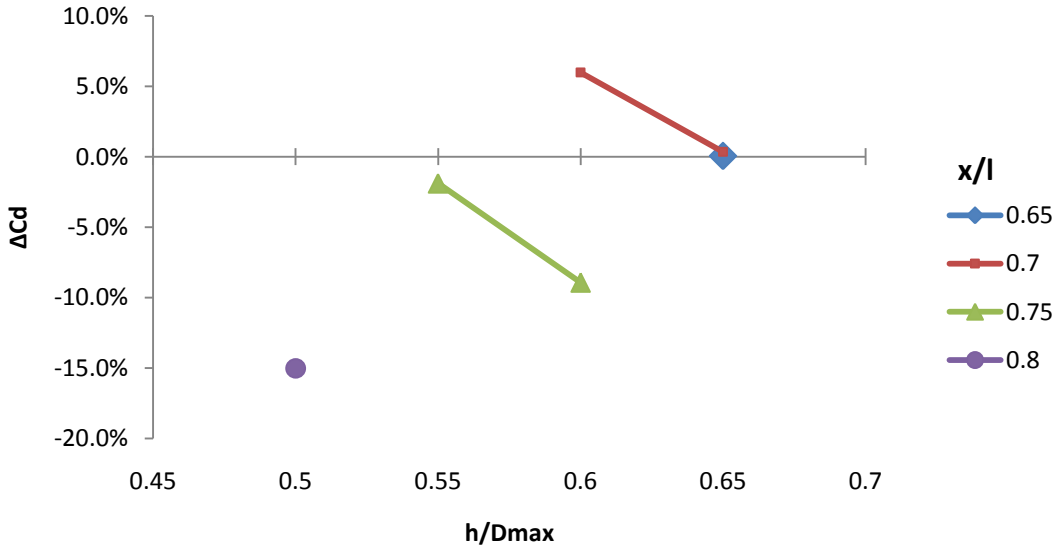

Figure 7.18 Impact of penetration and vertical positioning on interference drag.

8 Final Observations

The engine/airframe interaction is very important for the overall performance of the aircraft. The integration of the engine and airframe needs special care because the knowledge of several disciplines of the aeronautic area are required. As a global task, integration has to be tackled by a working group in order to discuss the pros and cons of the different design options seen from several points of view involved in the task. In this project only aerodynamics were considered, and even in the aerodynamics area more aspects could have been considered. Other issues like structure, propulsion, safety and others must be considered to optimize the integration of the optimum engine to an optimum airframe, and therefore obtain the optimum aircraft.

Calculation of drag is a very important parameter for aircraft design. It has a strong influence on the performance of the engine and the aircraft. To improve the overall performance of the aircraft proper calculations on drag must be made. The engine has to be integrated to the airframe considering how the interaction between airframe and engine must be minimized to improve the performance of the airplane. Pressure distributions on the wings might change due to the integration of the engine, this change must be as small as possible.

Experimental or CFD methods can be used to calculate the drag produced by the engines. The main issue of drag calculation is force bookkeeping. By the proper force bookkeeping the drag of GTE is calculated with a different methodology from that of the airframe.

The main benefit of the use of CFD over experimental methods is the lower cost. If proper computational resources are available, time cost is considerably reduced. Proper computational resources are required for good CFD results. Many of the main issues of CFD involve the use of computational resources available. The speed of the simulation will depend mainly on the size of the mesh and computer power to solve the simulation. The accuracy is also linked to the mesh size therefore the speed and accuracy have to be balanced to determine the final size of the mesh. The solver and models used also would have a big impact on the time required for a simulation to converge.

The final and probably most important observation is that validation is the most important requirement for a CFD task to be undertaken. Validation is the comparison of

experimental with computational data that will turn the latter into real. Without proper validation CFD results are approximations of what would happen in real life. A proper validation process is required for CFD results to be considered no matter how accurate they could be[11].

[11] There were not enough resources in this project to do proper validation.

9 Conclusions

Out of the work done during the project and the analysis of the results the following conclusions were taken:

- The methodology used for a parametric analysis of drag proved to be suitable based on the results obtained. The results obtained allowed important conclusions to be made that will enable the knowledge of engine/airframe interaction to progress. Future work based on the same methodology would allow more CFD results to be obtained in order to calculate mathematical approximations of drag generation of an installed VHBR engine for further applications.
- The Dmax has a great impact on both the AB and FB individually (see section 5). There is also a significant change on the MB drag, but mostly because of the change of the wet surface area. Although there is a big impact on the AB and FB, the changes are opposite to each other and cancel out in most of them as can be seen in Figure 6.13.

The Dmax changes the smoothness of the pressure changes. A Dmax similar to the Dhigh generates large changes of velocity and therefore will increase the spillage drag and may create shockwaves decreasing the pulling force of the FB (see Figure 6.8 and Figure 6.9). For the geometry and the range of values analyzed the total change of drag is very small although the change of drag on the AB and FB is quite significant.

- Highlight diameter has a high impact mostly on the FB and in the pre-entry drag. There is some influence on MB but it is very small. Pre-entry drag depends mostly on the Dhigh. Spillage drag is more dependant of the Dhigh than Dmax (see section 5.8). Something similar to the Dmax would happen with the changes of Dhigh. A Dhigh close to the Dmax will generate sudden velocity changes and could generate shockwaves increasing the drag.

The results of the simulations show how there is a critical point for the total force mainly determined by the changes of the forces on the FB and the velocity shockwaves for large Dhigh values (Figure 6.20).

- The big diameter of a VHBR engine makes the length of the nacelle lose the importance in the drag generation. The main impact of nacelle length on the drag generation of an engine of this size is on the interaction of the FB and AB. With a longer nacelle there is a lower pressure between the FB and AB and the airflow velocity over the FB decreases producing a lower suction force at that section of the nacelle.

Certainly the viscous drag increases with an increase of the nacelle MB length (and the overall length) but the total drag increase is not only because of the viscous drag but it is mainly because of the fall of the pulling force over the FB produced by the higher stream velocity around that section (see section 6.4.3.)

- The position of the engine makes forces on the nacelle and the wing vary drastically. The pressure changes make the total drag change by a large amount. Pressure distribution on the surfaces between the wing and the nacelle increases from the values of isolated nacelle and WB system. Drag changes according to the penetration of the nacelle. The different positions of the engine will determine the amount of pressure change and position of the force applied. Wing clearance is also important for the aerodynamics of the airplane but it is not very relevant to the drag generation, as can be seen in Figure 7.8. For the range of values of penetration and wing clearance considered in this project the only parameter having an impact on drag is penetration.

Wing clearance certainly has an impact on the drag but is not generated directly. The wing clearance changes the pressure distribution over the wing. The change of pressure would require a different angle of attack of the wings to compensate the loss of lift force. Interaction drag increases.

10 Further work

As a result of the work undertaken in this project and there are several tasks that could be embarked on.

- The most important work that should be done regarding this project is the validation of the results shown. For every kind of FEM simulation a validation of the results must be done in order to give the results more credibility. The validation for the CFD results shown could be done by the experimentation in a wind tunnel with scaled models. Measuring pressure, velocity and determining flight paths are good validation methods. Other validation methods are possible like real scale wind tunnel testing or in-flight testing.
- By using more powerful computational resources more extensive and accurate analysis can be made. Some of the analyses possible are mentioned below.
- A very important task is the analysis of the drag generated by a pylon for a VHBR engine. Positioning the engine was a big part of this project and positioning the engine considering a pylon should be a very important part of another project. The addition of pylons would not only require analyzing the positioning of the engine but also aspects like the shape of the pylon and its effect on the overall performance of the engine. Other types of analysis concerning the pylon aerodynamics and the interaction with the engine and wing are possible.
- The positioning of the engine with respect of the wing analysis can be a more extensive one. Parameters like the engine angle of attack, tilt angle, spanwise positioning, and other parameters already mentioned in section 7 could be included. Variations on the airframe geometry could be also included in future research. Also the effect on drag of control devices, flaps and slats are some areas where the research of the integration of novel engines can be included.
- Drag of other types of integration could be analyzed. For an engine of the size of a VHBR turbofan other options might be useful. Embedded, overwing or body mounted engines are some of the options that could be included in future research. The results should be compared in order to use the best option.
- The modelling of the drag produced by nacelle geometry and its integration to the airframe can be done by making a more extensive analysis for each of the parameters included in this project. The methodology developed in this project used in a more

extensive way would help to generate more data. Also more parameters and combinations can be analyzed.

- By creating drag models of VHBR engines and their integration to the airplane, these models can be used in optimization methods for future engine designs.
- The CFD simulations can be run with different models or solvers in order to evaluate their suitability for the geometry and conditions used.
- It would be important to generate sufficient information that would enable mathematical models of relationships between drag and nacelle geometry and positions in relationship to the wing, etc.

11 References

Fluent 6.2 documentation 2007-. Available: http://intranet.cranfield.ac.uk/cww/ccdocs/documentation/fluent/fluent6.2/ [06/2009, 2009].

Designing high-bypass nacelle inlets. 2005. Aerospace Engineering, 25(6), pp. 14-16.

NACA 1-series geometry representation for computational fluid dynamics. 1994.

Practical intake aerodynamic design. 1993. Washington, DC/Oxford, United Kingdom, American Institute of Aeronautics and Astronautics, Inc./Blackwell Scientific Publications.

The Jet Engine. 1986. 4th edition. Derby: Rolls-Royce.

Report of the Definitions Panel on Definitions to be Used in the Description and Analysis on Drag. 1958. ARC CP-369. London, UK: Aeronautical Research Council.

Report of the Definitions Panel on the Definitions of the Thrust of a Jet Engine and of the Internal Drag of a Ducted Body. 1955. ARC CP-190. London, UK: Aeronautical Research Council.

AIMER, B., 2005. *Gas Turbine Intake Design - Peak Mach Number Response to Changes of Intake Lip Shape*, (Unpublished MSc thesis), Cranfield University, Cranfield.

ALBERS, J.A., MILLER, B.A. and NATIONAL AERONAUTICS AND SPACE ADMINISTRATION. LEWIS RESEARCH CENTER, Cleveland, OH, 1973. *Effect of subsonic inlet lip geometry on predicted surface and flow Mach number distributions*. NASA-TN-D-7446; E-7522; Pagination 56P.

ANDERSON, B., 1988. *CFD application to subsonic inlet airframe integration*, VKI, Intake Aerodynamics, Volume 2 59 p (SEE N89-16748 09-02); United States, 1988.

ANDERSON, B., GIBB, J. and NATIONAL AERONAUTICS AND SPACE ADMINISTRATION. LEWIS RESEARCH CENTER, Cleveland, OH., 1992. *Application of computational fluid dynamics to the study of vortex flow control for the management of inlet distortion*, United States, 1992, .

ANDERSON, B.H. and TOWNE, C.E., 1993. *Application of computational fluid dynamics to inlets. Practical intake aerodynamic design* (A95-18876 03-02), Washington, DC/Oxford, Inc./Blackwell Scientific Publications, pp. 395-430.

ANDERSON,J. D. JR., 1995. *Computational fluid dynamics - The basics with applications*. Inc.: New York: McGraw-Hill.

ANDREW, T.L., YATES, D.E., CRUM, T.S., STOCKMAN, N.O. and LATAPY, M.O., 1993. *High speed test results of subsonic, turbofan scarf inlets*, AIAA, SAE, ASME, and ASEE, Joint Propulsion Conference and Exhibit, 29th, Monterey, CA; United States; 28-

30 June 1993; AIAA, SAE, ASME, and ASEE, Joint Propulsion Conference and Exhibit, 29th, Monterey, CA, 28-30 June 1993 1993, pp13.

ANTOINE, N.E. and KROO, I.M., 2002. *Optimizing Aircraft and Operations for Minimum Noise.* AIAA Paper, 5868, pp. 1-3.

BALKOTA, N., 2005. *Gas Turbine Intake Design - Quality Evaluation of Axisymmetric Intake Flow CFD Simulations*, (Unpublished MSc thesis), Cranfield University, Cranfield.

BELL, R.A. and CEDAR, R.D., 1991. *An inverse method for the aerodynamic design of three-dimensional aircraft engine nacelles*, In Pennsylvania State University, Third International Conference on Inverse Design Concepts and Optimization in Engineering Sciences (ICIDES-3) p 405-417 (SEE N92-13928 05-01); United States.

BENSON, T. J., 1988. *CFD application to supersonic/hypersonic inlet airframe integration*, VKI, Intake Aerodynamics, Volume 2 62 p (SEE N89-16748 09-02); United States, 1988.

BERRY, D.L., 1994. *The Boeing 777 engine/aircraft integration aerodynamic design process, ICAS*, Congress, 19th, Anaheim, CA, Proceedings. Vol. 2; 18-23 Sept. 1994, Washington. United States.

BOPPE, C.W., 1984. *Elements of computational engine-airframe integration, American Institute of Aeronautics and Astronautics*, Aerospace Sciences Meeting, 22nd, Reno, NV, Research supported by the Grumman Aerospace; 9-12 Jan. 1984

BORE, C.L., 1993. *Some contributions to propulsion theory - The Stream Force Theorem and applications to propulsion*. Aeronautical Journal, 97(964), pp. 138-144.

BRODERSEN, O., 2003. *Numerical Analysis of Aerodynamic Airframe-Engine Installation Effects for Transport Aircraft*.

BURGSMUELLER, W. and HOHEISEL, H., 2000. ENIFAIR- EU *research into engine integration on future transport aircraft*. Air & Space Europe, 2(2), pp. 81-85.

BURGSMUELLER, W., HOHEISEL, H. and DE LA PUERTA, B., 1996. *European research cooperation on jet engine airframe integration, aspects of engine airframe integration for transport aircraft; Proceedings of the DLR Workshop*, Braunschweig, Germany; 6-7 Mar. 1996; Cologne pp6-1 to 6-26.

BURGSMUELLER, W., HOHEISEL, H. and KOOI, J.W., 1994. *Engine/airframe interference on transport aircraft with ducted propfans - The European research program* Duprin, ICAS, Congress, 19th, Anaheim, CA, Proceedings. Vol. 3; United States; 18-23 Sept. 1994.

CAMPBELL, R.L., CARTER, M.B., PENDERGRAFT, O.C., FRIEDMAN, D.M. and SERRANO, L., 2005. *Design and Testing of a Blended Wing Body with Boundary Layer Ingestion Nacelles at High Reynolds Numbers(Invited).* 43rd AIAA Aerospace Sciences Meeting and Exhibit; Reno, NV; USA; 10-13 Jan. 2005. 11 pp.

CEDAR, R.D., DIETRICH, D.A. and OSTRANDER, M.J., 1993. *Engine/airframe installation CFD for commercial transports - An engine manufacturer's perspective*, SAE, Aerotech '93 Conference, Costa Mesa, CA; United States; 27-30 Sept. 1993.

CHANG, I. and RAJAGOPALAN, R.G. 2003, *CFD analysis for ducted fans with validation*. 21st AIAA Applied Aerodynamics Conference; Orlando, FL, United States; June 23-26, 2003.

CHEN, A.W., CURTIN, M.M., CARLSON, R.B. and TINOCO, E.N., 1989. *TRANAIR applications to engine/airframe integration*, AIAA Applied Aerodynamics Conference, 7th, Seattle, WA; United States; 31 July-2 Aug. 1989; pp53-58.

COHEN, H., ROGERS, G.F.C. and SARAVANAMUTTOO, H.I.H., 1987. *Gas turbine theory*. Third edition . Essex, England: Longman Scientific & Technical.

COLMENARES, J., GOMEZ, J., PASCOVICI, D. and OGAJI, S., 2007. *A preliminary feasibility study for future aero engines*. ISABE 2007-1194.

COVERT, E.E.,E.D., 1985. *Thrust and drag: Its prediction and verification*. New York, AIAA, Progress in Astronautics and Aeronautics. Volume 98, 1985.

CRUM, T.S., YATES, D.E., ANDREW, T.L. and STOCKMAN, N.O., 1993. *Low speed test results of subsonic, turbofan scarf inlets,* AIAA, SAE, ASME, and ASEE, Joint Propulsion Conference and Exhibit, 29th, Monterey, CA; United States; 28-30 June 1993, pp11.

DEVINE, R., CRAWFORD, B., BENARD, E., COOPER, R. and RAGHUNATHAN, S., 2004. *A Computational Investigation of Propulsion Integration*, AIAA 4th Aviation Technology, Integration and Operations (ATIO) Forum; Chicago, IL; USA; 20-22 Sept. 2004; pp1-7.

DITTMAR, J.H., GLIEBE, P.R. and JANARDAN, B.A., *Ultra-High Bypass Engine Aeroacoustic Study*. E-14087.

EASTWOOD, S., TUCKER, P., XIA, H., CARPENTER, P. and DUNKLEY, P., 2008. *Comparison of LES to LDA and PIV Measurements of a Small Scale High Speed Coflowing Jet.* 14th AIAA/CEAS Aeroacoustics Conference (29th AIAA Aeroacoustics Conference). 2008

EGGLESTON, B., 1985. *Some considerations in propeller and airframe integration, In AGARD Aerodyn. and Acoustics of Propellers* 11 p (SEE N86-11147 02-01); INTERNATIONAL ORGANIZATION; 1985.

FIELDING, J.P., 1999. *Introduction to aircraft design*, United Kingdom and New York: Cambridge University Press (Cambridge Aerospace Series, No. 11): Cambridge.

GODARD, J.L., HOHEISEL, H., ROSSOW, C.C. and SCHMITT, V., 1996. *Investigation of the interference effects for different engine positions on a transport aircraft configuration, Aspects of engine airframe integration for transport aircraft*;

Proceedings of the DLR Workshop, Braunschweig; Germany; 6-7 Mar. 1996; Cologne pp11-1 to 11-22.

GOMEZ-PARADA, J., 2007. *Modelling of the performance of a VHBR engine to assess thrust losses from engine/airframe integration*. PhD Student, 9th Month Review . Cranfield University, UK. (Unpublished).

GOMEZ, J., COLMENARES, F., SAVILL, M., OGAJI, S. and SINGH, R. 2009. *CFD calculations of drag sensitivity to VHBR engine nacelle geometry*. 19th ISABE Conference, Montreal, Can., September 7-11, 2009. ISABE 2009-1348. (Unpublished).

GREFF, E., BECKER, K., KARWIN, M. and RILL, S., 1993. *Integration of high bypass ratio engines on modern transonic wings for regional aircraft,* Aeronautical Journal. 1993

HALL, C.A. and HYNES, T.P., 2005. *Nacelle Interaction with Natural Wind Before Takeoff*. Journal of Propulsion and Power, 21(5), pp. 784-791.

HILBIG, R., KLEVENHUSEN, K., KRENZ, G. and SMYTH, R., 1980. *Application of advanced technology for improving the integration of engine and airframe for future transport aircraft*, International Council of the Aeronautical Sciences, Congress, 11th, Lisbon, Portugal; International Organization; 10-16 Sept. 1980, Cologne.

HOHEISEL, H., 1997. *Aerodynamic aspects of engine-aircraft integration of transport aircraft*. Aerospace Science and Technology (0034-1223), 1(7), pp. 475-487.

HOHEISEL, H., *Investigations on the aerodynamic interference effects of wing-mounted advanced engines - Analysis of high speed test results*. Cologne, 51170, Germany: Deutsches Zentrum fuer Luft- und Raumfahrt e.V.

HOHEISEL, H., KIOCK, R., ROSSOW, C.C., RONZHEIMER, A. and BAUMERT, W., 1990. *Aspects of theoretical and experimental investigations on airframe /engine integration problems*, ICAS, Congress, 17th, Stockholm, Sweden, Proceedings. Vol. 2; United States; 9-14 Sept. 1990.

HUGHES, P.F. and MCDONALD, H., 1965. *A correlation of high subsonic afterbody drag in the presence of a propulsive jet or support sting (Afterbody contribution to fuselage form drag at subsonic speeds in presence of propulsive jet, support sting or blunt base predicted by correlation method)*. Journal of Aircraft, 2, pp. 202-207.

HUMPHRIES, P., GILLAN, M. and RAGHUNATHAN, S., 1998. *A study of isolated nacelle flows at subsonic and transonic speeds,* AIAA, Aerospace Sciences Meeting & Exhibit, 36th, Reno, NV; United States; 12-15 Jan. 1998.

JOUBERT, H. and GOUTINES, M., 1993. *Use of CFD methods to design engine nacelles*, ASME, International Gas Turbine and Aeroengine Congress and Exposition, Cincinnati, OH; United States; 24-27 May 1993.

JOUBERT, H. and LECORDIX, J.L., 1996. *Engine/nacelle/aircraft integration - The engine and nacelle designer's viewpoint, aspects of engine airframe integration for*

transport aircraft; Proceedings of the DLR Workshop, Braunschweig; GERMANY; 6-7 Mar. 1996; Aspects of engine airframe integration for transport aircraft, 6-7 Mar. 1996 1996, Cologne pp5-1 to 5-15.

KEITH, B.D., UENISHI, K. and DIETRICH, D.A., 1993. *CFD-Based Three-Dimensional Turbofan Exhaust Nozzle Analysis System.* Journal of Propulsion and Power, 9(6), pp. 840-846.

KERN, P.R.A., PAYNTER, G.C., DVORAK, F.A. and CLARK, D.R., 1984. *A review of the status of the application of computational fluid dynamics (CFD) to the installation/integration of turbofans and turboprops in subsonic aircraft,* AIAA, SAE, and ASME, Joint Propulsion Conference, 20th, Cincinnati, OH; United States; 11-13 June 1984.

KOC, S., KIM, H. and NAKAHASHI, K., 2005. *Aerodynamic Design of Wing-Body-Nacelle-Pylon Configuration*, 17th AIAA Computational Flow Dynamics Conference; Toronto, Ontario; Canada; 6-9 June 2005; pp1-13.

KOESTER, H., ROHARDT, C.-., HORSTMANN, K.-. and RADESPIEL, R., 1990. *Aerodynamic design techniques at DLR Institute for Design Aerodynamics*, In AGARD, Computational Methods for Aerodynamic Design (Inverse) and Optimization 15 p (SEE N90-20976 14-05); INTERNATIONAL ORGANIZATION; 1990.

KOFF, B.L., 2004. Gas turbine technology evolution - A designer's perspective. Journal of Propulsion and Power, 20(4), pp. 577-595.

LAFIN, K.R., VASSBERG, J.C., WAHLS, R.A., MORRISON, J.H., BRODERSEN, O., RAKOWITZ, M., TINOCO, E.N. and GODARD, J., 2004. *Summary of data from the second AIAA CFD Drag Prediction Workshop (invited).* 42nd AIAA Aerospace Sciences Meeting and Exhibit; Reno, NV; Jan. 5-8, 2004.

LECORDIX, J., GIPPET , J. and DUPARCQ, J., 1992. *Design of an advanced nacelle for a very high bypass ratio engine.* Aeronautical Journal, .

LEWERENZ, W., 1987. *UHB demonstrator flight test program*, AIAA, SAE, ASME, and ASEE, Joint Propulsion Conference, 23rd, San Diego, CA; United States; 29 June-2 July 1987, 1987, .

LI, J., LI, F., E, Q., LIU, J. and QIAO, C., 2000. *CFD applications to airframe/propulsion integration for civil aircraft*, Fluids 2000 Conference and Exhibit, Denver, CO; United States; 19-22 June 2000.

LYNCH, F.T. and INTEMANN, G.A., 1994. *The modern role of CFD in addressing airframe/engine integration issues for subsonic transports*, ICAS, Congress, 19th, Anaheim, CA, Proceedings. Vol. 2; United States; 18-23 Sept. 1994; Washington pp1294-1304.

MAKINO, Y., IWAMIYA, T. and LEI, Z., 2001. *Fuselage shape optimization of a wing-body configuration with nacelles,* AIAA Applied Aerodynamics Conference, 19th, Anaheim, CA; United States; 11-14 June 2001.

MARX, J., 1989. *Installation features of advanced, very high bypass turbofan propulsion systems*, AIAA, AHS, and ASEE, Aircraft Design, Systems and Operations Conference, Seattle, WA; United States; 31 July-2 Aug. 1989, pp7.

MATTINGLY, J.D., HEISER, W.H. and DALEY, D.H., 2002. *Aircraft engine design*. Second Edition . AIAA, Education Series.

MORRISON, J.H. and HEMSCH, M.J., 2007. *Statistical Analysis of CFD Solutions from the Third AIAA Drag Prediction Workshop (Invited)*, 45th AIAA Aerospace Sciences Meeting and Exhibit; Reno, NV; USA; 8-11 Jan. 2007.

MULLENDER, A.J. and POLL, D.I.A., 1996. *Engine nacelle aerodynamics*. Aerospace Engineering (Warrendale, Pennsylvania), pp. 17-20.

OLIVEIRA, G.L., PUPPIN-MACEDO, A. and TRAPP, L.G., 2002. *Integration methodology for regional jet aircraft with underwing engines*. AIAA Paper 2003-0934.

PAN, F.L. and COUPLAND, J., 2005. *An Integrated Optimization System for Low Noise Nacelle Design*, 11th AIAA/CEAS Aeroacoustics Conference (26th Aeroacoustics Conference); Monterey, CA; USA; 23-25 May 2005 pp1-16.

PATE, L., LECORDIX, J.L. and DESSALE, B., 1995. *CFD tools for designing isolated and installed nacelles*, AIAA, ASME, SAE, and ASEE, Joint Propulsion Conference and Exhibit, 31st, San Diego, CA; United States; 10-12 July 1995.

PAYNTER, G.C., FORESTER, C.K. and TJONNELAND, E., 1987. *CFD for engine-airframe integration*. Transactions of the ASME. Journal of Engineering for Gas Turbines and, 109(2), pp. 132-141.

RAYMER, D.P., 1999. *Aircraft design: A conceptual approach (3rd revised and enlarged edition)*. VA: American Institute of Aeronautics and Astronautics, Inc.: Reston.

RONZHEIMER, A., RUDNIK, R., BRODERSEN, O. and ROSSOW, C., 1996. *Interference phenomena of upper-wing-mounted engines, Aspects of engine airframe integration for transport aircraft;* Proceedings of the DLR Workshop, Braunschweig; GERMANY; 6-7 Mar. 1996; Cologne pp12-1 to 12-14.

ROSEN, R. and FACEY, J., 1987. *Civil propulsion technology for the next twenty-five years*, International Symposium on Air Breathing Engines, 8th, Cincinnati, OH; United States; 14-19 June 1987.

ROSSOW, C., GODARD, J., HOHEISEL, H. and SCHMITT, V., 1992. *Investigations of propulsion integration interference effects on a transport aircraft configuration*, AIAA, SAE, ASME, and ASEE, Joint Propulsion Conference and Exhibit, 28th, Nashville, TN; United States; 6-8 July 1992.

ROSSOW, C. and HOHEISEL, H., 1994. *Numerical study of interference effects of wing-mounted advanced engine concepts*, ICAS, Congress, 19th, Anaheim, CA, Proceedings. Vol. 2; United States; 18-23 Sept. 1994; pp1272-1282.

RUBBERT, P.E. and TINOCO, E.N., 1983. *The impact of computational aerodynamics on aircraft design,* American Institute of Aeronautics and Astronautics, Atmospheric Flight Mechanics Conference, Gatlinburg, TN; 15-17 Aug. 1983; pp9.

RUBINI, P., 2004. *CFD Notes, Thermal Power MSc Course*, Cranfield University. Lecture Notes. Cranfield, UK (unpublished).

RUDNIK, R., ROSSOW, C. and VGEYR, H.F., 2002. *Numerical simulation of engine/airframe integration for high-bypass engines.* Aerospace Science and Technology, 6(1), pp. 31-42.

SAITOH, T., KIM, H., TAKENAKA, K. and NAKAHASHI, K., 2006. *Multi-Point Design of Wing-Body-Nacelle-Pylon Configuration,* 24th AIAA Applied Aerodynamics Conference; San Francisco, CA; USA; 5-8 June 2006.

SEDDON, J. and GOLDSMITH, E.L., 1985. *Intake aerodynamics*. First edition . U. K.: Collins Professional and Technical Books.

SKAVDAHL, H., ZIMBRICK, R.A., COLEHOUR, J.L. and SALLEE, G.P., 1988. *Very high bypass ratio engines for commercial transport propulsion*, ICAS, Congress, 16th, Jerusalem, Israel, Proceedings. Volume 2; United States; Aug. 28-Sept. 2 1988=], Washington.

SMITH, C.F. and CROSSLEY, W.A., 2000. *Investigating response surface approaches for drag optimization of a subsonic turbofan nacelle,* AIAA/USAF/NASA/ISSMO Symposium on Multidisciplinary Analysis and Optimization, 8th, Long Beach, CA; United States; 6-8 Sept. 2000.

SOKHEY, J.S., 1990. *Analysis of installed wind tunnel test results on large bypass ratio engine/nacelle installations,* AIAA, SAE, ASME, and ASEE, Joint Propulsion Conference, 26th, Orlando, FL; United States; 16-18 July 1990, pp10.

THOMAS, R.H., 2003. *Aeroacoustics of Propulsion Airframe Integration: Overview of NASA's Research*. Noise Con Paper, 105, pp. 23-25.

TINOCO, E.N., 2001. *An assessment of CFD prediction of drag and other longitudinal characteristics,* AIAA, Aerospace Sciences Meeting and Exhibit, 39th, Reno, NV; United States; 8-11 Jan. 2001.

TINOCO, E. and BUSSOLETTI, J., 2002. *Minimizing CFD uncertainty for commercial aircraft applications,* 41st AIAA Aerospace Sciences Meeting & Exhibit, Reno, NV; United States; 6-9 Jan. 2003.

TOMITA, J.T., BRINGHENTI, C., POZZANI, D., BARBOSA, J.R., JESUS, A.B.D., ALMEIDA, O.D. and OLIVEIRA, G.L., 2005. *Overview on Nacelle Design, Proceedings of the COBEM*: 18th International Congress of Mechanical Engineering; Ouro Preto, Minas Gerais; Brazil; 6-11 Nov. 2005, Associacao Brasileira de Engenharia e Ciencias Mecanicas.

UENISHI, K., PEARSON, M.S., LEHNIG, T.R. and LEON, R.M., 1992. *Computational fluid dynamics based three-dimensional turbofan inlet/fan cowl analysis system*. Journal of Propulsion and Power, 8(1), pp. 175-183.

UENISHI, K., PEARSON, M.S., LEHNIG, T.R. and LEON, R.M., 1990. *CFD-based 3D turbofan nacelle design system*, AIAA, Applied Aerodynamics Conference, 8th, Portland, OR; United States; 20-22 Aug. 1990; pp19.

VON GEYR, H.F. and ROSSOW, C., 2005. *A Correct Thrust Determination Method for Turbine Powered Simulators in Wind Tunnel Testing*, 41st AIAA/ASME/SAE/ASEE Joint Propulsion Conference & Exhibit; Tucson, AZ; USA; 10-13 July 2005.

WILCOX, D.C., 1993. *Turbulence modeling for CFD*. CA: DCW Industries, Inc.: La Canada.

WILLIAMS, D., 2006. *Airframe Engine Integration*. Lecture Notes. Cranfield University: School of Engineering (Unpublished.)

WU, J., SANKAR, L.N. and KONDOR, S., 2004. *Numerical modeling of Coanda jet controlled nacelle configurations.* 42nd AIAA Aerospace Sciences Meeting and Exhibit; Reno, NV; Jan. 5-8, 2004.

YAMAMOTO, K., OCHI, A., SHIMA, E. and TAKAKI, R., 2004. *CFD sensitivity of drag prediciton on DLR-F6 configuration by structured method and unstructured method*. 42nd AIAA Aerospace Sciences Meeting and Exhibit; Reno, NV; Jan.5-8, 2004.

ZHAO, Y. and MORRIS, P.J., 2005. *The Prediction of Fan Exhaust Noise Propagation*, 11th AIAA/CEAS Aeroacoustics Conference (26th Aeroacoustics Conference); Monterey, CA; USA; 23-25 May 2005; pp1-16.

ZIMBRICK, R.A. and COLEHOUR, J.L., 1990. *Investigation of very high bypass ratio engines for subsonic transports.* Journal of Propulsion and Power, 6, pp. 3002.

12 Appendixes

A. Mach Number Contours of 3D Isolated Nacelle simulations

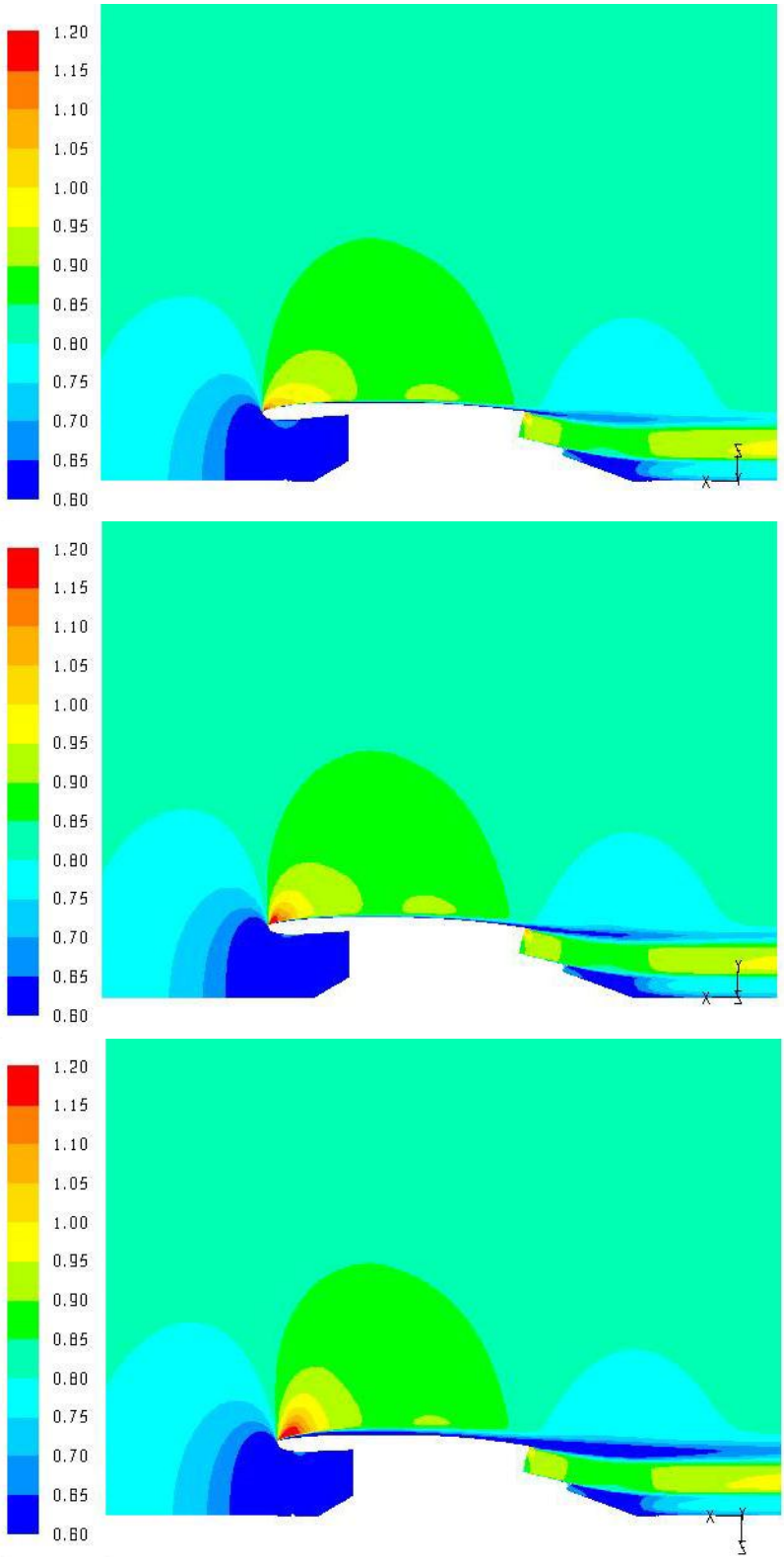

Figure A. 1 Mach number profiles of the Crown (top), Side (middle) and keel (bottom) sections of the nacelle of a Maximum diameter of - 6.0 % change with respect to the reference nacelle.

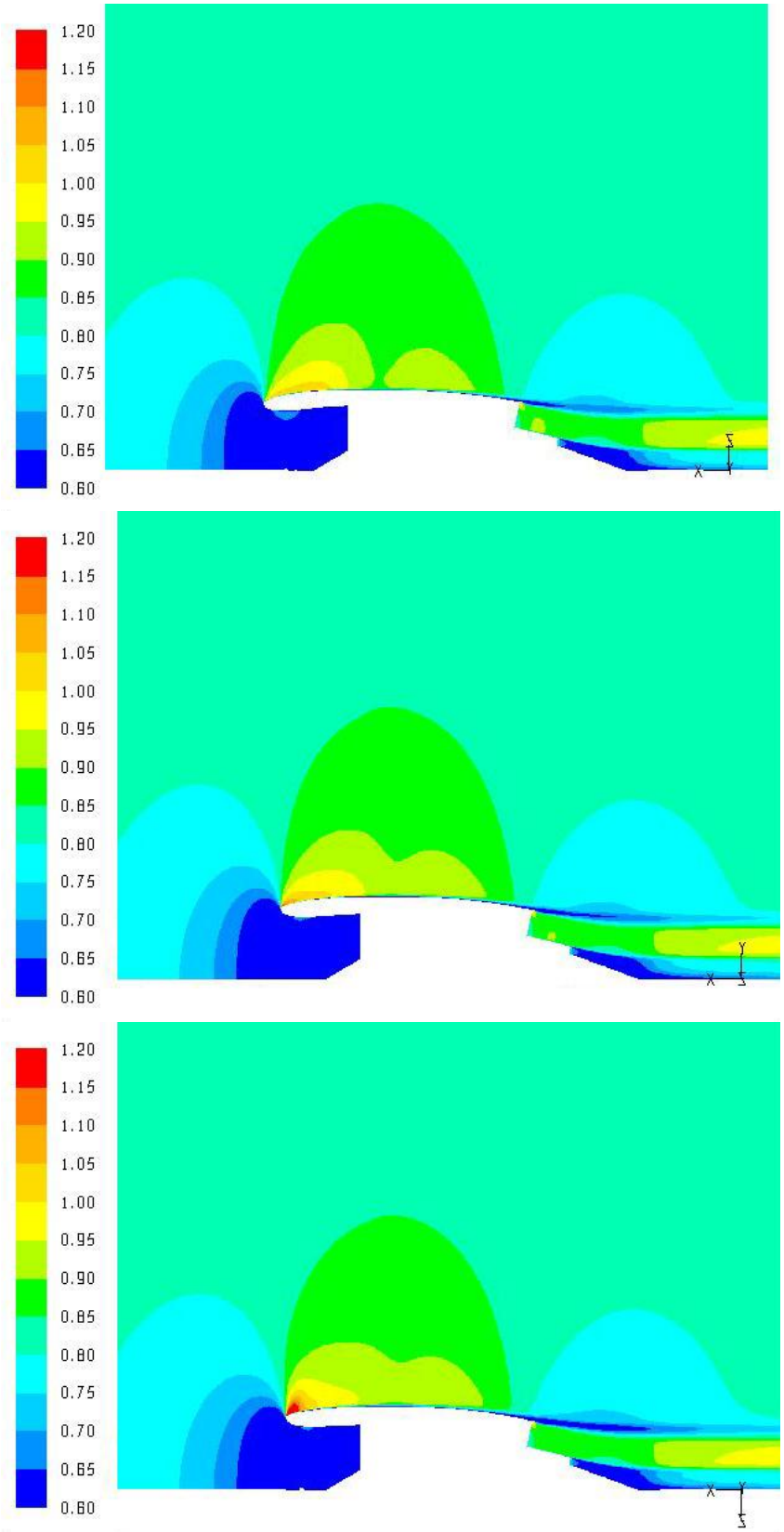

Figure A. 2 Mach number profiles of the Crown (top), Side (middle) and keel (bottom) sections of the nacelle of a Maximum diameter of - 2.0 % change with respect to the reference nacelle.

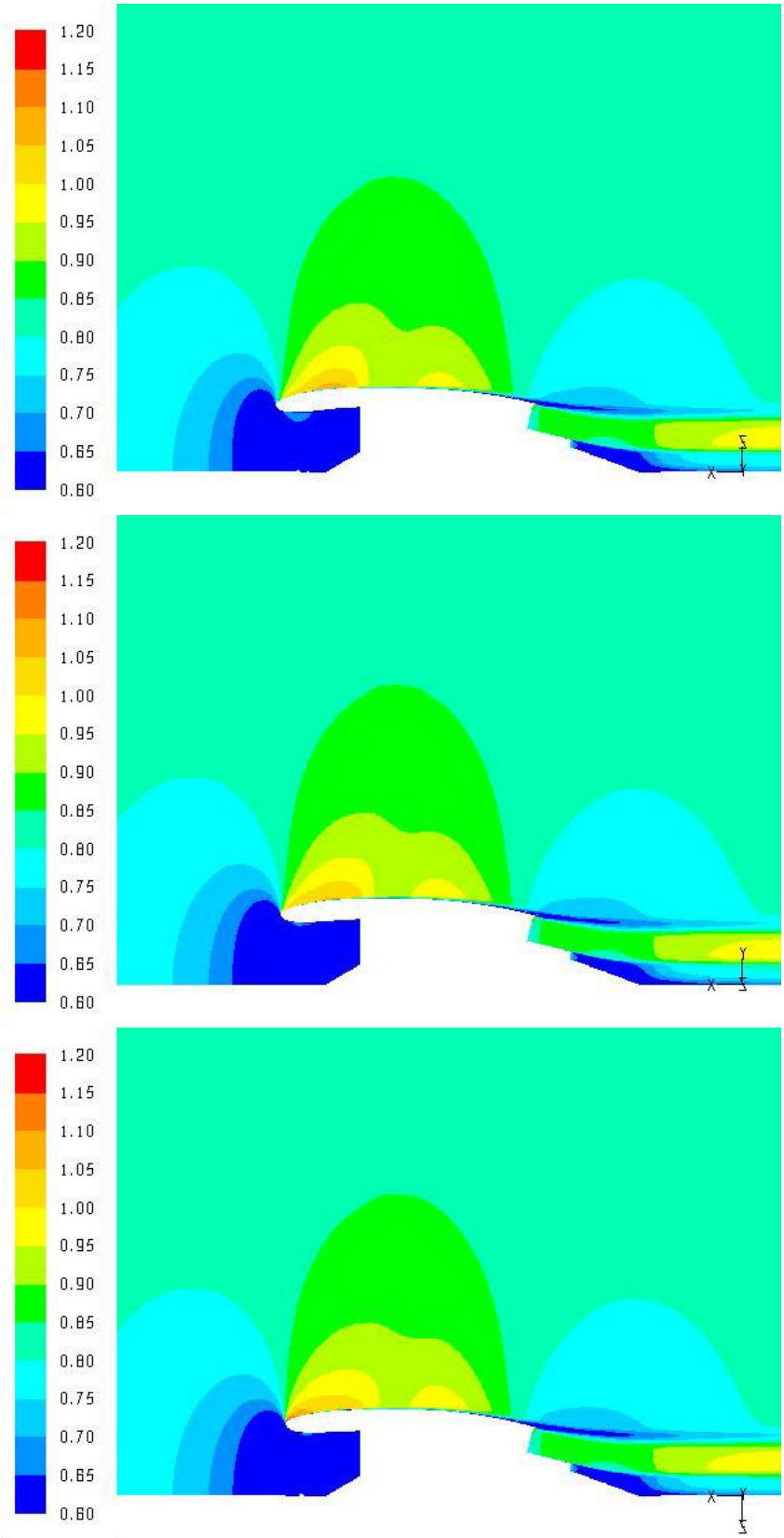

Figure A. 3 Mach number profiles of the Crown (top), Side (middle) and keel (bottom) sections of the nacelle of a Maximum diameter of + 2.0 % change with respect to the reference nacelle.

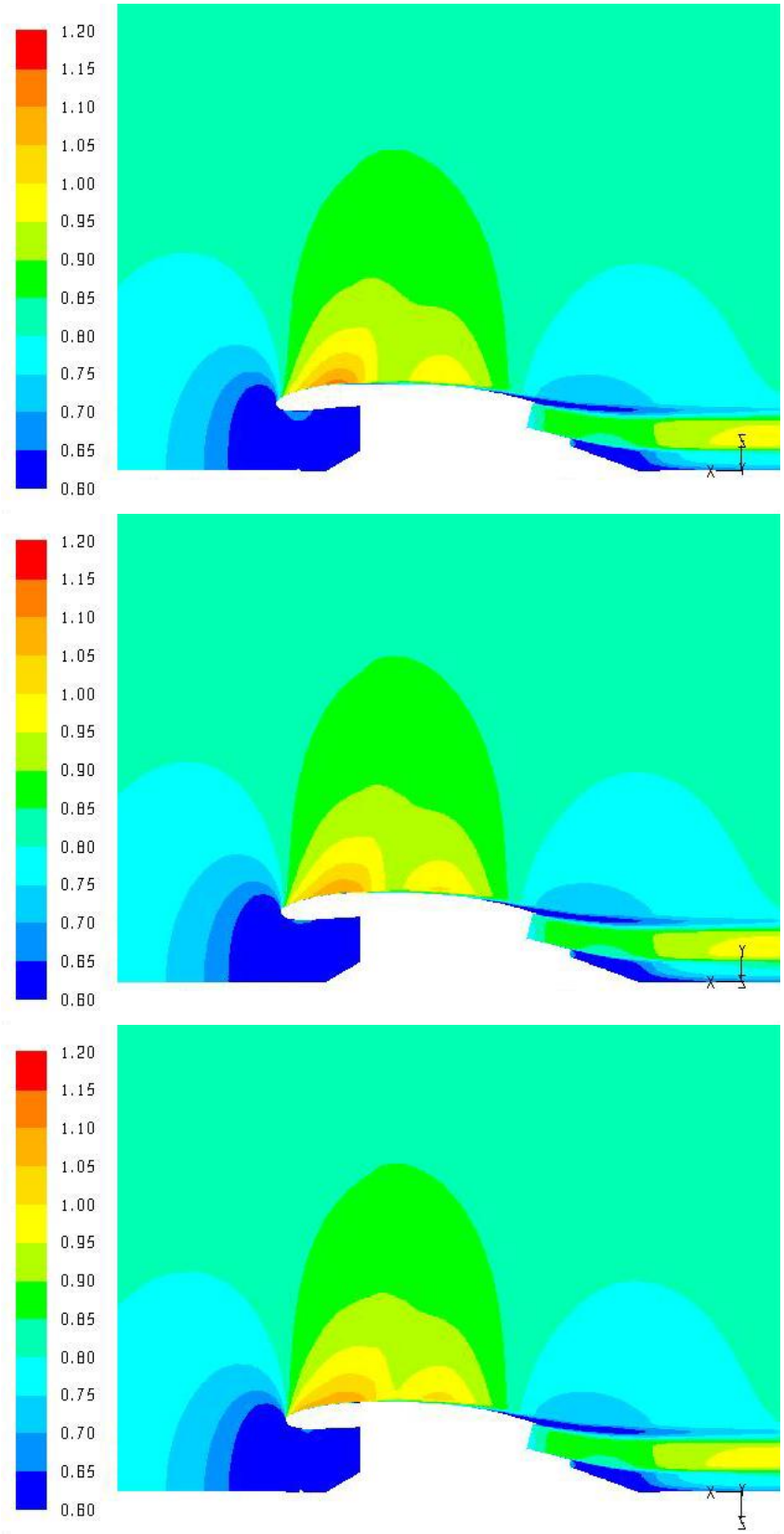

Figure A. 4 Mach number profiles of the Crown (top), Side (middle) and keel (bottom) sections of the nacelle of a Maximum diameter of + 6.0 % change with respect to the reference nacelle

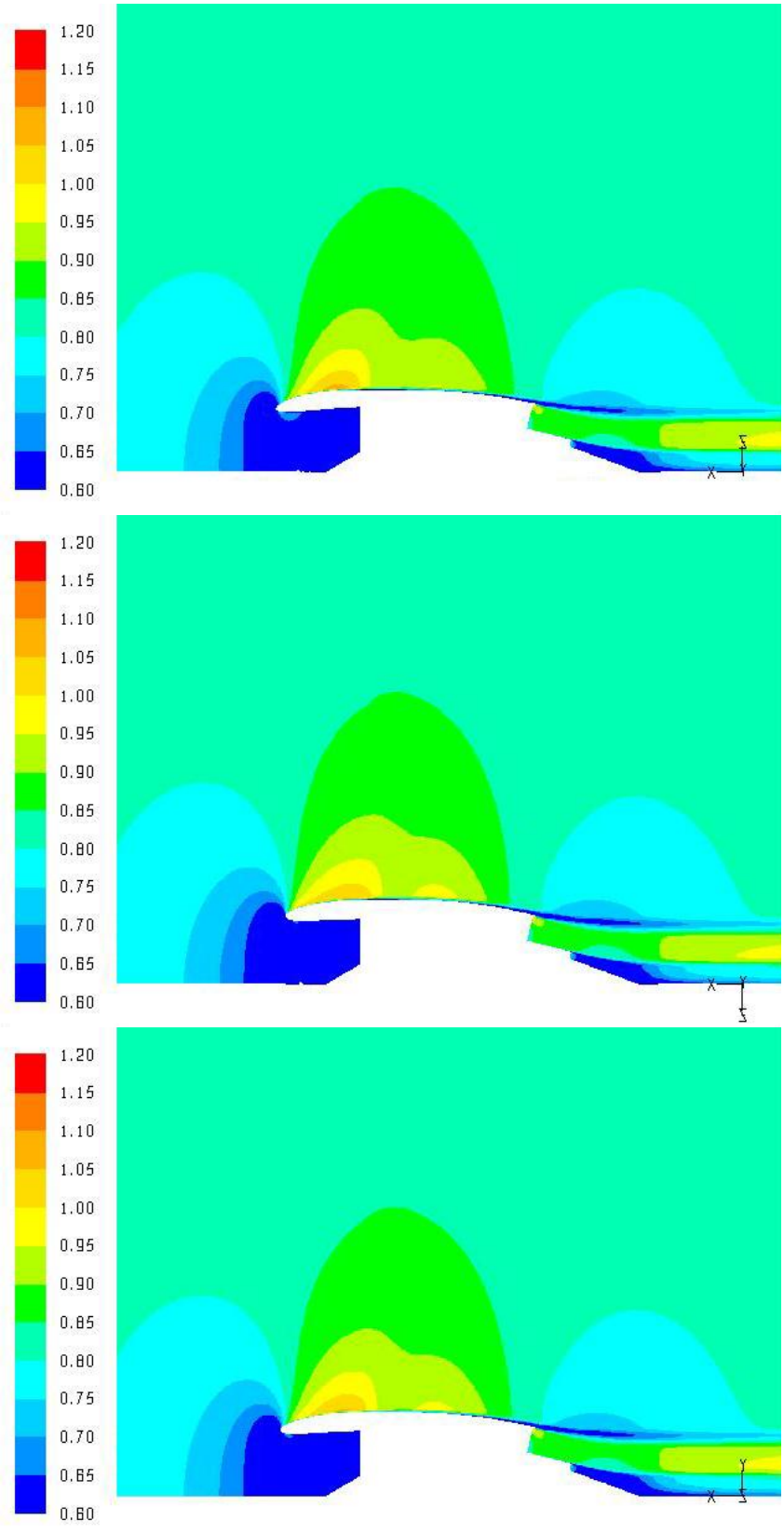

Figure A. 5 Mach number profiles of the Crown (top), Side (middle) and keel (bottom) sections of the nacelle of a Highlight diameter of -6.0 % change with respect to the reference nacelle.

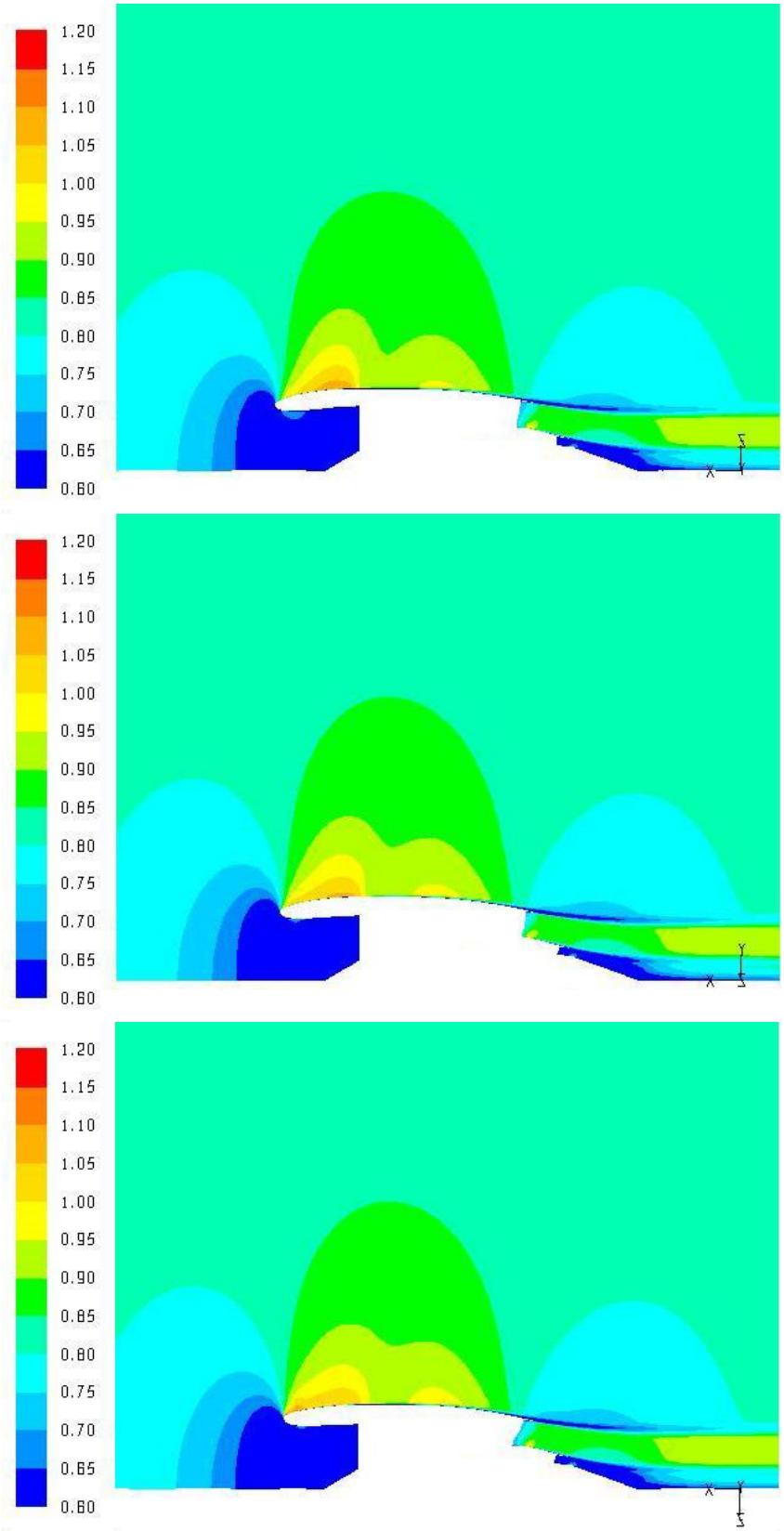

Figure A. 6 Mach number profiles of the Crown (top), Side (middle) and keel (bottom) sections of the nacelle of a Highlight diameter of - 2.0 % change with respect to the reference nacelle.

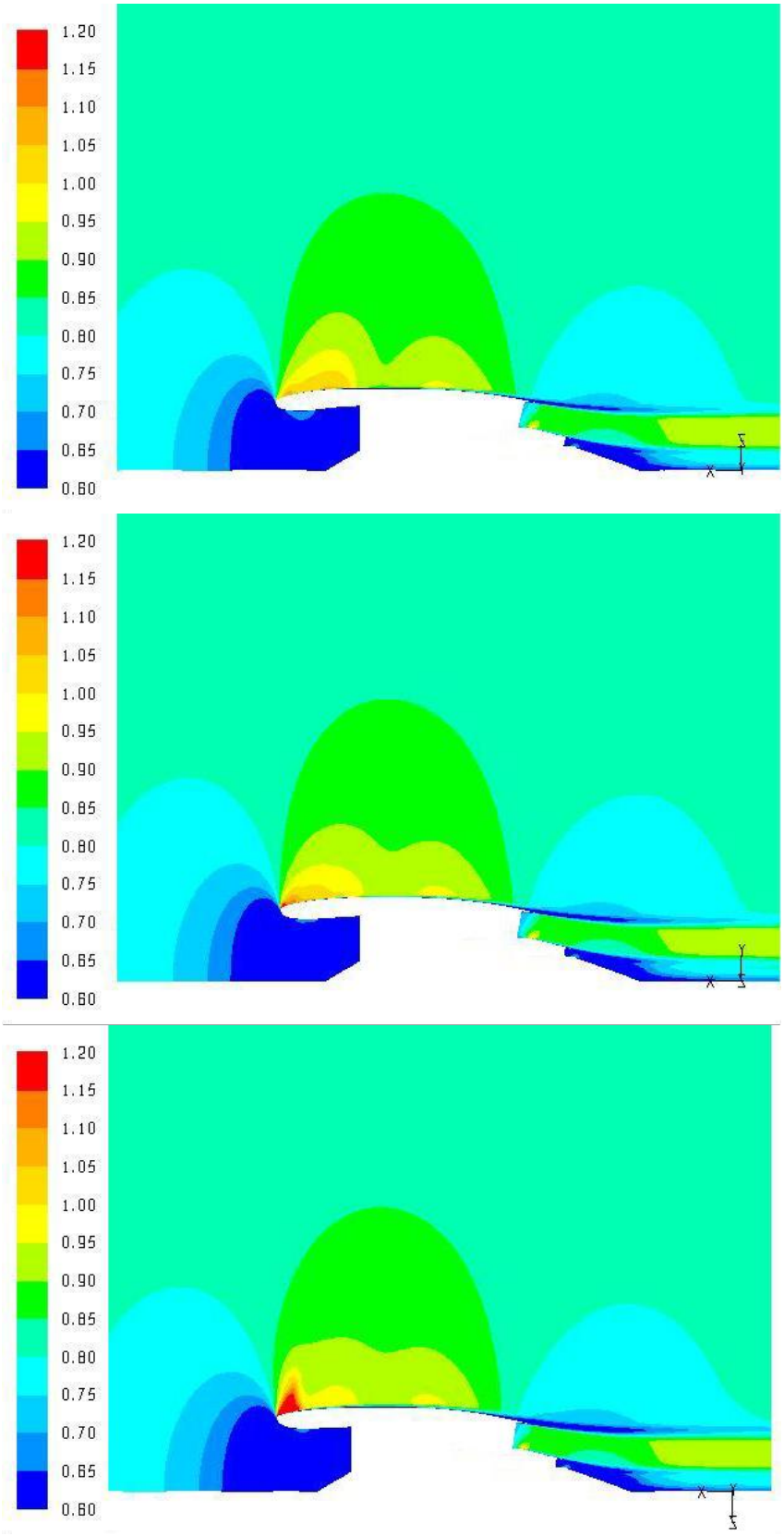

Figure A. 7 Mach number profiles of the Crown (top), Side (middle) and keel (bottom) sections of the nacelle of a Highlight diameter of + 2.0 % change with respect to the reference nacelle.

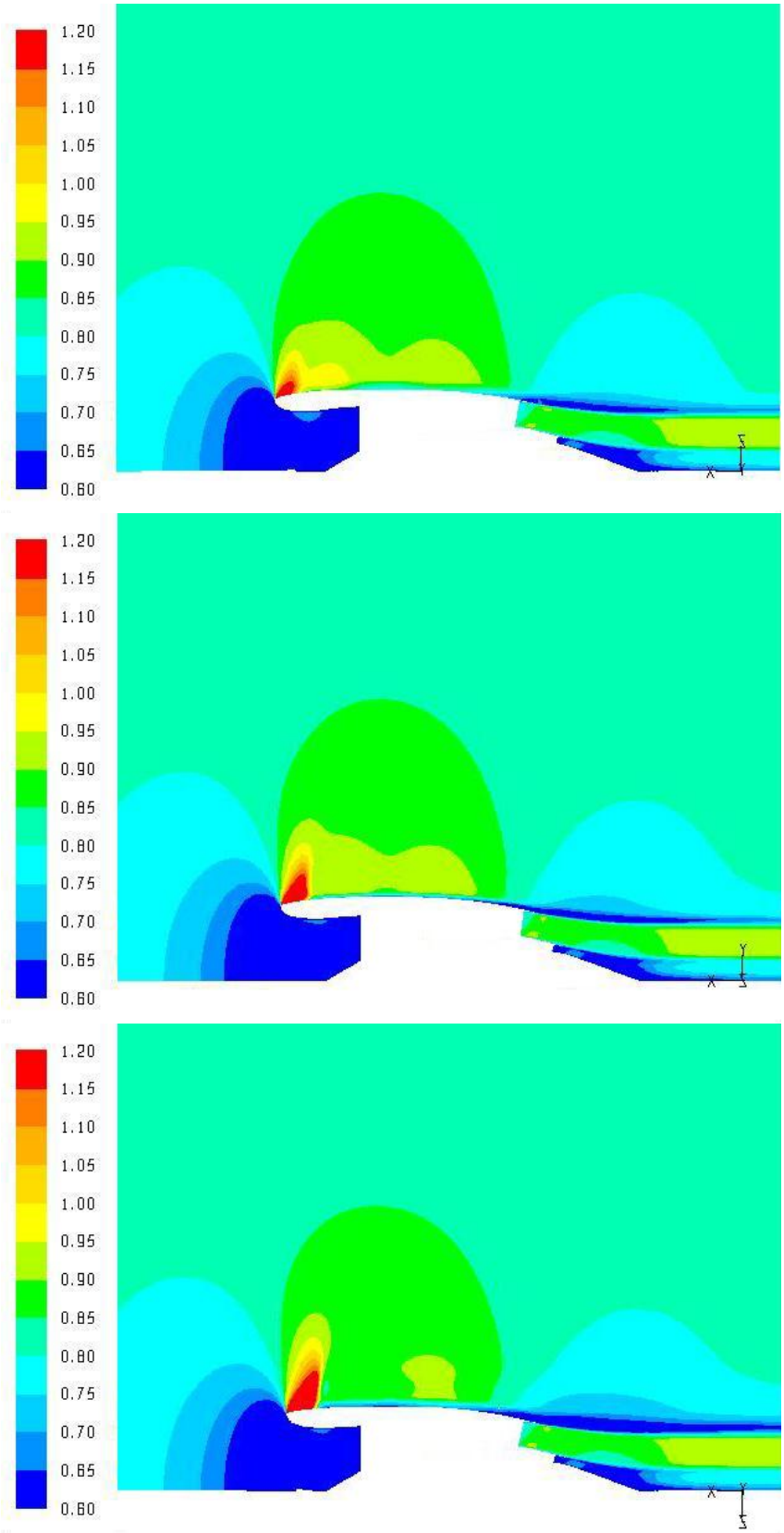

Figure A. 8 Mach number profiles of the Crown (top), Side (middle) and keel (bottom) sections of the nacelle of a Highlight diameter of + 6.0 % change with respect to the reference nacelle.

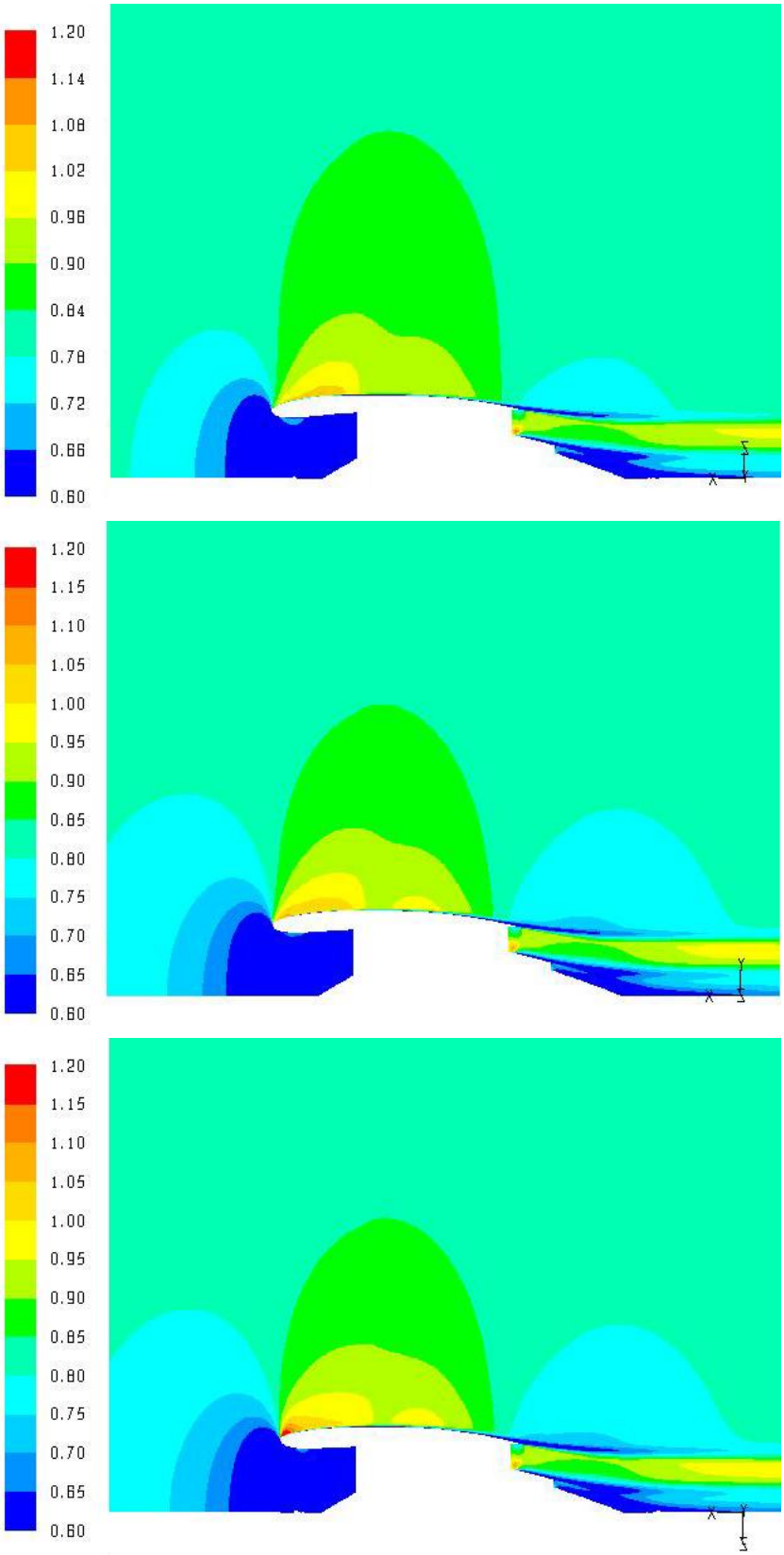

Figure A. 9 Mach number profiles of the Crown (top), Side (middle) and keel (bottom) sections of the nacelle of a length of - 6.0 % change with respect to the reference nacelle.

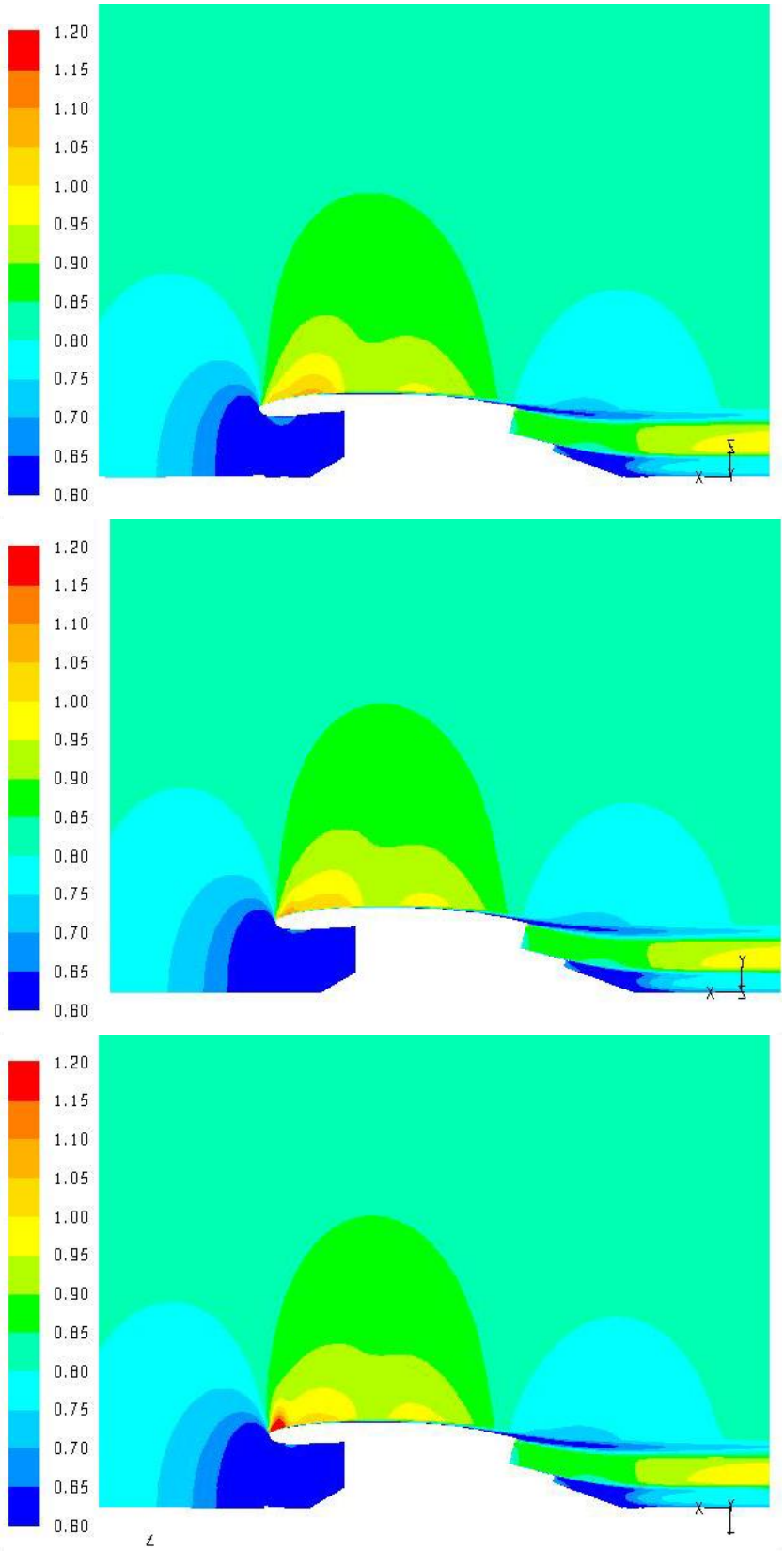

Figure A. 10 Mach number profiles of the Crown (top), Side (middle) and keel (bottom) sections of the nacelle of a length of - 2.0 % change with respect to the reference nacelle.

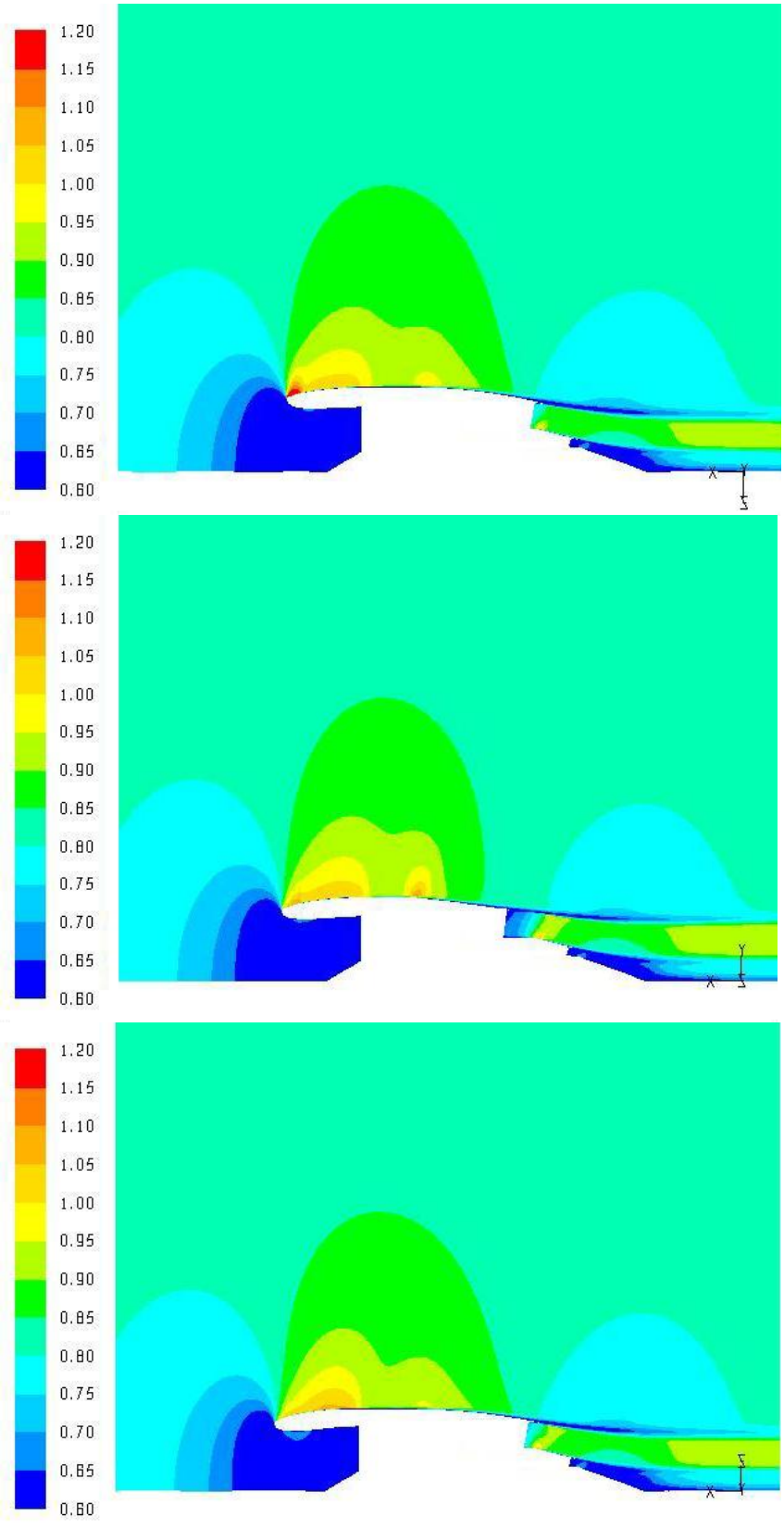

Figure A. 11 Mach number profiles of the Crown (top), Side (middle) and keel (bottom) sections of the nacelle of a length of + 2.0 % change with respect to the reference nacelle.

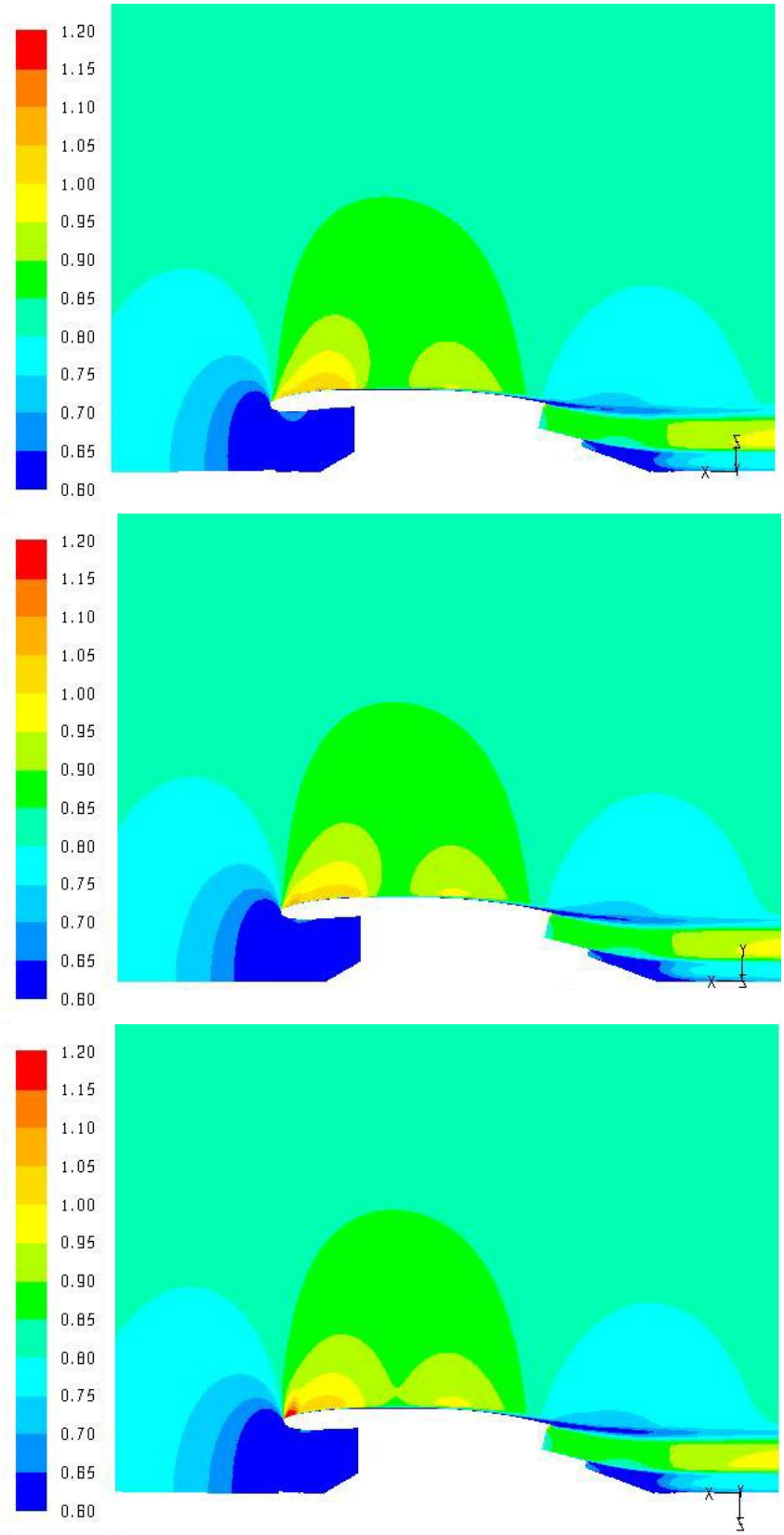

Figure A. 12 Mach number profiles of the Crown (top), Side (middle) and keel (bottom) sections of the nacelle of a length of + 6.0 % change with respect to the reference nacelle.

B. Profiles of Cp and Ma number of 3D Isolated Nacelle simulations

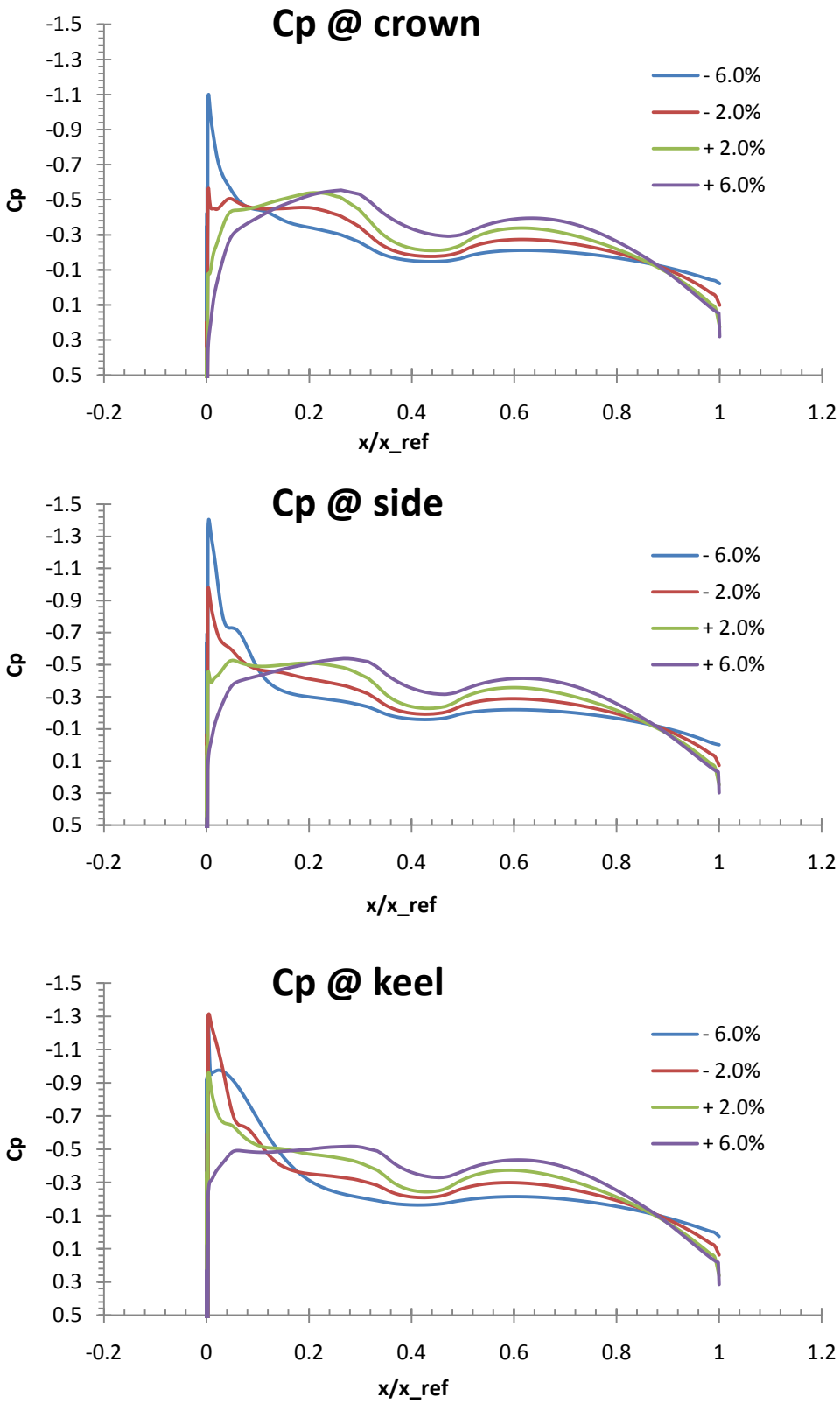

Figure B. 1 Cp profiles of 3D Isolated nacelle simulations with Dmax variations

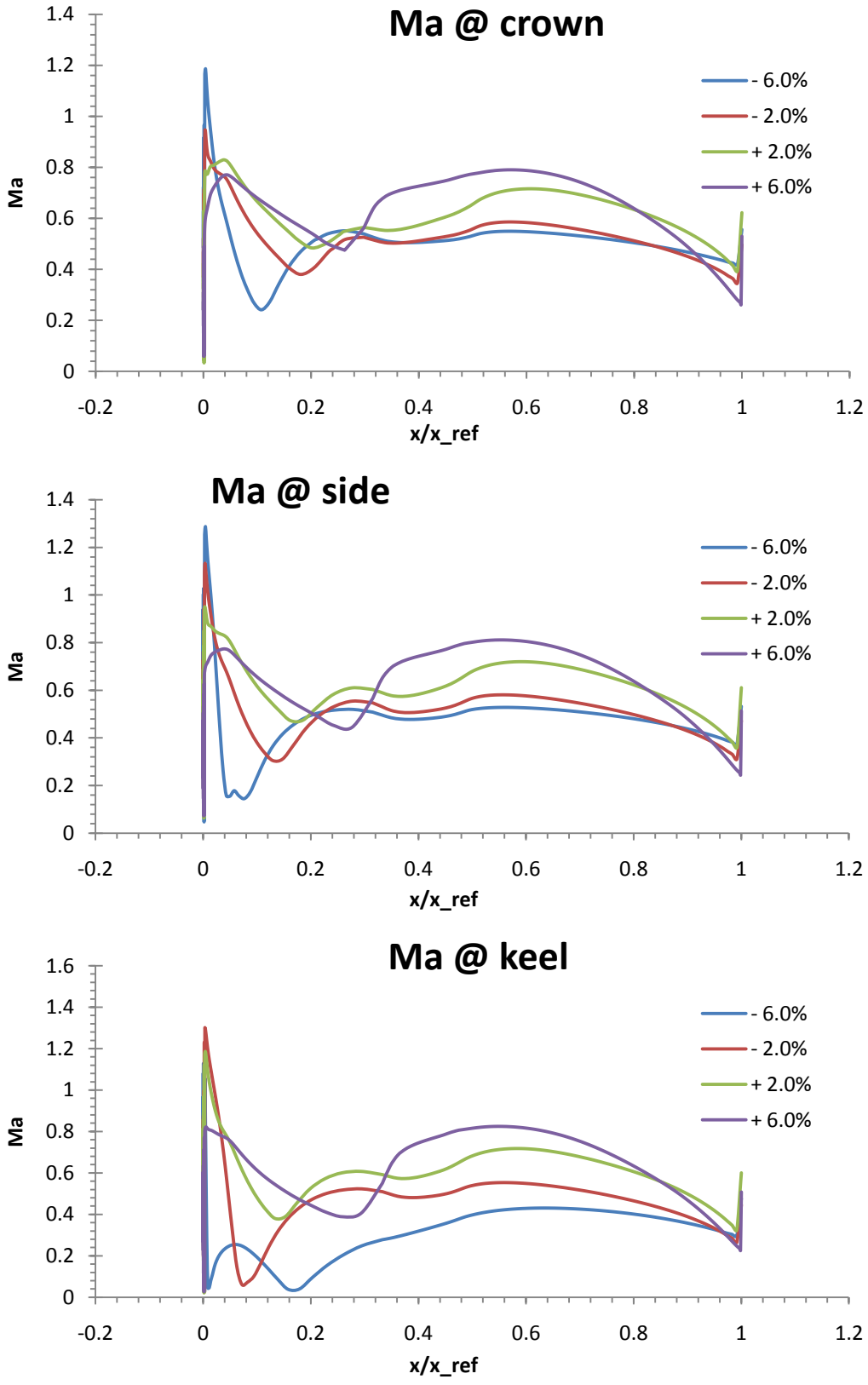

Figure B. 2 Ma profiles of 3D Isolated nacelle simulations with Dmax variations

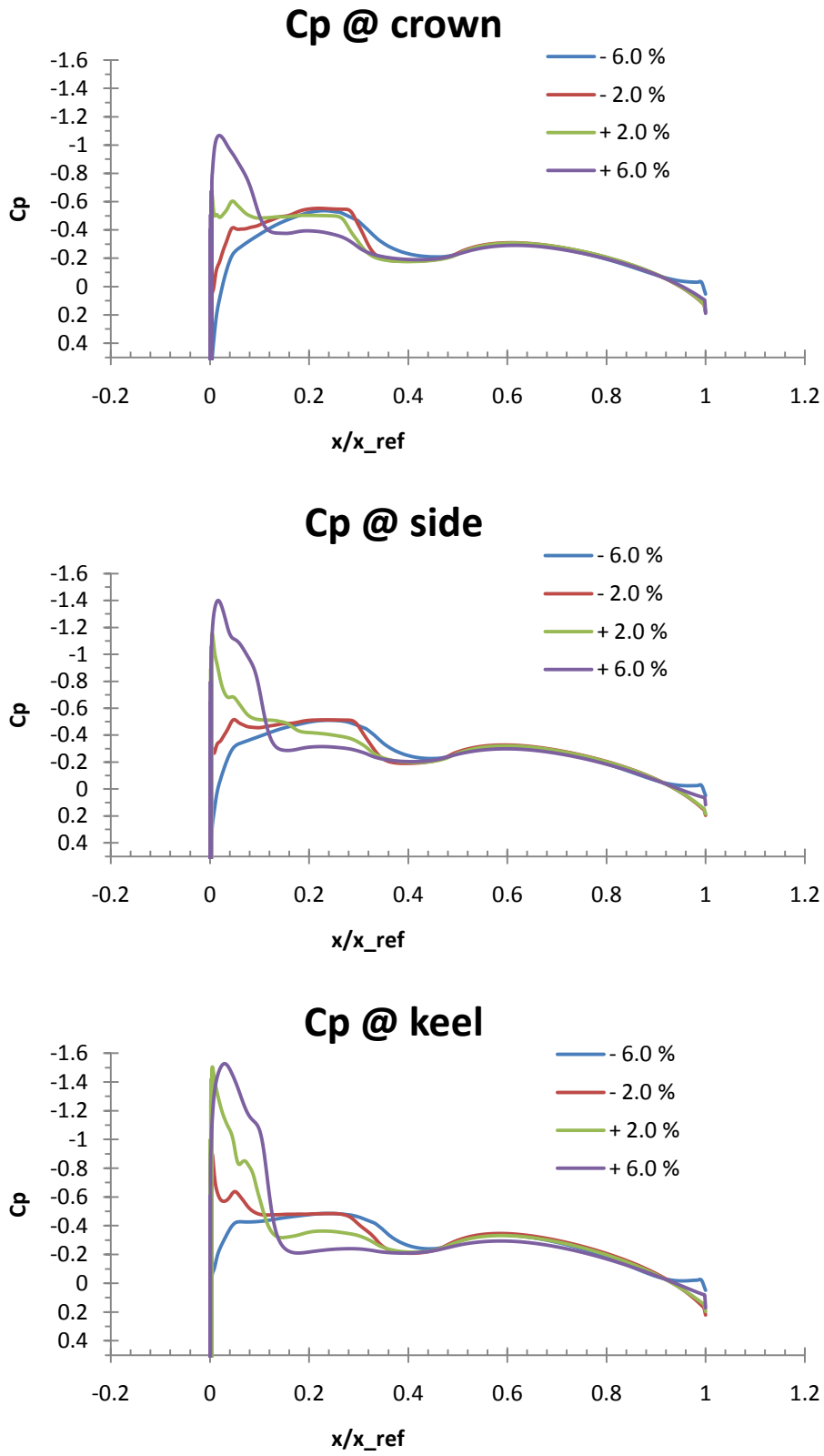

Figure B. 3 Cp profiles of 3D Isolated nacelle simulations with Dhigh variations

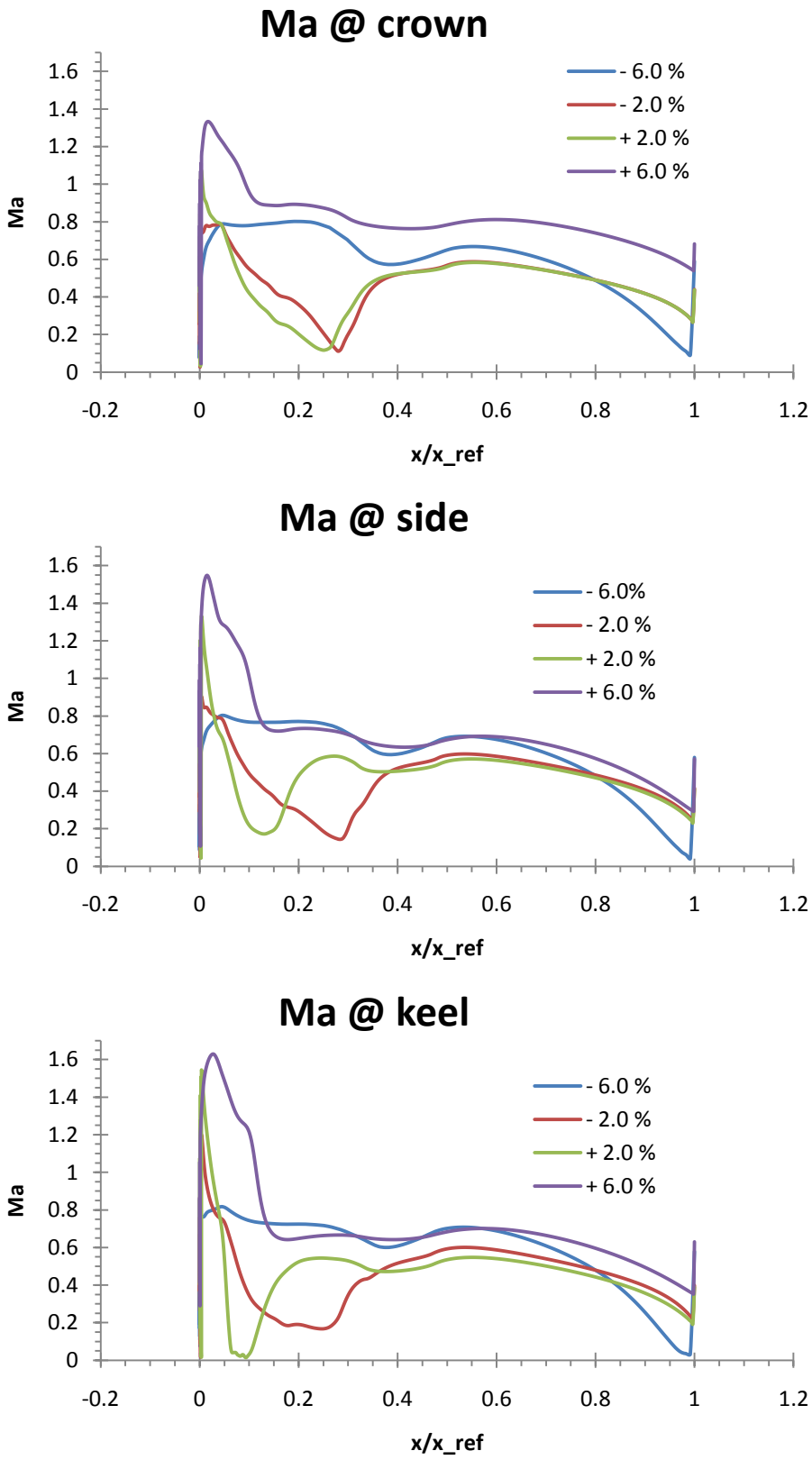

Figure B. 4 Ma profiles of 3D Isolated nacelle simulations with Dhigh variations

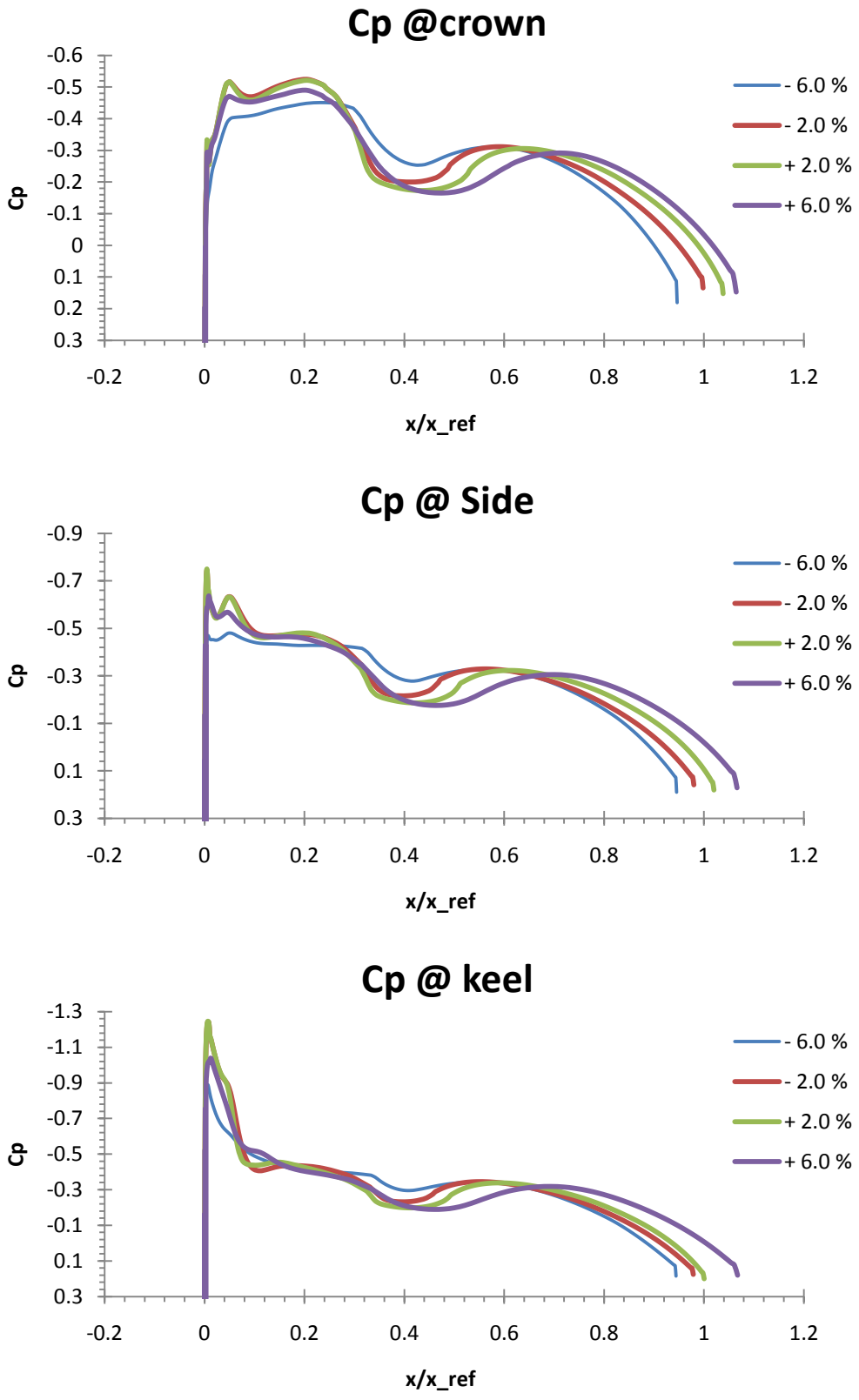

Figure B. 5 Cp profiles of 3D Isolated nacelle simulations with length variations

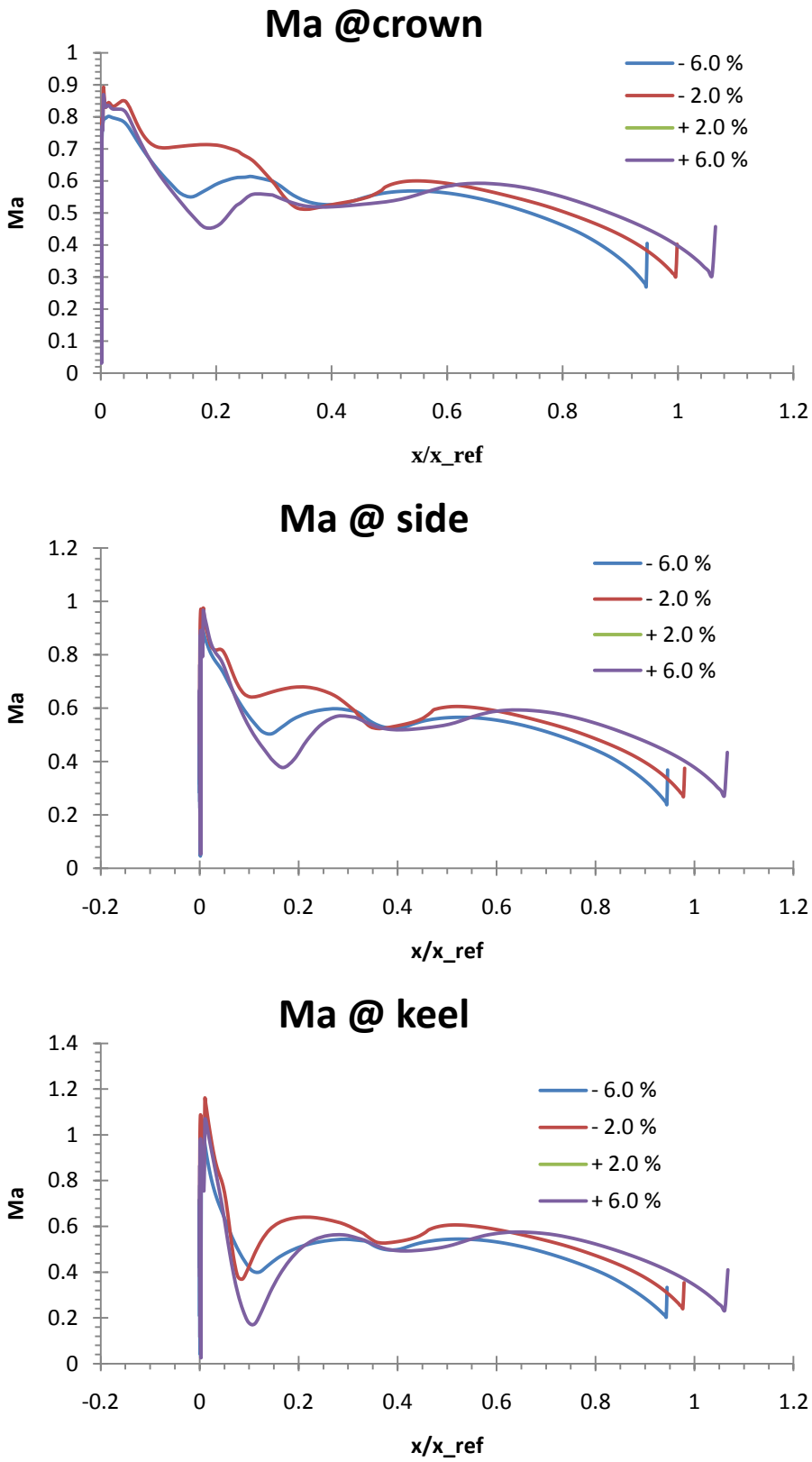

Figure B. 6 Ma profiles of 3D Isolated nacelle simulations with length variations

C. Cp profiles at the far section of the wing (w/Dmax=6.3).

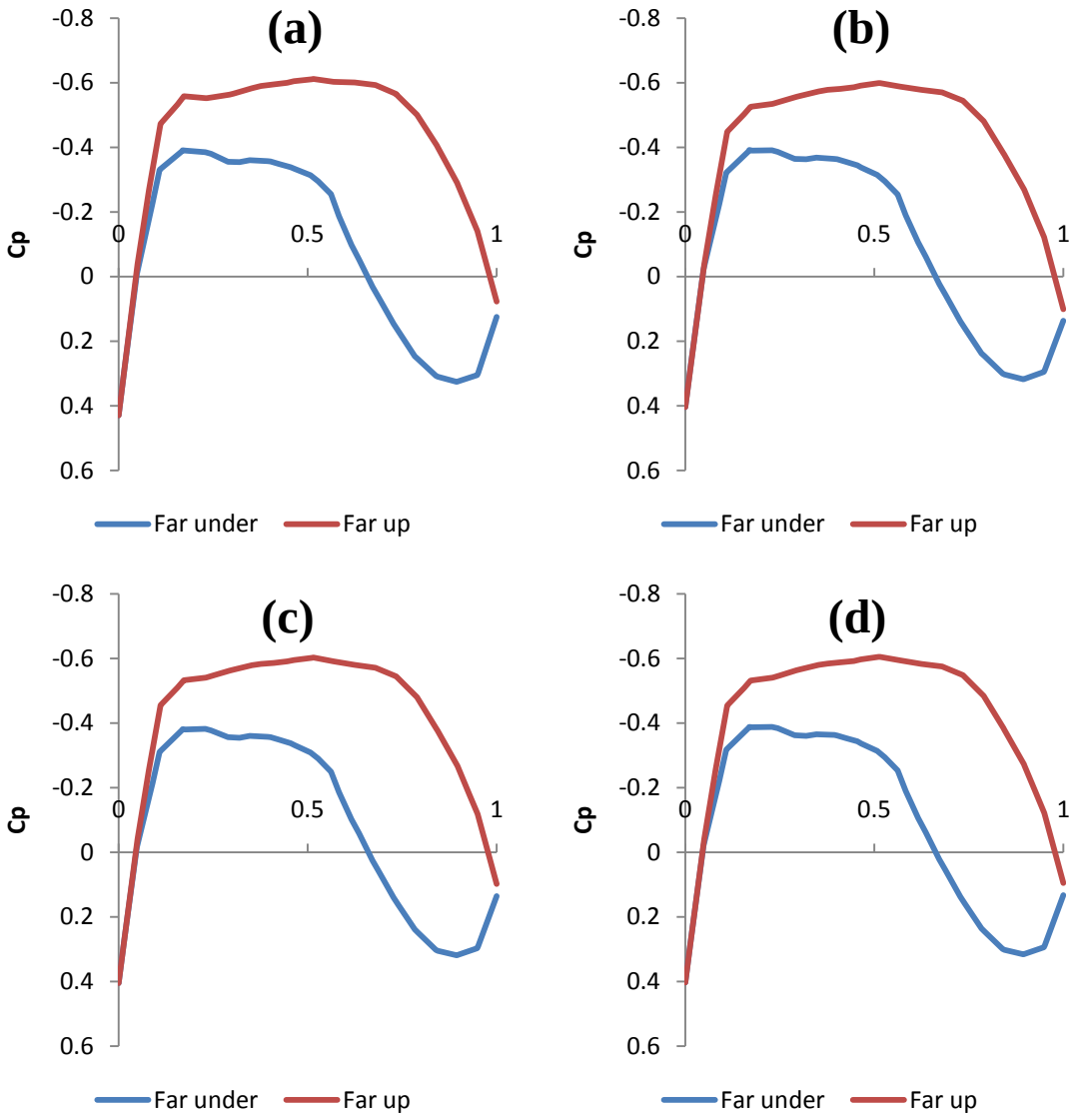

Figure C. 1 (a) h/Dmax= 0.547, x/l=0.7223 (Base value); (b) h/Dmax= 0.5, x/l=0.8; (d) h/Dmax=0.55 , x/l=0.75; (e) h/Dmax=0.6, x/l=0.7

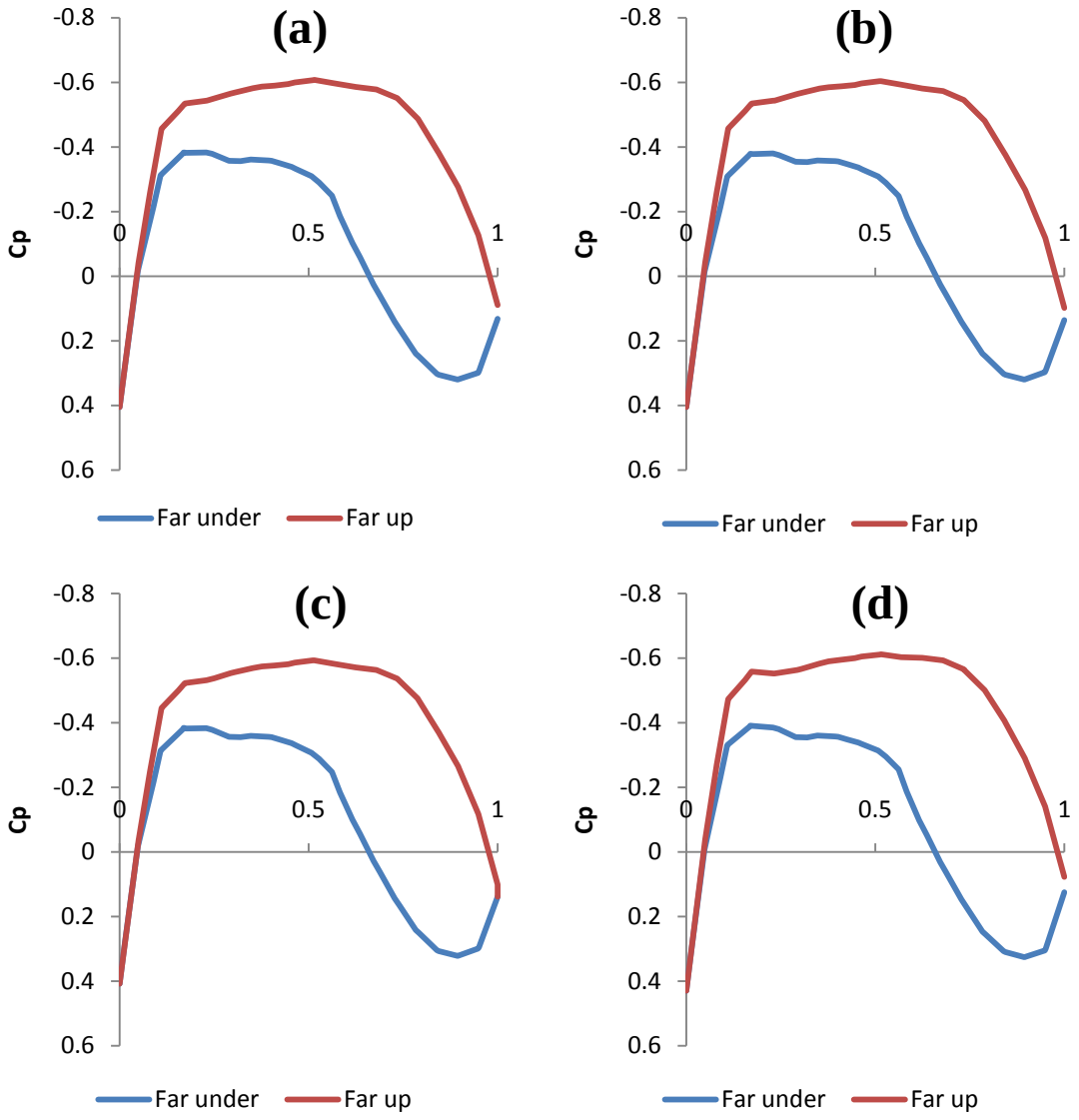

Figure C. 2 (a) h/Dmax=0.6 , x/l=0.75; (b) h/Dmax=0.6 , x/l=0.8; (d) h/Dmax= 0.65, x/l=0.65; (e) h/Dmax=0.65 , x/l=0.7